Abstract

Structural Basis for the Assembly of OmcS and OmcS-like Cytochrome Nanowires

in Diverse Microbial Species

Vishok Srikanth

2022

Microbial extracellular electron transfer (EET) via surface appendages called microbial nanowires is important in a wide range of globally significant environmental phenomena and for applications in bioremediation, bioenergy, and biofuels. Since 2005, these nanowires have been thought to be type IV pili composed solely of PilA-N protein. However, structural analyses demonstrated that during EET, rather than pili, cells produce nanowires made up of cytochromes OmcS and OmcZ. The micrometer-scale OmcS nanowires show seamless heme stacking along the length of the filament, allowing for efficient electron transfer to extracellular acceptors or syntrophic partner cells.

Polymerization of cytochromes is important in several biological processes, such as apoptosis, and for the development of bioelectronic materials. Although it has been known for more than half a century that cytochromes can form polymers, synthetic polymerization methods have yielded only short oligomers. Nevertheless, the physiological relevance of OmcS and OmcZ filaments has been strongly questioned, despite previous studies showing that OmcS and OmcZ are essential for EET to minerals and synthetic electrodes, respectively. Furthermore, the underlying polymerization mechanism of these cytochrome filaments is unknown, and their existence beyond *G. sulfurreducens* has not been established.

In this work, we explain previous results which demonstrated that perturbations to the type IV pili proteins in *G. sulfurreducens* had a strong influence on EET phenotypes. We find that *G. sulfurreducens* binds PilA-N to PilA-C to assemble heterodimeric pili which remain periplasmic under nanowire-producing conditions that require EET. PilA-N–C filaments lack π-stacking of aromatic side chains, previously hypothesized as a mechanism by which pili could efficiently transport electrons. These *G. sulfurreducens* pili show substantially lower conductivity than cytochrome nanowires. In contrast to

surface-displayed type IV pili, PilA-N–C filaments show structure, function, and localization akin to type 2 secretion pseudopili. Secretion of OmcS and OmcZ nanowires is lost when pilA-N is deleted and restored when PilA-N–C filaments are reconstituted. Substitution of *pilA-N* with type IV pilins of other microorganisms also causes loss of secretion of OmcZ nanowires. These findings have important implications for understanding EET in diverse bacteria and for efforts to design and assemble synthetic protein nanowires.

Our work also shows that metal coordination across inter-protomer interfaces is essential for OmcS nanowire biogenesis and EET *in vivo*, and enables pH-controllable reversible nanowire assembly *in vitro*. We thus show that chemically tuning metal-ligand coordination and protein-protein interfaces yields nanowires with controllable assembly. Our studies reveal a novel cytochrome polymerization mechanism distinct from previous examples of cytochrome assembly in engineered or disease conditions. Harnessing the ability of bacteria to construct self-assembling and environment-sensing supramolecular structures functional in acidic conditions and at high temperatures could yield stimuli-responsive bioelectronics.

Finally, we have examined genetic patterns in species encoding OmcS-like sequences, identifying a previously unknown gene cluster that colocalizes with OmcS-like sequences in diverse environmentally significant bacteria. We find that *Geoalkalibacter subterraneus* and *Anaeromyxobacter dehalogenans* also use OmcS-like nanowires for EET through the action of these gene clusters. Combining cryo-electron microscopy and structural modeling with functional studies, we show that these bacteria produce distinct OmcS-like nanowire structures with varied conductivity and redox properties. As OmcS-like sequences and this related gene cluster are widespread, this work suggests a specialized biogenesis system for cytochrome nanowires across diverse species and environments.

Overall, this work advances understanding of the biological context in which OmcS filaments are assembled, the protein-protein interactions within these filaments necessary for their function in EET, and the prevalence of these filaments in diverse environmentally important species.

Structural Basis for the Assembly of OmcS and OmcS-like Cytochrome Nanowires in Diverse Microbial Species

A Dissertation
Presented to the Faculty of the Graduate School
Of
Yale University
In Candidacy for the Degree of
Doctor of Philosophy

By
Vishok Srikanth

Dissertation Director: Nikhil S. Malvankar

December 2022

Table of Contents

Acknowledgements

I would like to offer my gratitude to my advisor, Professor Nikhil Malvankar, for providing me with the opportunity to conduct my graduate research in his laboratory, and to the other members of my research committee – Professors Gary Brudvig, Fred Sigworth, and Yong Xiong – for the expertise and time they so generously contributed to my work.

For their assistance, support, and camaraderie, I wish to thank all of the members of the Malvankar Lab whose time in the group overlapped with mine. I owe a special, additional thank-you to those members of the Malvankar group with whom I worked closely on a number of projects over the years: Patrick O'Brien, Yangqi Gu, Fadel Samatey, and Catharine Shipps.

I also would like to thank all the friends and family who supported me throughout my time in graduate school. In particular, I want to thank my parents for their willingness to foster my interest in science, for the way they prepared me to face the challenges I would encounter along the way, and for the unconditional love and support they have provided throughout every stage of this adventure.

Abbreviations

AFM	atomic force microscopy
aMD	accelerated molecular dynamics
BCA	bicinchoninic acid
CD	circular dichroism
cryo-EM	cryogenic electron microscopy
CT	charge transfer
CTF	contrast transfer function
DIET	direct interspecies electron transfer
DNA	deoxyribonucleic acid
DPV	differential pulse voltammetry
EET	extracellular electron transfer
EPR	electron paramagnetic resonance
EXAFS	extended X-ray absorption fine structure
ETA	ethanolamine
FSC	Fourier shell correlation
FT	Fourier transform
His16	histidine 16
HALS	highly anisotropic low spin
HS	high spin
IM	inner membrane
I-V	current-voltage
LC-MS/MS	liquid chromatography with tandem mass spectrometry
LS	low spin
MD	molecular dynamics

MM-GBSA	molecular mechanics generalized Born solvation area
(m)RNA	(messenger) ribonucleic acid
OM	outer membrane
OmcS/OmcZ	outer membrane cytochrome S/Z
PP	periplasm
RMSD	root mean square deviation
RSCC	real-space correlation coefficient
RT-(q)PCR	reverse transcription-(quantitative) polymerase chain reaction
SDS(-PAGE)	sodium dodecyl sulfate(-polyacrylamide gel electrophoresis)
SHE	standard hydrogen electrode
T2SS	type II secretion system
T4P	type IV pilin/type IV pili
TEM	transmission electron microscopy
UV-vis	UV-visible
WT	wild-type
XAS	X-ray absorption spectroscopy

List of Figures

List of Supplementary Figures

List of Tables

List of Supplementary Tables

Introduction

1.1 Extracellular electron transfer in environmentally abundant bacteria

Cellular respiration is a series of oxidation and reduction reactions key to the metabolism of cells across multiple domains of life[1]. Well-studied respiration mechanisms mostly require the terminal electron acceptor in these chains of reactions to be a small molecule that can enter the cell membrane, with a common example being molecular oxygen[2].

Many microbes inhabit environments where membrane-ingestible terminal electron acceptors are rare. Some of these microbes have developed mechanisms for utilizing terminal electron acceptors outside the cell – often minerals in the environment[3] or other microbes[4]. This requires cells to export electrons generated by intracellular metabolic reactions outside of the cell membrane. The terminal electron acceptors that these cells access may be micrometers[5, 6] or centimeters[7] away – distances that vastly exceed the size of a single cell.

The mechanism by which cells efficiently move electrons during this process of extracellular electron transport (EET) is of interest for several reasons, including but not limited to:

(1) An improved knowledge of microbes involved in significant biogeochemical processes[8-10]

(2) The potential to harness microbial EET for bioremediation and power generation[11-13]

(3) An interest in engineering biomaterials and cells that can interface with electronics[14-16]

1.2 *G. sulfurreducens* as a model system for microbial EET

One vein of research into microbial EET has focused on species of *Geobacter*, a genus of gram-negative bacteria that are abundant in aquatic sediments[17]. These bacteria show the ability to export electrons extracellularly to minerals in the environment[18], to syntrophic partners cells in cocultures[19], and to anodes[20] and cathodes[21] in microbial electrochemical and fuel cells. Many of these studies have utilized *Geobacter sulfurreducens* as a model system, due to its established culture methods[22, 23], relative genetic tractability[24, 25], and the high current density it produces in microbial fuel cells[26].

Initial characterization of *G. sulfurreducens* EET identified that micrometer-scale filaments on the outer cell surface, termed "microbial nanowires," were required for the reduction of extracellular

insoluble minerals such as Fe(III) oxide[5]. These nanowires were proposed to be protein polymers of PilA-N, sometimes referred to as PilA, a homolog of the N-terminal domain of type IV pilin proteins. In other species, these type IV pili (T4P) are extracellular filaments that primarily play a role in bacterial attachment and motility[27, 28]. The hypothesis that *G. sulfurreducens* EET was performed by pili, i.e., PilA-N homopolymers, was originally based on observations that *pilA-N* was highly transcribed during EET, and that deletion of PilA-N abolished the presence of extracellular filaments on the cell surface and prevented EET to minerals[5].

Subsequent studies demonstrated that other alterations to *pilA-N* impacted cells' capacity to perform EET to multiple terminal electron acceptors[29-31], altering the functional properties of *G. sulfurreducens* biofilms[32] and of purified preparations of extracellular filaments[33, 34] – in particular affecting their observed electronic conductivity. Perturbations of other type IV pilus system proteins in *G. sulfurreducens* have also been shown to negatively impact EET[35, 36]. In order to explain how PilA-N filaments could directly mediate EET by transporting electrons over micrometer-scale distances, it was hypothesized that *Geobacter* pili assembled into a unique-among-T4P structure that positioned aromatic amino acids within π-stacking distances[37, 38]. Such a structure was proposed to represent a unique mechanism by which protein filaments could mediate long-distance electron transport without the need for metal cofactors.

Along with T4P proteins, several *c*-type cytochromes – a type of redox-active protein post-translationally modified with covalently bound iron-containing heme porphyrin moieties – were known to be essential for *G. sulfurreducens* EET under various conditions, and deletion of many others negatively impacted cells' EET capacity[39]. Of particular note, OmcS was found to be essential for EET to insoluble Fe(III) oxides[40] and OmcZ was found to be essential for the formation of thick (ca. 100 µm), conductive biofilms in microbial fuel cells[41]. As cytochromes were not known to form micrometer-scale filaments, one model proposed that long-distance electron transport in *Geobacter* EET was performed by pili[42, 43]. In this view, cytochromes such as OmcS and OmcZ were thought to bind to pili and facilitate only the final electron transfer reactions, between pili and terminal electron acceptors. Though the assertion that *Geobacter* extracellular filaments were PilA-N polymers was not widely contested, a

competing model argued that cytochromes arranged along pili filaments were directly responsible for the observed electron transport behavior in *Geobacter* filaments[44, 45]. These competing models were controversial, in large part because the structures of *Geobacter* pili and the cytochromes essential for EET remained unknown.

1.3 Characterization of *G. sulfurreducens* OmcS

OmcS had been shown to be essential for *G. sulfurreducens* EET to Fe(III) oxide[40] and deletion of OmcS also impacted cell growth utilizing other extracellular electron acceptors[46], including syntrophic partner cells[19]. *G. sulfurreducens* grown in microbial fuel cells, e.g., on graphite anodes at a potential of +300 mV vs. standard hydrogen electrode (SHE), were slower to form thick, highly conductive biofilms when the *omcS* gene was deleted[20]. Localization studies of OmcS, conducted via immunogold labeling, reported that OmcS was detected along extracellular filaments; this was interpreted as having visualized monomeric OmcS protein 'decorating' PilA-N filaments[47]. An engineered strain that formed highly cohesive biofilms with enhanced EET properties was reported to produce an elevated abundance of OmcS and display an elevated number of extracellular filaments on the cell surface; the filaments were presumed to be PilA-N filaments[48].

OmcS was characterized[49] *in vitro* in a study which reported challenges solubilizing the protein – as a result, OmcS was purified by a procedure which included detergent extraction in 5% sodium dodecyl sulfate (SDS), followed by heating to 100 °C in the presence of trace SDS. The OmcS thus obtained was reported to show little defined secondary structure content as assayed by circular dichroism (CD) spectroscopy (estimated ~10% α helices, no noted β sheet content). The protein was shown to contain six covalently bound heme moieties, consistent with the number of *c*-type cytochrome-characteristic heme binding motifs in the primary protein sequence. Electron paramagnetic resonance (EPR) spectroscopy indicated that all six heme irons were coordinated by two histidine residues. The midpoint potential observed for the OmcS prepared in this manner was -212 mV vs. SHE – comparable to model compounds with bis-histidine-ligated, solvent-exposed hemes[50-52].

1.4 Molecular structure of OmcS filaments

Cryogenic electron microscopy (cryo-EM) was used to characterize filaments prepared from *G. sulfurreducens* cells, including cells that were grown in microbial fuel cell environments where EET is required for bacterial growth (Figure 1.1A)[53]. The OmcS protein assembled in the filament showed ~13% α and 3_{10} helices and ~6% β strands; the remaining ~81% of the protein was arranged in coils lacking any defined secondary structure motif. Protomers within the filament are arranged in a one-start helix with a rise of 46.7 Å and a rotation of -83.1° per subunit (Figure 1.1B-C). This arrangement of the protomers gives rise to a continuous chain of hemes along the length of the filament. The heme groups of OmcS are arranged in parallel-stacked pairs, with each such pair forming T-stacked arrangements with the neighboring heme pairs – both within individual protomers and across the protomer interfaces in the filaments (Figure 1.1D). This continuous arrangement of iron-containing heme groups along the

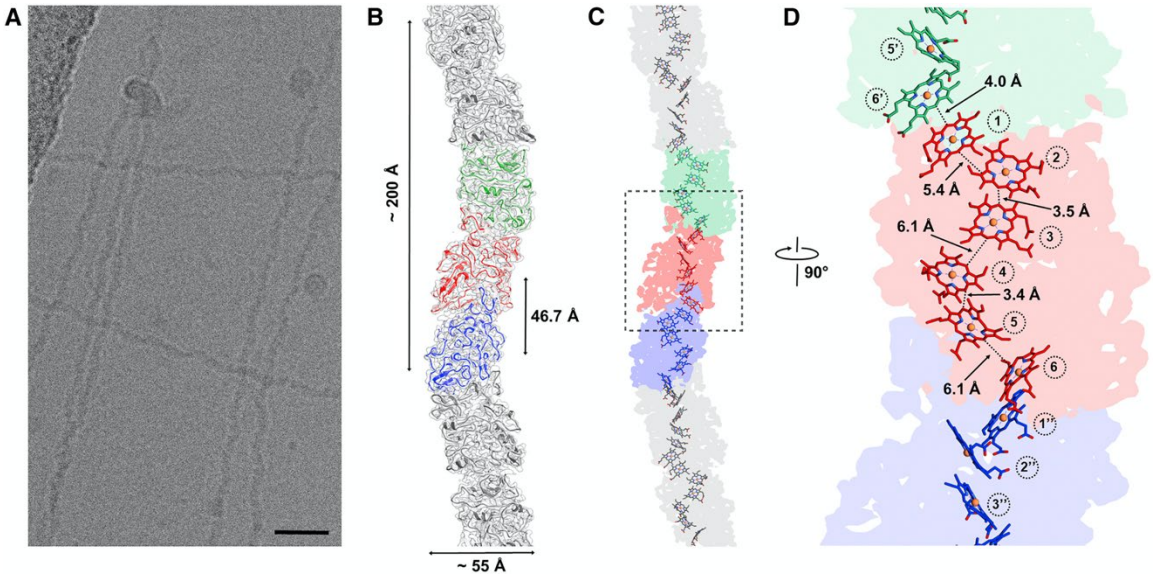

Figure 1.1. Structure of microbial nanowires reveals closely stacked hemes in an OmcS filament.

A, Cryo-EM image of the purified wild-type electrically conductive filaments showing a sinusoidal undulation, with a pitch of ~200 Å shown in (B). Scale bar, 200 Å. **B**, The surface of the reconstruction (transparent gray) with superimposed ribbon models of the OmcS subunits with three subunits in the center in three different colors. **C**, Each subunit contains six hemes closely stacked over the micrometer lengths of the filaments. **D**, A zoomed region of the box shown in (C) with the minimum observed edge-to-edge distances indicated between hemes numbered in circles. The distance between two hemes in adjacent subunits (heme 1 and heme 6') is comparable to the distances between parallel-stacked hemes within a subunit (heme 2:heme 3 and heme 4:heme 5).

This figure and its accompanying legend have been reproduced from Wang et al.[53].

micrometer length of the filament was proposed to be the key feature that allowed these filaments to efficiently move electrons along their length during EET.

Protomer interfaces were proposed to be stabilized by forces including protein-protein interactions at the large inter-subunit interface (Figure 1.2A). Of particular note was a metal coordination spanning the protomer interface, between residue histidine 16 of one subunit and a heme in the adjacent subunit (Figure 1.2B). This interaction appeared to be a key structural factor in the polymerization of OmcS, in addition to the energetic favorability of the parallel stacking of hemes from different protomers at the subunit interfaces (Figure 1.2C).

The initial structural studies of *G. sulfurreducens* extracellular filaments reported high-resolution structures of only homopolymers of OmcS[53, 54]. Failure to obtain a structure for PilA-N filaments was explained by one group as resulting from experimental challenges[54]. Some have questioned the biological relevance of OmcS filaments[55-57] – particularly since cytochromes have been known to form

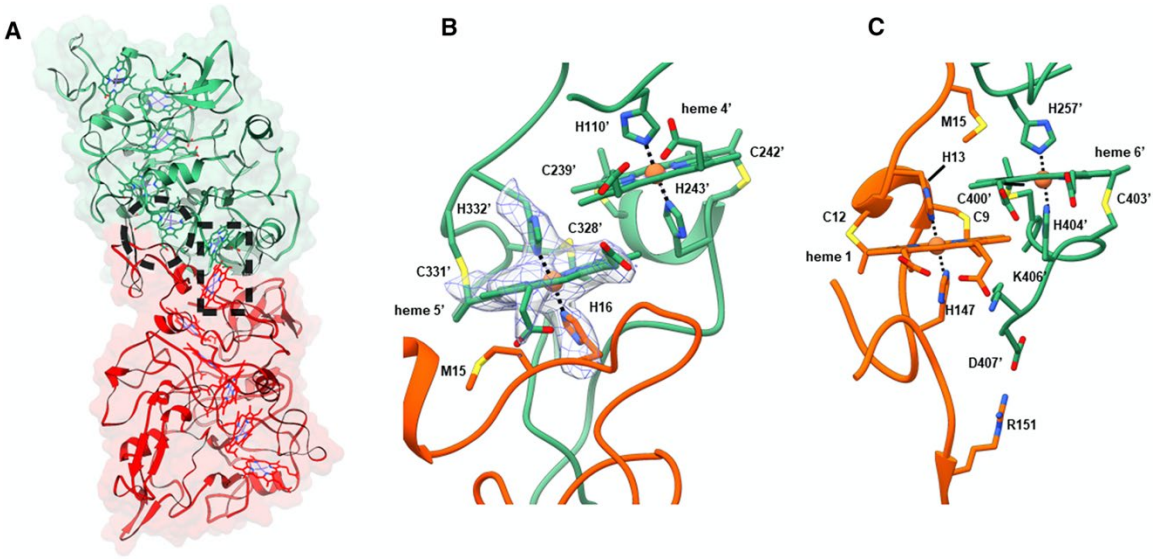

Figure 1.2. Subunit interface interactions within OmcS Filament.

A, The large interface in the filament (~2,600 Å^2 per subunit) is due to the complementarity between the upper portion of the bottom subunit (red) and the lower portion of the top subunit (green). Residues in one subunit strongly interact via hemes shown in the dashed circle and rectangle, and corresponding zoomed images are shown in (B) and (C), respectively. **B**, Histidine 16 of the bottom subunit is coordinating the iron atom in heme 5′ of the top subunit. The cryo-EM densities corresponding to histidine 16, histidine 332′, and heme 5′ are shown in a mesh. **C**, The stacking of heme 6′ from a top subunit with heme 1 from the subunit below.

This figure and its accompanying legend have been reproduced from Wang et al.[53].

short polymers under synthetic conditions[58-61]. Others have argued instead that the putative PilA-N filaments had been misidentified[53]. The assertion that previous reports of putative PilA-N filaments are in fact characterizations of cytochrome filaments, including OmcS filaments and the subsequently-described[62] OmcZ filaments, has been offered as an alternate explanation for previously reported mutations to *G. sulfurreducens pilA* that affected the properties of extracellular filaments[63].

1.5 Scope of this work

The studies described here consider three key topics pertaining to the discovery of extracellular OmcS filaments in *G. sulfurreducens*:

Chapter 2 shows that in wild-type *G. sulfurreducens*, PilA-N and PilA-C form the heterodimeric subunit of a periplasmic filament required for the proper localization of nanowire-forming cytochromes. This helps to explain how the underlying perturbation of *pilA* and related proteins in previous studies have led to the observed differences in the properties of *G. sulfurreducens* extracellular filaments during EET.

Chapter 3 demonstrates that protein-heme metal coordination interactions can be manipulated to control self-assembly of OmcS filaments *in vitro* and that specifically disrupting inter-subunit metal coordination interactions *in vivo* prevents *G. sulfurreducens* cells from assembling OmcS filaments and utilizing them for EET.

Chapter 4 considers the potential for EET-performing microbes beyond *G. sulfurreducens* to utilize OmcS-like filaments. In particular, this chapter uses cryogenic electron microscopy to determine the structure of OmcS-like filaments produced by *Geoalkalibacter subterraneus* and compare them to *G. sulfurreducens* OmcS filaments, thereby identifying key conserved features between these homologous structures that suggest a broadly conserved functional role.

G. sulfurreducens PilA-N assembles heterodimeric PilA-N–C filaments involved in cytochrome nanowire export

This chapter is a reformatted presentation of a published article: Gu, Y.*, Srikanth, V.*, Salazar-Morales, A.I., Jain, R., O'Brien, J.P., Yi, S.M., Soni, R.K., Samatey, F.A., Yalcin, S.E. and Malvankar Nikhil, S. "Structure of *Geobacter* pili reveals secretory rather than nanowire behaviour." Nature **597**, 430–434 (2021).

* These authors contributed equally.

Some materials published with the article, which can be accessed here, have been omitted for brevity.

The complete author contribution description accompanying this manuscript is reproduced below (emphasis added):

Y.G. prepared and optimized cryo-EM grids, collected data used to build the atomic model, performed the image analysis, reconstructed the pili filament structure, **generated and refined the filament model with help from F.A.S and V.S.**, biochemically analyzed filaments, performed AFM, circular dichroism, conductivity measurements, electrode fabrication and negative-staining TEM images. **V.S. identified and purified pili filaments.** A.I.S. performed adhesion and twitching motility assays. A.I.S. and R.J. carried out biochemical analyses and genetic experiments. J.P.O. grew biofilms on electrodes in microbial fuel cell. Y.G., S.M.Y. and R.K.S. carried out mass-spectrometric analyses. S.E.Y. performed AFM imaging of cell-attached filaments. N.S.M. supervised the project. **Y.G. V.S. and N.S.M. wrote the manuscript with input from all authors.**

2.1 Summary

Extracellular electron transfer by *Geobacter* species via surface appendages called microbial nanowires[5] is important in a wide range of globally-important environmental phenomena[53] and for applications in bioremediation, bioenergy, biofuels and bioelectronics. Since 2005, these nanowires have been thought to be type IV pili composed solely of PilA-N protein[5, 54]. However, structural analyses demonstrated that during EET, rather than pili, cells produce nanowires made up of cytochromes OmcS[53, 54] and OmcZ[62]. Here we show that *G. sulfurreducens* binds PilA-N to PilA-C to assemble heterodimeric pili which remain periplasmic under nanowire-producing conditions that require EET[32]. Cryo-electron microscopy revealed that C-terminal residues of PilA-N stabilize its copolymerization with PilA-C via electrostatic and hydrophobic interactions that position PilA-C along the outer surface of the filament. PilA-N–C filaments lack π-stacking of aromatic side chains and show conductivity 20,000-fold lower than OmcZ nanowires. In contrast to surface-displayed T4P, PilA-N–C filaments show structure, function, and localization akin to type 2 secretion pseudopili[64, 65]. Secretion of OmcS and OmcZ nanowires is lost when *pilA-N* is deleted and restored when PilA-N–C filaments are reconstituted. Substitution of *pilA-N* with T4P of other microorganisms also causes loss of secretion of OmcZ nanowires. As all major phyla of prokaryotes employ T4P-like systems[66], this novel nanowire translocation machinery may have widespread impact in identifying the evolution and prevalence of diverse electron-transferring microorganisms and in determining the nanowire assembly architecture for designing synthetic protein nanowires.

2.2 Introduction

T4P-like filaments are employed by almost all major phyla of prokaryotes for diverse functions such as adhesion, motility, protein secretion, and interspecies communication[66]. Electronically conductive filaments on the surface of the common soil bacteria *Geobacter sulfurreducens*, known as microbial nanowires, have been implicated in a wide range of globally-important environmental processes such as nutrient and element cycling, bioremediation, corrosion, and generation of methane and electricity[53]. These filaments were thought to be T4P composed of PilA-N protein[5, 55] because Δ*pilA-N* mutants lack

these conductive filaments[32] and do not transfer electrons to extracellular acceptors such as iron oxide[5] or electrodes in microbial fuel cells[67]. However, this hypothesis of the PilA-N filaments functioning as nanowires[55] is open to question[63] because:

(1) the deletion of *pilA-N* also inhibits the extracellular translocation of OmcS[68, 69] and OmcZ[68], which form nanowires essential for extracellular electron transfer to iron oxide[40] and electrodes[41] respectively;

(2) the presence of PilA-N in a filament of wild-type cells has not been established, only inferred from indirect evidence such as the presence of PilA-N monomer in filament preparations that also contain OmcS nanowires[3];

(3) conduction along the length of a purified PilA-N filament has not been demonstrated; and

(4) theoretical studies did not find significant conductivity in a hypothetical PilA-N filament structure[70, 71] except when aromatic residues were assumed within 3-4 Å of each other[72].

2.3 Results

2.3.1 Splitting of *pilA* into *pilA-N* and *pilA-C*

The *G. sulfurreducens* genome contains two neighboring genes related to *pilA*[9] (Figure 2.1A). The first gene is annotated as *pilA-N* (GSU1496) because this 61-amino acid protein shows high amino acid sequence identity to the N-terminal 53 amino acid α-helix of previously reported type IV pilin proteins, but lacks the C-terminal globular domain found in T4P[68, 73] (Supplementary Figure 2.1). Immediately downstream of *pilA-N* is a gene annotated as *pilA-C* (GSU1497) because it was thought to be the C-terminal globular domain missing from PilA-N[68, 73] (Figure 2.1A). These two genes are functionally related: *pilA-C* deletion mutants show reduced expression and lower stability of PilA-N[68, 74]. Similar to Δ*pilA-N* cells, a reduced abundance of OmcS and OmcZ was observed outside of Δ*pilA-C* cells in one study[74]. The unusually short length of PilA-N, the adjacent location of *pilA-N* and *pilA-C* in the genome of *Geobacter* species, and their co-expression[68, 75], suggested that a recent evolutionary event split an original, longer *pilA* gene into *pilA-N* and *pilA-C*[73, 75]. PilA-N was hypothesized to be the only protein within *G. sulfurreducens* pili[5, 73] due to the lack of sequence similarity between PilA-C and the globular

domain of type IV pilin proteins – even though all globular domains of T4P show low sequence conservation (Supplementary Figure 2.1), but high structural conservation, extending to the predicted structure of PilA-C[75]. Gene fission of pilins is widespread in *Desulfuromonadales* species including *Geobacteraceae* and other iron-reducing bacteria[75]. Our phylogenetic analysis of a fused PilA-N and PilA-C sequence showed an independent line of descent along with PilA-N–C subunits of other *Geobacter* species, indicating that *Geobacter* PilA-N–C are evolutionarily distant from both T4P and pseudopili of type 2 secretion systems (T2SS) (Figure 2.1B, Supplementary Figure 2.2, Supplementary Figure 2.3). As gene fission is a major contributor to the evolution of multi-domain bacterial proteins[76], we hypothesized that *G. sulfurreducens* pili could consist of a filamentous assembly of PilA-N and PilA-C heterodimers.

2.3.2 Discovery and identification of pili

We grew *G. sulfurreducens* wild-type (WT) cells using anodes of microbial fuel cells as sole electron acceptors[77]. These conditions require extracellular electron transport over hundreds of cell lengths and

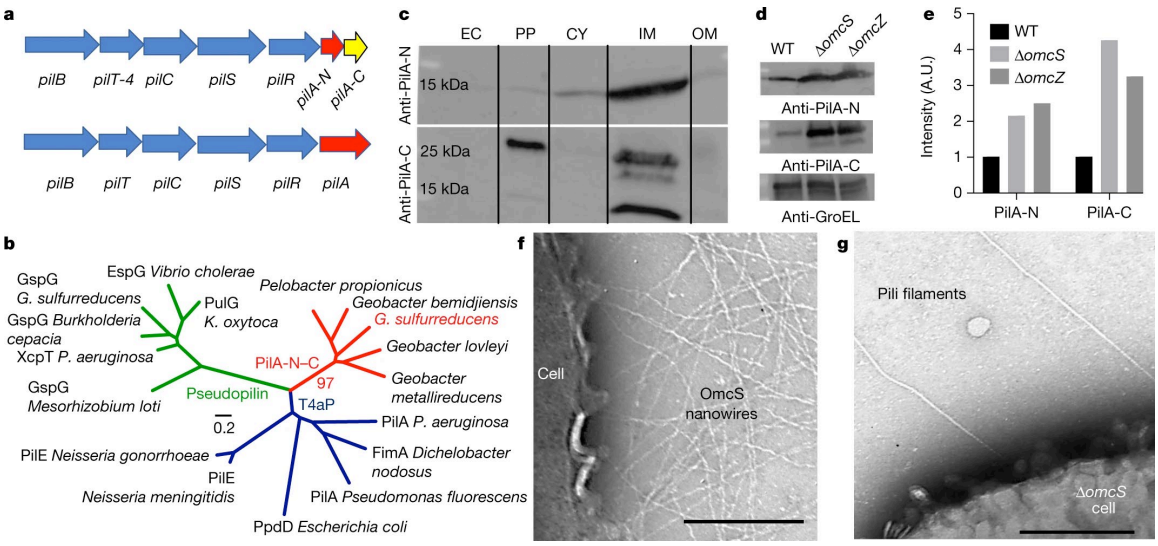

Figure 2.1. Discovery and identification of *G. sulfurreducens* pili.

a, Genomic organization of T4P biosynthesis genes in *G. sulfurreducens* and *M. xanthus*. **b**, Phylogenetic tree derived from amino acid sequence alignments (see Supplementary Figure 2.1, Supplementary Figure 2.2, Supplementary Figure 2.3). **c**, Immunoblot for subcellular fractionation of PilA-N (~6.5 kDa) and PilA-C (~11 kDa) in WT cells. EC: extracellular, PP: Periplasm, CY: Cytoplasm, IM: Inner-membrane, OM: Outer-membrane. **d**, Immunoblot for PilA-N and PilA-C in cell lysates with quantification in **e**. Control: Cytoplasmic protein GroEL. **f**, Negative-stain TEM image of WT *G. sulfurreducens* cell showed only OmcS filaments on the cell surface. **g**, Pili-like filaments emanated from Δ*omcS* cell. Scale bars, **f**, 100 nm and **g**, 200 nm.

therefore represent an ideal nanowire-producing condition[32, 63]. Purified filament preparations from WT cells grown under these nanowire-producing conditions failed to show either PilA-N or PilA-C using immunoblotting (Supplementary Figure 2.4), in agreement with our previous cryogenic electron microscopy analyses that did not find any T4P-like filaments[63, 78]. We further analyzed subcellular fractions of WT cells with anti-PilA-N antibodies and found that PilA-N is mainly associated with the inner membrane but is absent from the extracellular fractions. PilA-C is also similarly membrane-associated and absent from the extracellular fractions of WT cells[36] (Figure 2.1C). Control experiments using antibodies against the cytoplasmic protein GroEL confirmed that there is little or no cross-contamination in these subcellular fractions, as only cytoplasmic fractions showed GroEL (Supplementary Figure 2.5). These studies suggested that *G. sulfurreducens* PilA-N and PilA-C are ultimately anchored to the inner membrane, akin to T2SS pseudopili that form a membrane-associated filament structure to secrete proteins via elongation and retraction cycles[64, 65]. Similar to the overexpression of pseudopilins causing the pseudopilus filaments to extend beyond the outer membrane[64, 79, 80], we hypothesized that *G. sulfurreducens* filaments may extend outside the cell surface if PilA-N and PilA-C proteins were present at levels higher than that observed in WT. Both Δ*omcS* and Δ*omcZ* cells, lacking nanowire-forming cytochromes, showed an elevated abundance of PilA-N and PilA-C, and indeed we found pili-like filaments on the surfaces of these cells by negative-stain transmission electron microscopy (Figure 2.1D-G, Figure 2.2A-C). Overexpressing PilA-N and PilA-C from a plasmid in WT *G. sulfurreducens* also yielded extracellular pilus-like filaments (Figure 2.3) with a smooth morphology distinct from the sinusoidal morphology of cytochrome nanowires[53, 62] (Figure 2.1F-G, Figure 2.4A-B). In contrast to cytochrome nanowires[53, 62] or T4P[81] which need to be removed from cells via vortexing or blending, these pili-like filaments were loosely attached to cells, akin to pseudopili[80], and were shed in the media. Therefore, cell-free supernatant of Δ*omcS* cells was concentrated to obtain PilA-N–C filament preparations that minimized cellular and cytochrome contamination (Figure 2.2).

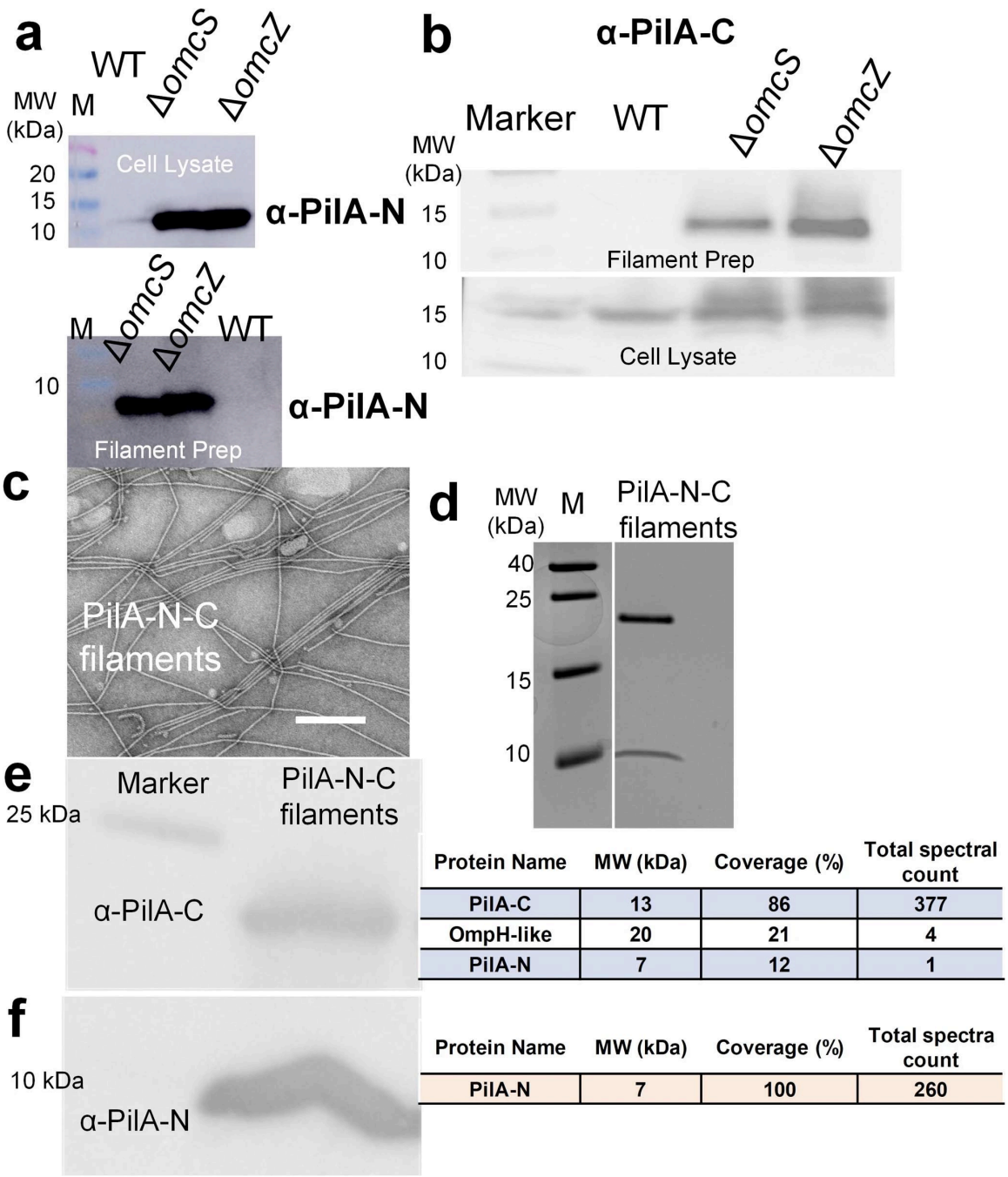

Protein Name	MW (kDa)	Coverage (%)	Total spectral count
PilA-C	13	86	377
OmpH-like	20	21	4
PilA-N	7	12	1

Protein Name	MW (kDa)	Coverage (%)	Total spectra count
PilA-N	7	100	260

Figure 2.2. Identification of PilA-N and PilA-C in pili.

a, **b**, Immunoblot of filament preparation and whole cells lysate for PilA-N (**a**) and PilA-C (**b**). M, marker. For gel source data, see Supplementary Figure 2.17 and Supplementary Figure 2.8 for PilA-N and PilA-C, respectively. **c**, **d**, TEM image (**c**) and sodium dodecyl sulfate-polyacrylamide gel electrophoresis (SDS-PAGE) resolution (**d**) of PilA-NC filaments purified from Δ*omcS* cells. M, marker. Scale bar, 200 nm (**a**). For gel source data, see Supplementary Figure 2.9. **e**, **f**, Immunoblot and corresponding mass spectrometry analysis for PilA-C (**e**) and PilA-N (**f**) containing band. For gel source data, see Supplementary Figure 2.10.

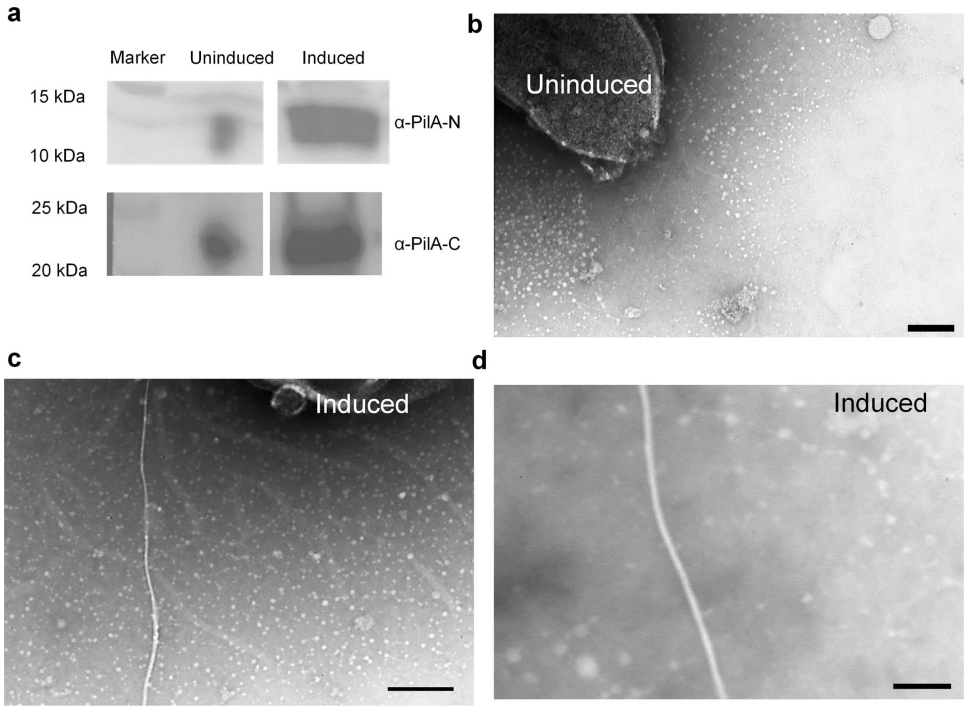

Figure 2.3. Overexpressing PilA-N and PilA-C in WT *G. sulfurreducens* yielded pili-like filaments on the bacterial surface.

a, Immunoblot of whole-cell lysate showing overexpression of PilA-N and PilA-C under induced conditions. For gel source data, see Supplementary Figure 2.11. **b**, **c**, Negative-stain TEM images of wild-type cells under uninduced (**b**) and induced (**c**) conditions. **d**, Zoomed image of pili-like filament shown in **c**. Scale bars, 200 nm (**b**, **c**), 50 nm (**d**).

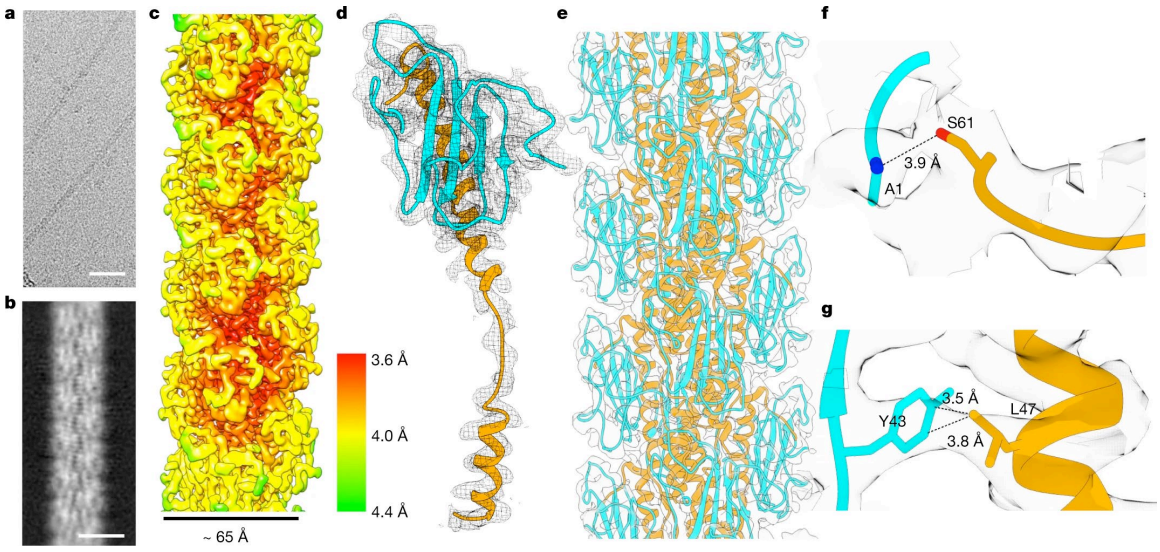

Figure 2.4. PilA-N recruits PilA-C to form a heterodimer that polymerizes into a filament.

a, Cryo-EM micrograph, **b**, 2D average and **c**, resolution distribution of PilA-N–C filament. Scale bars: **a**, 30 nm, **b**, 5nm. PilA-N (gold) and PilA-C (cyan) form **d**, a heterodimer that polymerizes into **e**, a filament. **f**, Charge interactions between S61 of PilA-N and A1 of PilA-C. **g**, Hydrophobic interactions between PilA-N and PilA-C.

2.3.3 PilA-N and PilA-C form a heterodimeric pilin

Analysis of cryo-EM images of these pilus-like filaments, using the iterative helical real space reconstruction approach, yielded a map at ~3.8 Å resolution according to the "gold standard" map:map and 3.9 Å according to the model:map Fourier Shell Correlation (FSC; Supplementary Figure 2.6). The overall structural features of the filament are similar to T4P, with a helical core and globular head domain arranged within a right-handed helix with helical rise of ~10.4 Å and rotation of 89.1° (Figure 2.4B). At such resolution, the C_α backbone could be traced to determine that the asymmetric unit contained ~160 amino acids. The protein constituents of the filaments were identified by combining mass spectrometry and immunoblotting with bioinformatic analysis, revealing PilA-N and PilA-C

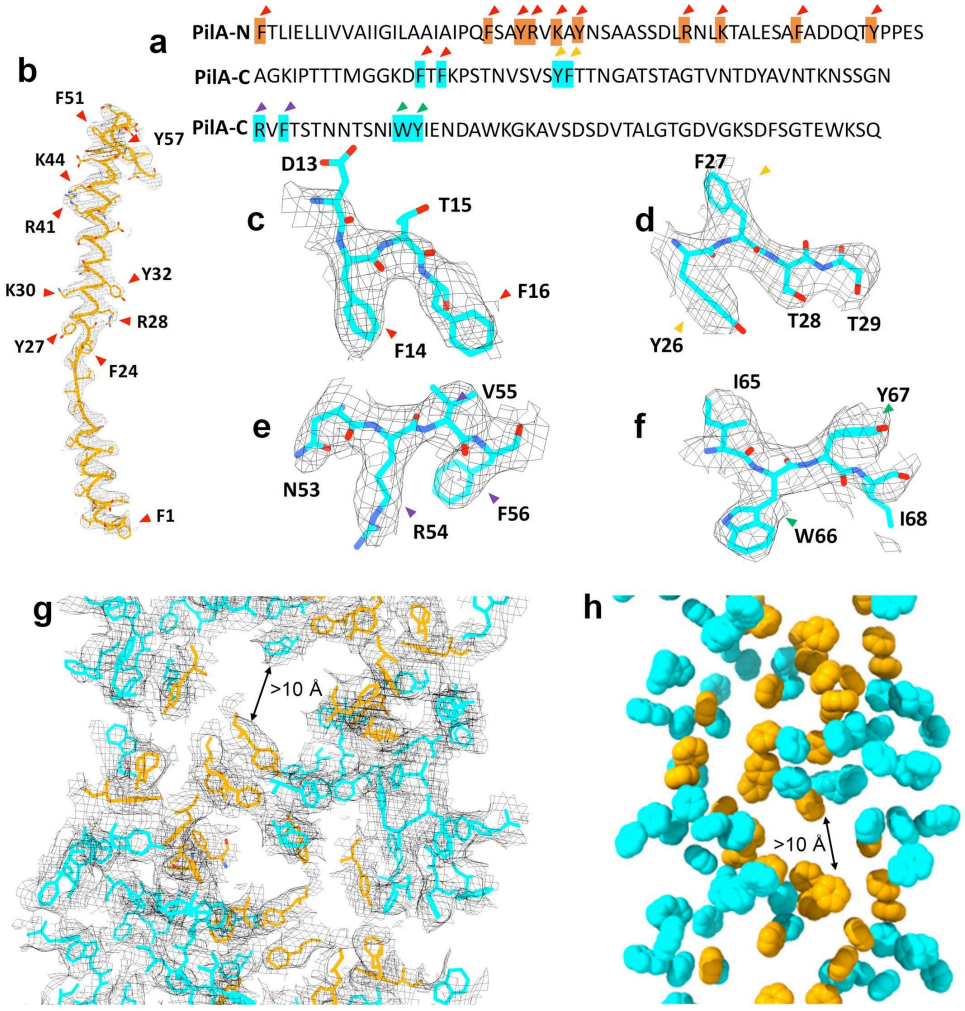

Figure 2.5. *De novo* atomic model of PilA-N–C filament fit into the cryo-EM map.

a, PilA-N and PilA-C sequences. **b**–**f**, Zoomed view of the regions indicated in a for PilA-N (**b**) and PilA-C (**c**–**f**). **g**, **h**, Zoomed view of electron microscopy density and aromatic amino acids in PilA-N–C filament.

exclusively (Figure 2.2C-F). The PilA-N sequence could be threaded through the helical core of the map and the PilA-C sequence could be threaded through the globular domains on the outer surface (Figure 2.4D, Figure 2.5). Overall, the excellent agreement between the model and the map, the good fit of side chains, and the refinement statistics (Table 2.1) confirm that PilA-N and PilA-C form a heterodimer that polymerizes into a filament (Figure 2.4E).

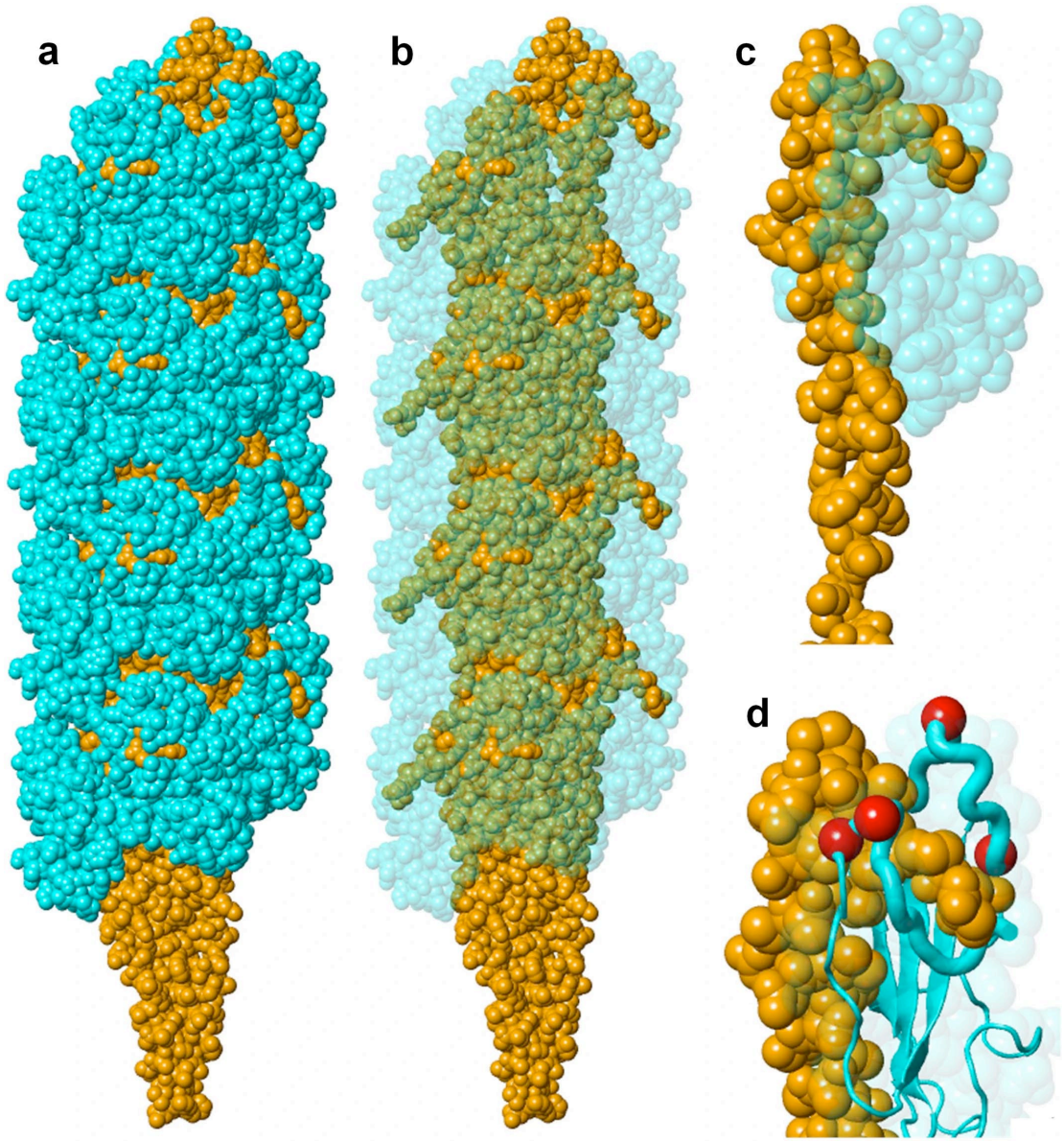

Figure 2.6. Contacts between PilA-N (orange) & PilA-C (cyan).

a, Pilus model. **b**, PilA-C translucent, showing protrusions of PilA-N. **c**, Heterodimer showing C-terminal residues 57–61 of PilA-N protruding to the right into PilA-C. **d**, Flaps of PilA-C (thick coils) enclosing protrusion of PilA-N. Four glycines (red balls) could provide hinges that may enable flaps to open.

Table 2.1. Cryo-EM data collection, refinement, and validation statistics for PilA-N–C filament.

	PilA-N–C filament (EMDB-21225) (PDB 6VK9)
Data collection and processing	
Magnification	165,000
Voltage (kV)	300
Electron exposure (e–/Å^2)	62
Defocus range (μm)	0.8 – 2.5
Pixel size (Å)	0.822
Symmetry imposed	89.1°/10.4 Å
Initial particle images (no.)	280,000
Final particle images (no.)	100,000
Map resolution (Å)	3.8
FSC threshold	0.143
Map resolution range (Å)	3.6 – 4.4
Refinement	
Initial model used (PDB code)	N/A
Model resolution (Å)	3.9
FSC threshold	0.5
Model resolution range (Å)	N/A
Map sharpening *B* factor (Å^2)	127
Model composition	
Non-hydrogen atoms	19,792
Protein residues	2,640
Ligands	N/A
B factors (Å^2)	
Protein	N/A
Ligand	N/A
R.m.s. deviations	
Bond lengths (Å)	0.01
Bond angles (°)	1.699
Validation	
MolProbity score	1.91
Clashscore	7
Poor rotamers (%)	0.7
Ramachandran plot	
Favored (%)	90.06
Allowed (%)	9.64
Disallowed (%)	0

PilA-N is composed of two α-helices, with segments F1-L16 forming an N-terminal helix and S25-F51 forming a C-terminal helix, linked by a short coil (Figure 2.4D). A staggered helical array of PilA-N subunits forms the core of the PilA-N–C filament (Figure 2.4E). PilA-C consists of four anti-parallel β-strands surrounded by a web of loops (Figure 2.4D). It binds at the second α-helix of PilA-N via an

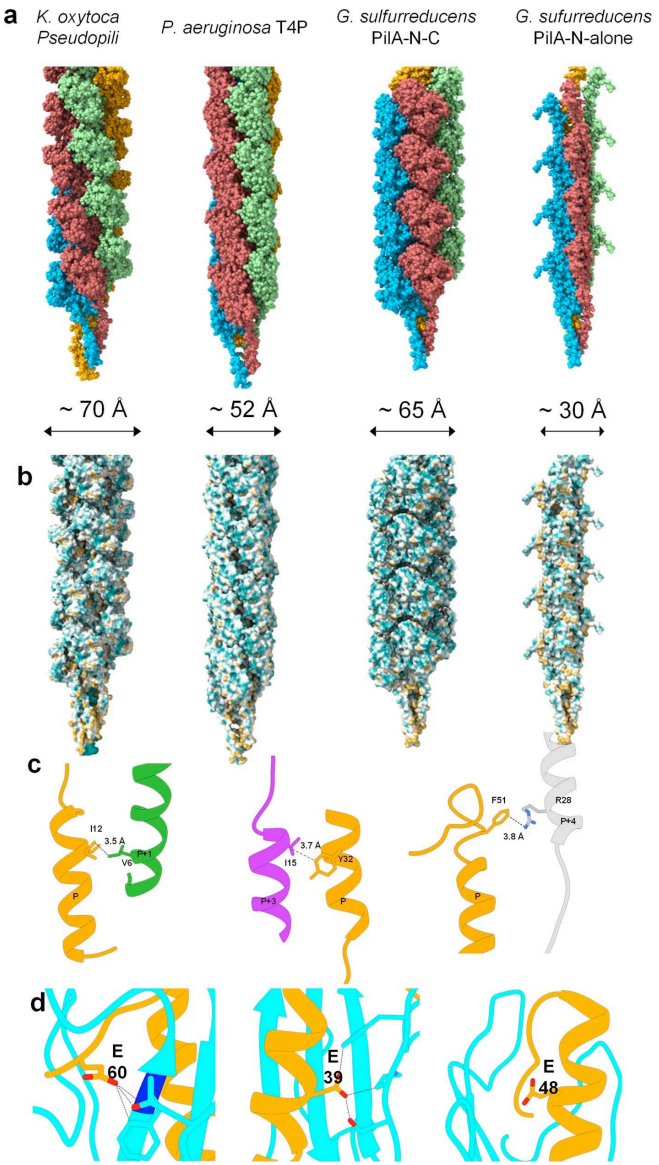

Figure 2.7. Comparison between *K. oxytoca* pseudopili (PDB code 5WDA), *P. aeruginosa* T4P (PDB code 5XVY), *G. sulfurreducens* PilA-N–C filament and *G. sulfurreducens* PilA-N-alone filament model.

a, Helical arrangement with P and P + 4 subunits shown in the same color. **b**, Hydrophobicity surface colored from yellow (hydrophobic) to blue (hydrophilic). **c**, Interactions between PilA-N determines the structure as 1-start, 3-start and 4-start helix. **d**, Interactions between PilA-N and PilA-C, which is consistent with the studies on monomers that mutating E39 or E60 could disrupt the interactions while mutating E48 showed no disruption.

extensive network of electrostatic and hydrophobic interactions that stabilizes the PilA-N/PilA-C heterodimer. In addition to extensive contacts between PilA-C and the C-terminal helix of PilA-N, the C-terminal 5-residues of PilA-N protrude and are held between two "flaps" of PilA-C (Figure 2.6). The N-terminus of PilA-C (Ala1) interacts with the C-terminus of PilA-N (Ser61) via hydrogen bonding or possibly a salt bridge (Figure 2.4F). Our structure explains the yeast two-hybrid assay with PilA-N and PilA-C monomers[36] which found that reversing the charged sites in PilA-N at [D39,R41,K44] and E60 inhibits its interaction with PilA-C by disrupting electrostatic interactions or introducing clashes between the monomers – whereas reversing the charges at K30, E48 and [D53,D54] does not (Figure 2.7D).

In addition to electrostatic interactions, hydrophobic interactions – such as the interactions between L47 from PilA-N and Y43 from PilA-C (Figure 2.4G) – also appeared critical for filament stability. The filament is mainly organized via the interactions between adjacent PilA-N subunits (Figure 2.7A,C), with little direct interaction between copies of PilA-C within the filament. The PilA-N–C filament did not show the post-translational modifications previously reported for the PilA-N monomer[82]. Rather, we observed N-terminal methylation of PilA-N (Figure 2.8) as seen in other T4P[81] and extra density around S94 for PilA-C. A glycoprotein detection assay suggested this density could be attributed to an O-linked glycosylation (Figure 2.8B-D). Such glycosylation on a serine residue near the C-terminus is commonly observed in other T4P[83, 84], where it is important in pilus biogenesis[85]. As the N-terminus of PilA-N is primarily composed of hydrophobic residues, binding to PilA-C prevents the exposure of the hydrophobic side chains to the aqueous environment (Figure 2.4E, Figure 2.7B).

2.3.4 PilA-N–C filaments are pseudopili-like

A comparison of T4P structures revealed that *G. sulfurreducens* PilA-N–C filaments lack several hallmarks of T4P structure[86] and instead show similarity to the structure of type 2 secretion system pseudopili[87] (Figure 2.9A-B). Firstly, a salt bridge between N-terminal F1 and E5 of neighboring subunits is highly conserved among all T4P and is crucial for their stability and assembly[86] (Figure 2.9B). However, this salt bridge is absent in *G. sulfurreducens* PilA-N–C filaments. Instead, the amine of F1 interacts with E5 from the same subunit to neutralize the buried charge. Adjacent PilA-N subunits are primarily

stabilized by hydrophobic interactions (Figure 2.9B). Such interactions between neighboring protomers have been observed in the pseudopili from *Klebsiella oxytoca*[87]. Secondly, the α-β loop in the globular head domain, which is involved in the subunit-subunit interactions in assembled T4P filaments[86], is absent in the PilA-N–C filament. Thirdly, the D-region in the globular head domain contains a disulfide bridge that is essential for assembly of some T4P filaments[86] but is notably absent in pseudopili[87] and in PilA-N–C (Figure 2.9A). The lack of disulfide bridges, combined with the observation that PilA-N–C filaments are easily detached under the conditions where they extend from the cell, suggested that the biological function of PilA-N–C filaments is not as a durable, extracellular structure like T4P, but rather as a comparatively fragile, periplasmic assembly akin to type 2 secretion pseudopili[65]. Purified PilA-N–C filaments further exhibit melting of secondary structure features, denaturation, and disassembly at

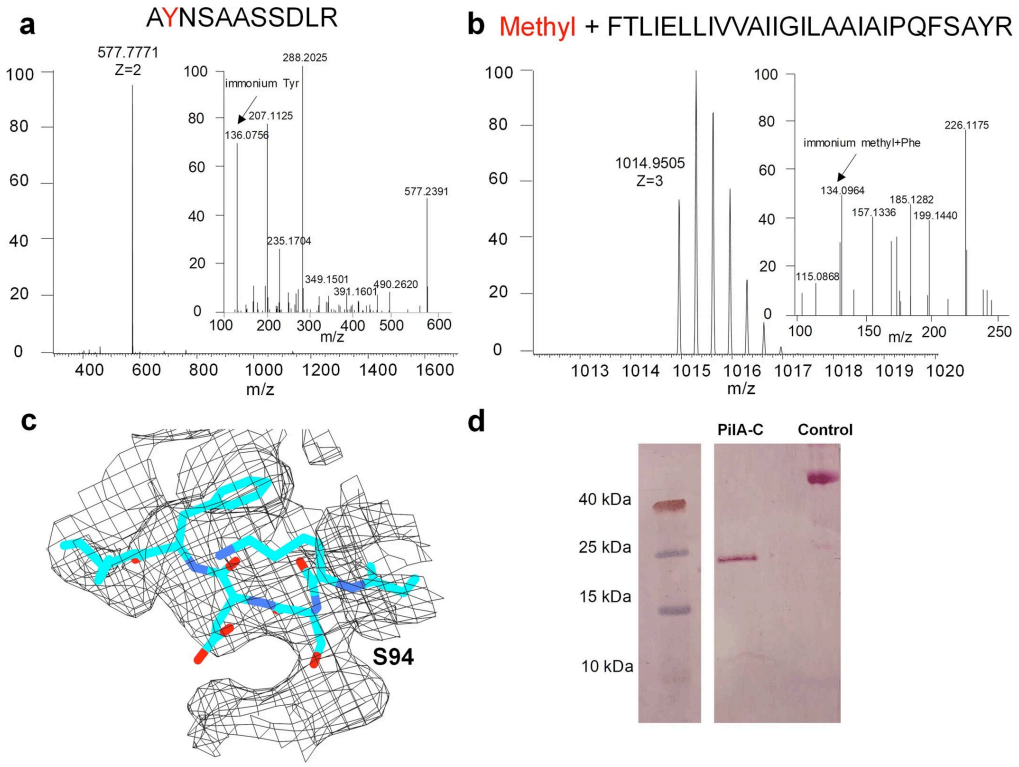

Figure 2.8. Post-translational modifications in PilA-N–C filament.

a, Lack of post-translational modification in Y32 of PilA-N. Mass spectra of PilA-N did not show any modified peptide in AYNSAASSDLR with expected mass of 1.154 kDa. Inset, MS/MS spectra showed no modification on Y32 in PilA-N. **b**, Mass spectra showed methylated peptide FTLIELLVVAIIGILAAIAIPQQFSAYR with mass 3.044 kDa. Inset, MS/MS spectra showed N-terminal methylation. **c**, Cryo-EM map for PilA-C showing an extra density on Ser94, suggesting a post-translational modification. **d**, Gel of purified filaments showing glycosylated PilA-C (left lane) and positive control using horseradish peroxidase (right lane).

much lower temperatures than T4P[88] (Figure 2.10). PilA-N–C filaments are very loosely attached to cells and readily dissociated into pilin subunits under the buffer conditions widely used to purify T4P[86], or upon the addition of mild detergents such as deoxycholate. All these studies demonstrate substantially lower stability of PilA-N–C compared to T4P filaments.

Likely due to this reduced stability, *G. sulfurreducens* PilA-N–C pili do not show any behaviors consistent with typical T4P functions such as adhesion and twitching motility (Figure 2.9C-D), even under the artificial conditions which result in their display on the cell surface. WT, Δ*omcS* and Δ*omcZ* mutant strains showed very low attachment to glass, comparable to Δ*pilA-N* cells (Figure 2.9C). Replacing *G. sulfurreducens pilA-N* with T4P-forming *P. aeruginosa pilA* (Gs-Pa) increased the attachment by 100-fold (Figure 2.9C). *G. sulfurreducens* strains displayed negligible twitching motility compared to *P. aeruginosa* (Figure 2.9D) and were comparable to *P. aeruginosa* Δ*pilA*. These data are therefore more consistent with WT *G. sulfurreducens* expressing periplasmic pseudopili rather than surface-displayed T4P filaments.

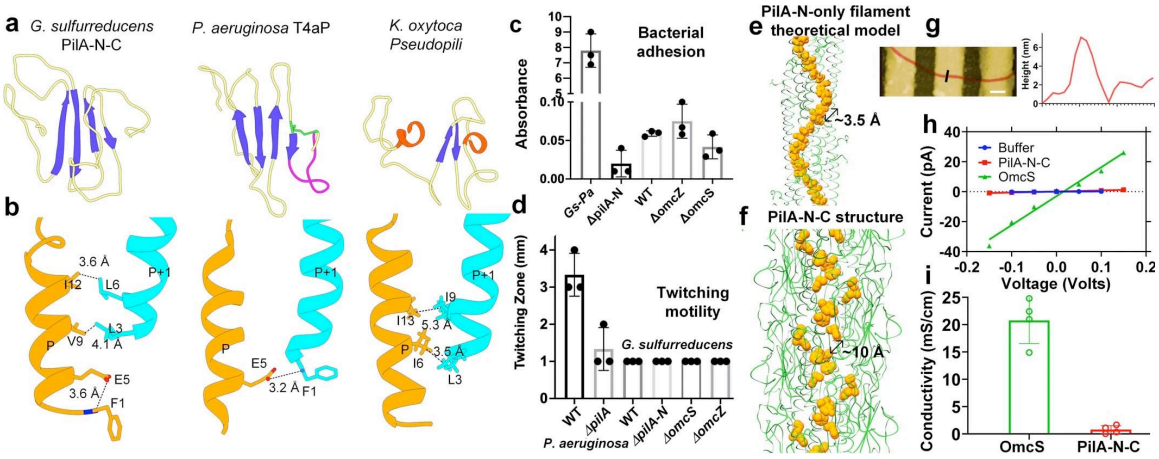

Figure 2.9. *G. sulfurreducens* PilA-N–C pilus is structurally similar to a type 2 secretion pseudopilus and does not show structure or functions of T4aP.

a, The globular domain of the PilA-N–C pilin protomer lacks hallmarks of T4P (PDB ID: 5XVY) - disulfide bridge (green), four beta strands motif (blue) and D-region (magenta), consistent with pseudopili (PDB ID:5O2Y). **b**, Hydrophobic interactions are the main interactions between PilA-N chains, similar to pseudopili, whereas T4P is additionally stabilized via electrostatic interactions between F1 and E5. Comparison of **c**, bacterial adhesion to glass and **d**, twitching motility. Error bars represent s.d. (n=3). Core aromatic residues in the **e**, theoretical model of PilA-N filament and **f**, cryo-EM structure of PilA-N–C filament. **g**, AFM image of a PilA-N–C filament (red) bridging gold electrodes and corresponding height profile at location shown by a black line. Scale bar, 200 nm. **h**, Current-voltage curve and **i**, corresponding conductivity comparison for individual PilA-N–C filaments (n=4) vs. OmcS nanowires.

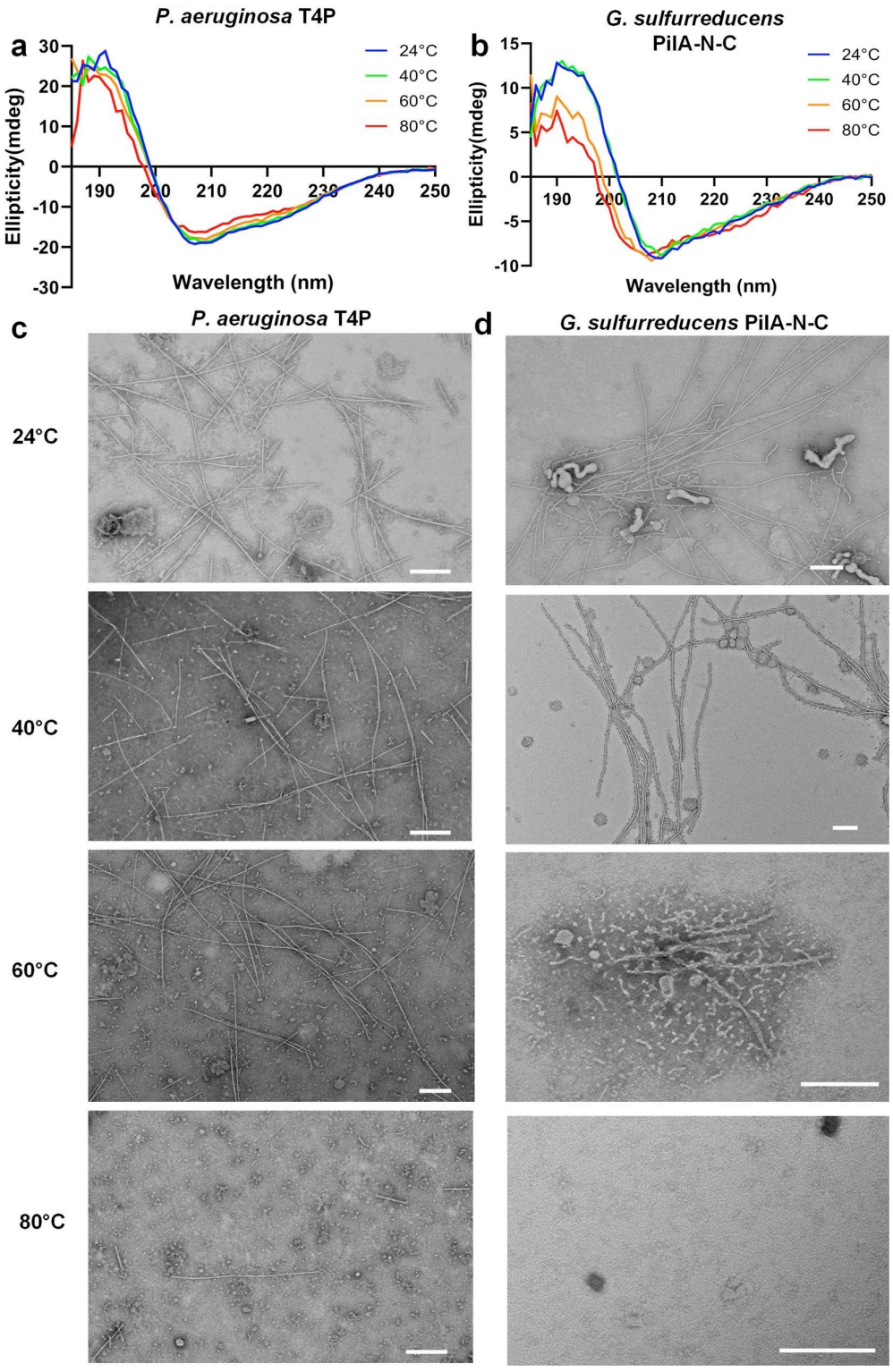

Figure 2.10. Thermal stability comparison between filaments of *G. sulfurreducens* PilA-N–C with *P. aeruginosa* T4P.

a, **b**, Circular dichroism spectra for *P. aeruginosa* T4P (**a**) and *G. sulfurreducens* PilA-N–C filaments (**b**) showing thermal denaturation. **c**, **d**, TEM images of *P. aeruginosa* T4P (**c**) and *G. sulfurreducens* PilA-N–C filaments (**d**) treated at the temperatures indicated for 5 minutes. Scale bars, 200 nm.

2.3.5 PilA-N–C show low electron conductivity

Biologically relevant electron transport along extracellular PilA-N-only filaments has long been postulated as a unique function of *Geobacter* T4P, separate from other classical T4P pilus functions[5]. However, computational studies predicted very low conductivity in a theoretical PilA-N-only filament model using either the NMR monomer structure or a hypothetical homology-based model that has not been observed in nature[70, 71]. Furthermore, there is no direct experimental evidence to support the existence of PilA-N filaments consistent with these hypothetical structures in WT *Geobacter*. It has been proposed that thin filaments observed in some cryo-EM images are PilA-N filaments (Figure 2.11A)[4]. However, our analysis of such images revealed that the morphologically similar filaments we observed are DNA and not pili (Figure 2.11B-E).

Some theoretical models of PilA-N had suggested that aromatic side chains could be 3-4 Å from each other to form π-stacking interactions[37, 38] (Figure 2.9E). A computational study based on these

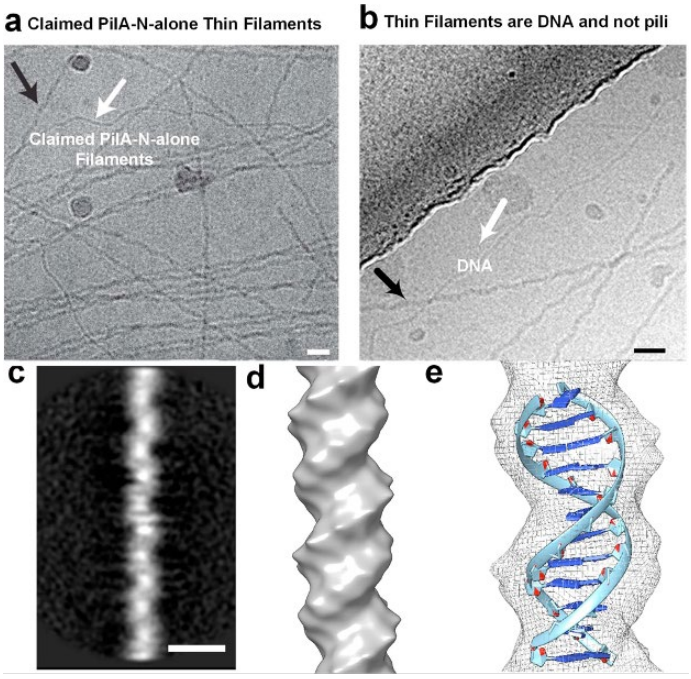

Figure 2.11. Cryo-EM reconstruction suggests that the previously claimed 'PilA-N-alone' filament could be DNA.

a, Cryo-EM image of filaments claimed to be PilA-N alone by Filman et al.[54] **b**, Cryo-EM images showed similar filaments in our OmcS filament preparations. Scale bars, 20 nm (**a**, **b**). Black arrows represent OmcS filaments in **a, b. c**, Two-dimensional average showed no helical features consistent with T4P. Scale bar, 5 nm. **d**, **e**, Cryo-EM density map (**d**) and docking with DNA molecule (**e**) (PDB code 1BNA), suggested the identity of the filaments to be DNA.

theoretical models of π-stacked PilA-N has predicted conductivity of 65-330 mS/cm[72]. However, conductivity measurements and theoretical studies yielded very low conductivity (~1 μS/cm) in synthetic proteins containing such π-stacking of aromatic side chains[89]. Furthermore, the cryo-EM structure of the PilA-N–C filament showed that ~10 Å gaps exist between aromatic residues along the PilA-N core of the filament (Figure 2.9F). Because electron transfer rate exponentially decreases with increasing distance[72], the PilA-N–C structure thus suggested very low conductivity for these pili, as predicted by theoretical studies of a similar PilA-N structure based on other T4P structures[70, 71].

To further evaluate whether *G. sulfurreducens* pili can function as nanowires, the direct current conductivity of individual PilA-N–C filaments was compared with OmcS nanowires. Atomic force microscopy (AFM) was used to locate individual pili bridging two gold electrodes (Figure 2.9G). AFM showed smooth-surfaced structures with 6-nm heights (Figure 2.9G), consistent with the filaments characterized by cryo-EM. Our purified pilus samples did not contain other filament-forming proteins such as OmcS and OmcZ as confirmed by mass spectrometry (Figure 2.2). Our conductivity measurements of individual filaments fully hydrated in buffer yielded low current values[53] (Figure 2.9H). The observed conductivity was ~1 mS/cm, 20-fold lower than OmcS nanowires[53] measured under conditions identical to pilus measurements (Figure 2.9I). As OmcZ nanowires are 1000-fold more conductive than OmcS nanowires[62], our measurements show that *G. sulfurreducens* pili are 20,000-fold less conductive than OmcZ nanowires. Previous physiological studies have shown that Δ*omcS* cells cannot transfer electrons to extracellular iron[40, 90] and electrodes[20, 41] whereas Δ*omcZ* cells cannot transfer electrons to electrodes beyond a few monolayers of cells[15]. The Δ*omcS* cells can adapt after prolonged growth on electrodes, but not Δ*omcZ* cells[32, 41]. As both Δ*omcS* and Δ*omcZ* cells were found to show PilA-N–C filaments on their surfaces (Figure 2.1G), these studies suggest that PilA-N–C filaments are unlikely to function as nanowires and that the above-mentioned phenotypes can be explained by the presence and absence of OmcS and OmcZ nanowires[63]. It remains possible that synthetic *pilA-N* assembles into a filament under artificial conditions[91-93]. However, these synthetic filaments' conductivity has not been demonstrated along their length, only across their diameter, and we found very low conductivity along the length of individual PilA-N–C filaments (Figure 2.9H-I). Furthermore,

such PilA-N-only filaments are unlikely to be responsible for biologically relevant electron transfer considering that we did not find any filament containing PilA-N located extracellularly under nanowire-producing conditions.

2.3.6 Nanowire secretion requires PilA-N–C pili

The lack of either nanowire or typical T4P functions suggests that the biological role of PilA-N–C filaments is not compatible with previous descriptions of *Geobacter* T4P function. In addition to classical T2SS, the *G. sulfurreducens* genome also contains an incomplete T2SS, lacking typical components of the machinery[64]. Deletion of the T2SS pseudopilin gene for the atypical T2SS was not found to affect the translocation of outer-surface cytochromes[94]. Furthermore, other species that use classical T2SS for extracellular translocation of *c*-type cytochromes[95] do not show any secretion defect in the absence of pili[96]. In *G. sulfurreducens*, deletion of *pilA-N* does inhibit the extracellular translocation of OmcS and OmcZ[68, 69], underscoring the involvement of pili in the secretion of nanowire-forming cytochromes. Our

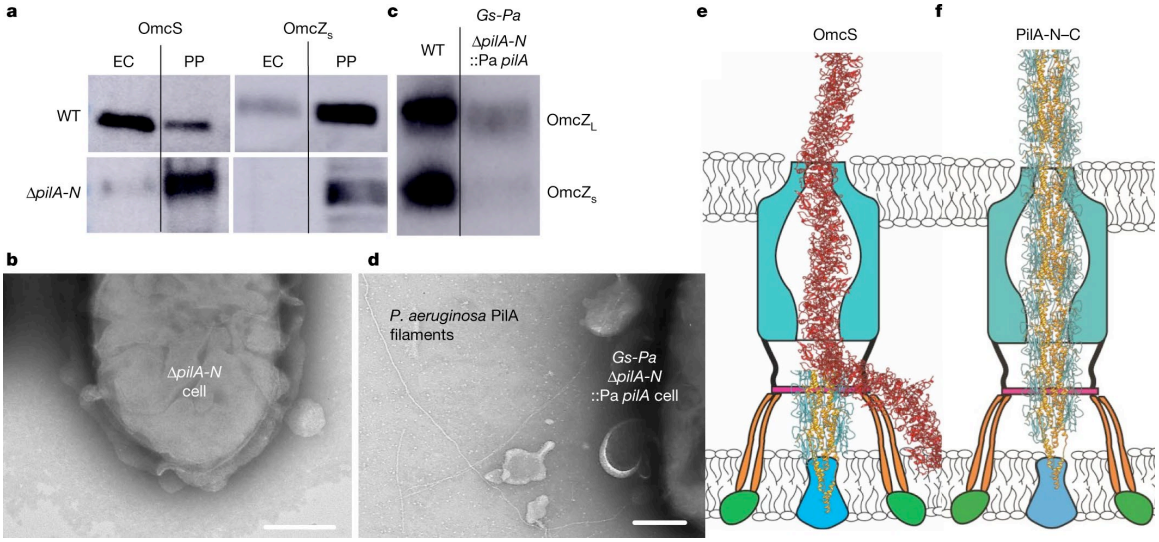

Figure 2.12. *Geobacter sulfurreducens* PilA-N–C pili are involved in the translocation of OmcS and OmcZ nanowires.

a, Immunoblot for subcellular fractionation of OmcS (about 45 kDa) and $OmcZ_s$ (about 30 kDa) in wild-type cells. EC, extracellular; PP, periplasmic, showing the lack of secretion of OmcS and $OmcZ_s$ in the Δ*pilA-N* strain. For gel source data, see Supplementary Figure 2.12. **b**, Negative-stain TEM images showed that the Δ*pilA-N* strain lacked OmcS filaments. Scale bar, 200 nm. **c**, Lack of nanowire-forming $OmcZ_s$ in filament preparations of a strain in which *pilA-N* was replaced with *pilA* of *P. aeruginosa* (*Gs-Pa* cells). Cells still produce intracellular $OmcZ_L$ (about 50 Da). For gel source data, see Supplementary Figure 2.13. *Gs*, *Geobacter sulfurreducens*; *Pa*, *P. aeruginosa*. **d**, TEM image of Δ*pilA-N* cell expressing *P. aeruginosa pilA*. Scale bar, 200 nm. **e**, **f**, Model for PilA-N–C-assisted secretion of nanowires in wild-type cells (**e**) and extracellular extension of PilA-N–C pili in the absence of nanowires in Δ*omcS* and Δ*omcZ* cells (**f**).

subcellular localization experiments revealed that both OmcS and OmcZ are present in the extracellular fraction of WT cells but remain in the periplasm for Δ*pilA-N* cells (Figure 2.12A). These results suggested a translocation defect for OmcS and OmcZ in Δ*pilA-N*. Consistent with these studies, transmission electron microscopy (TEM) imaging showed OmcS nanowires on the surface of WT cells (Figure 2.1F) but not on the surface of Δ*pilA-N* cells (Figure 2.12B). Notably, *in-trans* expression of an episomal copy of WT *pilA-N* and *pilA-C* in Δ*pilA-N* reassembled the PilA-N–C filaments on the bacterial surface and restored the secretion for both OmcS and OmcZ nanowires (Figure 2.13). As the primarily periplasmic localization (Figure 2.1C) and the filament structure (Figure 2.9A) of the PilA-N–C are similar to T2SS

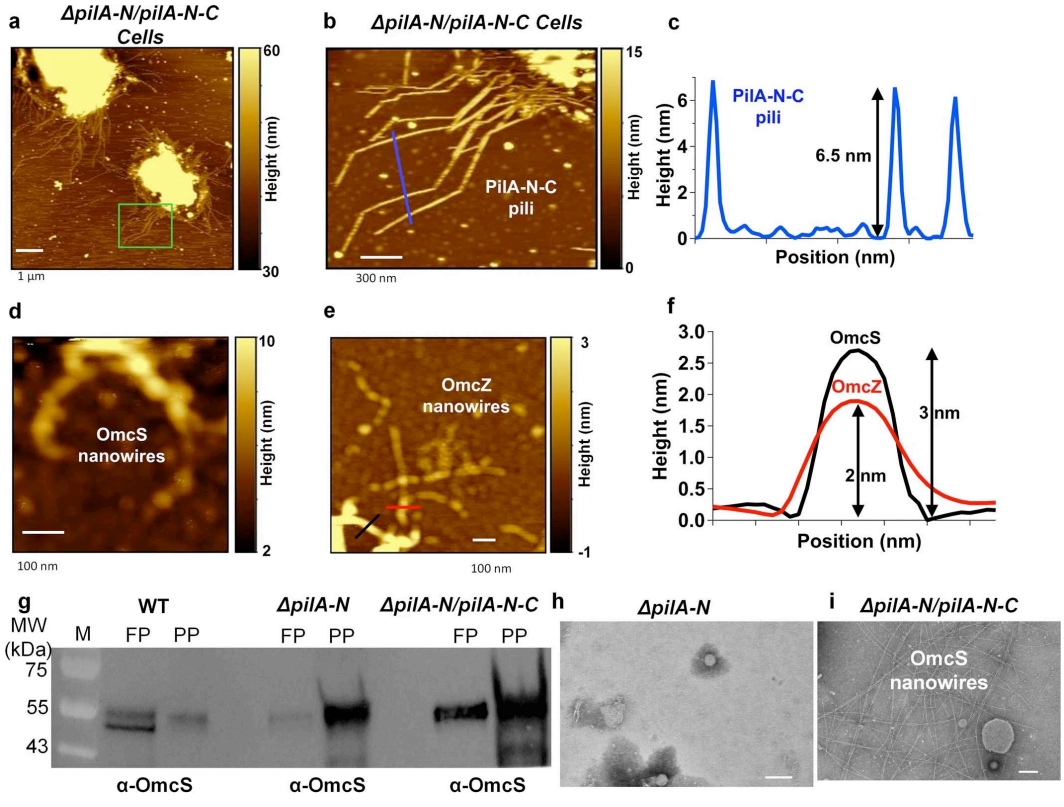

Figure 2.13. Expression of PilA-N–C filaments restores the secretion of OmcS and OmcZ nanowires in Δ*pilA-N* cells.

a, AFM images of Δ*pilA-N*/*PilA-N–C* cell showed pili on the surface of the cell. **b**, Zoomed-in image of Δ*pilA-N*/*PilA-N–C* cell. **c**, Height analysis of the pili consistent with PilA-N–C filament. **d**, **e**, Δ*pilA-N*/*PilA-N–C* cell showed the secretion of OmcS (**d**) and OmcZ (**e**) nanowires. Scale bars, 1 μm (**a**), 300 nm (**b**), 100 nm (**d**, **e**). **f**, Height analysis of filaments at locations shown in **e** showed the diameter consistent with OmcS and OmcZ filaments. **g**, Immunoblotting with OmcS antibody showing the restoration of secretion defect in OmcS nanowires in Δ*pilA-N*/*PilA-N–C* cells. FP, filament preparation; PP, periplasmic fraction; M, marker. For gel source data, see Supplementary Figure 2.19. **h**, **i**, TEM image of filament preparation from Δ*pilA-N* showing no filament (**h**) and OmcS filaments from Δ*pilA-N*/*PilA-N–C* (**i**). Scale bars, 200 nm (**h**, **i**). Δ*pilA-N*/*PilA-N–C*: in-trans expression of an episomal copy of wild-type *pilA-N* and *pilA-C* in Δ*pilA-N*.

pseudopili[65], these cytochrome localization studies further suggest that PilA-N–C filaments could be functioning similar to pseudopili by translocating the OmcS and OmcZ nanowires from the periplasm to the outer cell surface.

To further evaluate the function of the PilA-N–C filament, we analyzed the localization of cytochromes in mutant *G. sulfurreducens* strains in which the chromosomal *pilA-N* gene was replaced by *pilA* of *P. aeruginosa*[30] (*Gs-Pa*) (Figure 2.12C-D). This strain cannot transport electrons extracellularly to iron oxides or to electrodes in microbial fuel cells[30]. Our TEM images showed T4P-like filaments in *Gs-Pa* (Figure 2.12D). However, we found that filament preparations from electrode-grown *Gs-Pa* cells did not show the extracellular form of OmcZ ($OmcZ_S$)[90] that assembles into nanowires[62] and only showed the periplasmic form of OmcZ ($OmcZ_L$), confirming that the cells were able to produce OmcZ but could not secrete it (Figure 2.12C). This lack of $OmcZ_S$ could explain why these strains cannot transfer electrons to electrodes as $OmcZ_S$ is essential for electricity production[41]. In contrast, OmcS was translocated extracellularly by Gs-Pa[30], similarly to a strain in which *pilA-N* and *pilA-C* genes were fused[97]. Our studies thus show that the unique PilA-N–C filament structure is essential for the translocation of OmcZ nanowires, while the translocation of OmcS can be rescued as long as a T4P is present because surface-displayed T4P filaments are also capable of protein secretion[98] by localizing secreted proteins along or inside pili[28, 99]. In contrast, *Geobacter* pili are capable of secreting cytochromes without being displayed on the cell surface, in a manner analogous to T2SS pseudopili[64, 79, 80].

2.4 Discussion

Together, our findings unambiguously establish that PilA-N and PilA-C assemble into filaments that are involved in the proper localization of OmcS and OmcZ nanowires, and could explain the defect in extracellular electron transfer by strains with modified PilA-N[30, 97] because nanowire-forming OmcS and OmcZ are essential for extracellular electron transfer to iron oxide and electrode, respectively[63]. The unique structure of the PilA-N–C filament, its observed periplasmic location under nanowire-forming conditions, and its marked instability in comparison to all previously described T4P strongly suggest that PilA-N does not assemble an extracellular filament that directly mediates electron transfer and is

unlikely to form a stable filament by itself under natural conditions. Further biochemical characterization of the apparent DNA observed in extracellular fractions via cryo-EM could help clarify whether extracellular DNA could be responsible for previous reports of putative PilA-N-only filaments in *G. sulfurreducens* extracellular fractions. We hypothesize that PilA-N–C filaments participate in the translocation of OmcS and OmcZ nanowires from the periplasm to the extracellular environment. In the presence of cytochrome nanowires, the PilA-N–C filament remains periplasmic and may function analogously to pseudopili[65] by translocating nanowires to the cell surface (Figure 2.12E). In the absence of cytochrome nanowires, cells produce elevated levels of PilA-N and PilA-C, resulting in extension of PilA-N–C filaments outside the cell surface in a manner similar to type 2 pseudopili (Figure 2.12F). This model is consistent with our observation that PilA-N–C filaments are present on the cell surface only when these two proteins are present in higher-than-WT amounts, particularly when nanowire forming cytochromes are absent (Figure 2.1D-G). It further reconciles previous findings that Δ*pilA-N* or Δ*pilA-C* cells could not produce conductive filaments[32] and cannot transfer electrons extracellularly[5, 67], suggesting a previously unknown secretion machinery for the extracellular translocation of OmcS and OmcZ nanowires.

2.5 Methods

2.5.1 Bacterial strains and growth conditions.

Geobacter sulfurreducens wild-type strain PCA (designated DL-1) (ATCC 51573)[24], the *pilA-N* knock out strain (designated as Δ*pilA-N*)[32], *omcS* knock-out mutant strain[40] (designated as Δ*omcS*), the *omcZ* knock-out mutant strain[41] (designated as Δ*omcZ*), *G. sulfurreducens* strains in which *pilA-N* was replaced by *pilA* of either *P. aeruginosa*[30] (designated as DL1-PA or *Gs-Pa*) or *G. uraniireducens*[100] (designated DL1-Uranii or *Gs-Gu*), *Pseudomonas aeruginosa* WT strain PAO1, and *Pseudomonas aeruginosa* strain Δ*pilA*, were obtained from our laboratory culture collection. *G. sulfurreducens* cultures were maintained at 30 °C or at 25 °C under strictly anaerobic conditions in growth medium supplemented with acetate (10 mM) as the electron donor and fumarate (40 mM) as the electron acceptor. As described previously[53], the *G. sulfurreducens* cells were grown in sterilized and degassed NBAF medium[77], which contained the

following: 0.04 g/L calcium chloride dihydrate, 0.1 g /L, magnesium sulfate heptahydrate, 1.8 g/L sodium bicarbonate, 0.5 g/L sodium carbonate, 0.42 g/L potassium phosphate monobasic, 0.22 g/L potassium phosphate dibasic, 0.2 g/L ammonium chloride, 0.38 g/L potassium chloride, 0.36 g/L sodium chloride, and vitamins and minerals as listed in O'Brien et al.[77]. 1 mM cysteine was added as an oxygen scavenger. *G. sulfurreducens* cells were grown under nanowires-producing conditions as previously described[5], or grown using anodes of microbial fuel cells as sole electron acceptors[77]. The latter conditions require extracellular electron transport over hundreds of cell lengths and are therefore ideal nanowire-producing conditions that require long-range electron transport[32].

2.5.2 PilA-N–C overexpression

GSU1496 and GSU1497 were synthesized (Genscript) and cloned into pRKS-Geoi[25]. Transformation was performed as described previously[25]. WT cells were cultured as previously described[25] and supplemented with kanamycin (200 μg/mL) and vanillate to a final concentration of 500 μM.

2.5.3 Sequence alignment and phylogenetic analysis

Amino acid sequences of pilins were obtained from UniProt and NCBI databases. For PilA-N–C pilin sequences, the truncated pilins (PilA-N or homologs) were manually fused with PilA-C proteins, excluding the signal peptides (based on the annotation from UniProt). Multiple sequence alignments of pilins were generated in MEGA X[101] using the MUSCLE algorithm. The aligned file was used as an input for maximum likelihood approach phylogenetic analysis using the PhyML 3.0[102] online service provided by ATGC. The substitution model was automatically selected using Smart Model Selection (SMS)[103] and the Akaike Information Criterion (AIC) was used to evaluate the model. Distance and branching order were constructed via the BioNJ algorithm and optimized via nearest-neighbor interchange. The bootstrap analysis was performed to evaluate the reproducibility, and the values were determined from 100 replicates. Final figures were generated using the ggtree[104] package implemented in R[105].

2.5.4 PilA-N–C filament and OmcS/OmcZ cytochrome nanowire purification and biochemical characterization

Both Δ*omcS* and Δ*omcZ* cultures were grown until stationary phase, and then centrifuged at 8,000 x *g* for 20 minutes to separate cells from the media. The supernatant was then passed through a 0.22 um filter, to remove the remaining cells, and concentrated with a 100 kDa cut-off Amicon concentrator

(MilliporeSigma). The sample was diluted in phosphate-buffered saline and centrifuged at 100,000 x *g* for one hour. The pellet was resuspended in 20 mM Sorensen's buffer at pH 7.2 and used for cryo-EM.

For mass spectrometry, the sample was incubated with 2.5% styrene maleic acid (SMA) copolymer solution at room temperature and gently agitated on an orbital shaker. The sample was then centrifuged again at 100,000 x *g* and the pellet was collected and resuspended in 20 mM tris-HCl at pH 7.4. The sample was further purified using a gel filtration column packed with Sephacryl S-500 HR resin (Cytiva). Elution fractions were evaluated with negative-stain transmission electron microscopy and polyacrylamide gel electrophoretic separation. The final purified filament-containing sample was used for mass spectrometry analysis.

In contrast to PilA-N–C filaments that were purified from the cell-free supernatant, both OmcS and OmcZ nanowires were purified by blending the cells as described previously[53, 62].

2.5.5 Cell and protein normalization for comparative expression studies

Bacterial strains were grown to late exponential or stationary phase unless specified. For filament preparations, samples were normalized to the initial wet weight of the bacterial pellet. Equal volumes (1/20th of the final filament preparation protein) was loaded on the gels for comparison. Additional care was taken to collect the samples at a similar growth phase and optical density when comparing different strains.

2.5.6 SDS-PAGE

Samples were boiled in 1X SDS sample buffer that included β-mercaptoethanol for 12 minutes. The samples were run on a 16% tricine protein gel (Thermo Fisher Scientific) initially at constant voltage of 30 V for 2 hours before changing to 190 V for 30 minutes, at 4°C. Precision Plus Protein Prestained molecular weight standards (Bio-Rad) and Low Range Protein Ladder (Thermo Scientific) were used to compare the molecular weight of cytochromes in the filament preparations. Gels were stained with Coomassie R-250 stain for 1 hour (Thermo Scientific), and de-stained in deionized water overnight.

2.5.7 Immunoblotting

Polyclonal anti-PilA-N, anti-PilA-C, anti-OmcS and anti-OmcZ antibody was synthesized by LifeTein by immunizing two rabbits with synthetic peptide sequences containing a targeted epitope on the

native protein, and then affinity-purifying the serum against that peptide sequence. The antibody was used at a dilution of 1:5000 for immunoblotting. Filament samples were normalized to the initial cell mass of the starting material.

2.5.8 Mass spectrometry

For LC-MS/MS analysis of filaments, all the bands visible in SDS-PAGE were extracted from protein gels and digested with trypsin. Proteomic analysis of the cleaved peptides was performed by the Proteomics Mass Spectrometry Facilities at Yale University and Columbia University.

In-gel digestion. As described previously[106], filament samples were separated on 4-12% gradient SDS-PAGE, and stained with SimplyBlue (Thermo Fisher Scientific). Protein gel slices were excised and subjected to *in-gel* digestion. Gel slices were washed with 1:1 (acetonitrile: 100 mM ammonium bicarbonate) for 30 minutes; gel slices were then dehydrated with 100% acetonitrile for 10 minutes until gel slices had shrunk, at which point excess acetonitrile was removed, and slices were then dried in a speed-vac for 10 minutes using no heat. Gel slices were reduced with 5 mM DTT for 30 minutes at 56 °C in an air thermostat, the tube was chilled down to room temperature, and the sample was alkylated with 11 mM IAA for 30 minutes in the dark. Gel slices were then washed with 100 mM ammonium bicarbonate and 100 % acetonitrile for 10 minutes each. Excess acetonitrile was removed and dried in a speed-vac for 10 minutes with no heat, and gel slices were then rehydrated in a solution of 25 ng/µl trypsin in 50 mM ammonium bicarbonate, on ice, for 30 minutes. Digestions were performed overnight at 37 °C in an air thermostat. Digested peptides were collected and further extracted from gel slices in extraction buffer (1:2 vol/vol) 5% formic acid/acetonitrile) with high-speed shaking in an air thermostat. Supernatant from both extractions were combined and dried down in a speed-vac. Peptides were dissolved in 3% acetonitrile/0.1% formic acid.

LC-MS/MS analysis. A Thermo Scientific™ UltiMate™ 3000 RSLCnano system and Thermo Scientific EASY Spray™ source with a Thermo Scientific™ Acclaim™ PepMap™100 2 cm x 75 µm trap column and Thermo Scientific™ EASY-Spray™ PepMap™ RSLC C18 50 cm x 75 µm ID column were used to separate desalted peptides with a 5-30% acetonitrile gradient in 0.1% formic acid over 100 minutes at a flow rate of 250 nL/min. The column temperature was maintained at a constant 50 ˚C during all experiments.

A Thermo Scientific™ Orbitrap Fusion™ Tribrid™ mass spectrometer was used for peptide MS/MS analysis. Survey scans of peptide precursors were performed from 400 to 1500 *m/z* at 120K FWHM resolution (at 200 *m/z*) with a 2 x 10^5 ion count target and a maximum injection time of 50 ms. The instrument was set to run in top speed mode with 3-second cycles for the survey and the MS/MS scans. After a survey scan, tandem MS was performed on the most abundant precursors exhibiting a charge state from 2 to 6 of greater than 5 x 10^3 intensity by isolating them in the quadrupole at 1.6 Th. CID fragmentation was applied with 35% collision energy, and resulting fragments were detected using the rapid scan rate in the ion trap. The AGC target for MS/MS was set to 1 x 10^4 and the maximum injection time limited to 45 ms. The dynamic exclusion was set to 45 seconds with a 10 ppm mass tolerance around the precursor and its isotopes. Monoisotopic precursor selection was enabled.

Data analysis. Raw mass spectrometric data were analyzed using the MaxQuant environment[107] v.1.6.1.0, employing Andromeda for the database searches using default settings with a few modifications. The default was used for first search tolerance and main search tolerance: 20 ppm and 6 ppm, respectively. MaxQuant was set up to search with the reference *Geobacter sulfurreducens* database downloaded from UniProt. MaxQuant performed the search based on trypsin digestion with up to 2 missed cleavages. Peptide, site, and protein FDR were all set to 1%. The following modifications were used as variable modifications for protein identifications and quantification: oxidation of methionine, acetylation of the protein N-terminus, and deamination of asparagine or glutamine. Results obtained from the MaxQuant output combined folder were loaded into Scaffold (Proteome Software) for data visualization. Spectral counts were used for analysis to compare the samples.

2.5.9 Cryo-EM data collection and image processing

The PilA-N–C filament sample (3.5 µL) was applied to 400 mesh C-flat grids and plunge-frozen by a Vitrobot Mark IV (FEI). Frozen grids were imaged on a Titan Krios operating at 300 kV equipped with a K2 summit detector (Gatan). Micrographs were recorded with super resolution mode at 0.822 Å/pixel, with a total dose of ~62 $e^-/Å^2$ fractioned into 27 frames. A defocus range of 0.8 µm – 2.5 µm was used to collect ~7560 images in total. All movies were first motion-corrected with MotionCorr implemented in RELION 3[108], summing a total dose of ~20 e^- by using frames 2-10. The contrast transfer function (CTF) of

motion-corrected images was estimated by GCTF v1.08[109]. Filament segments were manually picked with RELION, and all the helices were further segmented into ~280,000 particles using a box size of 400 Å and inter-box distance at 31.5 Å including 3 asymmetric subunits to save computational time. After 2D classification, ~160,000 particles were selected for further data processing. Averaged power spectra and the power spectra of the class average were analyzed to determine the helical symmetry with SPRING[110]. The helical symmetry was first deduced from Fourier-Bessel indexing and then compared with a simulated power spectrum. After trial and error, a helical rise of 10.5 Å and twist of 89.0° were imposed for the final reconstruction. All of the ~160,000 particles were used to generate a consensus map in RELION[111] using the iterative helical real space reconstruction algorithm[112]. A simulated helical lattice (relion_helix_toolbox)[111] with the deduced helical symmetry was used as a starting reference, since featureless cylinder gave a suboptimal reconstruction. An initial reconstruction at ~4.5 Å was produced and filtered to 10 Å to be used as the reference for 3D classification (K=4, tau=20) to address heterogeneity in the particles. After 3D classification, 100,000 particles were combined for the final refinement and gave rise to a ~4.2 Å reconstruction. After iteratively applied CTF refinement until no further improvement of resolution was achieved, the particles were polished with the Bayesian polishing framework[113] implemented in RELION, which further improved the resolution to ~3.8 Å based on the gold standard FSC.

2.5.10 Bioinformatic analysis

About ~160 C_α atoms were successfully traced from the subunit density and this estimated protein length was used for bioinformatic analysis. The proteome (n=81491) of *G. sulfurreducens* was obtained from NCBI and proteins with a length of 150 – 190 residues were selected (n=3992). All 3992 candidates were further examined using the TMHHM2 server and only proteins predicted to have a single transmembrane domain were kept for further analysis. Using a Python script, proteins with a predicted TM helix longer than 20 amino acids within the first 60 residues were maintained and 13 potential candidates were used for further analysis.

2.5.11 Model building and refinement

The protomer density was segmented in UCSF Chimera[114] and the C_α backbone trace was manually constructed using Coot[115]. Based on the mass spectrometry and bioinformatic analyses and side chain density visible in the map, PilA-N and PilA-C were determined to be the constituents of the protomer and an all-atom model of the protomer was constructed and then refined using phenix.realspace_refine[116]. This refined protomer model was further extended to into a filament model in Chimera and refined against the filament density map using phenix.realspace_refine. The refined model was finally manually inspected and adjusted in Coot.

2.5.12 Atomic force microscopy

To visualize cells, 10 µL of buffer solution containing cell samples were deposited on mica. The excess buffer was absorbed with filter paper. The sample was air-dried and was mounted on a metal puck (Oxford Instrument, Cypher ES). To visualize individual filaments, 5 µL of buffer solution containing filaments were deposited on a silicon wafer insulated by a 300 nm silicon dioxide dielectric layer with gold electrodes patterned by electron beam as described previously[53]. AFM experiments were performed using soft cantilevers (OMCL-AC240TS-R3, OLYMPUS) with a nominal force constant of 2 N/m and resonance frequencies of 70 kHz. The free-air amplitude of the tip was calibrated with the Asylum Research software and the spring constant was captured by the thermal vibration method. The sample was imaged with a Cypher ES scanner using intermittent tapping (AC-air topography) mode. AFM showed that gold electrodes were bridged with individual filaments to facilitate conductivity measurements (Figure 2.9G). All AFM image analyses for cells and filaments were performed using Gwyddion[117]. The AFM height cross section has been analyzed using IGOR Pro software (WaveMetrics).

2.5.13 Electrode fabrication

Electrodes made of gold separated by a 300 nm non-conductive gap were designed using electron beam lithography as described previously[53]. Interdigitated electrode devices were designed in Layout Editor, a computer-aided design program. Two layers of resists (50-nm-thick poly(methyl methacrylate) and 60-nm-thick UV-curable resist) were then sequentially spin-coated onto the cleaned substrate. Circuit patterns including nanoelectrodes separated by nano-sized gaps, microscale fan outs, and

contact pads were transferred from a quartz mold to the UV resist with nanoimprint lithography in a homemade imprint chamber. The residual UV-resist layer and the poly(methyl methacrylate) underlayer were removed by reactive ion etching with fluorine-based (CHF_3/O_2) and oxygen-based gases respectively.

2.5.14 Conductivity measurement

All direct current measurement was carried out on interdigitated devices with a 300 nm gap. A single filament bridging two electrodes was first identified by AFM and the contact electrode was recorded. The device was then transferred to the stage of a probe station connected to a semiconductor parameter analyzer. A sweeping voltage from -1 V to 1 V was first applied to estimate the range of current response. Then, by selecting the proper sensitivity for current detection, a stepwise voltage was applied with 50 mV increments. Each filament was measured within a proper low voltage range (<0.25 V) to maintain the linear behavior of the current-voltage (I-V) curve. Each measurement was made over a long waiting period to ensure the stability of the current (> 200 s) and a lack of faradic currents or electrochemical leakage as is normally evident in a buffering system. The conductance (G) was extracted by fitting the current-voltage curve with a linear function and was further converted into conductivity (σ) by applying the relationship $\sigma = G\,(L/\pi r^2)$ where r is the radius of the pilus and L is the distance between two electrodes.

2.5.15 Cell attachment assays

Mid-log cells were inoculated at a 1/100 dilution into 10 mL glass tubes of fresh NBAF media. Cells were incubated for 4 days (until approximately mid-log phase) at 30°C. Cultures were gently inverted 5 times and planktonic cells were decanted. Tubes were washed with Mili-Q water and remaining cells were stained with 10 mL of 0.1% crystal violet for an hour and then washed with Mili-Q water. Crystal violet was dissolved utilizing 10mL of 1% acetic acid for an hour and measured at 580 nm using a NanoDrop 2000c spectrophotometer.

2.5.16 Subcellular fractionation

G. sulfurreducens cells were fractionated using a previously published protocol[36] with the following modifications. 300 mL of late-log phase culture grown in NBAF was pelleted at 6000 x *g* for 15 minutes

at 4 °C. The supernatant was filtered through a 0.22 µm filter and concentrated via a 10 kDa cut off Amicon concentrator. The final concentrate was labelled as the extracellular fraction. Other fractions were prepared as described previously[36].

2.5.17 Twitching motility assay

Twitching assays were performed by stab-inoculating *P. aeruginosa* and *G. sulfurreducens strains* in LB agar and NBAF agar plates, respectively[5]. Three colonies were stab-inoculated for each strain, and the diameter of the twitching zone was measured. *P. aeruginosa* strains were incubated overnight at 37 °C and then left at room temperature for 24 hours before removing the agar to measure the twitching zone. *G. sulfurreducens* strains were incubated in strict anaerobic conditions for 7 days at 30 °C before removing the agar.

2.6 Acknowledgments

We thank Lisa Craig, Stephen Lory, and Yong Xiong for discussions; Eric Martz for calling our attention to the "flaps" in PilA-N–C, for the Supplementary Videos, and for the Interactive 3D Visualizations available alongside the online version of this publication; Derek Lovley, Kengo Inoue, and Barbara Kazmierczak for providing strains; Shenping Wu and Marc Llaguno for help with cryo-EM; and Tukiet Lam and Jean Kanyo for help with mass spectrometry analysis. We thank Tristan Croll for help with ISOLDE. This research was supported by a Career Award at the Scientific Interfaces from the Burroughs Wellcome Fund (to N.S.M.), the National Institutes of Health Director's New Innovator Award (1DP2AI138259-01 to N.S.M.), and an NSF CAREER Award (no. 1749662 to N.S.M.). Research was sponsored by the Defense Advanced Research Project Agency (DARPA) Army Research Office (ARO) and was accomplished under Cooperative Agreement Number W911NF-18-2-0100 (with N.S.M). This research was supported by NSF Graduate Research Fellowship award 2017224445 (to J.P.O.) and NIH Training Grant T32 GM007223, which supported V.S. Research in the Malvankar laboratory is also supported by the Charles H. Hood Foundation Child Health Research Award, and the Hartwell Foundation Individual Biomedical Research Award.

2.7 Appendix

The following pages contain the supplementary figures published with the manuscript, some of which are referred to directly within this chapter.

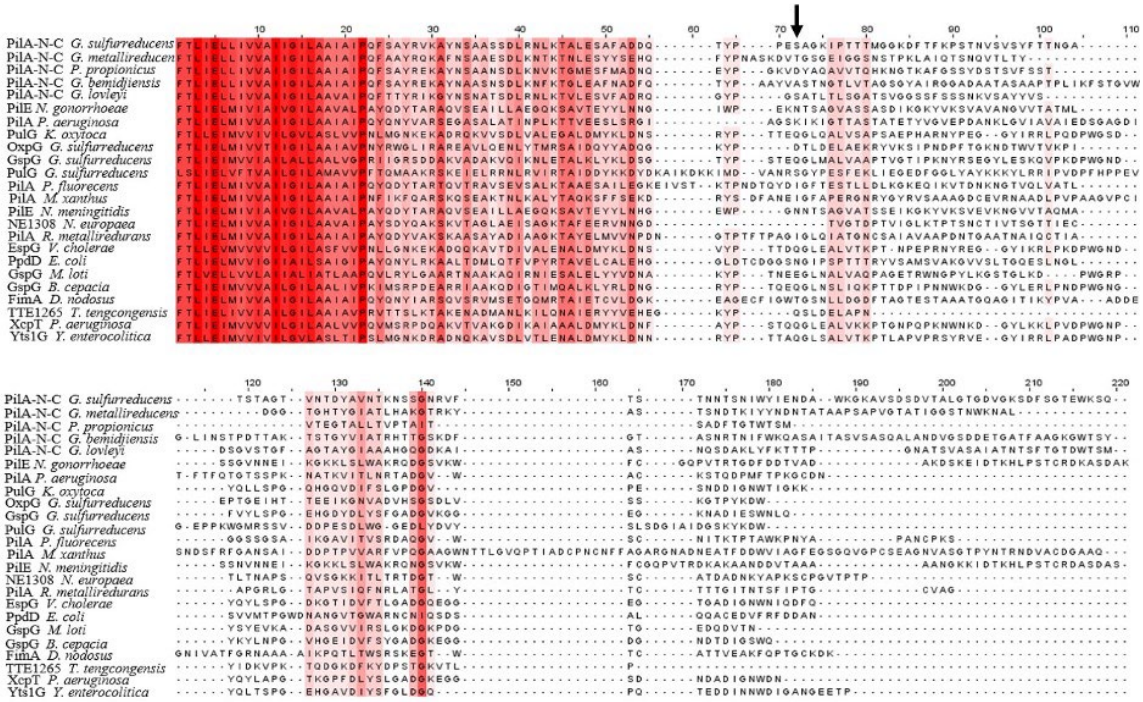

Supplementary Figure 2.1. Amino acid sequence alignment of T4P-like proteins.

Amino acid sequence alignment of the T4P-like proteins from different species showed that N-terminal are highly conserved, while the C-terminal is divergent. Sequence conservation is rendered in red, and a darker color represents a higher conservation score. For Geobacter-related species, PilA-N and PilA-C sequences were fused together for comparison. Black arrow shows the location where the PilA-N sequence ends. This sequence alignment was used to construct the phylogenetic tree shown in Supplementary Figure 2.2.

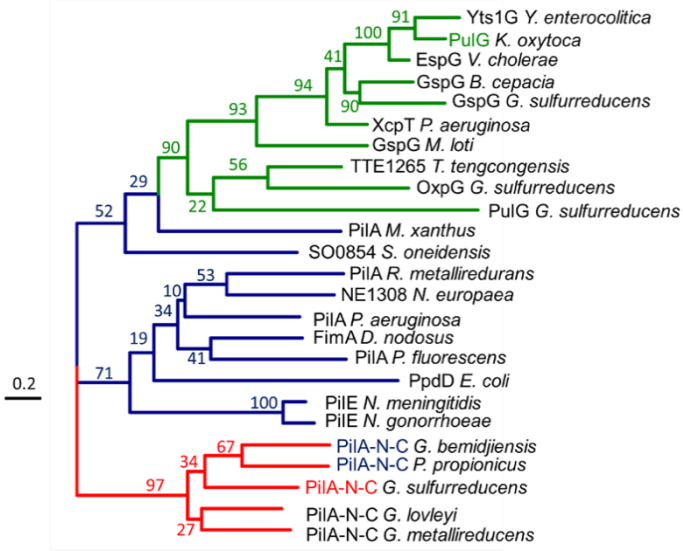

Supplementary Figure 2.2. Phylogenetic analysis of pilin amino acid sequence.

Phylogenetic analysis of pilin amino acid sequence alignment of the T4aP (blue) and T2SS pseudopili (green) from different species. For *Geobacter*-related species, PilA-N and PilA-C sequences were fused together for comparison (shown in red). Numbers represent bootstrap values for each branch.

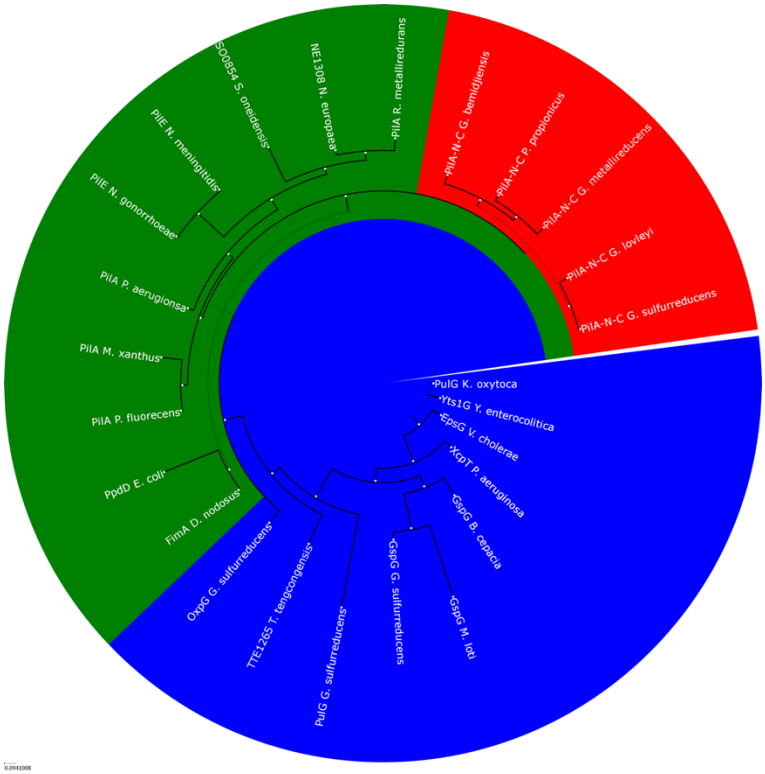

Supplementary Figure 2.3. Rooted tree representation of the phylogenetic analysis.

Rooted tree representation of the phylogenetic analysis of pilin amino acid sequence alignment of the T4aP (green) and T2SS pseudopili (blue) from different species. For Geobacter-related species, PilA-N and PilA-C sequences were fused together for comparison (shown in red).

Protein Name	MW (kDa)	Coverage(%)	iBAQ (x 10^8)
GSU3305	10	67	317
GSU3402	10	57	127
GSU0360	46	75	72.8
GroL	58	88	69.2
GSU3547	27	69	66.1
OmcZ	49	23	52.4
CpoB	31	71	44.2
Eno	46	78	40.1
PpcA	10	27	35.9
GSU0872	16	76	35.3
GlnA	53	86	32.4
DegP	50	81	31.3
GSU2429	39	74	29
GSU0800	29	63	28.1
OmcE	24	22	22.1
OmpB	140	58	21
OmcC	81	41	20.9
OmcB	77	19	7.8
OmcQ	36	16	0.24
OmcP	30	16	0.23
OmcS	45	25	0.17
OmcI	37	4	0.15

Supplementary Figure 2.4. Lack of pili filaments under nanowire-producing conditions that required long-range electron transport.

Solution mass spectrometry analysis of filament preparation from electrode-grown WT cells did not show either PilA-N or PilA-C.

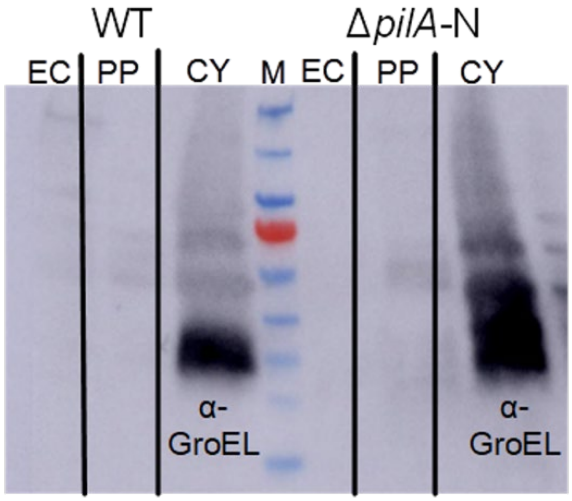

Supplementary Figure 2.5. Subcellular fractionation controls.

Immunoblot showing control for subcellular fractionation studies using cytoplasmic protein GroEL. EC: Extracellular, PP: Periplasmic and CY: Cytoplasmic fractions. M: Marker.

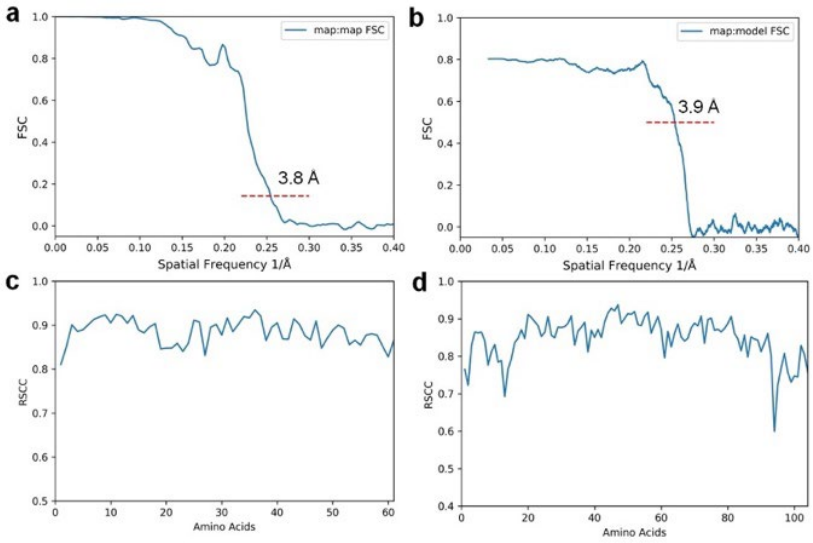

Supplementary Figure 2.6. Illustration of cryo-EM map quality.

a, The gold standard FSC calculated by RELION using 0.143 cutoff estimated the map to have a resolution at 3.8 Å. **b**, Map to model FSC using 0.5 criterion estimated the map resolution to be 3.9 Å. **c**, The per-residue real space correlation coefficient plot of the atomic model against the map for PilA-N. **d**, The per-residue real space correlation coefficient plot of the atomic model against the map for PilA-C.

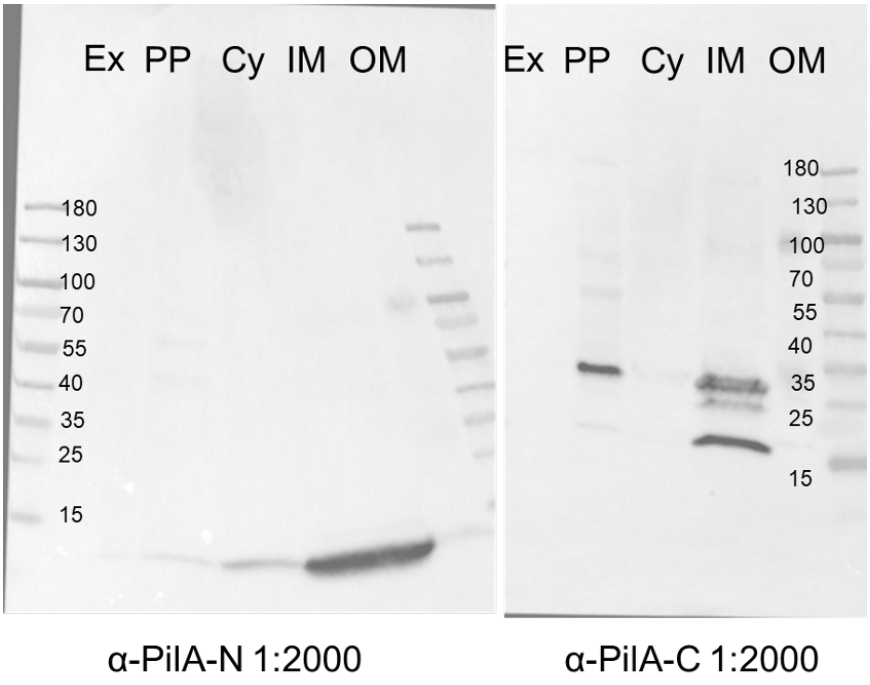

Supplementary Figure 2.7. Full-length gel showing lack of pili proteins in extracellular fractions.

Immunoblot for subcellular fractionation of PilA-N and PilA-C in WT cells. Ex: extracellular, PP: Periplasm, CY: Cytoplasm, IM: Inner-membrane, OM: Outer-membrane.

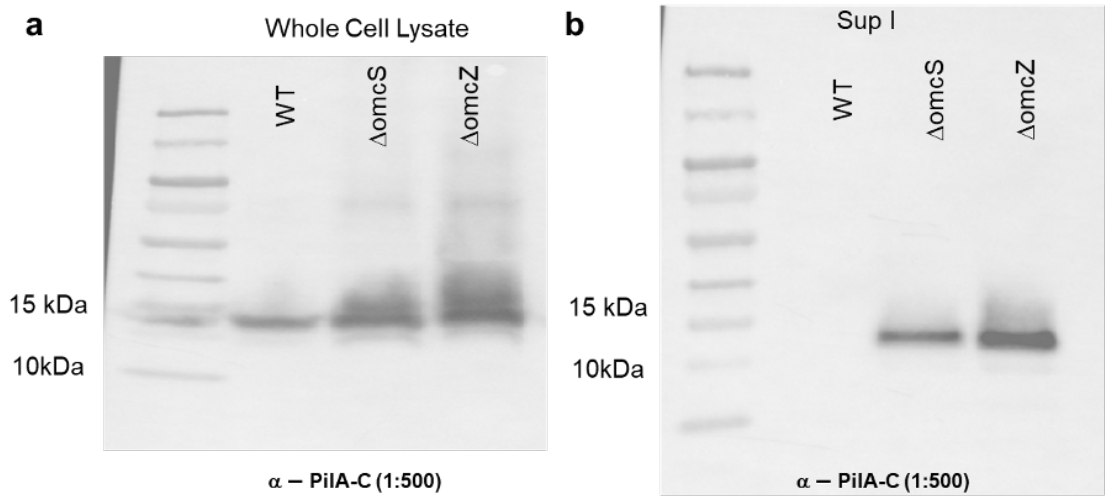

Supplementary Figure 2.8. Full-length gel showing overproduction of PilA-C in mutants lacking cytochrome nanowires.

Immunoblot of PilA-C in WT, Δ*omcS* and Δ*omcZ* cells.

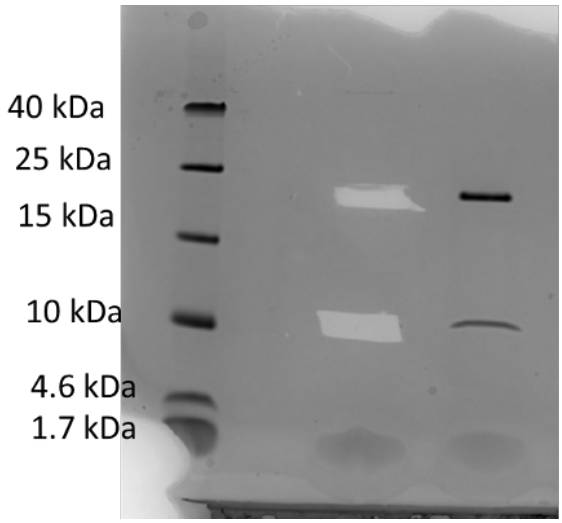

Supplementary Figure 2.9. Full-length SDS-PAGE gel of PilA-N–C filaments purified from Δ*omcS* cells.

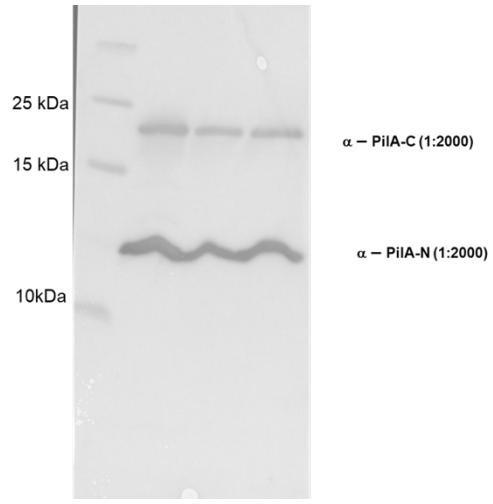

Supplementary Figure 2.10. Full-length immunoblot for PilA-N and PilA-C containing band.

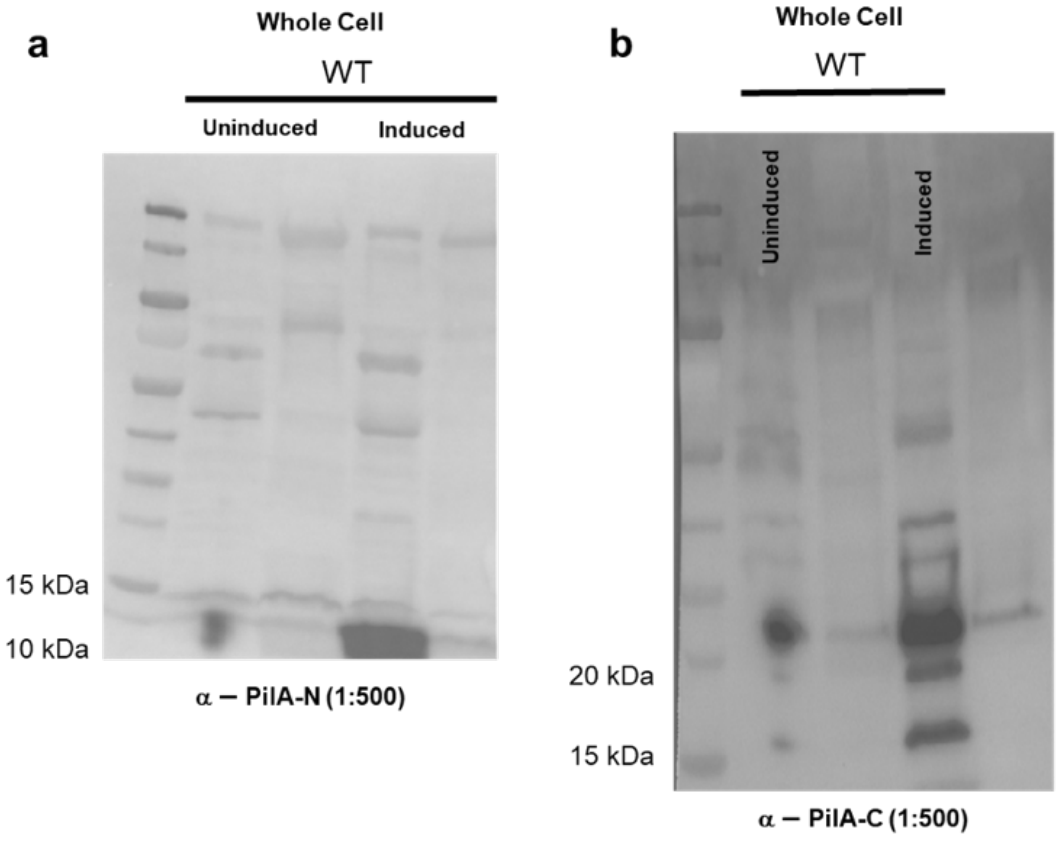

Supplementary Figure 2.11. Full-length immunoblot for overexpressing PilA-N and PilA-C in WT *G. sulfurreducens* yielded pili-like filaments.

Immunoblot of whole cell lysate showing overexpression of **a**, PilA-N and **b**, PilA-C under induced conditions.

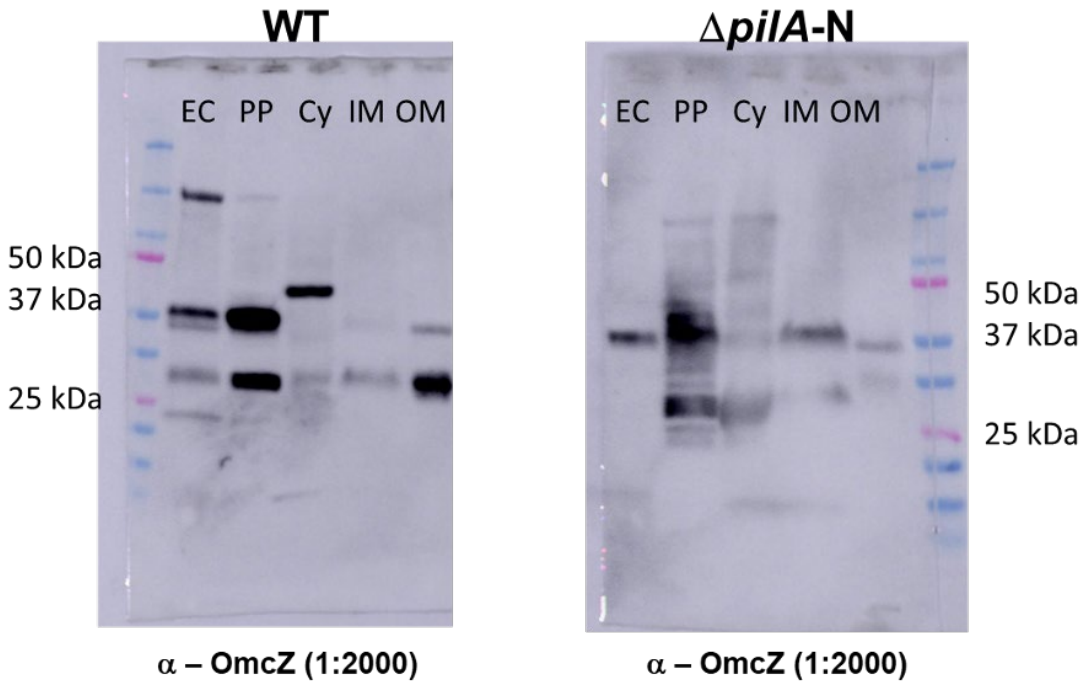

Supplementary Figure 2.12. Full-length gel showing lack of OmcZ nanowires in extracellular fractions of Δ*pilA*-N cells.

Immunoblot for subcellular fractionation of OmcZ in WT cells and Δ*pilA*-N cells. EC: extracellular, PP: Periplasm, CY: Cytoplasm, IM: Inner-membrane, OM: Outer-membrane.

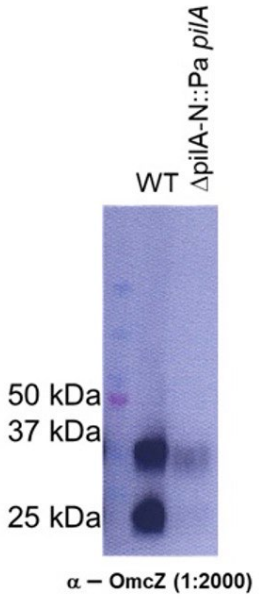

Supplementary Figure 2.13. Full-length gel showing lack of $OmcZ_s$ in filament preparations of *G. sulfurreducens* strains in which *pilA-N* was replaced with *pilA* of *P. aeruginosa* (*Gs-Pa*).

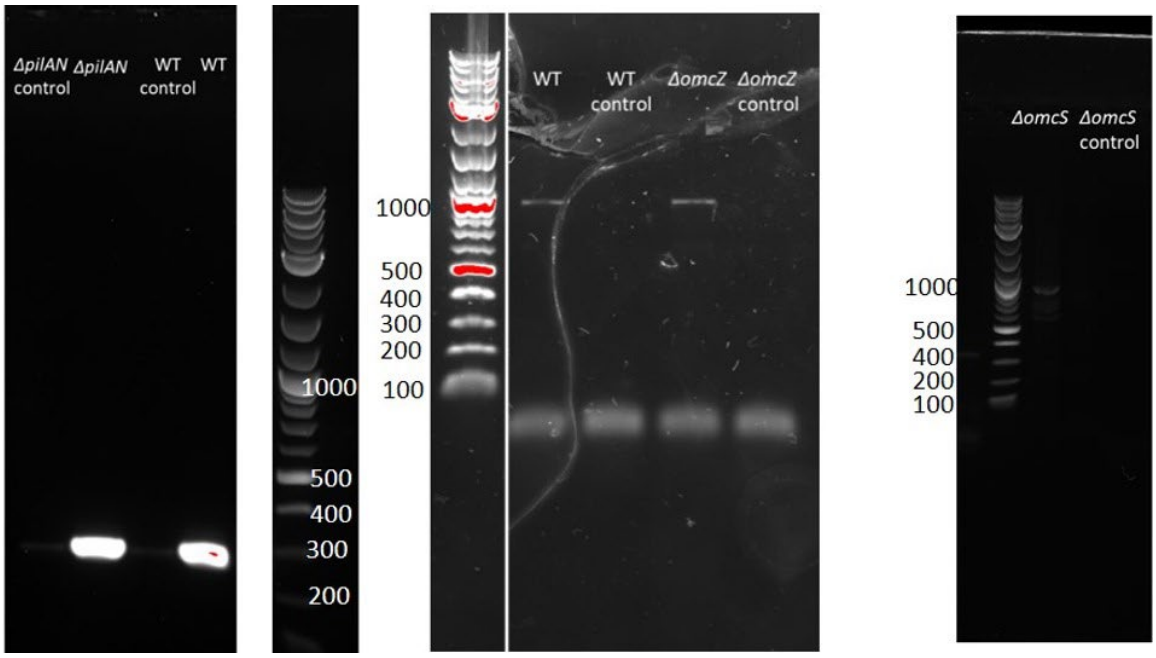

Supplementary Figure 2.14. Lack of polar mutations in Δ*pilA,* Δ*omcS* and Δ*omcZ* strains.

Lack of polar mutations in Δ*pilA,* Δ*omcS* and Δ*omcZ* probed by reverse transcriptase – polymerase chain reaction (RT-PCR) using primers of downstream gene. Markers shows molecular weights in bp.

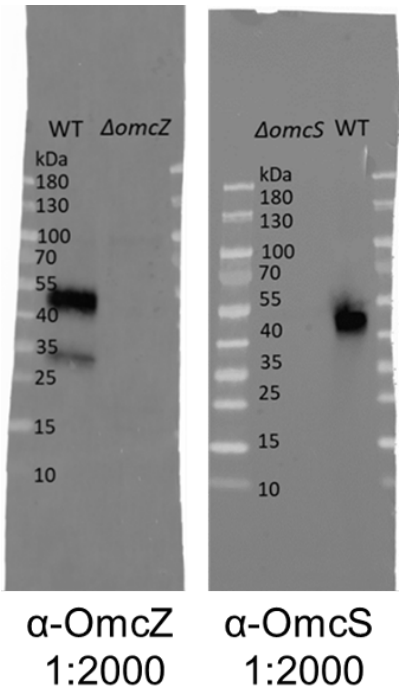

Supplementary Figure 2.15. Specificity of cytochrome antibodies using controls Δ*omcS and* Δ*omcZ*.

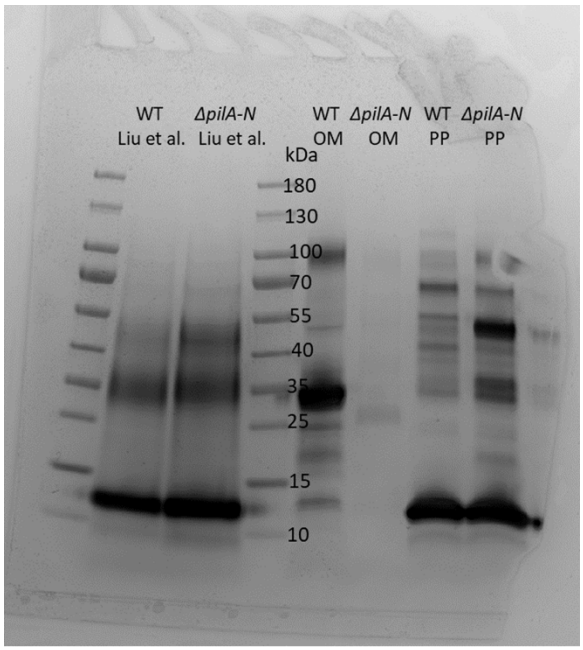

Supplementary Figure 2.16. Effect of periplasmic contamination in previous studies.

Side-by-side comparison of extracellular cytochrome preparation protocol used by Liu et al.[36] and the protocol used in this manuscript for outer-membrane (OM) and periplasmic (PP) fractions**.** The extracellular cytochrome preparation by Liu et al. seems to contain periplasmic contamination as evident by similarity with our periplasmic fractions.

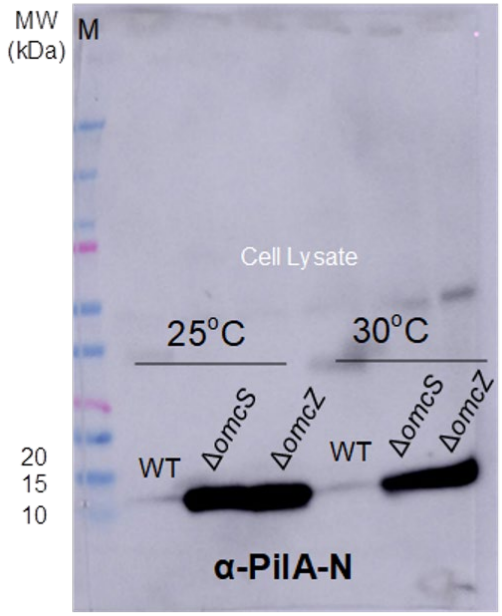

Supplementary Figure 2.17. Full-length gel of whole cell lysate showing overproduction of PilA-N in mutants lacking cytochrome nanowires.

Immunoblot of PilA-N in WT, Δ*omcS* and Δ*omcZ* cells grown at 25°C (left lanes) and 30°C (right lanes).

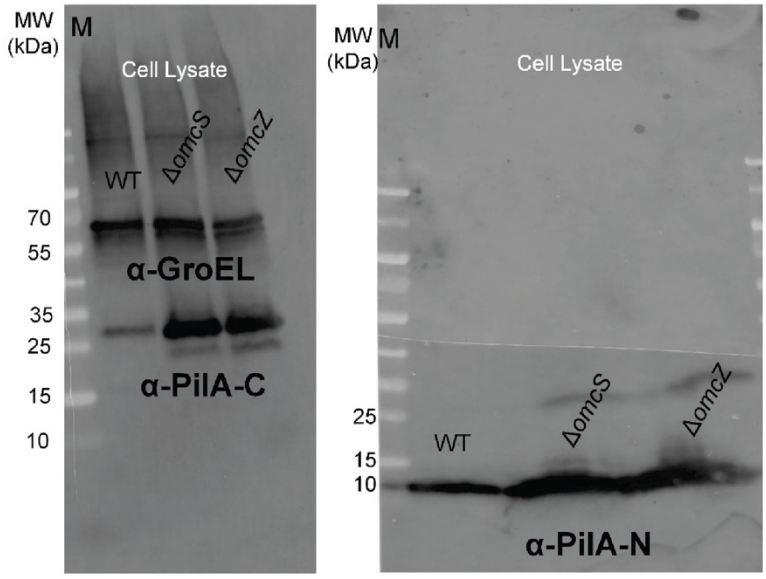

Supplementary Figure 2.18. Full-length gel of whole cell lysate showing overproduction of PilA-N and PilA-C in mutants lacking cytochrome nanowires.

Immunoblot of GroEL, PilA-N, and PilA-C in WT, Δ*omcS* and Δ*omcZ* cells. M: Marker.

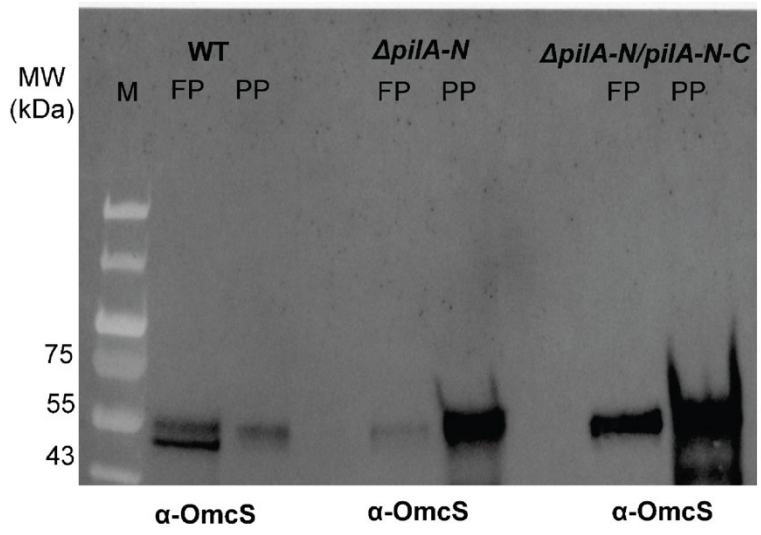

Supplementary Figure 2.19. Immunoblotting with OmcS antibody showing the restoration of secretion defect in OmcS nanowires in Δ*pilA-N*/*PilA-N–C* cells.

FP: Filament preparation. PP: Periplasmic fraction. M: Marker.

Supplementary Table 2.1. Namdinator remodeling results.

Namdinator remodeling, did not improve the Ramachandran statistics.

Stats	Input model	Refinement after Namdinator
Clash Score	16.05	18.05
Favored	83.85%	80.82%
Ramachandran Outliers	0	0.3%
Rotamer Outliers	0	0.65%
CC value	0.84	0.86

Supplementary Table 2.2. ISOLDE remodeling results.

ISOLDE remodeling improved the statistics significantly.

Stats	Input model	Refinement after ISOLDE
Clash Score	16.05	6.63
Favored	83.85%	90.06%
Ramachandran Outliers	0	0
Rotamer Outliers	0	0
CC value	0.84	0.84

Inter-subunit metal coordination in OmcS nanowires is essential for EET *in vivo* and enables reversible assembly *in vitro*

This chapter is a reformatted presentation of a submitted manuscript:

Srikanth, V.*, Yi, S.M.*, Salazar-Morales, A.I.*, Guberman-Pfeffer, M.J., Jain, R., O'Brien, J.P., Gu, Y., Dahl, P.J., Yalcin, S.E., Frenkel, A.I., Batista, V.S., Brudvig, G.W., & Malvankar, N.S. "Controllable assembly of *Geobacter* cytochrome nanowires via tuning metal coordination is essential for extracellular electron transfer."

* These authors contributed equally.

The complete author contribution description accompanying this manuscript is reproduced below (emphasis added):

V.S. established methods for nanowire depolymerization and self-assembly by carrying out gel filtration, UV-vis, CD and TEM characterization, and purified and characterized nanowires for these studies. S.M.Y. performed EPR spectroscopy and XAS data analysis. M. J.G-P performed molecular dynamics simulations to assess filament stability as a function of pH. A.I.S-M. and R.J. constructed the H16A mutant strain and A.I.S-M. performed biochemical and functional characterization of the strain. S.M.Y. purified OmcS nanowires for EPR and XAS. J.P.O. performed initial nanowire purification and UV-vis and CD spectroscopy. Y.G. assisted with CD and TEM characterization. P.J.D. performed initial molecular dynamics simulations to compute dihedral angles under the guidance of V.S.B. S.E.Y. contributed to analysis and interpretation of UV-vis data. A.I.F. guided XAS measurements and data analysis, and G.W.B. guided EPR measurements. N.S.M. supervised the project. **V.S., S.M.Y., and N.S.M. co-wrote the manuscript with input from all authors.**

3.1 Summary

Polymerization of cytochromes is important in several biological processes, such as apoptosis, and for development of bioelectronic materials. Although it has been known for more than half a century that cytochromes can form polymers, synthetic polymerization methods have yielded only short oligomers. In contrast, common soil bacteria *Geobacte*r have evolved micrometer-long filaments of cytochrome OmcS, which show seamless stacking of hemes for efficient electron transfer to extracellular acceptors or syntrophic partner cells. However, the underlying polymerization mechanism and its physiological relevance are unknown. Here we show that cytochrome polymerization is essential for bacterial survival and is driven by pH-tunable inter-protomer metal coordination. We thus demonstrate the controllable synthesis of cytochrome nanowires that have a remarkable ability to function in extreme environments.

Microbial extracellular electron transfer is essential for a wide range of globally-important environmental processes and for applications in bioenergy, biofuels, bioelectronics, and bioremediation. Since 2005, type IV pili have been thought to mediate long-range (>10 μm) EET in diverse species. However, recent studies revealed that during EET, conductive "nanowires" on the surface of *Geobacter sulfurreducens* are made up of cytochromes OmcS and OmcZ – whereas pili remain intracellular, show low conductivity, and are required for the secretion of cytochrome nanowires. Out of 111 cytochromes, only OmcS and OmcZ are essential for EET – to minerals and electrodes, respectively. Nevertheless, the physiological relevance of OmcS and OmcZ filaments has been strongly questioned. Furthermore, the filaments' underlying polymerization mechanism is unknown. Here, we show that pH-tunable metal coordination across inter-protomer interfaces is essential for OmcS nanowire biogenesis and EET *in vivo*, and enables reversible nanowire assembly *in vitro*. Electron paramagnetic resonance and X-ray absorption spectroscopies reveal that hemes partially lose their axial histidine coordination at low pH, a finding supported by UV-visible (UV-vis) and circular dichroism spectroscopies. Our studies suggest that inter-protomer metal coordination provides a latch to direct subunit orientation, driving nanowire assembly. We thus show that chemically tuning metal-ligand coordination and protein-protein interfaces yields nanowires with controllable assembly. Our studies reveal a novel cytochrome

polymerization mechanism distinct from previous examples of cytochrome assembly in engineered or disease conditions. Harnessing the ability of bacteria to construct self-assembling and environment-sensing supramolecular structures functional in acidic conditions and at high temperatures could yield stimuli-responsive bioelectronics.

3.2 Introduction

In most cells, the biochemical chains of redox reactions that define the energy harvesting pathways of life[118] take place wholly within cellular compartments. The relevant electron transport mechanisms are commensurate with the 1-2 nanometer length scales across which these reactions occur, relying on electron tunneling/hopping between molecules and the diffusion of small electron carriers[119, 120]. However, many environmental microbes exhibit the remarkable capacity to expand their electron transport chain to span micrometers[5, 6, 32, 121] or even centimeters[122-125], reaching electron acceptors and syntrophic partner cells over distances vastly exceeding the size of a single cell. Understanding the ability of diverse bacteria to perform extracellular electron transport to and from organisms and inorganic materials in their environment is critical – both for understanding environmentally important biogeochemical processes, and for unlocking the potential of these biophysical mechanisms for applications in engineering, renewable energy devices, and mixed biotic-abiotic systems[126-130].

Several longer-range EET processes are mediated by extracellular appendages referred to as microbial nanowires[5, 6, 124]. Studies of the nanowires used by *Geobacter sulfurreducens* (Figure 3.1A) to transfer electrons over micrometers to extracellular minerals[40], syntrophic partner cells[19], or electrodes in bioelectrochemical systems[20] identified that PilA, the hypothesized protein building block of these filaments, was critical for certain EET processes involving microbial nanowires[5, 29]. These claims inspired debate over whether aromatic amino acids in PilA could give rise to electron transport along such putative filaments[42, 43], or whether instead EET in *Geobacter* was likely to be mediated by the abundant cytochromes produced in the biofilms performing EET[44, 131]. Direct structural and biochemical studies of the nanowires obtained from cells under conditions requiring EET demonstrated the existence of

protein polymers consisting of multiheme outer membrane cytochromes OmcS[53, 54] and OmcZ[62]. To date, the only experimentally determined high-resolution structures available for microbial nanowires from *G. sulfurreducens* are those of OmcS filaments. However, the physiological role and natural assembly of cytochrome nanowires has been questioned[55, 63].

Further driving interest in OmcS filaments[132, 133] is the fact that protein-based electronic nanomaterials have the potential to offer features critically needed for the next-generation of bioelectronics, including mechanical flexibility, controlled biological properties, and mixed electronic

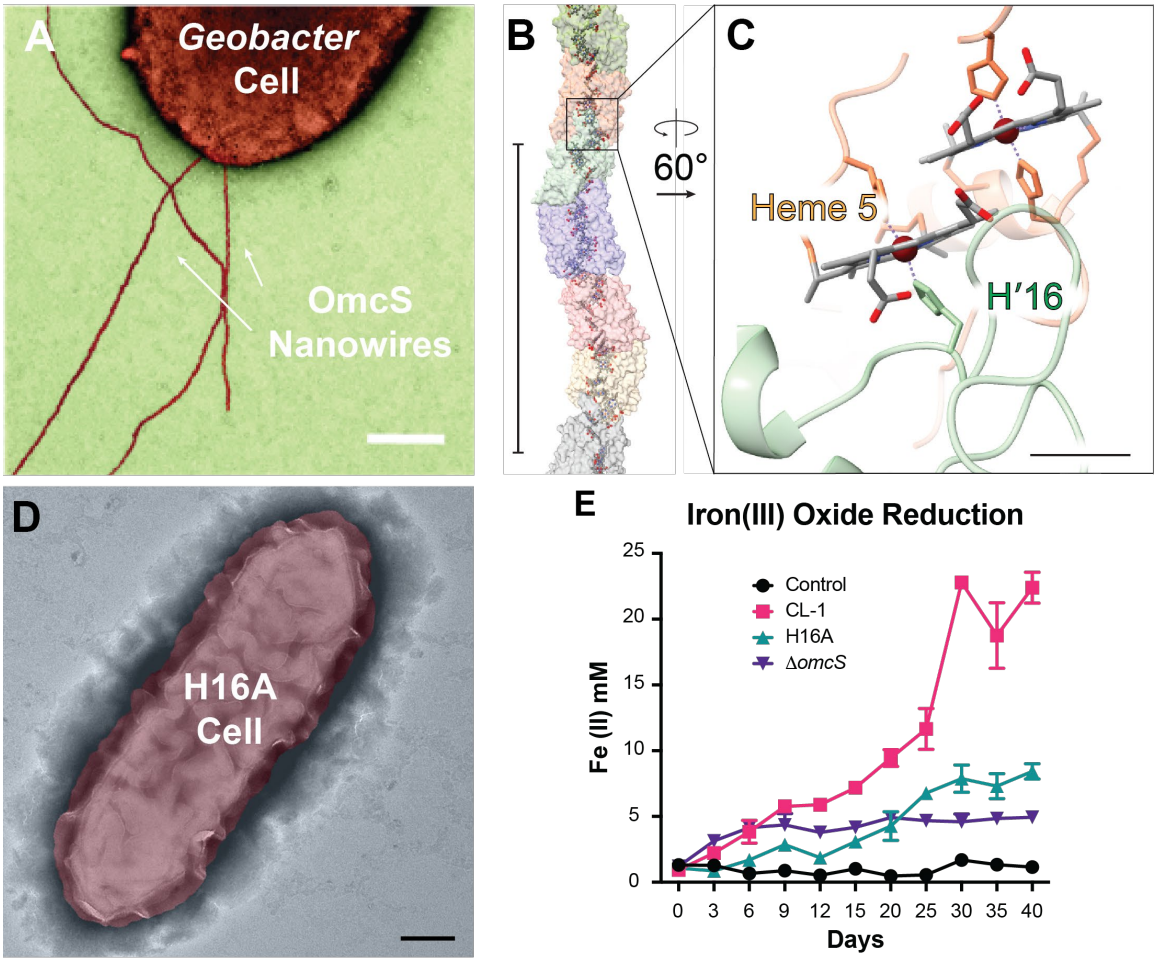

Figure 3.1. Histidine 16 is required for OmcS filament assembly and EET.

A, TEM image of intact OmcS nanowires emanating from a *Geobacter sulfurreducens* CL-1 cell (scale bar, 200 nm). **B**, Cryo-EM structure of OmcS nanowires (PDB ID: 6EF8) showing the stacked hemes (grey) along the filament core (scale bar, 20 nm), and **C** the inter-subunit site of heme iron coordination associated with residue His16 (scale bar, 5 Å). **D**, H16A mutation in *omcS* abolishes OmcS filament production in strain CL-1 (scale bar, 200 nm). **E**, Growth on insoluble Fe(III) oxide shows reduced ability of strain H16A (teal) to transfer electrons extracellularly compared with the parent CL-1 strain (pink), similar to cells in which the *omcS* gene was deleted (purple). Error bars show standard deviation, n = 3 biological replicates.

and ionic conductivity[134]. Aside from protein-based microbial nanowires, proteins have long been considered to be electronic insulators, transferring electrons over only 1-2 nanometers and losing functionality under non-physiological conditions[135-137]. OmcS nanowires can transport electrons efficiently over micrometers due to their long-range seamless arrangement of hemes stacked within edge-to-edge distances of ~3.5-6 Å (Figure 3.1B)[53, 54]. Cryogenic electron microscopy showed that the six bis-histidine ligated hemes in each OmcS protomer are arranged in three parallel-stacked pairs, with each heme pair perpendicular to the other pairs in a T-shaped geometry. The interface between subunits shows axial coordination of heme 5 in each subunit by histidine 16 (His16) in the neighboring subunit (Figure 3.1C). This long-range polymerization of OmcS was itself surprising, given that supramolecular assemblies of heme proteins had been studied for over fifty years[58] prior without any indication that such an assembly could be physiologically required for cell respiration. Prior studies have examined the engineering potential of cytochrome *c* oligomerization that relies on a protein domain-exchange mechanism[59-61]. However, this mechanism does not appear compatible with the OmcS cryo-EM structures, as the OmcS protomers within the filament do not appear to have multiple domains that could be exchanged during the polymerization process. Therefore, a novel mechanism must be invoked to explain the formation of OmcS nanowires. The inter-subunit metal coordination observed in OmcS had previously been observed in other cytochrome dimers[138, 139], but no prior work had suggested that such an interaction could support the incorporation of thousands of monomers into a stable micrometer-scale assembly.

In this work, we address fundamental questions about the physiological role of OmcS filaments in *G. sulfurreducens* EET, and advance our understanding of the biophysical mechanism by which OmcS filaments are assembled. To directly understand the biological function of OmcS nanowires, we made a targeted mutation to the His16 residue responsible for inter-protomer metal coordination in the cryo-EM structures. If the well-established physiological importance of OmcS[40, 47, 49] were to be attributable solely to OmcS monomers – and OmcS polymers were to be considered biologically irrelevant[55] – then this nanowire-disrupting mutation should have no effect on EET. Instead, we find that disruption of inter-protomer metal coordination affects OmcS nanowire biogenesis and that the resultant lack of cell-

attached OmcS filaments results in a defect in extracellular reduction of insoluble Fe(III) oxide. Furthermore, we find that His16 is required for localization of OmcS to the outer membrane and that WT OmcS expressed in cells is not monomeric when localized to the outer membrane. This finding is incompatible with previous models which proposed that OmcS mediates EET via monomers localized extracellularly along non-cytochrome filaments. Our experiments thus provide direct evidence that polymerization of cytochromes into nanowires is essential for EET.

To determine the mechanism of OmcS polymerization, we directly probe the role of metal coordination in the oligomerization of OmcS. Iron-coordinating histidine residues become deprotonated to form imidazolate at high pH; at low pH they form imidazolium, potentially disrupting histidine-metal coordination interactions[140, 141]. We find that, due to the flexible nature of ligation[142], controlling the protonation of these residues via pH manipulation drives reversible disassembly and self-assembly of OmcS nanowires, and we confirm via a suite of complementary spectroscopic methods that these transitions between monomers and polymers are accompanied by the expected changes in metal coordination without denaturation of the OmcS protein. We further utilize computational modelling to compare the strength of the inter-subunit metal coordination interactions to the strength of protein-protein interactions at the subunit interfaces and find that the strength of these interactions is comparable. Our findings suggest a model wherein inter-protomer metal coordination serves as a latch to stabilize the relative orientation of subunits during nanowire assembly.

3.3 Results

3.3.1 His16 is necessary for *in vivo* OmcS polymerization and EET to Fe(III)

We substituted His16 for an alanine in the *omcS* gene of OmcS-overexpressing CL-1 strain[48] *G. sulfurreducens*, creating strain H16A. Unlike wild-type CL-1 cells (Figure 3.1A), strain H16A cells do not display any OmcS-like filaments (Figure 3.1D). As the *omcS* gene is essential for reduction of insoluble Fe(III) oxide[40, 47, 49], we further examined whether the absence of OmcS filaments would affect this EET process. We found that strain H16A cells have a reduced ability to transfer electrons extracellularly to Fe(III) oxide (Figure 3.1E) compared with the parent CL-1 strain.

Compared to strain CL-1, H16A cells also produce a lower amount of OmcS protein (Figure 3.2A, Figure 3.3). Despite this difference in observed protein abundance, the transcription level of *omcS* in the mutant strain was higher than in the parent strain (Figure 3.3A-B), indicating that an inability to polymerize impacts the stability of OmcS protein *in vivo*. To further understand how the H16A mutation impacted potential assembly of OmcS filaments, we assayed subcellular fractions of the H16A and CL-1 strains for the presence of OmcS protein. We detected OmcS protein in the cytoplasmic, periplasmic, and outer-membrane associated fractions of strain CL-1 – but found no OmcS associated with the outer membrane in strain H16A (Figure 3.2C). This suggested that OmcS may be required to polymerize in order to be properly localized to the outer membrane.

Since we have observed that OmcS filaments are stable in the presence of SDS if they are not heated, we devised a simple assay to check whether or not the OmcS we observed in the subcellular fractions was in a monomer form. We further evaluated the subcellular fractions using SDS-PAGE with and without the heat treatment that is usually applied when preparing SDS-PAGE samples, creating quasi-"native" and "denatured" versions of each fraction. By including purified filamentous and

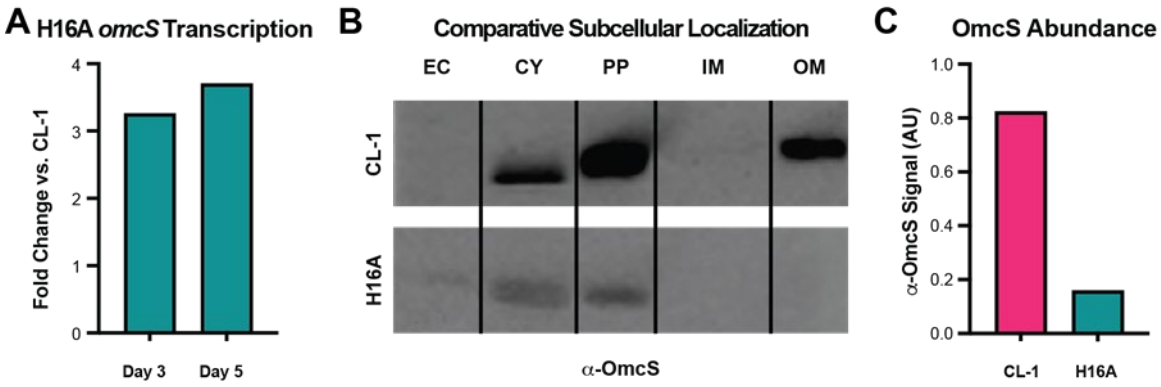

Figure 3.2. Comparative localization of wild-type and H16A OmcS suggests no role for OmcS monomers in EET.

A, RT-qPCR analysis of RNA extracted from strains CL-1 and H16A indicates that OmcS transcripts are more abundant in the mutant. **B**, Immunoblotting of subcellular fractions of strains CL-1 and H16A indicates that the H16A mutation prevents localization of OmcS to the outer membrane. **C**, Immunoblotting of whole cell lysates (20 µg protein each lane) after five days of growth in fumarate media indicated that strain H16A produces a lesser abundance of OmcS protein than strain CL-1 (quantified immunoblot signal visualized, see Figure 3.3).

monomeric samples of OmcS (see subsequent results sections), we could correlate the appearance of OmcS at the expected molecular weight to a high abundance of either polymeric or monomeric OmcS in a sample; samples which showed ~50 kDa OmcS only in the denatured version of a sample indicated that OmcS was present in a polymerized form (Figure 3.4C).

The amount of OmcS protein in the subcellular fractions is greatly reduced compared to our control for monomeric OmcS, making it difficult to detect OmcS in any of the "native" subcellular fractions even

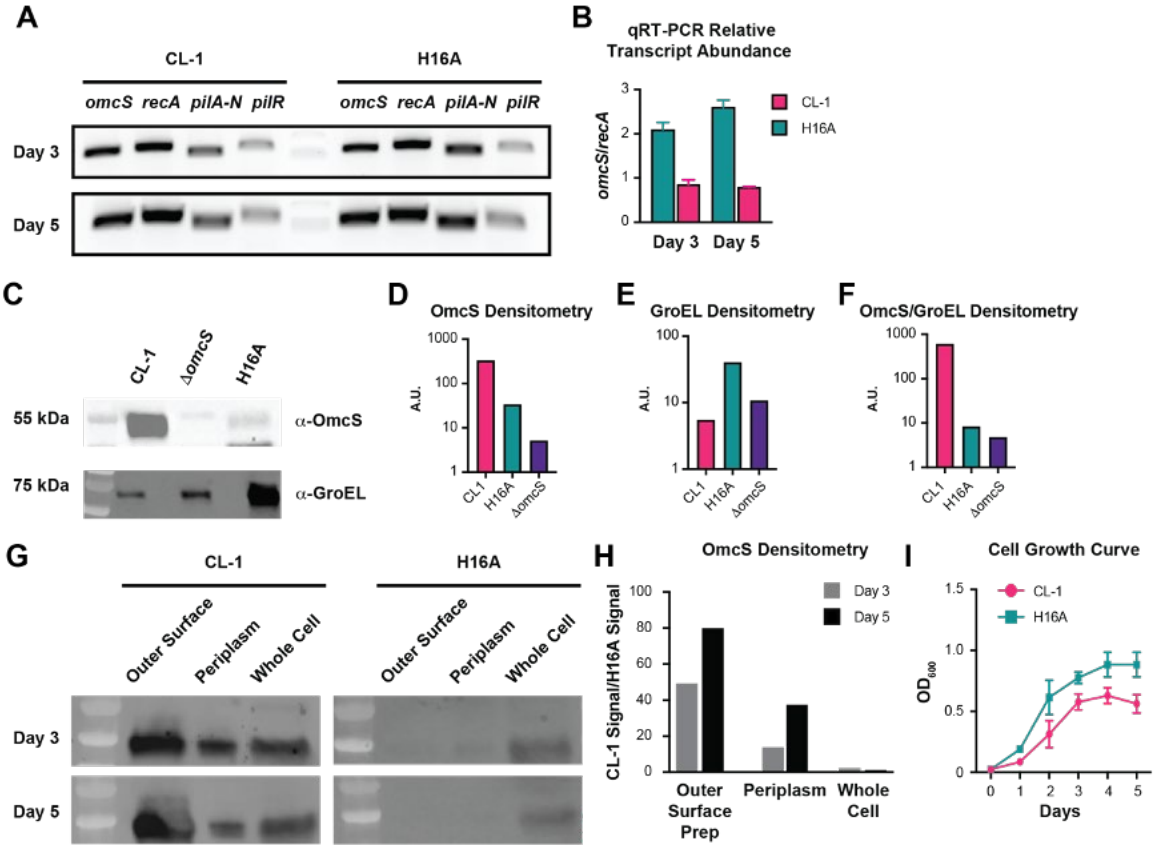

Figure 3.3. Assessment of OmcS production in CL-1 and H16A strains cultured in NBAF liquid media.

A, Agarose gel visualization of RT-PCR products produced from *omcS*, *recA*, *pilA-N*, and *pilR* transcripts present in total RNA extracted from strain CL-1 or H16A cells after either 3 or 5 days of growth. **B**, Relative abundance of *omcS* transcripts normalized to *recA* transcript, as assayed by RT-qPCR. **C-F**, Immunoblots and subsequent densitometry analysis illustrating the abundance of OmcS and GroEL proteins in whole cell lysates of strain CL-1, Δ*omcS*, and H16A; lanes from each strain correspond to comparable culture volumes. **G-H**, Immunoblot and subsequent densitometry analysis visualizing OmcS abundance in outer surface preparations, periplasmic fractions, or whole cell lysates of strains CL-1 and H16A. **I**, Typical growth curve illustrating cell density observed when growing strains CL-1 and H16A in liquid media.

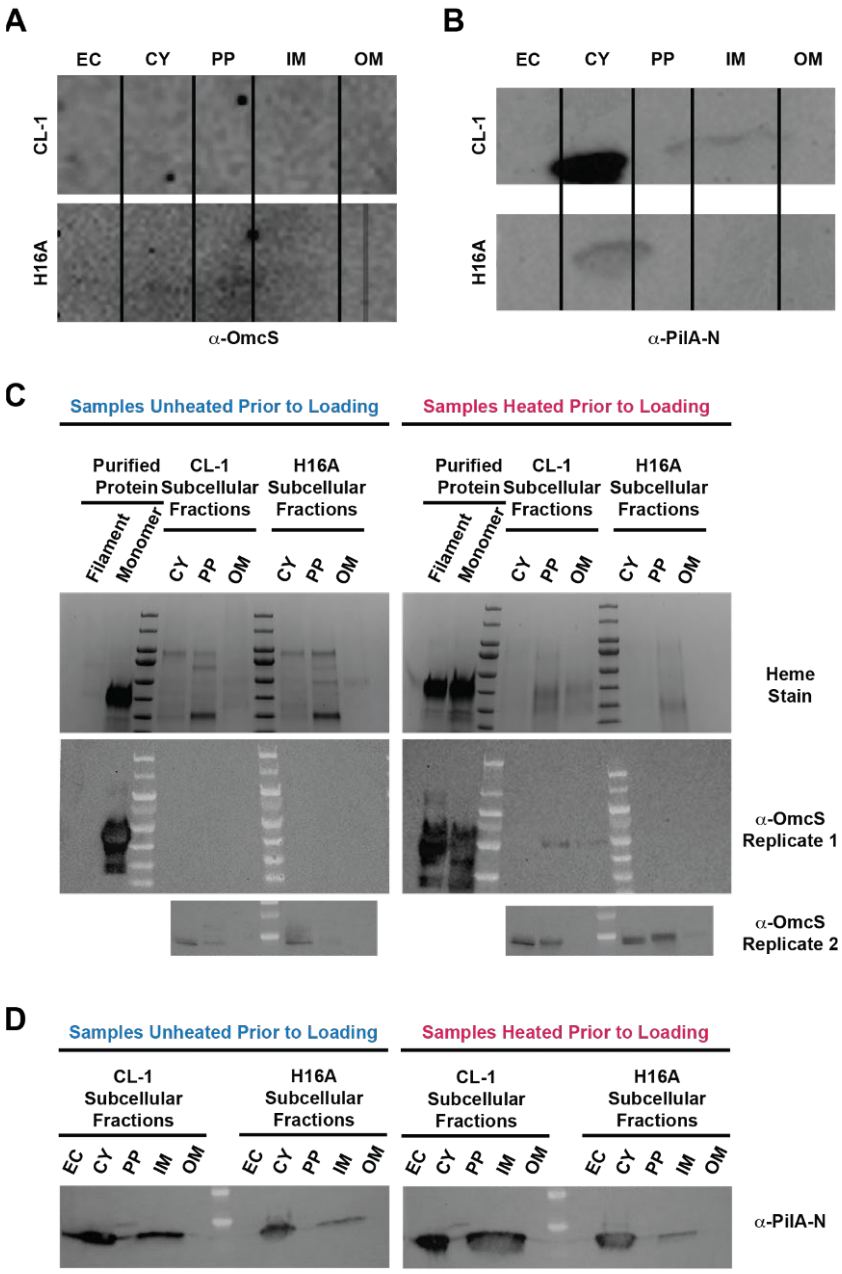

Figure 3.4. Assessment of OmcS and PilA-N protein abundance in subcellular fractions from strains CL-1 and H16A.

A, Anti-OmcS immunoblot of soluble component of the subcellular fractions presented in Figure 3.2B; lack of meaningful signal in any lanes indicates that OmcS present in these fractions is not well solubilized in these samples. **B**, Anti-PilA-N immunoblot of the same, soluble component of the subcellular fractions, indicated that soluble PilA-N was present in these samples, though notably not in outer membrane-associated or extracellular fractions. **C**, Heme staining visualization of c-type cytochromes and anti-OmcS immunoblot of the insoluble component of subcellular fractions from strains CL-1 and H16A, here compared when samples were or were not boiled prior to resolution in SDS-PAGE. Purified OmcS filament and monomer samples are provided for comparison and to illustrate the differential effect of heating or not heating the sample on monomeric and polymeric OmcS. Molecular wieght standard utilized includes markers at 180, 130, 100, 70, 55, 40, 35, 25, 15, and 10 kDa. **D**, Anti-PilA-N immunoblot of the same, insoluble component of the subcellular fractions.

from compartments (e.g., cytoplasm) where the protein would be very likely to be present in a monomer form. However, fractions which contained polymeric OmcS showed a clear difference between the "native" and "denatured" conditions with ~50 kDa OmcS being absent in the "native" condition and present in the "denatured" condition. This differentiation indicated that in the CL-1 strain, OmcS appears to already be in a polymeric state in the periplasmic and outer membrane associated-fractions. Together, our results indicate that the ability to polymerize is necessary for the proper localization of OmcS, and that monomeric OmcS is not present at or beyond the outer membrane, where OmcS is known to be involved in EET.

3.3.2 Nanowires disassemble into monomers at low pH

Having established the role of inter-protomer metal coordination in biological OmcS filament assembly, we sought to further understand the role of metal coordination in *in vitro* filament stability. We purified nanowires from *G. sulfurreducens* CL-1[48], which produces a high abundance of OmcS (Figure 3.5). Nanowires exhibit a sinusoidal morphology with a pitch of approximately 20 nm in negative-stain

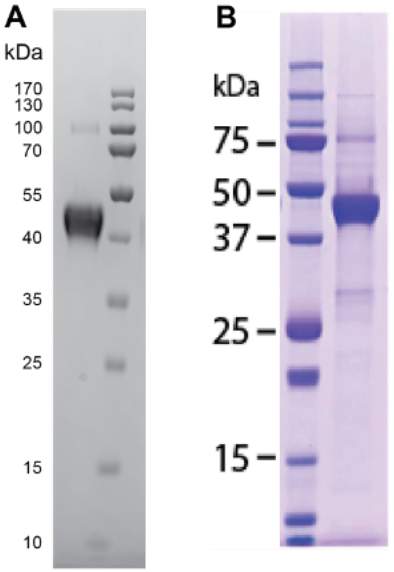

C

Protein Name	MW (kDa)	Coverage (%)	iBAQ (x10^8)
OmcS	45	53	79.7
HybL	62	71	15.8
GSU2493	32	82	15.6
GSU3547	24	83	9.2
OmpB	140	56	8.6
GSU3242	8	42	8.4

D Matched peptides in OmcS shown in **bold**.

1 MKKGMKVSLS VAAAALLMSA PAAFAFHSGG VAECEGCHTM HNSLGGAVMN
51 SATAQFTTGP MLLQGATQSS SCLNCHQHAG DTGPSSYHIS TAEADMPAGT
101 APLQMTPGGD FGWVKKTYTW NVR**GLNTSEG ER**KGHNIVAG DYNYVADTTL
151 TTAPGGTYPA NQLHCSSCHD PHGKYR**RFVD GSIATTGLPI KNSGSYQNSN**
201 **DPTAWGAVGA YRILGGTGYQ PKSLSGSYAF ANQVPAAVAP STYNRTEATT**
251 **QTR**VAYGQGM SEWCANCHTD IHNSAYPTNL R**HPAGNGAKF GATIAGLYNS**
301 **YKKSGDLTGT QASAYLSLAP FEEGTADYTV LKGHAKIDDT ALTGADATSN**
351 **VNCLSCHRAH ASGFDSMTRF NLAYEFTTIA DASGNSIYGT DPNTSSLQGR**
401 **SVNEMTAAYY GRTADKFAPY QRALCNK**CHA KD

Figure 3.5. Sodium dodecyl sulfate polyacrylamide gel electrophoresis and mass spectrometry analysis of OmcS samples used in this work.

A, Resolution on a 4-12% bis-tris non-reducing polyacrylamide gel of OmcS samples used for TEM, CD, and UV-visible spectroscopy characterizations, showing that the majority of the protein in the sample has a mobility suggesting a mass of approximately 45 kDa, consistent with the expected molecular weight of OmcS with six covalently bound heme moieties. **B**, SDS-PAGE analysis of OmcS samples used for EPR (and EXAFS) characterizations shows a similar profile, and the dominant band was extracted, subjected to tryptic digest, and analyzed by LC-MS/MS shown in the following **C**, iBAQ scores for identified proteins and **D**, matched peptides in the OmcS sequence.

TEM imaging that remains unchanged from pH 12 to 2.3 (Figure 3.6A-B), consistent with the cryo-EM structures (Figure 3.1B)[53, 54]. Several protein-denaturing agents or specific reagents expected to disrupt histidine-metal interactions[143, 144] have no apparent effect on the filaments, demonstrating the high stability and robustness of OmcS nanowires (Figure 3.7A-E). However, nanowires disassemble into monomers at pH 1.8 (Figure 3.6C). Treatment with guanidine-HCl, extended heating with detergent, or disruption of metal coordination with imidazole[144, 145] also results in disruption of the OmcS filaments (Figure 3.7F-H). The pH 1.8-treated OmcS shows a monodisperse elution profile in gel filtration corresponding to a smaller molecular size than was observed for the intact filaments (Figure 3.6D), consistent with the TEM results.

We examined the secondary structure of filamentous and depolymerized OmcS via circular dichroism spectroscopy (Figure 3.6E, Figure 3.8A). CD can readily capture structural changes in proteins, as exemplified by our analogous measurements of horse heart cytochrome *c* and of PpcA, a tri-heme periplasmic cytochrome *c* from *G. sulfurreducens* (Figure 3.8B-C). Our measurements of horse heart cytochrome *c* are consistent with prior work[146]. Our far-UV CD spectra of OmcS nanowires show a mostly

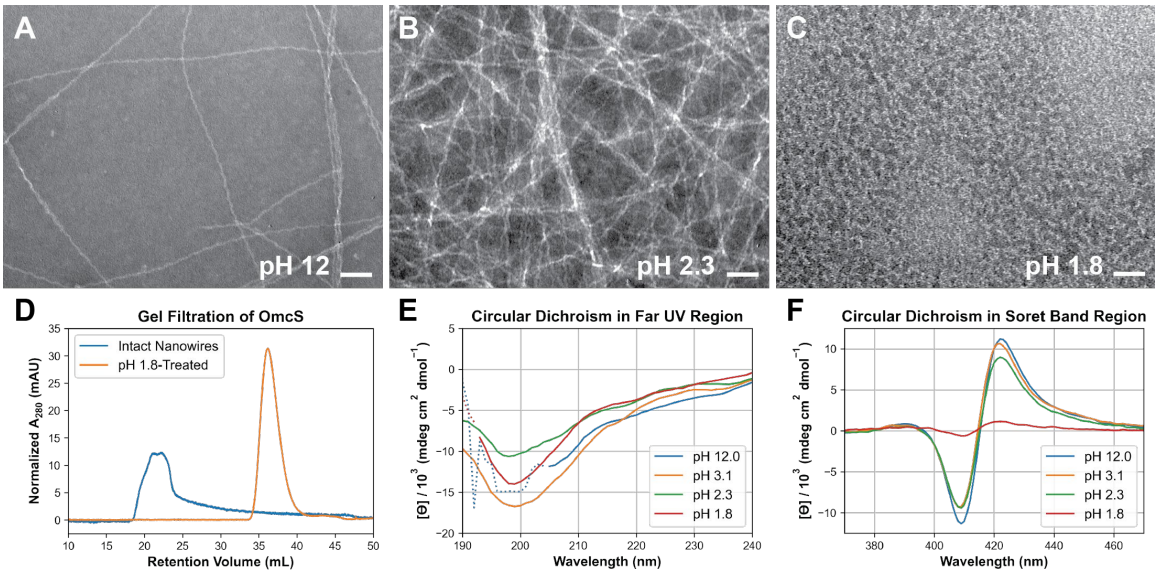

Figure 3.6. Disassembly of OmcS nanowires at low pH.

A, **B**, TEM images of purified OmcS filaments at pH 12 (**A**) and in a dense film at pH 2.3 (**B**). **C**, At pH 1.8, filaments disappear in TEM (**A**-**C**, scale bar, 50 nm) and **D**, gel filtration of pH 1.8-treated OmcS indicates a large decrease in particle size consistent with filament disassembly. **E**, **F**, CD spectra showing that secondary structure content (**E**) remains similar, but the heme environment (**F**) is altered upon low-pH OmcS filament disassembly (red).

coil structure[147], consistent with the cryo-EM structure[53, 54]. OmcS depolymerized at pH 1.8 shows secondary structure content similar to the filamentous state. These studies provide no indication that the depolymerization induced substantial structural change in OmcS.

The CD spectra in the Soret band region reflect the heme environment[148, 149]. Intact OmcS nanowires show a bisignate Cotton effect centered at 415 nm which is suppressed in OmcS depolymerized into monomers (Figure 3.6F, Figure 3.8D). PpcA also shows similar behavior, but horse heart cytochrome *c* does not, suggesting that the high-pH presence and low-pH suppression of strong CD features in this region could be unique to multiheme cytochromes with hemes in close proximity to one another (Figure 3.8D-F). Such Cotton effects are attributable to excitonic coupling of the hemes and are sensitive to the heme environment[150-152]. Therefore, the lack of a Cotton effect in OmcS monomers suggests a large change in the heme environment upon depolymerization.

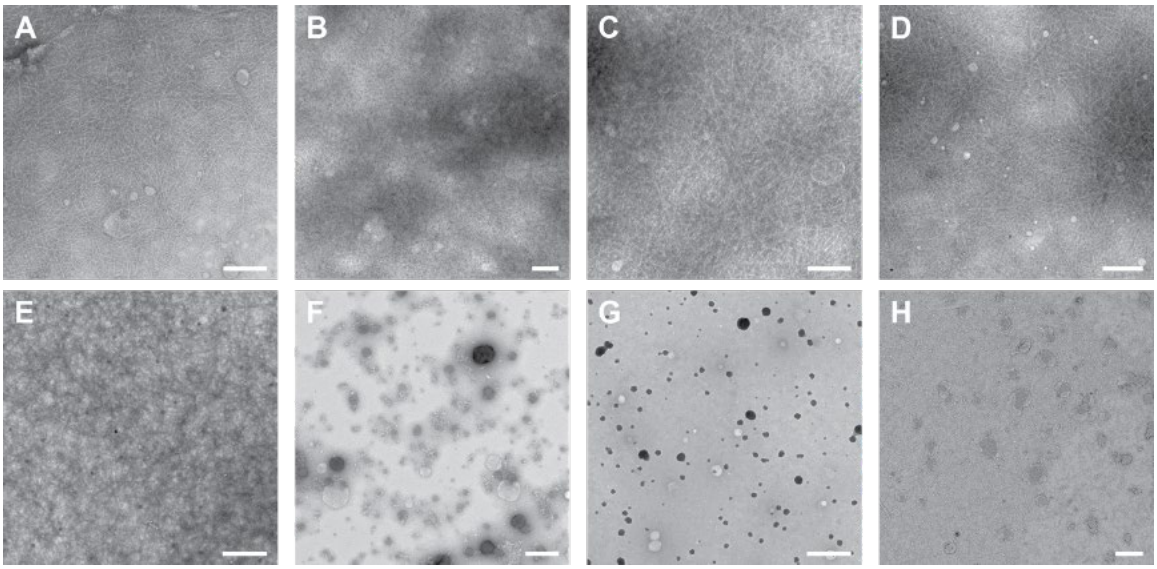

Figure 3.7. OmcS filaments remain intact under many conditions but can be disrupted by several specific chemical treatments.

A, Crude-extracted OmcS filament samples in pH 10.5 ethanolamine solution (scale bar, 400 nm) retain their appearance when equilibrated against a similar solution with the addition of 200 mM sodium azide (**B**, scale bar, 200 nm) or 5 mM sodium cyanide (**C**, scale bar, 200 nm), which were considered reagents that specifically targeted metal coordination interactions in cytochromes c, or with the addition of 4 M urea (**D**, scale bar, 600 nm), which was considered a generic protein denaturant. Filaments are also unaffected by the addition of 100 mM histidine (**E**, scale bar, 1 µM), but addition of 4 M imidazole, which was expected to disrupt metal coordination interactions via a similar mechanism, leads to the disappearance of nearly all filaments in TEM (**F**, scale bar, 200 nm). OmcS filaments can also be mostly or completely disrupted by some generic protein-denaturing conditions, e.g., addition of 4 M Gdm-HCl (**G**, scale bar, 400 nm) or incubation for 2 hours at 80 °C in the presence of 0.01% Triton X-100 (**H**, scale bar, 200 nm).

3.3.3 UV-vis spectroscopy suggests loss of histidine coordination in OmcS monomers

OmcS filaments remain dispersed in solution at pH 10.5, but sediment into a hydrogel after centrifugation in a variety of low ionic strength solutions from pH 3-10 (Figure 3.11A-C). Intact OmcS nanowires show characteristic features of oxidized *c*-type cytochromes with low spin (LS) hemes, with a strong Soret absorption at ~410 nm and broad Q-bands at ~530 nm and ~565 nm[142] (Figure 3.9A-B, Figure 3.10A-C). In contrast, OmcS monomers exhibit a visible color change (Figure 3.11D). The Soret band blue shifts by ~20 nm to ~390 nm and decreases in maximum intensity, whereas intensity in the 350 nm region typically associated with the δ peak[135] increases. The Q-band absorptivity is also blue-shifted, by roughly 30 nm. Blue shifts in the Soret and Q-bands have been attributed to the appearance of high spin hemes in other cytochromes *c* due to loss of metal coordination[135, 142]. pH-depolymerized OmcS monomers also exhibit the appearance of a new absorption band around 635 nm (Figure 3.9C), likely the porphyrin → Fe(III) charge transfer (CT) band observed in high spin hemes[135, 153, 154]. PpcA also

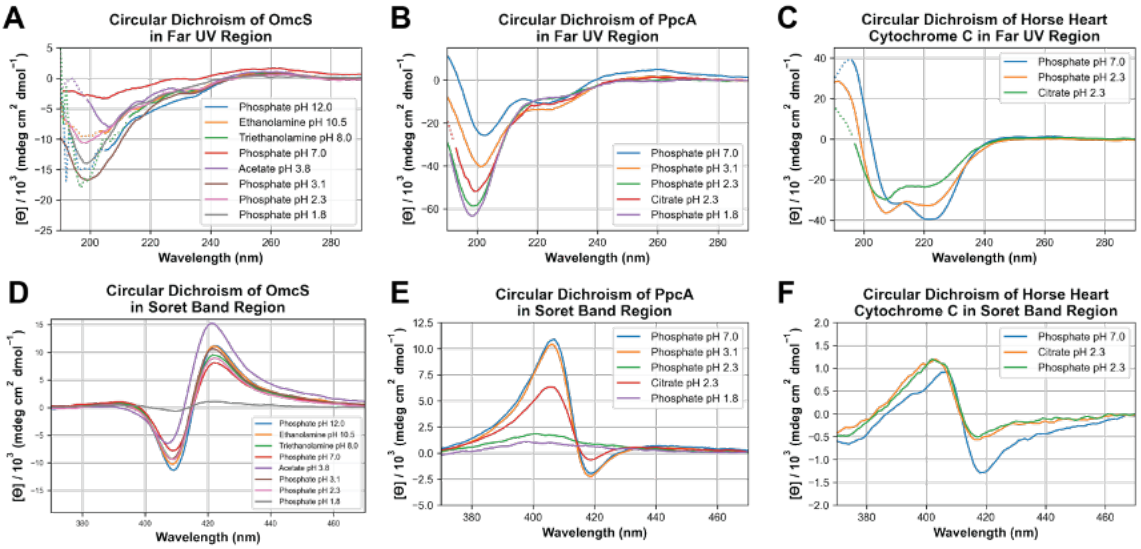

Figure 3.8. Circular dichroism spectroscopy indicates that OmcS secondary structure is relatively invariant across a wide pH range, while heme environment-related features appear unique to intact nanowires.

A, Molar ellipticity of OmcS in the far-UV region does not vary significantly across a broad pH range. Tri-heme cytochrome *c* PpcA (**B**) and mono-heme horse heart cytochrome *c* (**C**) show changes in far-UV CD as the pH was lowered. Molar ellipticity in the Soret band region shows that the OmcS absorptivity (**D**) was relatively invariant as a function of pH or buffer, except when the pH was lowered such that the filament was depolymerized. PpcA (**E**) and horse heart cytochrome *c* (**F**) have distinct features at circumneutral pH compared to filamentous or depolymerized OmcS. The intensity of the features for PpcA and horse heart cytochrome c show a more straightforward pH titration effect that is dissimilar to the binary behavior of OmcS. Phosphate, citrate, etc. as indicated in these and other plots refer to dilute solutions of the pure acid form titrated with HCl or NaOH, see methods.

shows a bimodal absorption feature near the Soret region when equilibrated at low pH, but horse heart cytochrome *c* shows only the expected blue shift[135]. This suggests that the combination of the blue shift with the change to the absorption feature shape at low pH is unique to multiheme cytochromes (Figure 3.10D-I) and could potentially arise from unique interactions between the protein, high spin hemes, and solvent at low pH.

We purposely denatured a low-pH OmcS sample by adding sodium dodecyl sulfate, an anionic detergent widely used to disrupt protein folding, to differentiate between depolymerization and denaturation. Notably, the UV-vis absorptivity of denatured OmcS is substantially different from that of OmcS monomers (Figure 3.9D). The bimodal peak shape in the Soret region collapses into a single peak with a similar maximum position near 390 nm. The lack of the bimodal absorption feature in SDS-denatured OmcS confirms that this unique spectral property arises from heme interactions involving the protein residues and structure, and thus further demonstrates that low pH alone does not cause denaturation of OmcS.

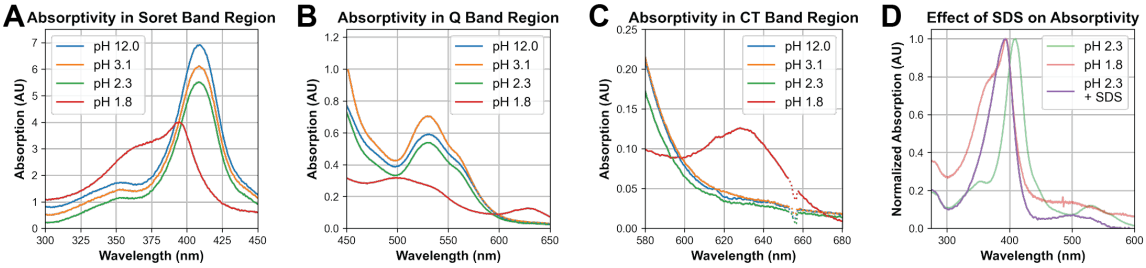

Figure 3.9. OmcS shows features suggestive of high spin hemes when depolymerized at low pH.

A, Low-pH depolymerization of OmcS results in a blue shift of the Soret absorbance, a decrease in peak intensity, substantial broadening due to peak overlap and an increase at 350 nm near the δ peak region (red). **B**, Q band absorption of pH-depolymerized OmcS is blue-shifted similarly to the Soret absorbance, and also decreased in maximum intensity (red). **C**, pH-depolymerized OmcS exhibits a charge transfer band in the region of 630 nm that is absent in the intact filament. **D**, Overall shape of UV-vis spectral features in the Soret and δ peak overlap region (ca. 350 nm) observed in pH-depolymerized OmcS (red) collapse to a single peak in SDS-treated sample at low pH (purple). (Results of SDS addition at pH 1.8 are similar to those for pH 2.3).

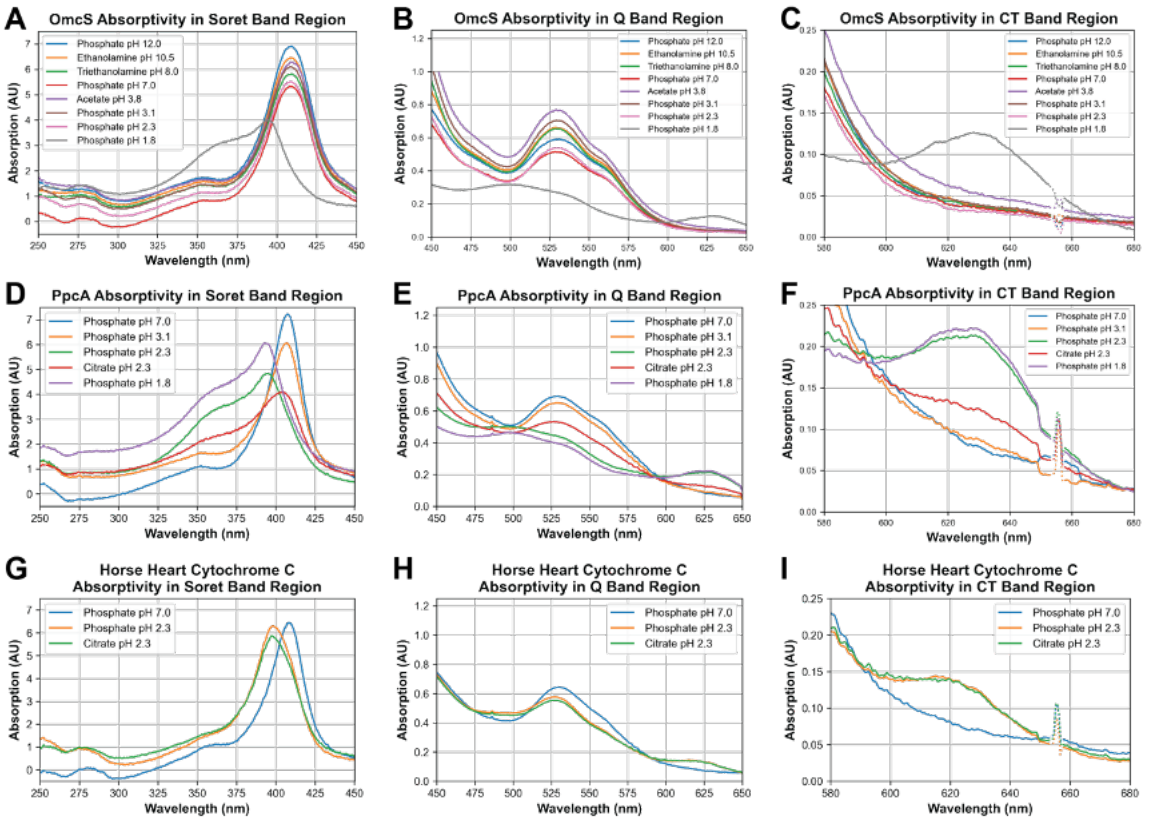

Figure 3.10. UV-visible spectroscopy shows changes associated with OmcS depolymerization that appear typical for multiheme cytochromes *c* equilibrated at low pH.

A, **B**, **C**, Absorptivity of OmcS in the region of the Soret (**A**), Q (**B**), and CT (**C**) bands does not appear significantly affected by the phase separation or precipitation behavior. Blue shifts in the Soret and Q bands, and appearance of the CT band, are observed when the filament is depolymerized at low pH. **D**, **E**, **F**, Absorptivity of PpcA in the region of the Soret (**D**), Q (**E**), and CT (**F**) bands shows three distinct spectra, suggestive of only low spin hemes in phosphoric acid pH 7-3.1, a mixture of low- and high spin hemes in citric acid pH 2.3, and a further increase in the proportion of high spin hemes in phosphoric acid pH 2.3-1. The shape of the Soret band absorption at low pH is similar to that of depolymerized OmcS. **G**, **H**, **I**, Absorptivity of horse heart cytochrome c in the region of the Soret (**G**), Q (**H**), and CT (**I**) bands shows spectral shifts previously attributed to appearance of high spin heme at low pH, lacking the complex feature in the Soret region.

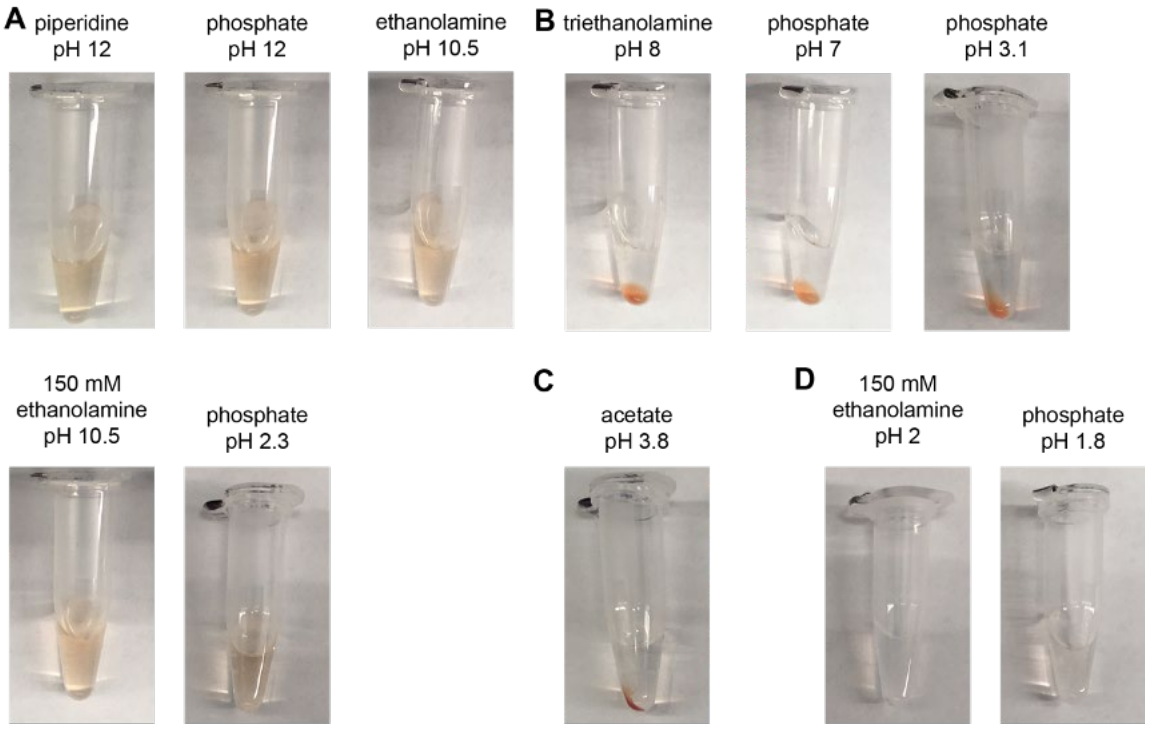

Figure 3.11. Characterization of OmcS filament phase separation, precipitation, and color change.

Ca. 10 μM OmcS filament samples were exhaustively dialyzed against the indicated solutions and subsequently diluted 1:4 in the indicated buffer, then centrifuged. **A**, Solutions with low ionic strength in the approximate pH ranges of 2-3 and 10-12 result in nanowires remaining dispersed after centrifugation. **B**, Solutions with low ionic strength in the approximate pH range 3-10 result in nanowires separating from the solution into a gel-like phase. Based on the cytochrome-characteristic color, this material likely contains a significant amount of water. **C**, Certain buffering agents, as well as high ionic strength solutions, result in a sedimentation of nanowires into a highly compact pellet. **D**, Low pH solutions that depolymerize the filaments result in a color change in the sample which appears as a decrease in color intensity at low OmcS concentrations and a change in color from red to brown at high OmcS concentrations. The pictured sample for the 150 mM ethanolamine pH 2 condition consists only of the material not precipitated after the dialysis step (see Figure 3.14). Buffering agent concentration and type are as described in methods below, except where indicated.

3.3.4 EPR spectroscopy reveals features unique to filamentous OmcS and a more homogeneous heme environment at the physiological pH

We have used low-temperature (< 10 K) X-band electron paramagnetic resonance spectroscopy to directly characterize the electronic configuration of Fe(III) ions at the centers of the heme cofactors[155-157]. The EPR analysis allows us to further probe specific changes in metal coordination implicated in filament disassembly. A previous EPR study of OmcS was performed using samples purified under extreme conditions using SDS detergent and boiling[49], which likely resulted in non-native, depolymerized OmcS. Here we performed EPR spectroscopy under conditions that maintained intact OmcS nanowires. As the cryo-EM structure of the OmcS nanowires[53] was solved at pH 10.5, we first analyzed the EPR spectrum at pH 10.5 to assign spectroscopic species to hemes of the intact nanowire structure. The EPR spectrum at pH 10.5 shows characteristic low spin (S = 1/2) ferric heme features

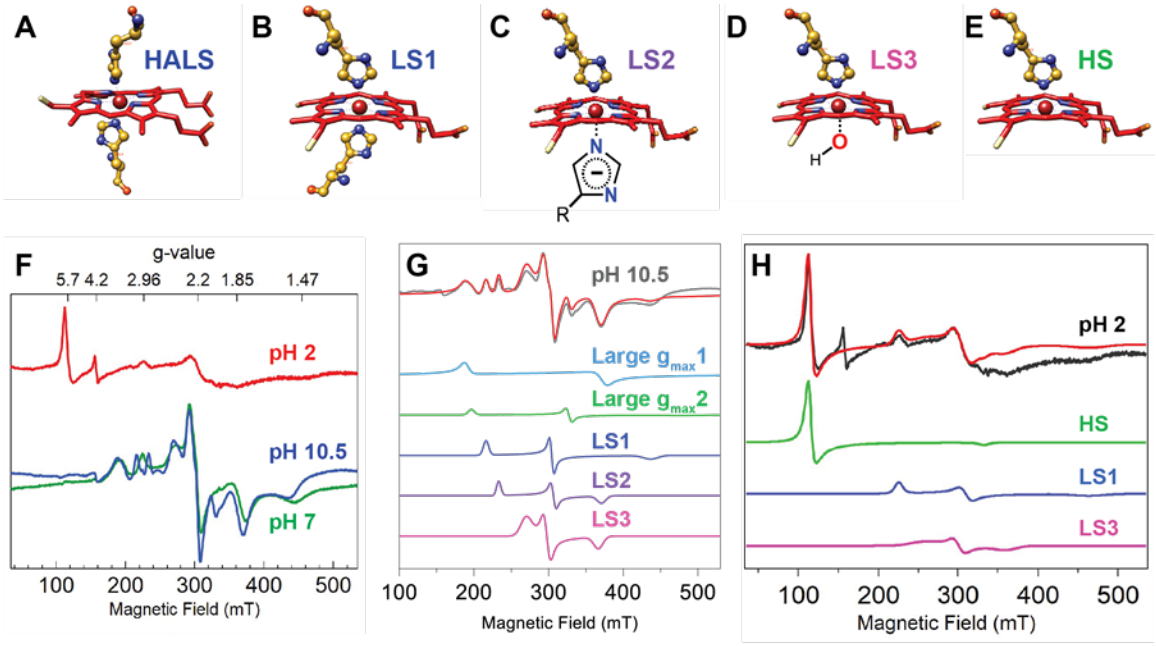

Figure 3.12. EPR spectroscopy reveals appearance of high spin heme subpopulation associated with depolymerization of OmcS.

Representative structures for simulated low spin hemes: **A**, Highly anisotropic low spin, with perpendicular dihedral angle between two imidazole ring planes of histidine, **B**, LS1, with parallel dihedral angle between two imidazole ring planes, **C**, LS2, with deprotonated, anionic form of one of the imidazole rings, and **D**, LS3, with hydroxide ligand. **E**, Representative structure for simulated high spin heme. **F**, Spectrum at pH 2 (red) and overlay of spectra at pH 7 (green) and pH 10.5 (blue) with g-values on the top x-axis. **G**, Deconvolution of spectrum at pH 10.5. Experimental spectrum (grey) is overlaid with sum of simulation of heme components (red) with two HALS hemes (light blue and green) and three LS hemes (blue, purple, and pink). **H**, Deconvolution of the pH 2 spectrum. Experimental spectrum (black) is overlaid with the sum of the simulation of heme components (red).

(Figure 3.12A-D,F-G), consistent with the cryo-EM structure. We deconvoluted the EPR spectrum at pH 10.5 (Figure 3.12F-G, Table 3.1 and Table 3.2) to distinct ferric heme features for bis-histidinyl coordination with either perpendicular (large g_{max}1 and 2) or parallel (LS1) alignment of imidazole-ring planes found for the axial histidine ligands[157]. Other ferric heme signals identified are indicative of an axial coordination by an anionic histidine or imidazolate[156, 158] (LS2) and of metal coordination involving a hydroxide ligand[153, 159] (LS3). Thus, the EPR spectrum of intact OmcS filaments is substantially different than the spectrum reported for detergent- and heat-treated OmcS[49], emphasizing the unique electronic structure of filamentous OmcS. We also measured EPR spectra of OmcS filaments in a pH 7 solution and found a more homogenous heme environment in this condition due to the disappearance of signals for hemes coordinated by imidazolate (Figure 3.12F and Figure 3.13).

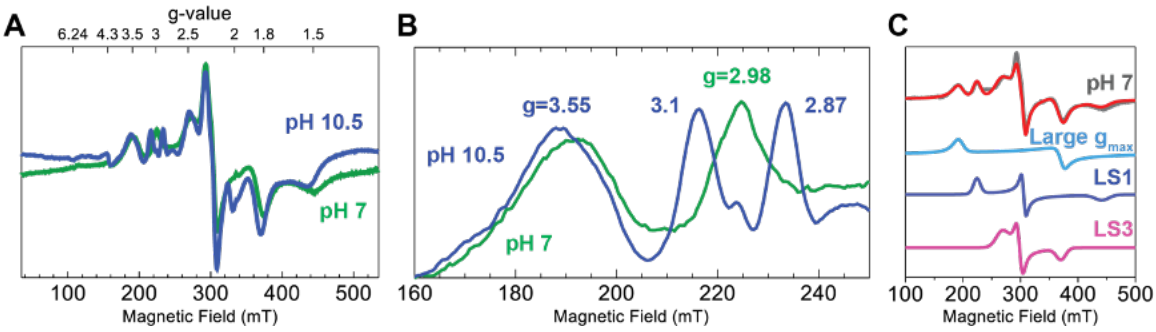

Figure 3.13. EPR spectroscopy reveals a more homogenous heme environment at pH 7 compared to pH 10.5.

A, **B**, Overlay of spectra at pH 7 and 10.5 in full (**A**) and zoomed near g=3 (**B**). **C**, Experimental pH 7 spectrum (grey) is overlaid with sum of simulation of heme components (red) shown separately below. As the pH is lowered from 10.5 to 7, heme species LS2 with imidazolate diminish in signal intensity and converge into LS1 hemes with g_z=2.98, decreasing the five heme environments observed at pH 10.5 to only three major species: a HALS species with only one g_{max} value of 3.40 and two low spin species, LS1 (g_z=2.98) and L3 (g_z=2.52). The g_z =2.98 peak for the more rhombic low spin species is highly asymmetric, indicating contributions from minor heme species. This reduced number of heme species is likely due to increased protonation and hydrogen-bonding at pH 7 that could cause heme 3 and 6 at pH 7 to have similar dihedral angles, making both HALS species nearly identical, giving one large g_{max} signal. The absence of LS2 heme signal at pH 7 is consistent with instability of the anionic form of histidine at lower pH.

Table 3.1. Principal g-tensor values of heme species contained in OmcS nanowires determined by simulations of the X-band EPR data at different pH conditions.

	g_z	g_y	g_x
pH 10.5			
Large $g_{max}1$	3.5199	1.7896	0.5331
Large $g_{max}2$	3.4072	2.044	0.7041
LS1	3.0995	2.2019	1.5322
LS2	2.8734	2.1858	1.8054
LS3	2.487	2.2514	1.8268
pH 7			
Large g_{max}	3.42953	1.79154	0.762921
LS1	2.98924	2.19152	1.51517
LS2	2.51809	2.24881	1.81346
pH 2			
HS	2.0114	5.8698	5.8427
LS1	2.9676	2.1571	1.4372
LS2	2.6169	2.2299	1.8596

Table 3.2. Ligand field parameters of heme species in OmcS nanowires determined by simulations of the X-band EPR data.

	V/λ	Δ/λ	$\Sigma(a,b,c)^2$	V/Δ
pH 10.5				
Large $g_{max}1$	0.78	1.15	0.999	0.29
Large $g_{max}2$				
LS1	1.62	2.4	1	0.29
LS2	1.97	1.47	0.999	0.5
LS3	4.08	11.33	1	0.44

3.3.5 EPR and X-ray absorption spectroscopy confirm the loss of an axial histidine ligand in depolymerized OmcS

At pH 2, an axial EPR signal ($g_z \neq g_y = g_x$) is observed near $g = 6$ from a high spin (HS) ferric heme with S=5/2 (Figure 3.12E-F,H). This resonance signal indicates a tetragonal symmetry of the high spin heme due to the 4-fold symmetry of the porphyrin-ring around the magnetic z-axis[155, 159] and is indicative of loss of an axial histidine ligand. The sample used for TEM, CD, and UV-vis characterizations, when prepared in this pH 2 condition, exhibits noticeable precipitation (Figure 3.14A). The fraction of the sample which remains well-solubilized shows UV-vis spectral shifts similar to pH-depolymerized OmcS (Figure 3.14B-D). The observed insolubility may limit pH-induced depolymerization in this condition, yielding a mixture of filamentous and pH-depolymerized OmcS. X-ray absorption spectroscopy (XAS) is another powerful method to probe the role of ligand binding on heme conformation[160, 161]. We found the rising-edge energy positions of heme irons in OmcS at 7118.8 eV and 7120.6 eV for pH 10.5 and pH 2, respectively, at the 1st inflection point (Figure 3.15A-B). Thus, our work shows that the high spin heme irons in OmcS at pH 2 are shifted ~1.8 eV higher in energy compared to the low spin heme irons at pH 10.5 in a manner similar to hydroxy-myoglobin, which also shows a comparable edge-shift (~4 eV) due to spin-state change[162]. Extended X-ray Absorption Fine Structure (EXAFS) spectra for OmcS nanowires

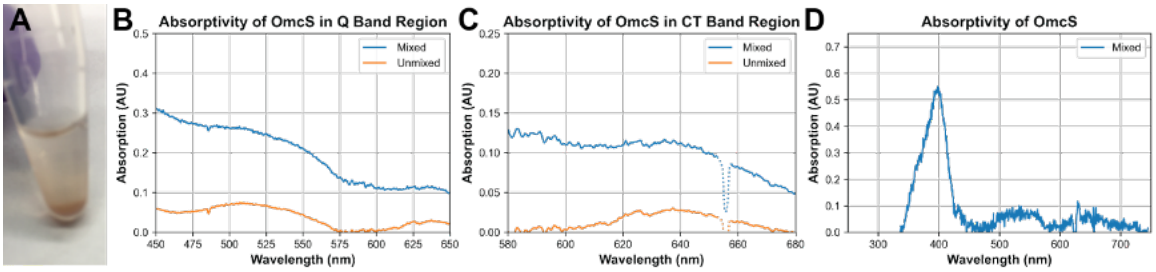

Figure 3.14. OmcS filaments in pH 2 ethanolamine exhibit UV-visible spectroscopic features suggestive of high spin along with readily visible precipitation.

A, Dialysis of approximately 10 μM OmcS filament sample against pH 2 150 mM ethanolamine solution results in precipitation of material without any centrifugation and light scattering visible as apparent turbidity of the mixture. **B**, **C**, Attempts to measure the UV-vis absorption spectrum of this sample were hindered by the aforementioned scattering, so measurements were made of the absorptivity of both the portion of the sample which remained in solution ("unmixed") and for the sample after suspension of the visible aggregates ("mixed") in the region of the Q (**B**) and CT bands (**C**). Both the mixed and unmixed sample show some evidence of the blue shift of the Q bands and appearance of the CT band which was observed in more homogenous samples of pH-depolymerized OmcS. (**D**) Overall UV-visible spectrum collected from the mixed sample suggests a blue shift in the Soret band from the ~410 nm low spin position, against a background of very high scattering. Data in this panel is presented without any baseline correction, see methods.

at pH 10.5 display a first peak which corresponds to an Fe-N distance[163, 164] of 1.88 Å (Figure 3.15C-D, Table 3.3).

The ligand coordination number, averaged over all heme iron ions determined from EXAFS is 3.4 ± 0.7 for OmcS nanowires at pH 10.5. Given that four porphyrin-ring nitrogens and two imidazole-rings axial nitrogens contribute to the EXAFS spectrum (Figure 3.15A inset), this result indicates that the axial Fe-N bonds are much weaker than those of the porphyrin-ring nitrogens and, consequently, have much larger bond length disorder compared to the equatorial ones, preventing their detection by EXAFS[163, 164]. In contrast, EXAFS at pH 2 shows 5.3 ± 1.0 ligands, indicating that, in addition to the 4 equatorial ligands from the porphyrin ring, a contribution from an axial ligand (from an imidazole ring) is also detectable. This finding of a strong contribution of one axial ligand partner for heme irons in OmcS at pH 2, in contrast to weak contributions of two axial ligands for heme irons at pH 10.5, explains the more intense 1st peak in EXAFS at pH 2 than at pH 10.5 (Figure 3.15C-D). These EXAFS results therefore

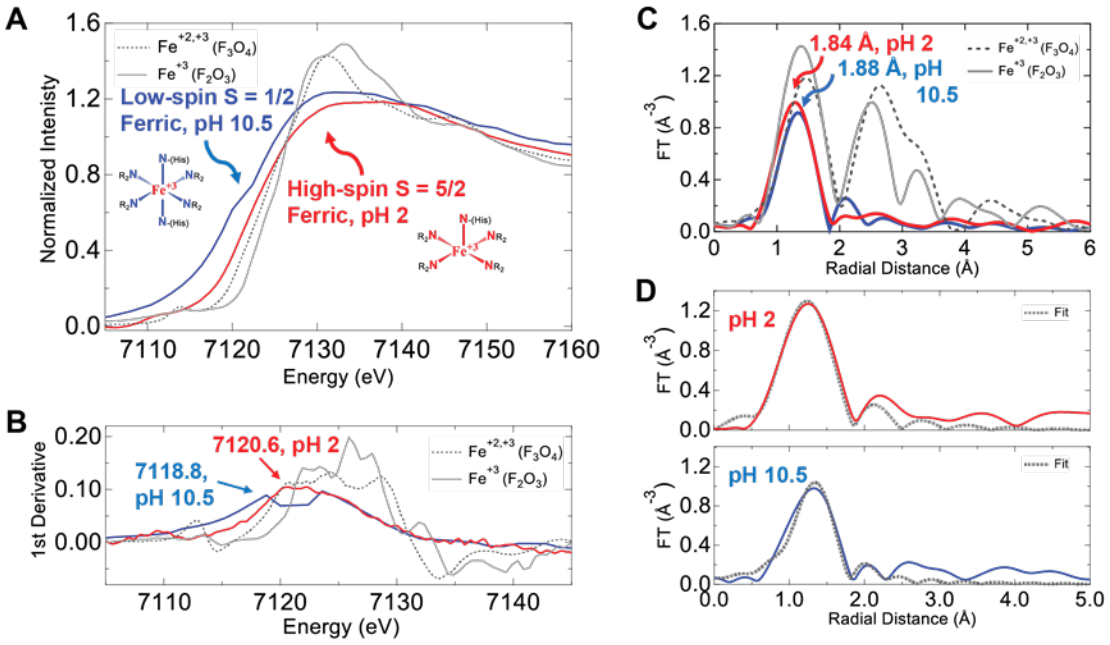

Figure 3.15. XAS confirms a loss of histidine coordination in depolymerized OmcS.

A, Fe K-edge XAS data for OmcS in pH 10.5 (blue) and pH 2 (red), ferric (Fe^{3+}) iron standard (grey), and mixed ferrous and ferric (Fe^{2+}, Fe^{3+}) iron standard (black dotted line). **B**, The Fe K-edge first-derivative spectra with first inflection-point energies. **C**, Magnitudes of Fourier transforms (FTs) of the k^2-weighted Fe K-edge EXAFS spectra for OmcS and iron standards (k-range: 1.5-8 $Å^{-1}$) show an increased intensity in pH 2 for a larger Fe-N coordination. **D**, FTs of the EXAFS data and fits for OmcS at pH 2 (red) and 10.5 (blue).

suggest that the loss of an axial histidine ligand at low pH leads to a stronger N-Fe bond from the remaining axial ligand. Thus, the EPR and EXAFS results confirm that the observed low-pH depolymerization of OmcS was associated with the loss of histidine ligands from the heme iron centers.

Table 3.3. Structural parameters (coordination numbers (CN), bond lengths, and their mean square deviations for Fe-N pairs) obtained from EXAFS analysis for OmcS nanowires at pH 10.5 and 2.

Sample	CN	R (Å)	σ^2 (Å^2)
pH 2	5.3 ± 1.0	1.84 ± 0.02	0.0042 (fixed)
pH 10.5	3.4 ± 0.7	1.88 ± 0.02	0.0042 ± 0.0030

3.3.6 Controllably reversible nanowire assembly

Low-pH disassembly of nanowires is reversible as evinced by the reappearance of the typical filament morphology in TEM at higher pH (Figure 3.16A). A fraction of such samples shows the same pH-dependent bulk behavior that we observed for filaments extracted from *Geobacter* (Figure 3.17A-B). We compared TEM images of these re-polymerized filaments to images of untreated filaments. Power spectrum analysis of the untreated and re-polymerized filaments' helical symmetry indicates no

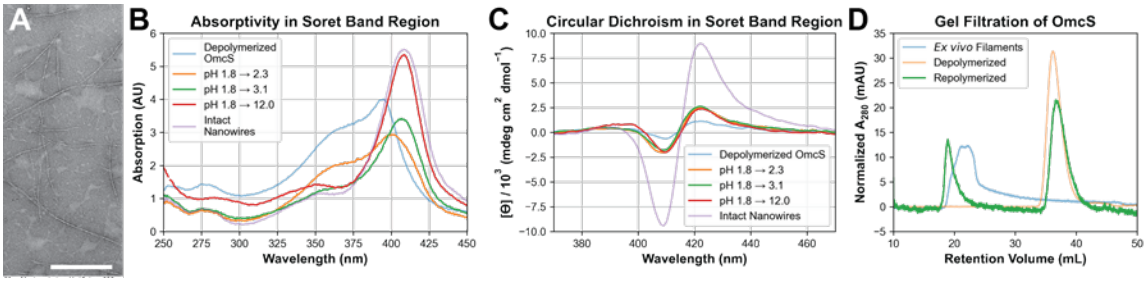

Figure 3.16. Repolymerized OmcS recovers filament-like characteristics in a pH-dependent manner.

A, TEM imaging of a pH-depolymerized sample after incubation at pH 12 shows reappearance of typical OmcS filament morphology (scale bar, 500 nm). **B**, UV-visible spectroscopy indicates that blue shifts associated with low-pH depolymerization of OmcS were reverted as the pH-depolymerized sample was incubated in solutions of increasing pH. Reference curves are provided for "intact" OmcS nanowires (pH 2.3 data from Figure 3.9A) and "depolymerized" OmcS (pH 1.8 data from Figure 3.9A). **C**, CD spectroscopy shows the filament-specific Cotton effect in the Soret region was partly recovered. **D**, pH 1.8-depolymerized OmcS was dialyzed to pH 2.3, incubated for an extended period to allow for OmcS repolymerization (green), and resolved by gel filtration. The chromatogram (at 280 nm) of this partially repolymerized sample is compared with that of intact OmcS filaments (blue) and pH-depolymerized samples (orange) at pH 2.3 (identical to Figure 3.6D).

substantial structural difference between the *in vitro* self-assembled OmcS nanowires and those assembled *in vivo*. (Figure 3.18). The UV-vis spectral shifts observed in pH-depolymerized OmcS are reverted in the pH range 2-3.5 (Figure 3.16B, Figure 3.19A-C). The reversibility of these changes further suggests that disrupting the OmcS nanowires by incubation at low pH did not denature the protein. SDS-PAGE indicates that the low-pH incubation described here did not chemically degrade OmcS (Figure 3.19D). The CD spectra of the 're-polymerized' OmcS shows partial recovery of the Cotton effect (Figure 3.16C).

We further assessed the degree of self-assembly in pH-depolymerized OmcS via gel filtration. Incubating a pH 1.8-treated sample at pH 2.3 for an extended period, rather than resolving it on the

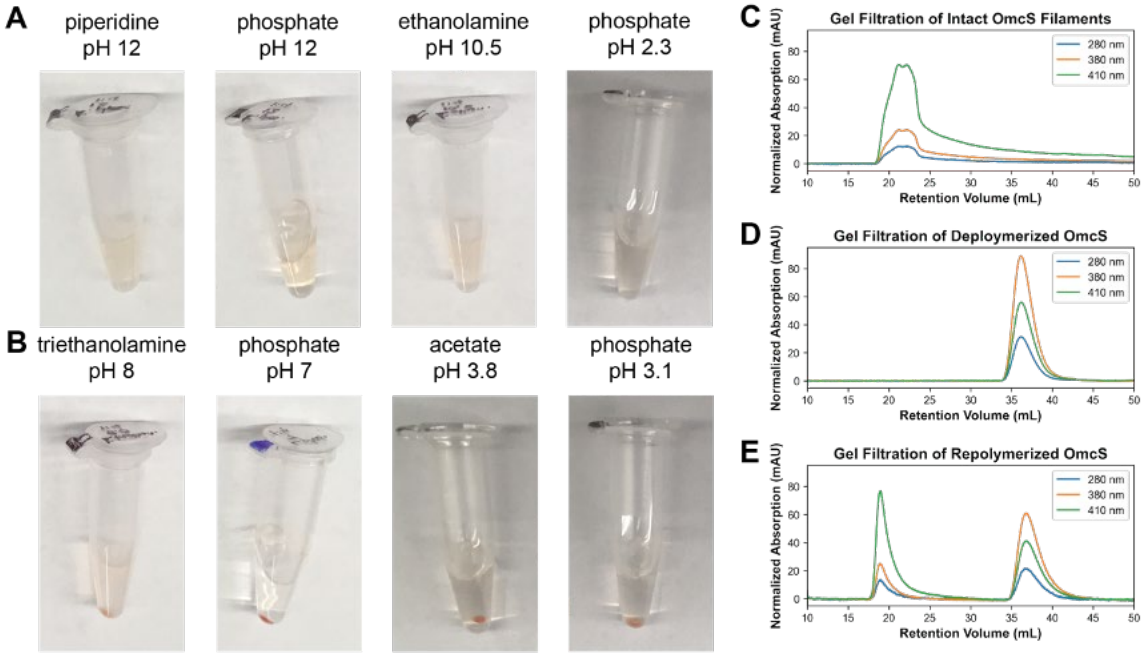

Figure 3.17. Characterization of OmcS phase separation in "repolymerized" samples shows partial recovery of filament-like properties.

OmcS filament samples purified from *G. sulfurreducens* (ca. 10 μM) were dialyzed against 50 mM phosphate pH 1.8 followed by the indicated solutions, then were diluted 1:4 in the indicated buffer and centrifuged. **A**, Solutions in which intact filaments were soluble show no pellets; the solution color appears similar to the starting material at high pH and is intermediate at pH 2.3. **B**, Solutions in which intact filaments formed gels or precipitated exhibit sedimentation of some part of the repolymerized sample. Except at pH 7, the predicted pI of OmcS, the solution in these "repolymerized" samples also retains some color after centrifugation, consistent with the notion that some OmcS monomers with different solubility properties than the nanowires are present under these conditions. Buffering agent concentration and type are as described in methods. **C**, **D**, **E**, Chromatograms showing the sample absorption at 280, 380, and 410 nm vs. retention volume for the intact (**C**), depolymerized (**D**), and repolymerized (**E**) samples shown in Figure 3.16D. $A_{410}/A_{380} < 1$ indicates a blue shift in the Soret region vs. intact OmcS filaments, cf. Figure 3.9A.

column immediately, causes a substantial shift in the elution profile (Figure 3.16D) wherein roughly one-third to one-half of the OmcS protein elutes in the void volume of the column – indicating a large molecular weight species similar to *in vivo*-assembled OmcS filaments. Spectroscopic analysis of absorbances at different wavelengths during gel filtration further suggested that the high molecular-weight species contains only low spin hemes, indicating that the filament form of OmcS is always associated with low- spin heme species (Figure 3.17C-E). The low-molecular weight species also present in this mixture appears to still contain some hemes that remain in a high spin state at pH 2.3.

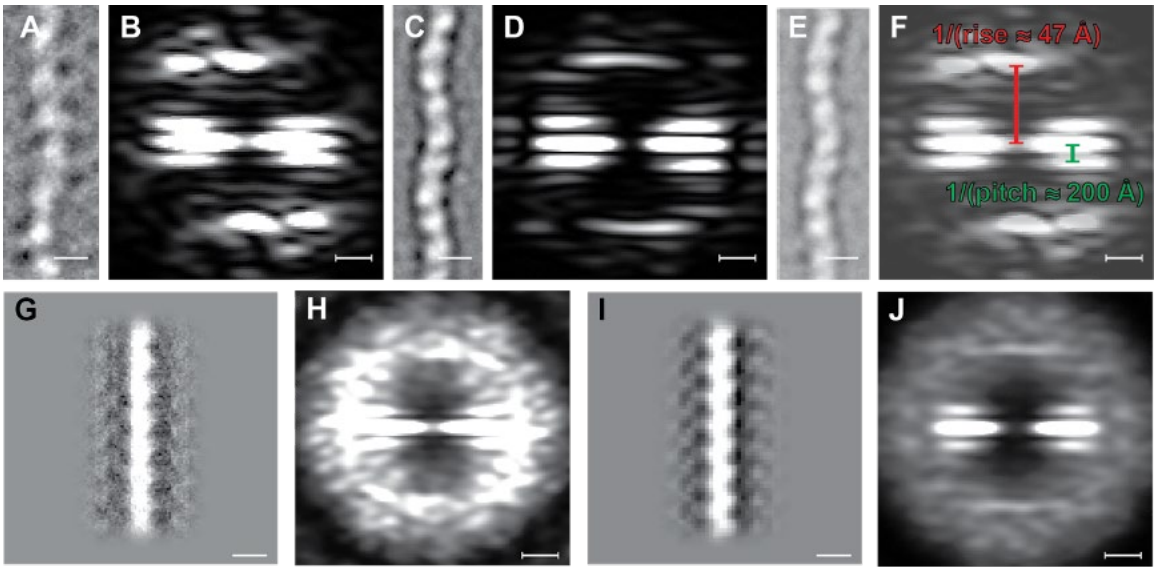

Figure 3.18. Power spectra of *in vivo*- and *in vitro*-assembled OmcS filaments indicates that the helical assemblies are identical.

A, **B**, 2D average of untreated OmcS filaments isolated from *Geobacter* and imaged at pH 12 (**A**, scale bar, 5 nm) and the power spectrum derived from this average (**B**, scale bar, 0.01 $Å^{-1}$). **C**, **D**, 2D average of repolymerized OmcS filaments imaged at pH 12 (**c**, scale bar, 5 nm) and power spectrum (**D**, scale bar, 0.01 $Å^{-1}$) indicates that the helical parameters of the *in vitro* assembled filaments are identical. **E**, **F**, overlay of 2D averages (**E**, scale bar, 5 nm) and power spectra (**F**, scale bar, 0.01 $Å^{-1}$) with layer lines corresponding to the characteristic helical rise (red) and pitch (green) of OmcS filaments indicated. **G**, **H**, **I**, **J**, Display of 2D averages and power spectra of helical particles extracted from TEM images without prior alignment of the particles, to confirm that no alignment errors obscured helical features or led to erroneous power spectra. Panels are analogous to **A**, **B**, **C**, and **D**, respectively, with corresponding scale bars.

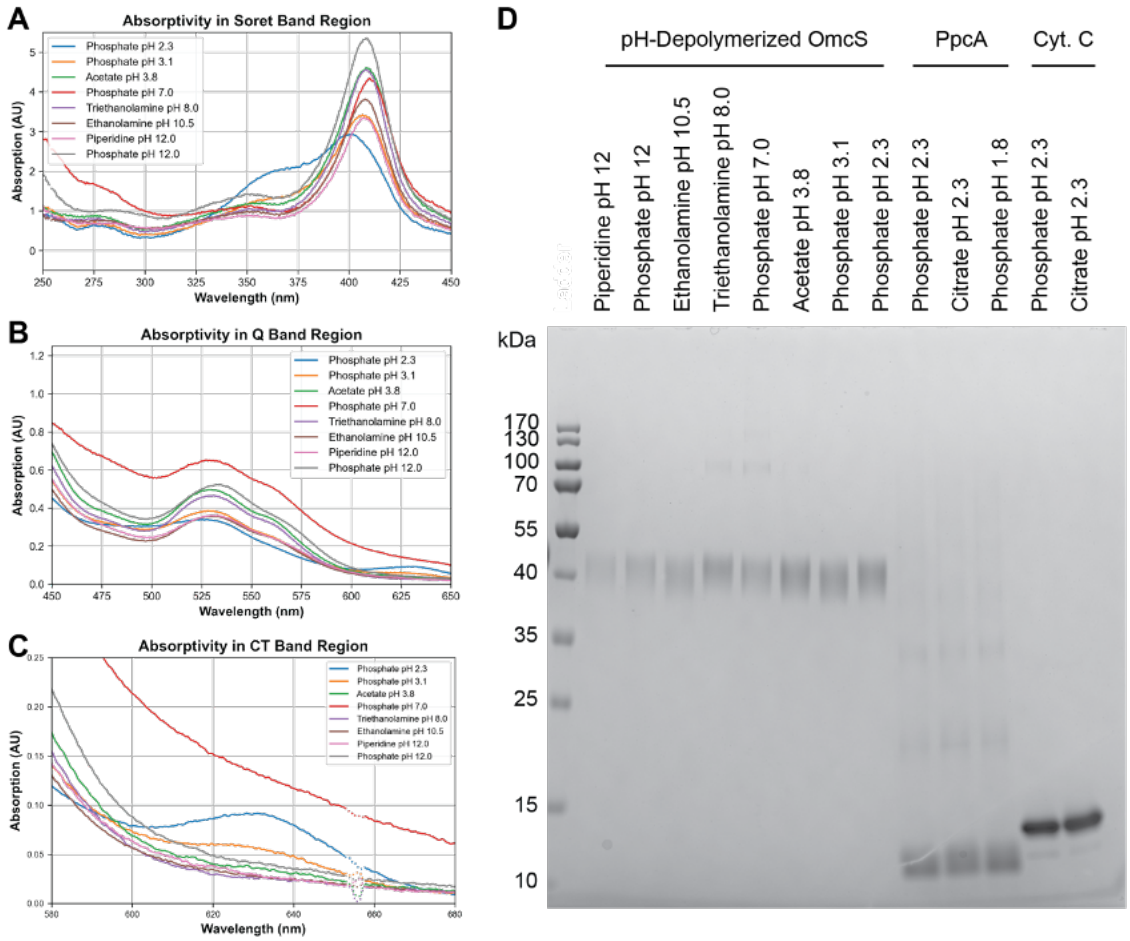

Figure 3.19. UV-visible spectroscopy indicates spectral changes associated with OmcS depolymerization are reverted when the sample is returned to higher pH in a range of solutions; SDS-PAGE indicates that none of the electronic absorption changes described in this study are a result of proteolytic degradation.

A, **B**, **C**, Absorptivity changes associated with pH-depolymerization of OmcS in the region of the Soret (**A**), Q (**B**), and CT (**C**) bands partially disappear in the pH range 2.3 – 3.8 and appear completely reverted at higher pH. Remaining differences in spectra do not appear to be substantial, but rather could be attributable to variation in concentration from handling errors or spectrum baseline issues due to increased scattering under certain conditions. Buffering agent concentration and type are as described in methods. **D**, Resolution on a 4-12% bis-tris non-reducing polyacrylamide gel of horse heart cytochrome c, PpcA, and pH-depolymerized OmcS samples stored in the indicated solutions for several weeks indicate that all proteins retained their expected mobilities. There is therefore no evidence that any spectral changes observed at low pH are due to acid hydrolysis or other degradation of the protein samples.

3.3.7 Computational studies suggest that His16 serves as a "latch" to direct protein subunit orientation during nanowire assembly

We have also evaluated the contribution of non-bonded protein-protein interactions to the reversible polymerization process by analyzing the binding energy of the OmcS inter-protomer interface at neutral and acidic pH. Our computational analysis provides fundamental understanding of the essential role of metal coordination for filament self-assembly. Notably, irrespective of whether His16 crosslinking is included in the computation, the surface binding energy between monomers becomes less favorable by ~67 kcal/mol upon protonation (Figure 3.20, Table 3.4). This change in the binding energy is primarily due to van der Waals and polar solvation (i.e., electrostatic) forces and is comparable to the previously reported imidazole(N)-Fe coordination bond strength of ~20-32 kcal/mol[165]. The overall stabilization due to non-bonding interactions is significant (i.e., comparable to the strength of metal-coordination interactions), supporting a mechanism wherein His16 metal coordination serves as a "latch" to stabilize the polymerized conformation at the inter-protomer interface once the OmcS subunits come together via protein-protein interactions. Our computational studies show that pH-induced changes in the metal-coordination and protein-protein affinity at the

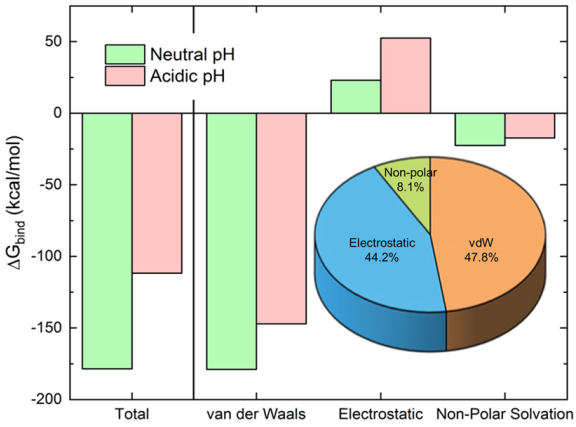

Figure 3.20. OmcS filament assembly is energetically more favorable at neutral pH than in acidic conditions.

Bar chart, binding free energy analyses of the nonbonded protein-protein interactions between the subunits of an OmcS dimer modelled at neutral and low pH (with the His16 crosslink detached in the latter condition). Total energy shown at left is the sum of components shown at right, indicating that inter-protomer association is less favorable in the low-pH condition. Inset, relative contribution of free energy components to the change in the total binding free energy upon protonation and His detachment; most of the change is driven by electrostatic and van der Waals interactions.

subunit interface are of similar magnitude and can work together to drive nanowire self-assembly *in vitro*.

Table 3.4. MM-GBSA binding energies and error analysis (in kcal/mol) describing energetic contributions of non-bonded interactions at the inter-protomer interface for different states of protein side chain residue protonation and of the His16 cross-link.

	Standard Protonation, His Attached			Fully Protonated, His Attached			Fully Protonated, His Detached		
	Avg.	St. Dev.	St. Error	Avg.	St. Dev.	St. Error	Avg.	St. Dev.	St. Error
ΔG_{bind}	-178.5	8.9	1.2	-116.1	27.4	3.9	-111.7	40.0	5.8
ΔVDW	-178.9	9.2	1.2	-136.4	24.0	3.4	-147.1	35.1	5.1
Δ(EEL + GB)	23.0	71.6	9.2	36.4	377.5	54.1	52.5	582.3	84.1
ΔSURF	-22.5	0.5	0.1	-16.1	2.6	0.4	-17.2	4.1	0.6

*Note: St. Dev. and St. Error are computed as the square-root of the sum of the squares of these quantities over multiple trajectory segments for both simulations with OmcS fully protonated. Similarly, the St. Dev. and St. Error for the Δ(EEL+GB) (i.e., polar solvation) term are computed as the square-root of the sum of the squared St. Dev. or St. Error for the EEL and GB terms.

3.4 Discussion

Since 2005, many studies of *G. sulfurreducens* microbial nanowire samples have asserted that the protein filaments being studied were exclusively type IV pili. The discoveries of OmcS and OmcZ nanowires[53, 54, 62] in filament preparations suggest an alternate interpretation of this prior work. Recent studies have suggested that previous studies measured cytochrome nanowires[53, 62, 63], that the role of T4P in *G. sulfurreducens* extracellular electron transfer is their involvement in the proper assembly and localization of cytochrome filaments, and that T4P filaments do not exist outside wild-type cells under nanowire-producing conditions that require EET[166]. It has been argued instead that *Geobacter* nanowire samples used in previous studies[54, 55, 167-170] do not contain cytochrome nanowires in any significant quantity[169]. However, in that study, cells were grown with soluble electron acceptors and not under conditions that require EET[169]. Our studies show that cytochrome nanowires are utilized by living cells during EET.

Related to the assertion that *G. sulfurreducens* uses T4P rather than cytochrome filaments for EET, the physiological role of OmcS filaments in *G. sulfurreducens* electron transfer has been questioned due to previous studies which proposed a model where monomeric OmcS 'decorated' extracellular T4P filaments[42, 47]. The primary evidence for this model was immunogold detection of OmcS, which was performed via TEM of whole cell samples, where gold particles were observed to be localized to extracellular protein filaments[47]. The authors of this work asserted that the spacing of gold particles observed in their micrographs directly established the spacing of OmcS monomers 'aligned' on T4P filaments, though no direct evidence was provided that the visualized filaments are in fact T4P. Fundamental to these analyses was an underlying assumption that the labeling efficiency of OmcS in their immunogold experiment was 100%, which to our knowledge is not supported by any evidence either in this literature or elsewhere, and represents a fundamental misunderstanding of this technique. A far simpler, alternate explanation is that these authors observed gold nanoparticles localized to extracellular protein filaments in their immunogold experiment designed to detect OmcS because the extracellular protein filaments visualized in their experiment were OmcS filaments. However, the model of OmcS monomers involved in EET that arose from this literature has persisted. Our direct characterization of subcellular fractions instead suggests that OmcS monomers are not present at or beyond the outer membrane, and therefore cannot play a role in EET. The finding that the H16A mutant cannot localize OmcS to the outer membrane further supports the notion that only the filament form of OmcS is directly relevant to the function of this outer membrane cytochrome.

We also highlight uncertainty about the protein identity of *Geobacter* protein nanowires in order to note that characterizations of pH manipulations in samples which may have or were known to contain OmcS filaments have been widely reported[33, 62, 167]. However, those earlier studies focused on the measured conductivity of nanowires, often utilizing approaches optimized for inorganic nanomaterials where intact OmcS filaments were deposited on electrode surfaces and pH-altering treatments were applied afterward. These approaches could have caused filament morphology to be retained, unlike our observations of OmcS equilibrated in solution at low pH. Compared to our observations, previous measurements of OmcS extracted by boiling in the presence of trace SDS[49] reported qualitatively similar

UV-vis spectra and protein secondary structure content. However, differences in the heme environment characterized by CD and EPR in that study, compared to our measurements, suggest that the previous study's preparation method yielded a non-native protein structure. Other systems, including cytochrome *c*-554[153] and hemoglobin[171], show metal coordination changes at low pH. However, the disassembly and self-assembly of OmcS filaments in solution due to reversible changes in histidine coordination and the energetic favorability of inter-protomer association represents a novel method to chemically tune the assembly of nanowires that is distinct from manipulating monomeric, non-conductive proteins. Previous experimental studies have shown that constraints provided by the protein structure on the metal-ligating methionine residue in cytochrome *c* contribute to the energetic stability of this coordination interaction; changes in this coordination interaction toggle the function of cytochrome *c* between one in respiration and one in apoptosis[172]. Our computational studies showing the commensurate energetics of the His16 interaction with the heme iron from the adjacent subunit and the protein-protein interactions at the subunit interface suggests that in the case of OmcS, the protein structure could be considered as providing entatic control to maintain the polymerized state once the filament is assembled.

In addition to helping explain how soil bacteria use protein nanowires to transport electrons for respiration and energy sharing with electron acceptors[32] and syntrophic partners[19] that are hundreds of micrometers away, our studies suggest microbial nanowires are a new class of metalloproteins that can reversibly self-assemble highly functional nanostructures in response to environmental conditions. These nanowires further represent a nanoscale laboratory for fine-tuning of catalytic and electron transfer rates by rationally engineering the cofactors and amino acid residues. Non-natural amino acid ligands serving as histidine analogs[173] have been shown to change the catalytic properties of metalloenzymes[173, 174]. Therefore, similar to monomeric metalloproteins[175], our studies provide the foundation for targeted substitution of ligands as a promising strategy to systematically fine-tune the reactivity, conductivity, and assembly of microbial nanowires based on our insight into the relationship between metal coordination and filament assembly. Such rational design could achieve different regimes of electron transport for a new field of metalloprotein-based self-replicating and highly resilient

electronic materials for a wide range of applications including artificial photosynthesis, catalysis, and bioelectronics.

Aggregation of heme proteins has long been established as a process that can negatively impact the biology of living cells. Among the most well-known examples is the aggregation of hemoglobin into filamentous structures, which leads to some forms of sickle cell disease in humans[176]. Cytochrome polymerization has also been suggested to impact the nucleic acid-binding properties of cytochromes in eukaryotic mechanisms of cytochrome-mediated apoptosis[177]. Our work shows that OmcS polymerization is required for proper function of this cytochrome in cellular respiration. This differs from prior studies of polymerization that was either synthetic, a cause of biological dysfunction, or an event associated with biological function of cytochromes in a process other than electron transfer. Our finding that metal coordination of heme irons is central to this functional polymerization of OmcS relates somewhat to studies that have shown structural protein-heme interactions can have implications for the function of cytochromes[178]. However, our work again distinguishes itself as the first direct exploration of the role of protein-heme metal coordination interactions in assembling a molecular wire capable of electron transport over micrometer-scale distances.

The aggregation behavior of assembled OmcS filaments may play a role in effective electron transport in nanowire networks *in vivo*. The pH-dependence of this aggregation behavior also suggests a role for electrostatic interactions. Such interactions can be exploited to generate multidimensional hierarchical protein nanostructures[179]. We anticipate that understanding of protein-protein interactions as well as protein-metal interactions will be needed in order to design useful higher-order structures based on cytochrome nanowires, similar to how our computational studies provide insight into the transition between OmcS monomers and polymers. The more homogenous heme environment found in OmcS nanowires at pH 7 also suggests that evolution has optimized the nanowire structure to function efficiently under these physiological conditions. Hemes in more similar electronic environments present a lower energy barrier for electron transfer. Therefore, more homogeneous heme environments will confer greater electron transport efficiency to the nanowire. Overall, our direct demonstration that cytochrome nanowires are involved in biological EET underscores the need for

further study of these nanowires' biophysical properties to aid understanding of the electron transport modes they enable.

In conclusion, our present studies advance understanding of cytochrome nanowires and their biological role in microbial EET. These developments could also help to create next-generation electronics technology using synthetic biology for broad applications – ranging from programmable living cells to implantable electronic devices – and enable the harnessing of latent metabolic diversity in microbial communities toward uses in bioremediation and renewable energy applications.

3.5 Methods

3.5.1 Bacterial strains and growth conditions

Geobacter sulfurreducens strain CL-1[48] and was used to obtain the OmcS nanowires. *G. sulfurreducens* cultures were maintained at 25 or 30 °C under strictly anaerobic conditions in sterilized and degassed NBAF growth medium[24], supplemented with 1 mm cysteine and with resazurin occasionally omitted as described previously[53]. NBAF media is composed of 0.38 g/liter KCl, 0.2 g/liter NH_4Cl, 0.42 g/liter KH_2PO_4, 0.22 g/liter K_2HPO_4, 0.36 g/liter NaCl, 0.04 g/liter $CaCl_2{\cdot}2H_2O$, 0.1 g/liter $MgSO_4{\cdot}7H_2O$, 1.8 g/liter $NaHCO_3$, 0.5 g/liter $Na_2CO_3{\cdot}H_2O$, and 1.0 mL/liter of 1 mM Na_2SeO_4. Media was supplemented with a) 10 mL/liter of a chelated mineral mix composed of 1.5 g of nitrilotriacetic acid (NTA), 0.1 g/liter $MnCl_2{\cdot}4H_2O$, 0.5 g/liter $FeSO_4{\cdot}7H_2O$, 0.17 g/liter $CoCl_2{\cdot}6H_2O$, 0.1 g/liter $ZnCl_2$, 0.03 g/liter $CuSO_4{\cdot}5H_2O$, 0.005 g/liter $AlK(SO_4)2{\cdot}12H_2O$, 0.005 g/liter H_3BO_3, 0.09 g/liter Na_2MoO_4, 0.05 g/liter $NiCl_2$, 0.02 g/liter $NaWO_4{\cdot}2H_2O$, and 0.10 g/liter Na_2SeO_4; and b) 15 mL/liter DL vitamin mix composed of 0.002 g/liter biotin, 0.005 g/liter pantothenic acid, 0.0001 g/liter cyanocobalamin, 0.005 g/liter p-aminobenzoic acid, 0.005 g/liter nicotinic acid, 0.005 g/liter thiamine, 0.005 g/liter riboflavin, 0.01 g/liter pyridoxine HCl, and 0.002 g/liter folic acid. Acetate was added as electron donor to a final concentration of 10 mM and fumaric acid was added as an electron acceptor to a final concentration of 40mM. For media containing Fe(III) (100 mM) as electron acceptor, a non-chelated mineral mix was used; an Fe(III) solution was prepared by neutralizing an $FeCl_3$ 0.4M solution with NaOH. Precipitated Fe(III) was washed and then resuspended in dH_2O for further use.

G. sulfurreducens PpcA was recombinantly expressed in BL21(DE3) *Escherichia coli* constitutively co-expressing *c*-type cytochrome maturation genes *ccmA-H*[180] and cultured at 30 °C in 2xYT medium as previously described[181]. S17-1 *Escherichia coli* cells were grown in LB media supplemented with 50 µg/ml kanamycin for selection at 37 °C.

3.5.2 mRNA extraction

For mRNA extraction, *Geobacter sulfurreducens strains* were grown to mid- and late-log phase as previously described[182]. Cells were treated with RNAprotect Bacteria Reagent (Qiagen) and then harvested at 4 °C with centrifugation at 5,000 x *g* for 10 minutes. Cells were resuspended in TE buffer containing lysozyme and proteinase K to obtain the genomic material. An on-column DNAse digestion was performed according to the manufacturers protocol (Qiagen, RNeasy Plus Mini Kit) to eliminate DNA traces, and then mRNA was eluted. Triplicates were made from this mRNA extraction for downstream analysis via reverse transcription-quantitative polymerase chain reaction (RT-qPCR).

3.5.3 RT-qPCR

To verify any expression defect in H16A, we compared gene expression of *omcS, recA, pilA-N, and pilR* using previously published primer sets[182]. A total of 1 µg of mRNA was used as template to synthesize cDNA following SuperScript First-Strand's (Invitrogen) protocol, using random hexamer as primers, and then treating with an RNAse to remove traces of mRNA. A 1:5 dilution from the mRNA product was made to be used as template to amplify *omcS, recA, pilA-N, and pilR amplicons using* GoTaq G2 Master Mix (Promega) for RT-PCR analysis; KAPA SYBR Fast qPCR Master Mix Kit (KAPA Biosystems) was used for RT-qPCR analysis. A 53 °C annealing temperature was used for RT-PCR and 60 °C for RT-qPCR. RT-qPCR analysis was performed in a CFX Opus 384 Real-Time PCR System (Bio-Rad) with the following settings: Enzyme Activation 95 °C for 30 seconds; Denaturing 95 °C for 3 seconds; Annealing 60 °C for 30 seconds for 40 cycles. Melt curve analysis was performed from 65-95 °C.

Primer pairs for RT-qPCR analysis[182]:

pilA-F: ATCGGTATTCTCGCTGCAAT

pilA-R: AATGCGGACTCAAGAGCAGT

pilR-F: TTTCCGGGAGGATCTCTTTT

pilR-R: TTATGATGCGGTCGCTGTAG

omcS-F: TGGTTGGCGAAGGCATAGG

omcS-R: CCATCAAGAACAGCGGTTCC

recA-F: CACCGGCATAATCTCCAAGT

recA-R: ATCTTGCGGATATCGAGACG

3.5.4 Protein purification, preparation, and biochemical characterization

For presented electron microscopy images and analyses, as well as gel filtration analysis, circular dichroism and UV-visible spectroscopies, and presented photographic images, OmcS nanowires were separated from stationary-phase *G. sulfurreducens* cells using a modified version of a previously described protocol[53]. Cells collected via centrifugation were resuspended in 150 mM ethanolamine (ETA), pH 10.5 solution and then blended for two minutes on the low setting using a commercial unit (Waring). Cells and cell debris were removed via centrifugation, the remaining solution was retained, and Triton X-100 was added to a final concentration of 0.05%. Detergent-insoluble contaminants were removed via ultracentrifugation and the remaining solution was dialyzed against 20 mM triethanolamine, pH 8.0. OmcS nanowires were collected via centrifugation and resuspended in 20 mM ethanolamine, pH 10.5. The presence, integrity, and expected morphology of nanowires in the initial OmcS sample thus obtained was verified via negative-stain TEM. Recombinantly expressed PpcA was purified from *E. coli* periplasmic fractions using cation exchange chromatography followed by gel filtration as previously described[181]. Horse heart cytochrome *c* was obtained commercially (MilliporeSigma).

For comparisons of the properties of OmcS, PpcA, and horse heart cytochrome *c* in different buffers, equal aliquots of one original sample of each protein were dialyzed exhaustively against the indicated solutions as a method to ensure the concentrations of the measured samples were approximately equal. All buffers used for these characterizations were prepared by dissolving the appropriate free or concentrated buffering agent, rather than a salt form thereof, in double-distilled water and adjusting the pH as needed with concentrated NaOH or HCl. Concentration of ethanolamine, triethanolamine, piperidine, and citric acid solutions used was 20 mM; concentration of phosphoric and acetic acid

solutions was 50 mM. After all other characterizations were completed, samples were treated at 95 °C in 2.5% SDS for 20 minutes and the protein concentration estimated via the standard bicinchoninic acid (BCA) assay, but the results showed buffer-dependent variation that did not correlate with the signal intensity in any spectroscopic characterization. Resultantly, the approximate concentration of each protein in characterizations which were performed in an equimolar manner (aside from handling errors and relative dilutions occurring during dialysis) was estimated based on the calculated concentration of the original sample for each protein species calculated from the averaged results from the BCA for each protein across all buffers used in the study. The starting OmcS sample, as well as selected OmcS, PpcA, and horse heart cytochrome *c* samples used in spectroscopic characterizations, were further analyzed via sodium dodecyl sulfate-polyacrylamide gel electrophoretic separation by mixing the samples with 4X LDS sample buffer (Thermo Fisher Scientific) with no added reducing agent, incubating the sample at 95 °C for 20 minutes, and then loading the samples on a 4-12% bis-tris polyacrylamide gel (Thermo Fisher Scientific). Samples were resolved alongside a PageRuler Prestained Protein Standard, 10 to 180 kDa (Thermo Fisher Scientific) for 37 minutes at 200 V and then visualized using Novex SimplyBlue staining reagent (Thermo Fisher Scientific) according to the manufacturer's instructions, followed by imaging using a ChemiDoc imaging system (Bio-Rad). Samples for immunoblotting were whole cell lysates prepared from cultures of strain CL-1 and H16A grown in NBAF media and sampled at the indicated time points, with each gel lane loaded with 20 µg of total protein. These samples were resolved on a 4-20% TGX (tris-glycine) gel and transferred using an iBlot2 Western Blot Transfer system (Thermo Fisher Scientific) utilized in accordance with the manufacturer's instructions. The polyclonal anti-OmcS primary antibody (LifeTein) was synthesized by immunizing two rabbits with a synthesized peptide sequence containing residues 323-339 of the mature OmcS protein (EGTADYTVLKGHAKIDD) and then affinity-purifying the serum against that peptide sequence. The primary antibody was used at a dilution of 1:2000 for immunoblotting. Visualization was achieved using an Immun-Star Goat Anti-Rabbit-Alkaline Phosphatase Detection Kit (Bio-Rad) and a ChemiDoc imaging system (Bio-Rad), following the manufacturer's instructions. Quantification was performed using ImageJ software.

For EPR and EXAFS studies, as described previously[53], OmcS nanowires were separated from bacteria by vortexing for 1 minute and extracted via centrifugation[34] and maintained in 150 mM ethanolamine buffer at pH 10.5 in a manner similar to structural studies on bacterial filaments[81], dialyzed into 50 mM tris-HCl, 150 mM NaCl buffer for pH 7 EPR studies and in and 150 mM ETA in pH 2 for pH 2 EPR studies. Cell-free filament preparations were imaged first with TEM and SDS-PAGE and liquid chromatography with tandem mass spectrometry (LC–MS/MS) analysis of filament preparations to ensure sample quality as described previously[53].

3.5.5 Transmission electron microscopy imaging

Carbon film-coated copper grids, mesh size 400 (Electron Microscopy Sciences), were cleaned by treatment in a PDC-001-HP plasma cleaner (Harrick Plasma) on the medium setting for 30 seconds. 5 µL of OmcS samples were deposited onto the carbon film face of the grid and incubated for 10 minutes to allow proteins in the sample to adhere to the surface, then the remaining solution was removed with blotting paper. Samples were subsequently negatively-stained using a 1% phosphotungstic acid (PTA), pH 6 solution by two rounds of floating the grid face-down on a 50 µL drop of the staining solution for 30 seconds and then blotting the remaining liquid away. Grids were air-dried and then stored covered prior to imaging using a JEM-1400Plus microscope operating at 80 kV (JEOL).

Power spectra analysis of OmcS filaments imaged by negative-stain TEM was performed using SPRING software[110]. Raw images of OmcS filaments with a pixel size of either 1.9 or 3.1 Å were processed into 384 Å-long segments used to generate the power spectra based on an estimated helical rise of 47 Å per subunit[53] and a conservative estimate of the helix width as 100 Å, either with or without prior alignment and classification of the segments as implemented in SPRING.

3.5.6 Gel filtration analysis

Aliquots of the original OmcS nanowire sample used for TEM, CD, and UV-vis characterizations were dialyzed to 50 mM phosphate at pH 1.8 or pH 2.3. The sample dialyzed to pH 2.3 is presented as such in Figure 3.6 and as the "*Ex vivo* Filaments" in Figure 3.16D. The sample dialyzed to pH 1.8 was dialyzed to 50 mM phosphate pH 2.3 and further separated into aliquots that were analyzed either immediately (presented as "pH 1.8-Treated" in Figure 3.6G and as "depolymerized" in Figure 3.16D) or after

continued incubation at pH 2.3 for approximately one week (presented as "repolymerized" in Figure 3.16D). Analysis was performed using a 60 cm column (approximate bed volume, 47 mL) packed with Sephacryl S-500 HR resin (Cytiva) and run at a linear flow rate of 15 cm/hour using an ÄKTA pure 25 system (Cytiva). Eluate absorptivity was monitored simultaneously at 280, 380, and 410 nm. Absorption data are presented based on a normalization scheme where the absorption of each sample at all monitored wavelengths is scaled by a linear multiplier specific to each sample, so that the integral of absorption at 280 nm for each sample across the entire elution volume is approximately equal for all samples. The 380- and 410-nm absorptions are scaled and presented based on this comparison of the 280 nm absorption in each sample, rather than on any direct comparison of the absorption at these other wavelengths across samples.

3.5.7 CD spectroscopy

Samples of OmcS, PpcA, and horse heart cytochrome *c* in the indicated buffers were measured using a 1 mm-pathlength quartz cuvette. Ellipticity from 185 to 480 nm was measured with three repeats using a Chirascan spectrometer (Applied Photophysics). Protein samples were measured at two concentrations to ensure that a useable spectrum was collected in all regions of interest for each condition; the concentrations used for each protein were estimated using the BCA assay and correspond to approximately 7 and 1.75 μM for OmcS, 16 and 3.2 μM for PpcA, and 20 and 3.3 μM for horse heart cytochrome *c*. Spectra were similarly collected for the relevant buffer solutions, and spectra for both buffer and protein samples were averaged across repeat measurements. Data were further smoothed using a Savitsky-Golay filter[183] implemented in Python[184], using a first-order polynomial and smoothing window of 3 for the protein measurements and a window of 5 for the buffer measurements (to compensate for the lower signal-to-noise ratio). The final CD data for each sample condition was calculated by subtracting the smoothed background data for the relevant buffer condition from the averaged sample data before applying the smoothing to the sample data. The following formula[147] was used to convert raw ellipticity values (mdeg; millidegrees) to molar ellipticity values ([θ]; deg cm^2 / dmol):

$$[\theta] = \frac{mdeg \cdot MW}{l \cdot C}$$

where *MW* is the mean residue weight, *l* is the pathlength in centimeters, and *C* is the concentration in mg/ml. CD spectra are presented as dashed lines where the raw absorption reported by the CD instrument for the corresponding ellipticity datapoint exceeds 1.5, a more conservative exclusion criteria than the value of 2.0 suggested in the instrument documentation.

3.5.8 UV-visible absorption spectroscopy

Except where noted below, experiments were performed in solution using 1-, 2-, or 10-mm path lengths in an Avaspec model 2048CL ultra-low stray light fiber optic spectrophotometer with a 50 µm slit width coupled to a Avalight-DHS halogen-deuterium combined light source (Avantes). Data from 185-745 nm was collected using an integration time of 150 µs and a smoothing pixel value of 1. Samples of OmcS, PpcA, and horse heart cytochrome *c* were measured at the same concentrations used for CD spectroscopy, again to ensure that regions of interest in the spectrum were captured accurately. Collected spectra for buffer solutions were subtracted from that of protein samples measured in the corresponding buffer. Buffer-subtracted spectra were further baseline-corrected by subtracting the average absorptivity from 735-740 nm in each spectrum from all values across the entire spectrum. Presented buffer-subtracted, baseline-corrected spectra are shown in terms of absorptivity (in arbitrary units) for the higher of the two concentrations measured for each sample and for a 10 mm path length – to facilitate comparison of spectra measured for the same protein across different buffer conditions, deliberate dilution factors, and measurement pathlengths. Spectra are shown as dashed both where the raw absorptivity value for the original collected spectrum exceeded 1 (to indicate saturated regions of the spectra) and in the region of 652.5-657.5 nm where a peak from the deuterium light source is observable in the presented spectra.

For Figure 3.9D, OmcS samples equilibrated in 20 mM citric acid pH 2.3, 50 mM phosphoric acid pH 1.8, and 20 mM citric acid pH 2.3 with 2.5% SDS were measured using 2-mm pathlength cuvettes in a NanoDrop 2000c spectrophotometer. Spectra were presented for comparison by dividing each sample spectrum by the maximum recorded value over the data collection range, to facilitate visualization of peak position. No baseline correction was applied to the UV-vis absorption data collected from OmcS

samples in 150 mM ethanolamine pH 2, in order to straightforwardly display the effect of scattering caused by aggregation in the sample.

3.5.9 EPR interpretation

In heme proteins, the iron can exist in a variety of oxidation and spin states that depend on the protein environment[157]. Oxidized heme cofactors with ferric (Fe^{3+}) iron typically manifest two spin states, either as low spin (S=1/2) or high spin (S=5/2), which are determined by the energy-level splitting between the three lower-energy d-orbitals and the two higher-energy d-orbitals[155]. EPR spectroscopy can accurately monitor the changes in geometrical symmetry around heme iron arising from the nature of the axial ligands, their orientations, and the electron configuration of the metal, ranging from a high-symmetry tetragonal form to a low-symmetry rhombic form[155].

We used the ligand-field correlation analysis, based on the formalism introduced by Griffith[185] and developed by Taylor[186], to find the rhombic (V/λ) and axial (Δ/λ) crystal field parameters. The corresponding V/Δ ratio was applied for determination of system rhombicity and analysis of hemes coordination[157]. A previously described model *G. sulfurreducens* multiheme cytochromes[157] for the heme molecular orbitals characterization and correlation of empirical g-value to the axial ligand geometry was used in this study. Data processing was performed using Igor Pro 7 (WaveMetrics). Simulations, deconvolution analysis, and least square fitting (Table S1) were performed using EasySpin software package (version 5.2.24). Further adjustment in assignments of *g*-tensor principal values were based on the complete EPR spectrum simulations. The best fits of the experimental spectrum are presented in Figure 3.12. For simulation, the g_y and g_x parameters of high g_{max} low spin signals were estimated based on the normalization requirement[185, 186] $g_z^2 + g_y^2 + g_x^2 = 16$.

The relative orientation (measured as dihedral angles) of the imidazole planes of histidine residues coordinating to heme determines the type of EPR signal[155, 157, 187]. HALS hemes are present in other *G. sulfurreducens* multi-heme cytochromes such as hemes I and IV in PpcA[157], and show *bis*-His coordination with perpendicular alignment of the imidazole-ring planes and a large g_{max} value (> 3.2) with increased *g* anisotropy[155, 157, 187]. We detected only the largest principal *g*-value and not the g_y and g_z values due to broadening by the *g*-strain. We found two subspecies of HALS hemes in OmcS nanowires

with different g_{max} values (3.55 and 3.4) and classified them as large g_{max}1 and 2 (Figure 3.12G). Low spin hemes with close to parallel orientation of the two axially-coordinating imidazole-ring planes (dihedral angle < 57-90°) produce a conventional rhombic EPR spectrum[157, 159, 188,] with a lower g_{max} value, small *g* anisotropy, and all three principal components of the *g*-tensor values. We further classified the observed LS heme signals as follows:

(1) LS1 hemes yielded *g*-values of $g_{(z,y,x)}$ = 3.09, 2.20, 1.53 which are similar to *c*-type hemes such as the low spin hemes found in a decaheme cytochrome MtrF[189], cytochrome *c*[190] and heme III in PpcA ($g_{(z,y,x)}$=2.96, 2.21, 1.47) with a parallel alignment of the axial histidine ligands[157].

(2) LS2 hemes showed *g*-values of $g_{(z,y,x)}$ = 2.87, 2.18, 1.80 at pH 10.5, similar to hemes with an anionic form of histidine ligand or imidazolate[156, 158]. A similar g_z value was observed in MtrF[189].

(3) LS3 hemes showed *g*-values of $g_{(z,y,x)}$ = 2.48, 2.25, 1.82 which are similar to hemes with a hydroxide ligand[153, 159]. Similar *g*-values were found for hemoglobin A (g_z=2.56)[159] and tetra-heme cytochrome *c*-554 above pH 10 when ~100% of the hemes showed the low spin species (g_z=2.67)[153].

These simulated fits accounted for all the major signals at pH 10.5 (Figure 3.12G), indicating that the exchange interaction observed in some parallel-stacked hemes[187, 191] is not present or detectable. This

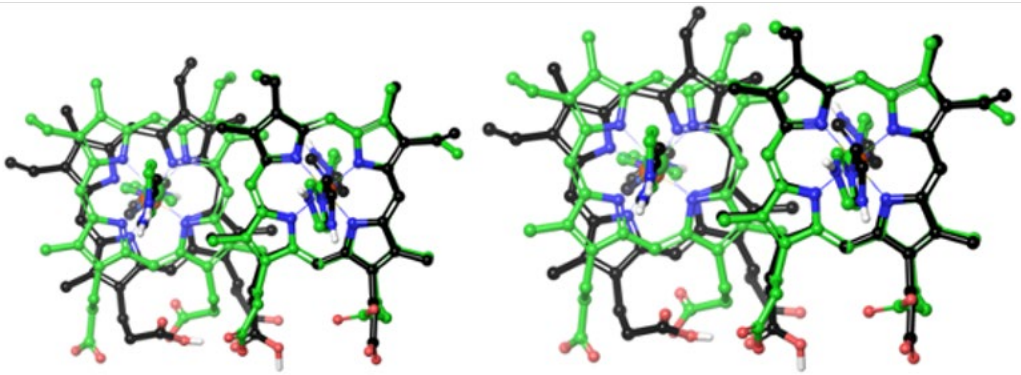

Method	OmcS Dimer	HAO Dimer	Exp. HAO [a]
BS-DFT	0.09 cm^{-1}	0.1 cm^{-1}	0.8 cm^{-1}

Supplementary Figure 3.1. Benchmarking computation of exchange interaction in OmcS nanowires and Hydroxylamine oxidoreductase HAO.

DFT calculation of hemes 4 & 5 of OmcS nanowire (left) and hemes 3 & 5 of HAO (right).

lack of exchange interaction was further supported by computational studies (Supplementary Figure 3.1, Supplementary Figure 3.2).

The low spin heme species LS1 and LS3 found at pH 10.5 were also present at pH 2 (Figure 3.12H). The LS3 signal observed at pH 10.5 is similar to the spectra of hemes with a hydroxide ligand[153, 159]. The hydroxide ligand was not observed in the cryo-EM structure of OmcS nanowires, indicating that its source in the pH 10.5 spectrum is likely the ends of the nanowire. LS3 hemes signals are absent in other monomeric multi-heme cytochromes such as MtrF[189]. Therefore, these hemes could be due to the filamentous nature of the OmcS structure, with solvent-exposed hemes at the ends of nanowires. However, the LS3 signals observed at pH 2 and 7 are unlikely to be from hydroxide-coordinated hemes because a hydroxide ligand should be protonated at low pH. Therefore, the LS3 signal could signify a feature specific to heme arrangement in the nanowire. The signal at $g \sim 4.2$ observed at pH 2 (Figure 3.12H) is a signal impurity arising from non-heme iron and was not included in fitting analysis.

3.5.10 Molecular dynamics simulations of heme ligation for coordination spectroscopy interpretation

To determine the range of dihedral angles between the imidazole planes of the histidine ligands, we performed molecular dynamics (MD) simulations of the OmcS nanowire structure to sample the orientation of the imidazole rings of the histidine residues coordinating the heme iron atoms. We

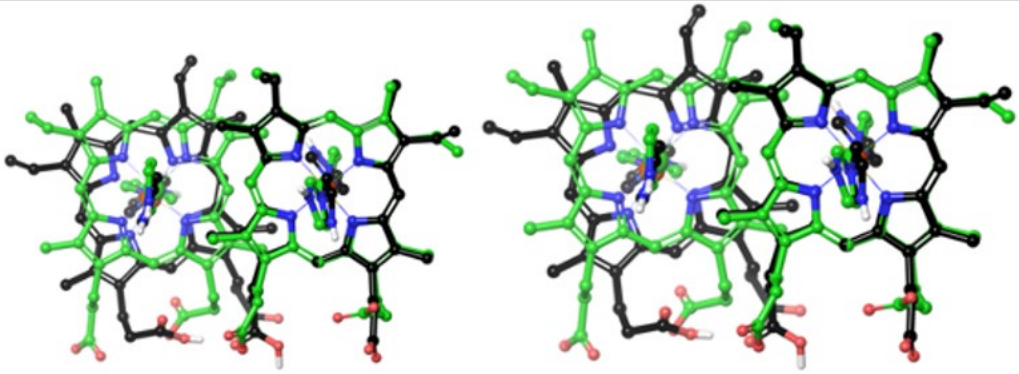

Method	OmcS Dimer	HAO Dimer	Exp. HAO [a]
BS-DFT	0.09 cm^{-1}	0.1 cm^{-1}	0.8 cm^{-1}

Supplementary Figure 3.2. Suppression of exchange interaction due to heme fluctuations. DFT calculation showing that 1 Å displacement of hemes completely diminishes exchange interaction or suppresses it by 60%.

obtained the starting coordinates from the protein data bank (accession PDB ID: 6EF8) and built a dimer model of OmcS, composed of two consecutive protomers from 6EF8. We modelled the hemes in their deprotonated state and all ionizable protein residues were protonated according to their standard pK_a values. The hemes were modelled in an oxidized state using previously computed partial charges[192] for the heme atoms and covalently bound histidine and cysteine residues.

The MD simulations were performed using NAMD[193] with the CHARMM36[194] force field parameters. The force field parameters for the hemes were obtained from Autenrieth et al.[195]. We minimized the system, followed by a 2.5 ns relaxation of the solvation water box. The model was equilibrated to 310 K in the NVT ensemble for 3.5 ns under harmonic restraints with a force constant of 0.1 kcal/mol to the amino acid sidechains and a force constant of 1.0 kcal/mol to the protein backbone and the hemes. A production run was then performed in an NPT ensemble for 20 ns with frames being written to the trajectory every 2.5 ps. The RMSD of the system was observed to converge within the first 10 ns of the simulation.

The orientation of the imidazole rings was extracted from a set of 1000 equally spaced snapshots (10 ps spacing) using a custom Tcl script. The angle between imidazole rings was determined by computing the angle between the two planes of the imidazole rings with defining basis vectors using the $N_\varepsilon - C_\delta$ and $N_\varepsilon - C_\varepsilon$ bonds following translation of the N_ε atoms to the origin. The angle between the planes is computed via computation of the angle formed by the normal vectors of the two planes.
We classified dihedral angles into three types as small, large and intermediate (Table S5): 1) hemes 1, 2 and 5 showed small dihedral angles (~20°), 2) hemes 3 and 6 showed large dihedral angles (~90°) and 3) heme 4 showed an intermediate dihedral angle (37.5° in the structure and ~70° in MD simulations), latter of which showed a disagreement between structure and MD simulations, due to limitations of the heme force field. Values from MD simulations used normal basis vector of ring planes because it was not possible to compute dihedral angles directly. The force field allows the imidazole ring to displace along the dihedral angle defined by the N_δ, C_ε, N_ε, and Fe atoms, and there is no parameter restricting this motion. Despite this limitation, MD simulations correctly computed dihedral angles for all hemes except heme 4 (Table S5). We assigned hemes 3 and 6 as highly anisotropic low spin (HALS) heme-iron centers

(Figure 3.12A). HALS hemes 3 and 6, present in higher pH's, were absent in the pH 2 spectrum. We classified hemes 1, 2, 4 and 5 into the above-described LS groups due to their low dihedral angles and significant differences found in peak position and linewidth.

Supplementary Table 3.1. Structural parameters of OmcS nanowires including angles between imidazole-ring planes of the histidine axial ligands for hemes obtained from cryo-EM and MD simulations.

			Dihedral angle between imidazole planes	
Hemes contained in OmcS	Axial ligands	Distance between ligand and Fe ion (Å)	Dihedral angle by cryo-EM structure[3]	Dihedral angle by MD simulation[4]
heme 1	His13[1], His147	2.04[1], 2.06	21.7°	21.77 ± 9.28°
heme 2	His51[1], His2	2.07[1],2.07	20.2°	24.24 ± 13.49°
heme 3	His144[1], His335	2.04[1], 2.04	68.6°	75.93 ± 12.93°
heme 4	His243[1], His110	2.04[1], 2.05	37.5°	69.0 ± 15.16°
heme 5	His332[1], His16[2]	2.04[1], 2.02	26.8°	17.55 ± 9.89°
heme 6	His404[1], His257	2.07[1], 2.07	78.8°	88.02 ± 9.15°

[1]Proximal histidine.
[2]Histidine from adjoining subunit.
[3]Values obtained from PDB: ID 6EF8.
[4]Values from MD simulation, using normal basis vector of ring planes. Parameters set to sample a range of configurations available at 310 K.

3.5.11 X-ray absorption spectroscopy interpretation

The XAS spectrum of a metalloproteins informs metal oxidation state, metal spin state, the number and type of ligands bound to the metal, and metal-ligand bond lengths. The maximum of the first derivative of the X-ray absorption coefficient at the K-edge energy of iron corresponds to the excitation energy of the core shell electron. The X-ray absorption edge is directly related to the oxidation state of the iron in the protein and can be used to probe the flow of electron density between the metal center and surrounding ligand. For higher oxidation states, the X-ray absorption edge shifts to higher energies

due to an increase in the core shell electron binding energy[160, 161]. The limited spatial resolution in EXAFS spectra does not allow us to discriminate between the contributions of the four porphyrin-ring nitrogens vs. the two axial nitrogens of imidazole-rings that are expected to have different bonding distances from iron[163, 164].

3.5.12 H16A mutant construction

omcS was cloned into pk18mobsacB using *omcS* F and *omcS* R primers (see below) to amplify *omcS* and 500 bp up- and downstream of the gene using BamHI and XbaI to digest. Ligation was performed with T4 DNA Ligase following NEB's protocol. Sequence-verified plasmid was used as a template to introduce a point mutation using NEB's Q5 Site-Directed Mutagenesis Kit following the manufacturer's protocol and using H16A F and H16A R primers. Sequence-verified plasmid was transformed into the donor strain S17-1 for subsequent transformation into *G. sulfurreducens* strain CL-1. Conjugation was performed as described by Chan et al.[25] on NBAF agar plates supplemented with 200 μg/ml Kanamycin for selection. Single colonies were isolated on kanamycin plates and flanking primers (*omcS* Flanking F and R) were used to confirm the plasmid integration. Colonies with a successful plasmid integration were then plated in NBAF plates with 10% sucrose to identify second recombinant cells. Resistant colonies were then plated on kanamycin plates to test sensitivity. Kanamycin-sensitive cells were sent for sequencing to confirm the point mutation.

omcS F (-500 bp)- 5'- acggttggatccttcggcaagcggggcagc

omcS R (+500 bp) – 5' gatgttctagcgcccttgcgctcgccgtgg

H16A F – 5' ccacacgatggcaaactcgctgggcggc

H16A R – 5' caccttcgcactcggca

omcS Flanking F (-50 bp)- 5'- ggagcgggatccggccgggttgccggagaa

omcS Flanking R (+50 bp) – 5'- cctttctagcgcggaccccggcggaatcac

3.5.13 Iron oxide measurements

Soluble iron was measure using a ferrozine assay as previously described[196]. 100 μL of culture were taken at different time points and solubilized in 0.5 N HCl in the dark. This sample was used for the ferrozine assay ([1 g/liter] in 50 mM HEPES [N-2-hydroxyethylpiperazine-N-2-ethanesulfonic acid] buffer)

to determine soluble iron in the media. Fe(II) standards were prepared from ferrous ethylenediammonium sulfate and measured at OD_{562}.

3.5.14 Molecular dynamics simulation of inter-protomer interactions

System setup and parameterization: Starting from the cryo-EM structure of an OmcS filament (PDB accession code 6EF8)[53], a dimer model was constructed from chains A and B. Each of these chains contain six *c*-type, bis-histidine-coordinated heme cofactors, which were modelled in the oxidized (+3 charge) state. A segment composed of the first 20 residues of chain D was also included in the model to provide the His16 coordination for Heme #5 (PDB designation HEC-501 in chain B) that is present in the full-length filament. Importantly, the dimer model captures the inter-protomer interface, which is of primary focus for understanding the (de-)polymerization process.

The dimer model has 38 Asp, 24 Glu, 13 His, 28 Lys, 26 Arg, 44 Tyr, and 2 Cys residues that are titratable. The counts for His and Cys exclude residues of these types that are (covalently or coordinatively) bonded to the heme groups. The titratable residues were assigned standard protonation states (e.g., deprotonated Asp and Glu; singly protonated His; protonated Lys, Arg, Cys, and Tyr) to simulate circumneutral pH conditions. In separate simulations designed to simulate very acidic (pH < 2) conditions, all titratable residues were assumed to be protonated, including doubly protonated in the case of His. The propionate groups on the 12 heme cofactors were assumed to be deprotonated or protonated, respectively, in the circumneutral and low pH simulations. We expect that these protonation state assignments provide an upper-bound estimate for the dramatic effect of pH on the stability of the polymerized protein.

Using tLEaP in the AmberTools20 package[197, 198] hydrogen atoms were added to the OmcS dimer assuming standard or full protonation of titratable residues. The dimer was placed at the center of a box of explicit water with at least a 15 Å buffer region to the boundary of the box. A sufficient number of counterions (18 Na^+ or 81 Cl^- at circumneutral and low pH, respectively) was added to achieve charge neutrality. Standard proteinogenic residues were modelled with the AMBER FF99SB force field[199]. Parameters for the heme cofactor were adopted from Crespo et al.[200] and Henriques et al.[201], and used as

in previous studies for single- and multi-heme systems[202, 203]. The TIP3P water model[204] and the monovalent ion parameters of Joung and Cheatham[205] were used to model the solution state.

As demonstrated in the main text, EPR experiments suggest that axial histidine coordination to some of the heme groups is lost under acidic conditions. Detachment of the axial His coordination donated to a heme group across the inter-domain interface in the filament is presumably a precondition for the observed depolymerization. However, the exact role of the crosslinking His in the (de)polymerization process has yet to be elucidated.

To explore how the His crosslink influences inter-protomer stability at low pH, we simulated the fully protonated dimer model with and without coordination of His16 in chain B to HEC-501 in chain A. Because our focus was on large-scale protein dynamics and inter-protomer interactions, we approximated the detachment of the inter-domain His coordination by deleting the bonded parameters for the C_α-C_β bond of the His residue. In the employed AMBER force field, the His sidechain coordinated to the heme is part of the heme residue definition (residue name HEH), whereas the backbone is given its own residue type (name HIO). Deletion of the C_α-C_β bonded parameters cleaved the covalent connection between the HIO and HEH groups, each of which belong to separate OmcS protomers in the filament. Because native residue definitions remained intact, integer charges were maintained, and a charge re-parameterization was not necessary. It was assumed that the non-bonded interactions neglected by not passivating the broken bond with hydrogen atoms had a minor impact on the conclusions regarding inter-protomer binding free energy at low *versus* circumneutral pH.

In summary, the dynamics and inter-protomer binding free energy were considered for three model systems: An OmcS dimer with (1) standard protonation and the inter-domain His coordination, (2) full protonation and the inter-domain His coordination, and (3) full protonation and lacking the inter-domain His coordination.

Pre-production simulations: Each solvated dimer model was subjected to 2000 steps of steepest descent, followed by 8000 steps of conjugate gradient minimization. A 10 kcal/(mol Å^2) restraint was applied to the heavy atoms of the protein backbone, as well as selected atoms (PDB names FE, NA, NB, NC, ND, C3D, C2A, C3B, C2C, CA, CB) of each heme group during the minimization. The system was

subsequently heated from 10 to 300 K at a rate of 0.29 K/ps in the NVT ensemble and held at the final temperature for 1 ns. The restraints on the protein backbone and heme groups were reduced to 1.0 kcal/(mol Å^2) for the heating stage. These restraints were further reduced to 0.1 kcal/(mol Å^2) for a subsequent 8 ns simulation at 300 K in the NVT ensemble. Finally, the density of the system was equilibrated over an 8 ns simulation in the NPT ensemble at 1 bar and 300 K.

All NVT and NPT simulations (including the production-stage trajectories described below) employed periodic boundary conditions, the Particle Mesh Ewald[206] treatment of electrostatic interactions with a direct sum cut-off of 10.0 Å, the SHAKE algorithm[207, 208] to rigidify bonds to hydrogen atoms, a Langevin thermostat with a collision frequency of 2 ps^{-1}, and an integration timestep for the Langevin equation of motion of 2 fs. Pressure in NPT simulations was regulated with a Monte Carlo barostat having a relaxation time of 1 ps. PMEMD in its CPU and GPU[209] implementations in the Amber20 package[198] was used to perform the minimization and dynamical simulations, respectively.

Conventional (unbiased) production-stage simulations: The simulation at circumneutral pH was propagated with conventional (or unbiased) MD for 72 ns in the NVT ensemble at 300 K. The simulations of the fully protonated OmcS dimer, with or without the His16 crosslink present, were each propagated for 51 ns in the NVT ensemble at 300 K.

Accelerated (biased) production-stage simulations: Previous experimental work has indicated that a dramatic structural change in OmcS occurs under acidic conditions, at least when the protein is deposited on a substrate[62]. Whether the structural change is pH- or surface-induced is an open question that is under investigation in our laboratory. Cognizant of the limitations of conventional MD to efficiently sample large-scale conformational changes, we employed accelerated MD (aMD), which increases the escape-rate from potential energy minima by applying a boost potential if the energy falls below a threshold level[210]. The potential energy surface is unmodified if the energy is greater than or equal to the threshold value. The boost potential takes the form[210]

$$\Delta V(r) = \frac{\big(E - V(r)\big)^2}{\alpha + \big(E - V(r)\big)^2} \qquad \textbf{(1)}$$

where V(r) is the unmodified potential as a function of the atomic positions, E is the threshold energy, and α is a tuning parameter that defines the depth of the basins on the modified potential energy surface.

In this work, we employed a dual boost methodology[211] in which separate boost potentials were applied to the overall potential energy function to facilitate large-scale diffusive motions, and to torsional terms to accelerate local protein backbone dynamics. The parameters for these boost potentials—$E_{threshP}$ and α_{tot}, and $E_{threshD}$ and α_{dihed}, respectively—were computed by Equations 2 and 3 based on the average total and torsional potential energies from the 51-ns conventional, production-stage MD simulations. By this procedure, $E_{threshP}$, $E_{threshD}$, α_{tot}, and α_{dihed} were assigned values of -543390.98, -12148.839, 13064.32, and 696 kcal/mol for the fully protonated OmcS dimer with the inter-domain crosslink, and -543725.18, 12139.571, 13064.32, and 696 kcal/mol for the fully protonated model lacking the crosslink.

$$E_{threshP} = E_{avg,tot} + \alpha_{tot} \quad \textbf{(2a)}$$

$$\alpha_{tot} = 0.16 \frac{kcal}{mol \times atom} * N_{atoms} \quad \textbf{(2b)}$$

$$E_{threshD} = E_{avg,dihedral} + (5 \ * \ \alpha_{dihedral}) \quad \textbf{(3a)}$$

$$\alpha_{dihed} = \frac{1}{5}\left(4 \frac{kcal}{mol \times residue}\right) * N_{residues} \quad \textbf{(3b)}$$

Significant advantages of the aMD methodology include the fact that a reaction coordinate does not need to be pre-defined and that the boost potential preserves the shape of the underlying potential energy surface. Canonical ensemble averages of observables can be obtained, in principle, by an energetic reweighting procedure, although care may be needed to avoid numerical instabilities in the reweighting process[212, 213].

Time in an aMD simulation is one of the quantities that must be reweighted by an ensemble average of the Boltzmann factor of the boost potential energy. However, if the boost potential modifies the transition state region for a state-to-state transition, which is likely to occur on the very rough and hyperdimensional energy landscape of a biomolecule, this time reweighting procedure is no longer valid[214, 215]. Correction schemes have been explored but have only so far been shown to recover the

correct kinetics for simple processes (e.g., *cis-trans* isomerization of the peptide bond in *N*-methylacetamide and the glycyl-prolyl dipeptide)[214, 215]. We therefore refrain from reweighting time, and instead report the nominal length of the aMD simulations of the fully protonated dimer with and without the His crosslink to be 306 and 510 ns, respectively. These nominal times represent the lower-bound of the actual timescale for the kinetic processes sampled in these trajectories.

3.5.15 Molecular mechanics generalized Born solvation area (MM-GBSA) binding free energy estimation

The MM-GBSA end-point binding free energy approach[78, 216] was used to estimate the change in stability of the OmcS dimer upon the protonation of all titratable residues. A thermally averaged protein-protein binding free energy was obtained under circumneutral pH conditions by sampling configurations every 600 ps from the last half of a 72-ns conventional (unbiased) MD simulation (i.e., 60 configurations were analyzed in total).

Because of the length of the aMD simulations for the fully protonated OmcS dimer with or without the His16 crosslink, the following protocol was devised: The aMD simulation was divided into segments of a nominal 38-44 ns within which the unbiased total potential energy of the simulation was found to be normally distributed. In each of these simulation segments, configurations with unbiased potential energies within one standard deviation of the mean were concatenated into separate trajectories from which every 30th frame was taken for analysis with MM-GBSA. A total of 45 to 50 frames were analyzed for each simulation segment (Supplementary Table 3.2). The average of these MM-GBSA results is reported in the main text.

In all the MM-GBSA calculations, chain A of the OmcS dimer was defined as the "ligand" for the "receptor," which was composed of chains B and the capping-fragment of chain D. The MM-GBSA method is intended for studying non-covalent binding interactions. To apply the method to the OmcS dimer models with an inter-domain (ligand-receptor) bond, the bonded energy terms that do not cancel in the thermodynamic cycle were subtracted from the total binding energy. This correction was no greater than 14 kcal/mol and does not change the conclusion regarding pH-induced destabilization of the polymerized state.

MM-GBSA, as implemented in the AmberTools20 package, does not natively include the atomic radius of Fe for the implicit solvent models. It was necessary to add the parameters to the mdread2.f90 source file as documented in an Amber Mailing List post (http://archive.ambermd.org/201303/0230.html), and to recompile the package.

Supplementary Table 3.2. MM-GBSA binding free energies (in kcal/mol) for OmcS dimer models varying in protonation state and the presence of the inter-domain His crosslink.

	Avg.	St. Dev.	St. Error
With the Inter-Domain Crosslink			
Standard Protonation			
Full trajectory	-178.5	8.9	1.2
Full Protonation			
Seg. #1	-123.3	15.3	2.2
Seg. #2	-112.8	10.1	1.4
Seg. #3	-117.6	7.4	1.1
Seg. #4	-110.5	8.5	1.2
Seg. #5	-116.7	9.3	1.3
Seg. #6	-115.6	9.5	1.4
Seg. #7	-116.0	10.5	1.5
Without the Inter-Domain Crosslink			
Full Protonation			
Seg. #1	-96.0	10.9	1.6
Seg. #2	-105.8	10.2	1.5
Seg. #3	-104.8	15.8	2.3
Seg. #4	-97.9	7.4	1.1
Seg. #5	-112.6	11.9	1.7
Seg. #6	-131.7	8.6	1.2
Seg. #7	-123.3	10.4	1.5
Seg. #8	-110.5	16.6	2.5
Seg. #9	-103.5	11.4	1.6
Seg. #10	-115.3	11.5	1.7
Seg. #11	-115.6	8.1	1.2
Seg. #12	-124.0	12.0	1.7

3.6 Acknowledgments

We thank Hannah Lant for help with EPR, Amani Ebrahim and Yang Liu for help with XAS, Catharine Shipps, Jens Neu, and Eric Martz for helpful discussions, Fadel A. Samatey and Yuri Y. Londer for providing purified PpcA protein, Derek Lovley for providing the CL-1 strain, and Cong Shen for providing the Δ*omcS* strain in the CL-1 background. This research used beamline 7-BM (QAS) of the National Synchrotron Light Source II, a U.S. DOE Office of Science User Facility operated for the DOE Office of Science by Brookhaven National Laboratory under Contract No. DE-SC0012704 and 12-BM beamline of the Advanced Photon Source at Argonne National Laboratory, supported by DOE under Contract No. DE-AC02-06CH11357. This research was supported by the National Institutes of Health Director's New Innovator award (1DP2AI138259-01 to N.S.M.), the NSF CAREER award no. 1749662 (to N.S.M.), NSF Early-Concept Grant for Exploratory Research (EAGER) Award No. 2038000. (to N.S.M. and V.S.B.), NSF CHE award no. 1903576 (to A.I.F.), NSF Graduate Research Fellowship award 2017224445 (to J.P.O.), and NIH Training Grant T32 GM007223 (supporting V.S.). Research was sponsored by the Defense Advanced Research Project Agency (DARPA) Army Research Office (ARO) and was accomplished under Cooperative Agreement Number W911NF-18-2-0100 (with N.S.M. and V.S.B.).

3.7 Appendix

The following pages contain the raw images used to prepare figures presented in this chapter.

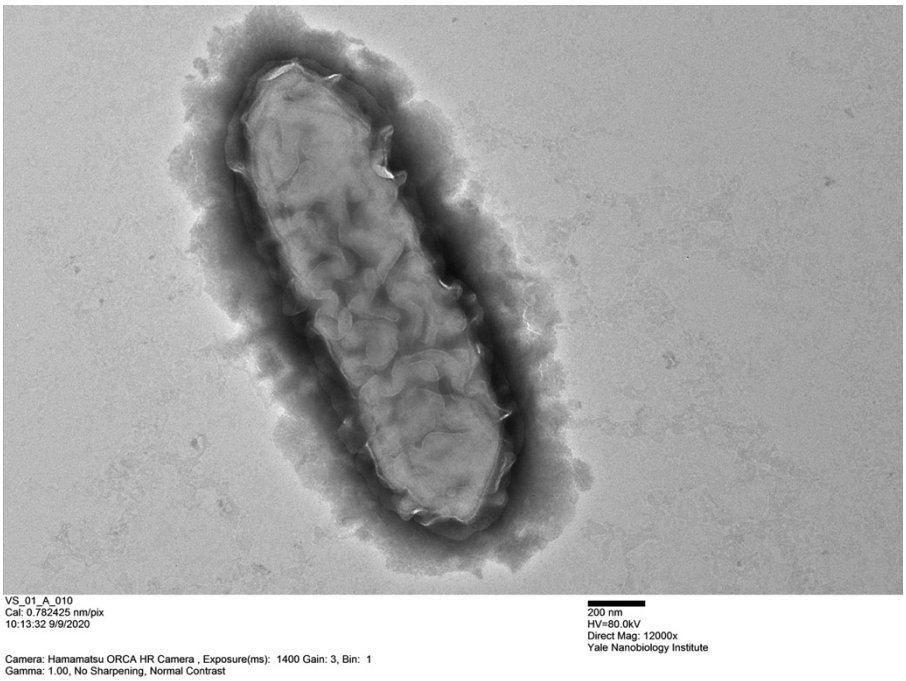

Supplementary Figure 3.3. Unmodified TEM image used to prepare Figure 3.1D.

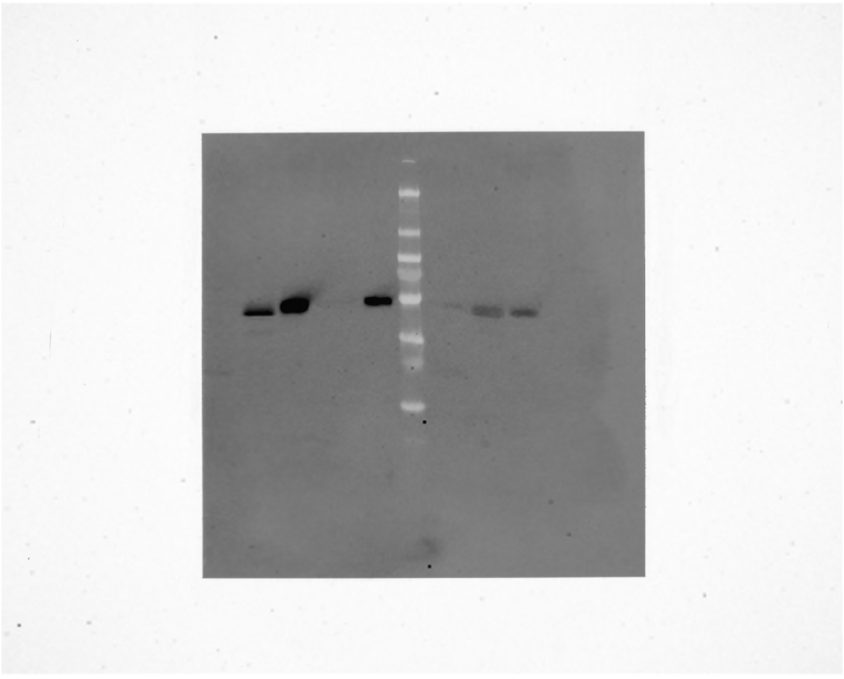

Supplementary Figure 3.4. Unmodified immunoblot image used to prepare Figure 3.2B.

Molecular weight standard utilized includes markers at 180, 130, 100, 70, 55, 40, 35, 25, 15, and 10 kDa.

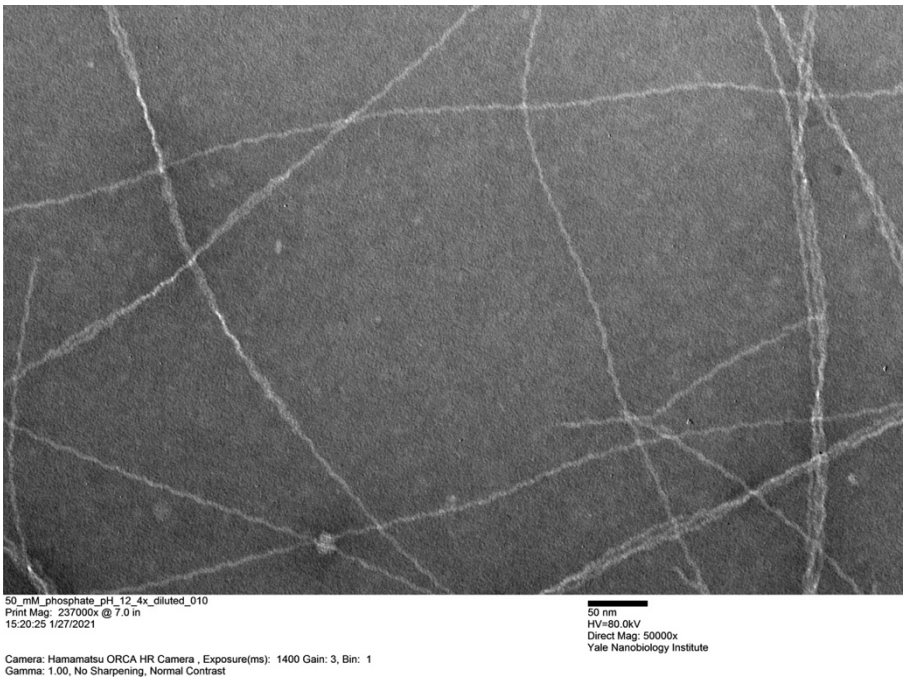

Supplementary Figure 3.5. Unmodified TEM image used to prepare Figure 3.6A.

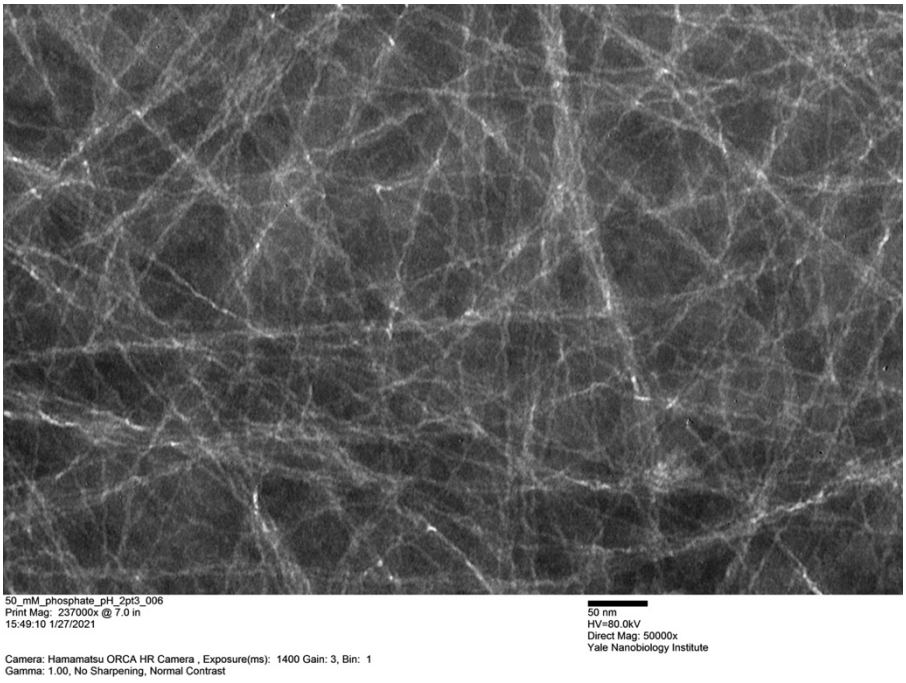

Supplementary Figure 3.6. Unmodified TEM image used to prepare Figure 3.6B.

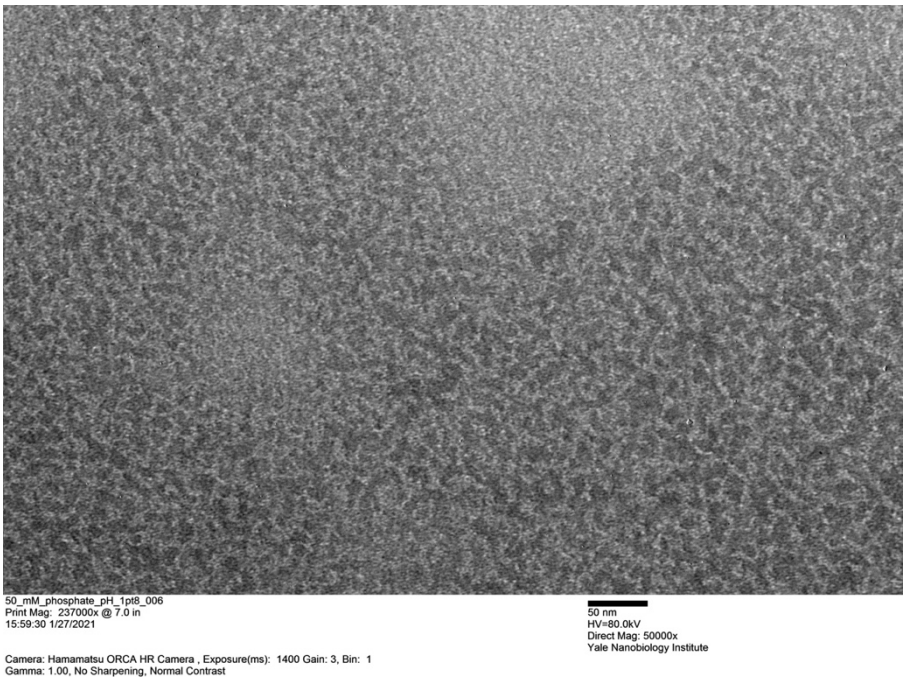

Supplementary Figure 3.7. Unmodified TEM image used to prepare Figure 3.6C.

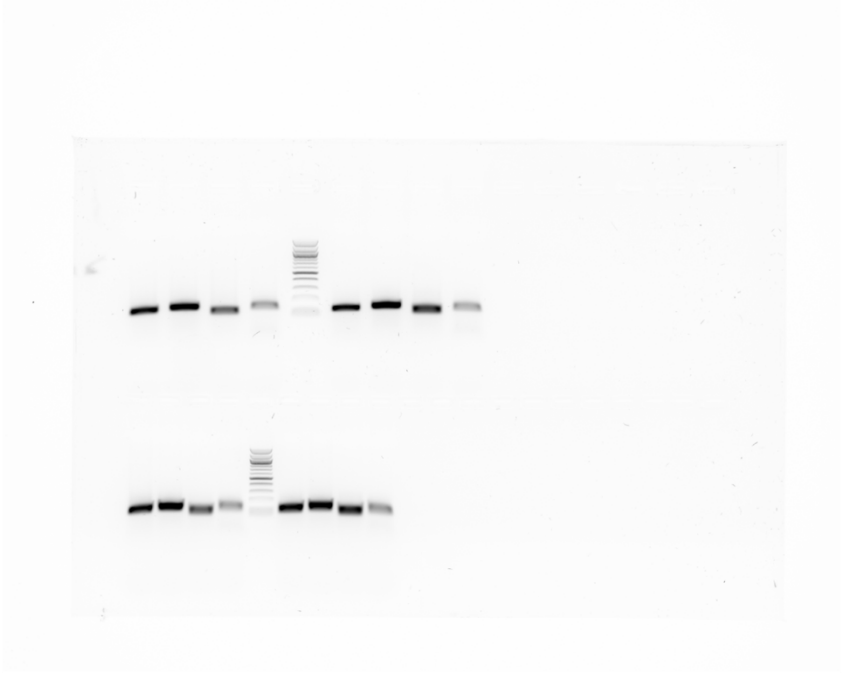

Supplementary Figure 3.8. Unmodified agarose gel image used to prepare Figure 3.3A.

Ladder used includes markers at 1517, 1200, 1000, 900, 800, 700, 600, 500, 400, 300, 200, 100 bp.

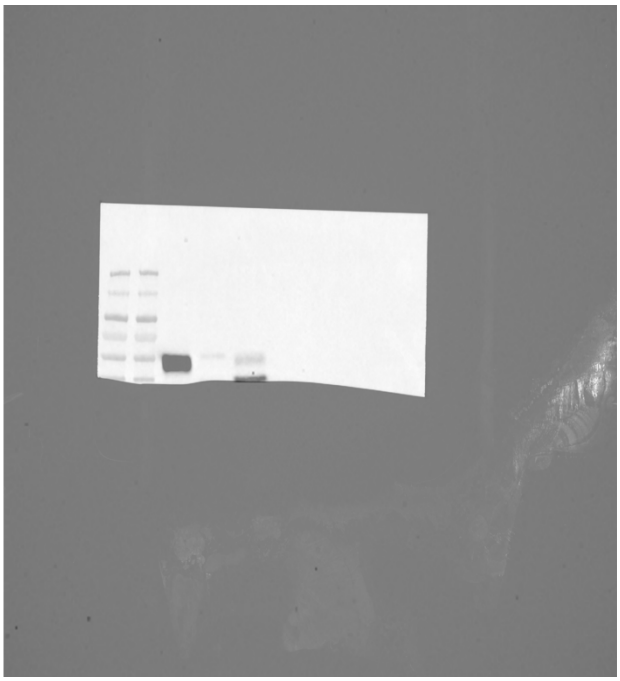

Supplementary Figure 3.9. Unmodified anti-OmcS immunoblot image used to prepare Figure 3.3C.

Molecular weight standard utilized includes markers at 180, 130, 100, 70, 55, 40, 35, 25, 15, and 10 kDa.

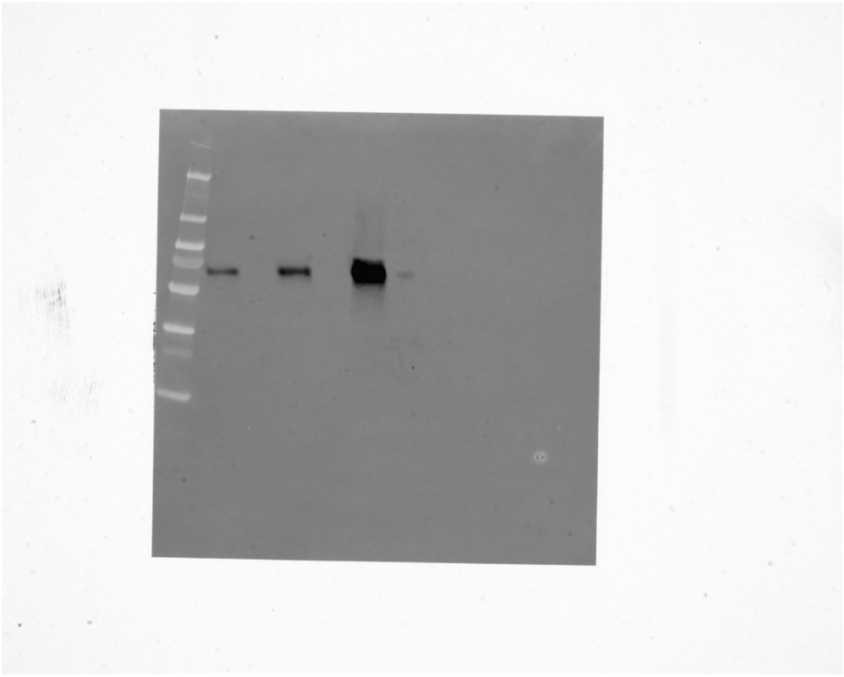

Supplementary Figure 3.10. Unmodified anti-GroEL immunoblot image used to prepare Figure 3.3C.

Molecular weight standard utilized includes markers at 180, 130, 100, 70, 55, 40, 35, 25, 15, and 10 kDa.

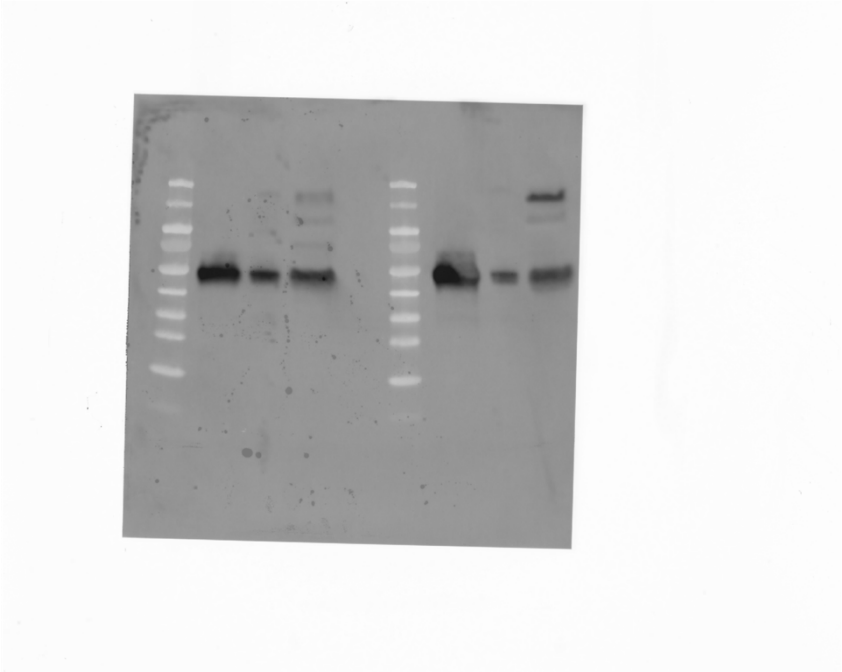

Supplementary Figure 3.11. Unmodified immunoblot image used to prepare characterization of strain CL-1 in Figure 3.3G.

Molecular weight standard utilized includes markers at 180, 130, 100, 70, 55, 40, 35, 25, 15, and 10 kDa.

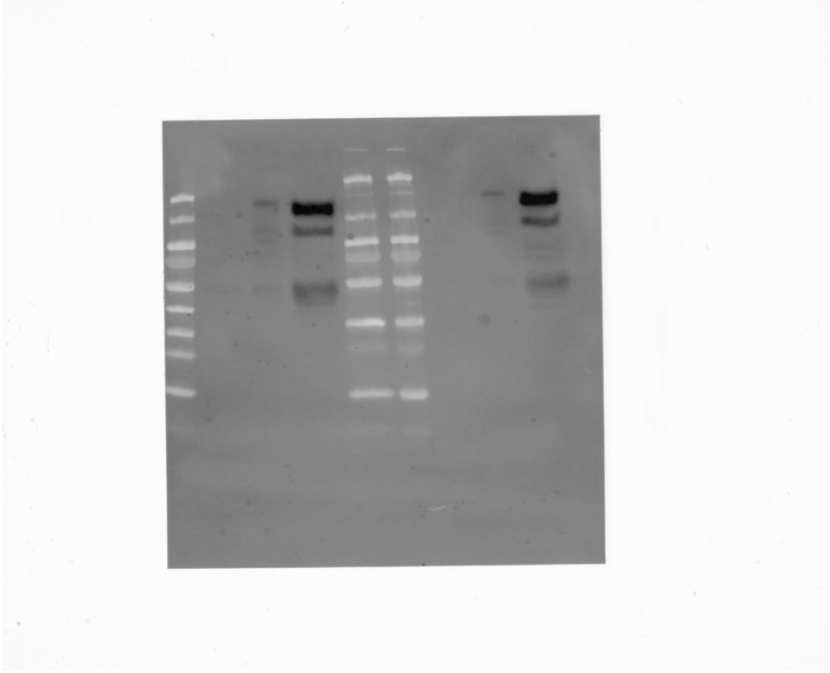

Supplementary Figure 3.12. Unmodified immunoblot image used to prepare characterization of strain H16A in Figure 3.3G.

Molecular weight standard utilized includes markers at 180, 130, 100, 70, 55, 40, 35, 25, 15, and 10 kDa.

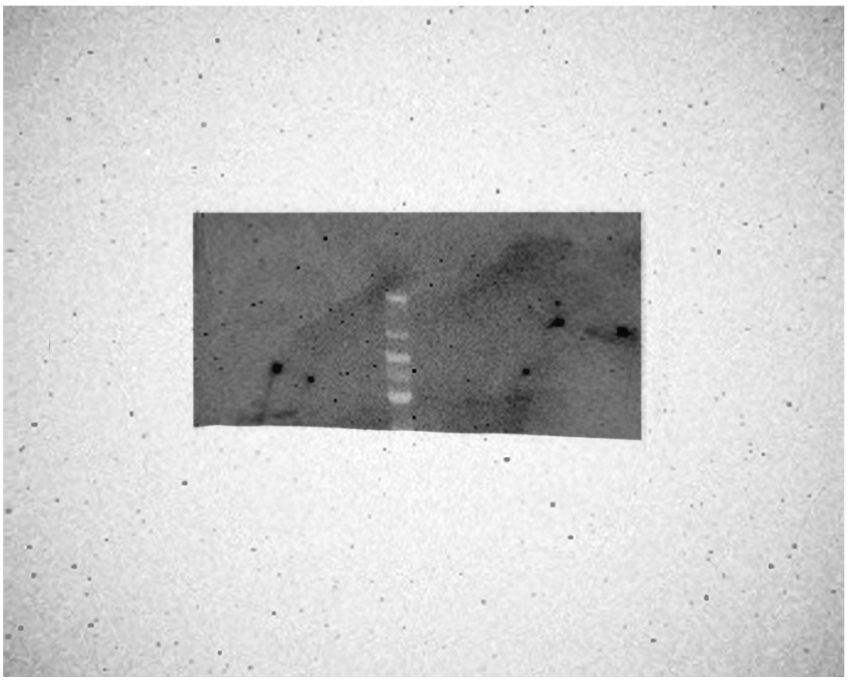

Supplementary Figure 3.13. Unmodified immunoblot image used to prepare Figure 3.4A.
Molecular weight standard utilized includes markers at 180, 130, 100, 70, 55, 40, 35, 25, 15, and 10 kDa.

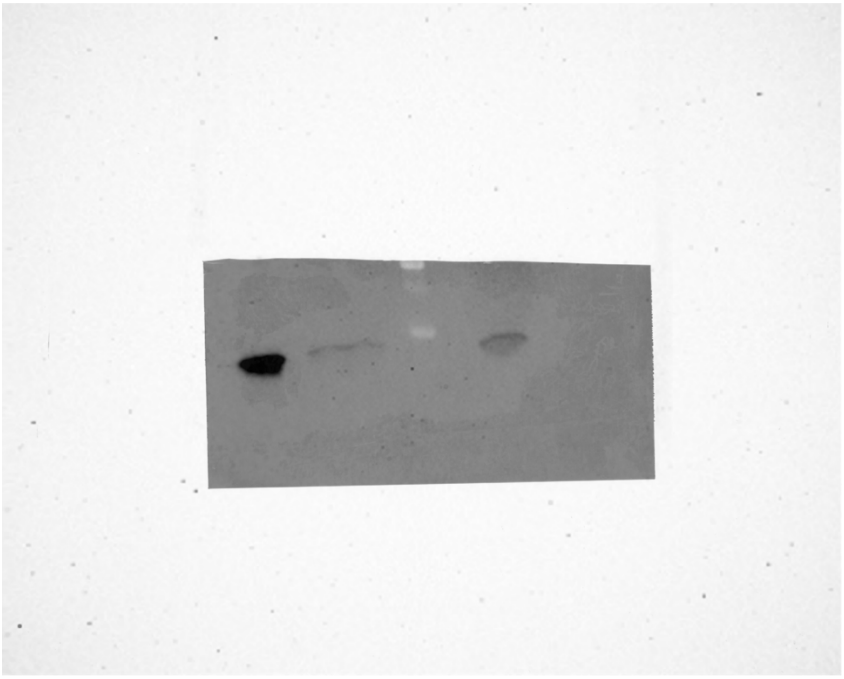

Supplementary Figure 3.14. Unmodified immunoblot image used to prepare Figure 3.4B.
Molecular weight standard utilized includes markers at 180, 130, 100, 70, 55, 40, 35, 25, 15, and 10 kDa.

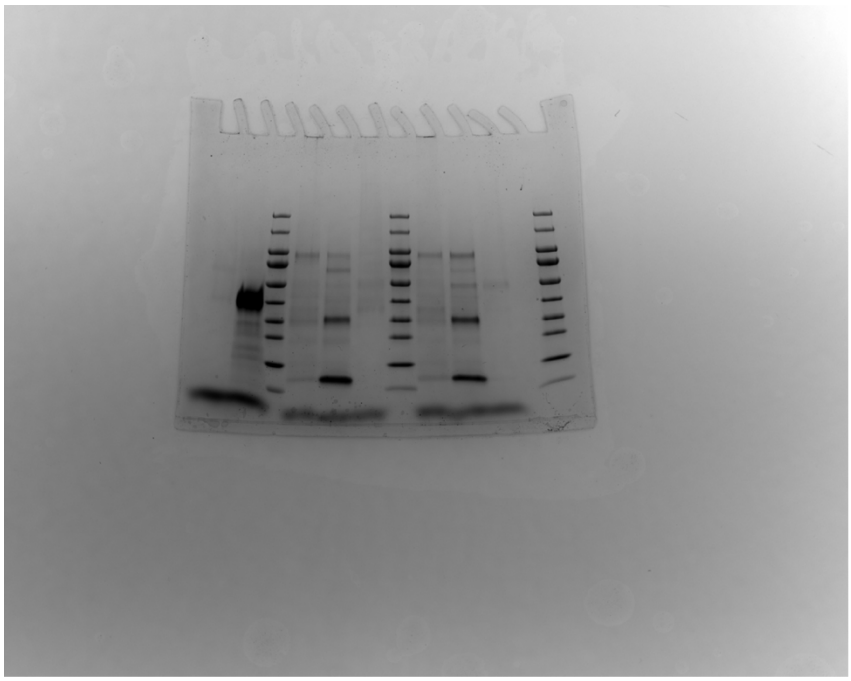

Supplementary Figure 3.15. Unmodified gel image used to prepare heme staining characterization of samples unheated prior to loading in Figure 3.4C.

Molecular weight standard utilized includes markers at 180, 130, 100, 70, 55, 40, 35, 25, 15, and 10 kDa.

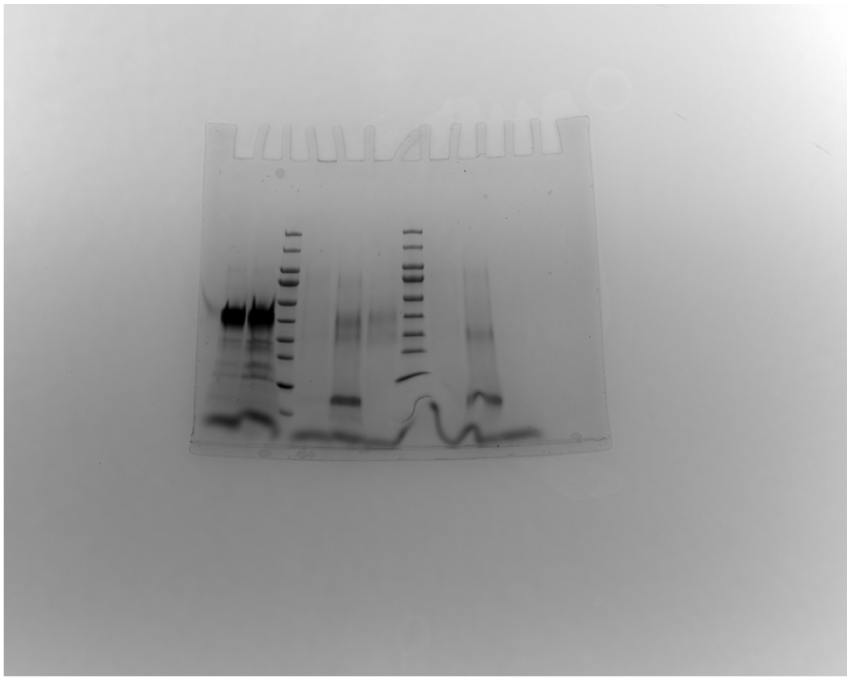

Supplementary Figure 3.16. Unmodified gel image used to prepare heme staining characterization of samples heated prior to loading in Figure 3.4C.

Molecular weight standard utilized includes markers at 180, 130, 100, 70, 55, 40, 35, 25, 15, and 10 kDa.

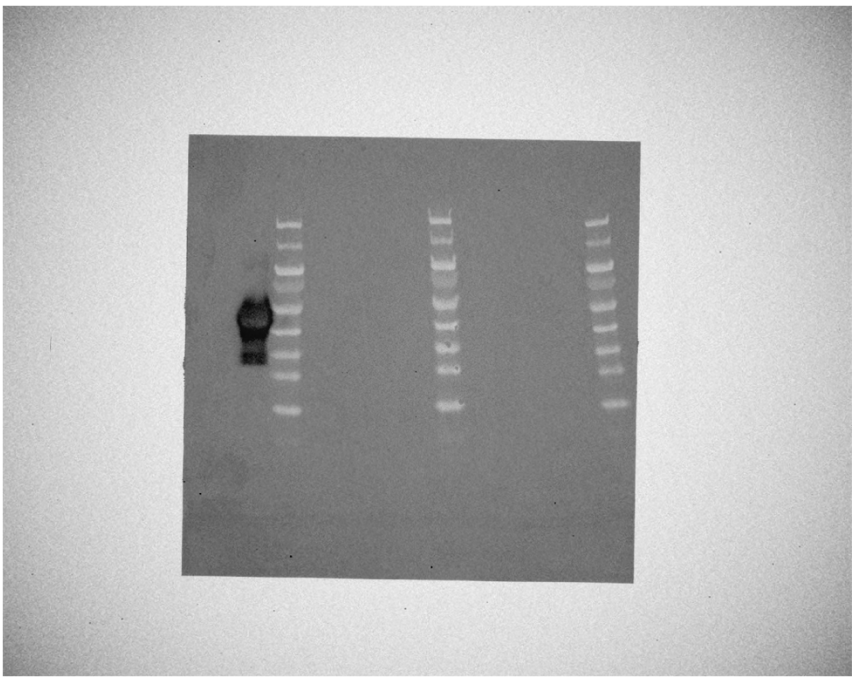

Supplementary Figure 3.17. Unmodified immunoblot image used to prepare characterization of samples unheated prior to loading presented as "Replicate 1" in Figure 3.4C.

Molecular weight standard utilized includes markers at 180, 130, 100, 70, 55, 40, 35, 25, 15, and 10 kDa.

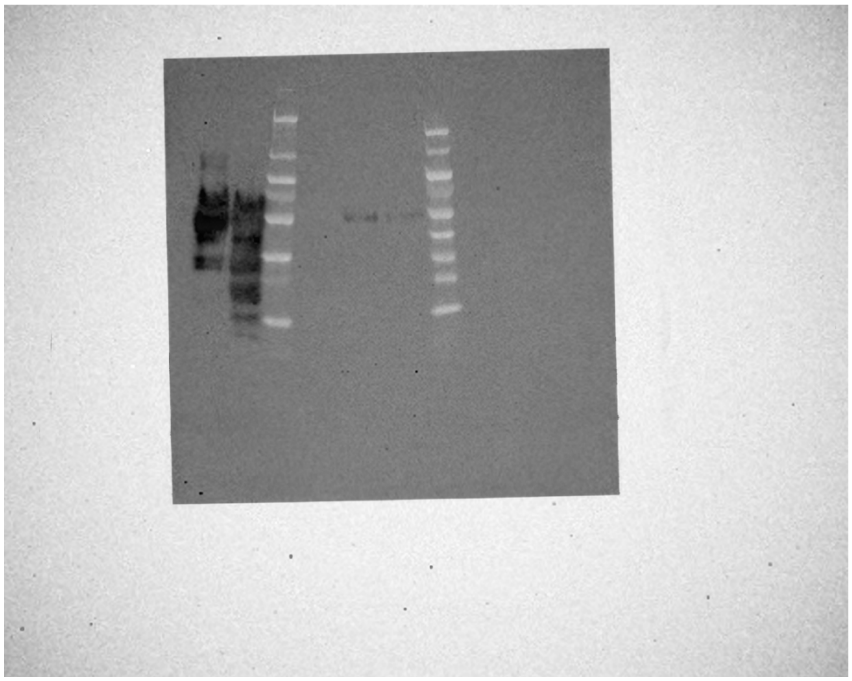

Supplementary Figure 3.18. Unmodified immunoblot image used to prepare characterization of samples heated prior to loading presented as "Replicate 1" in Figure 3.4C.

Molecular weight standard utilized includes markers at 180, 130, 100, 70, 55, 40, 35, 25, 15, and 10 kDa.

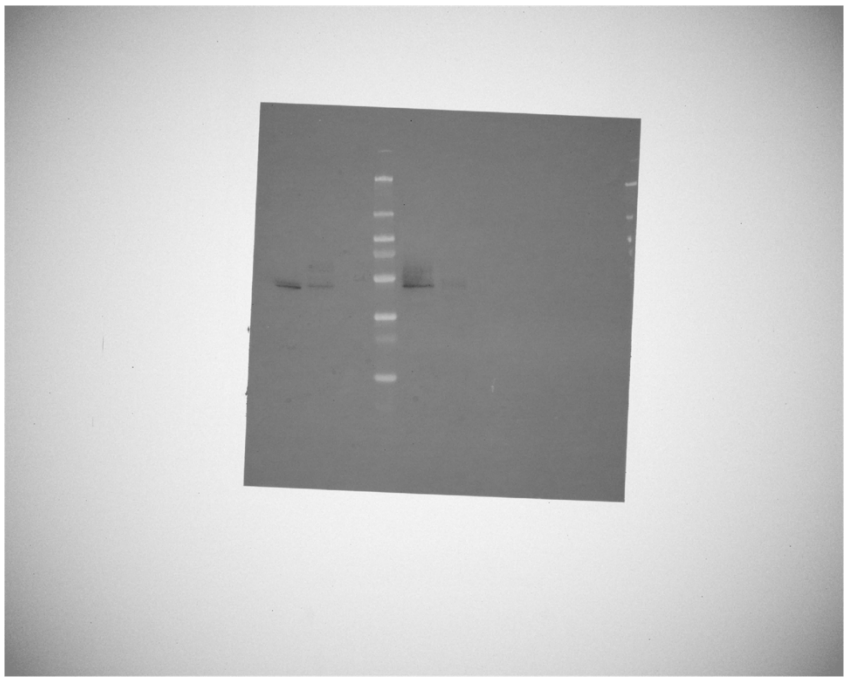

Supplementary Figure 3.19. Unmodified immunoblot image used to prepare characterization of samples unheated prior to loading presented as "Replicate 2" in Figure 3.4C.

Molecular weight standard utilized includes markers at 180, 130, 100, 70, 55, 40, 35, 25, 15, and 10 kDa.

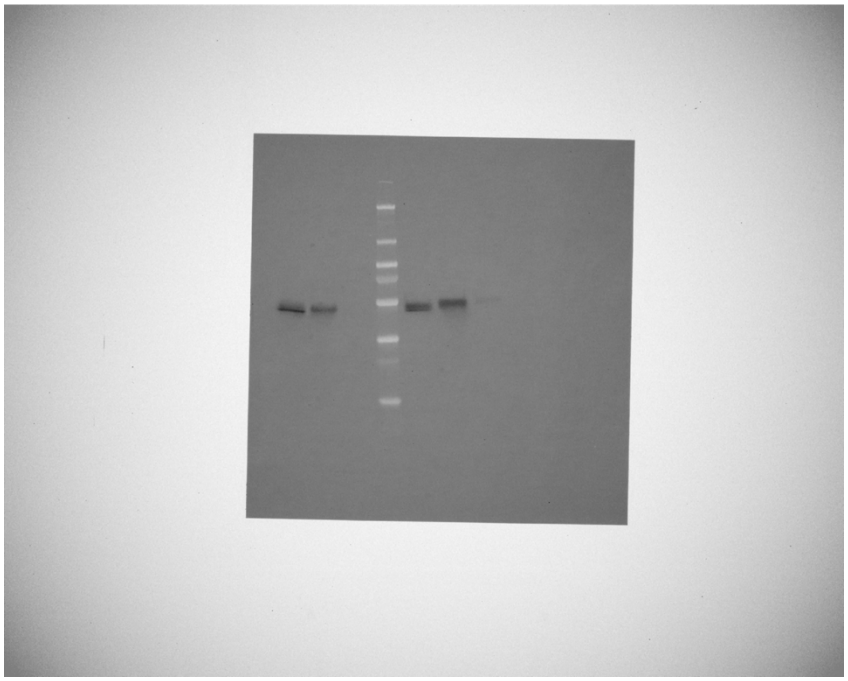

Supplementary Figure 3.20. Unmodified immunoblot image used to prepare characterization of samples heated prior to loading presented as "Replicate 2" in Figure 3.4C.

Molecular weight standard utilized includes markers at 180, 130, 100, 70, 55, 40, 35, 25, 15, and 10 kDa.

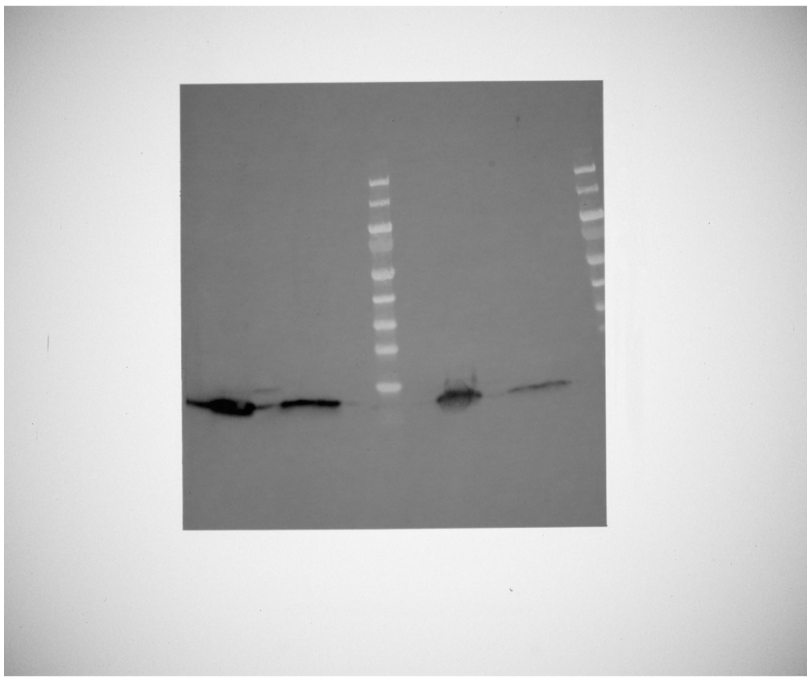

Supplementary Figure 3.21. Unmodified immunoblot image used to prepare characterization of samples unheated prior to loading in Figure 3.4D.

Molecular weight standard utilized includes markers at 180, 130, 100, 70, 55, 40, 35, 25, 15, and 10 kDa.

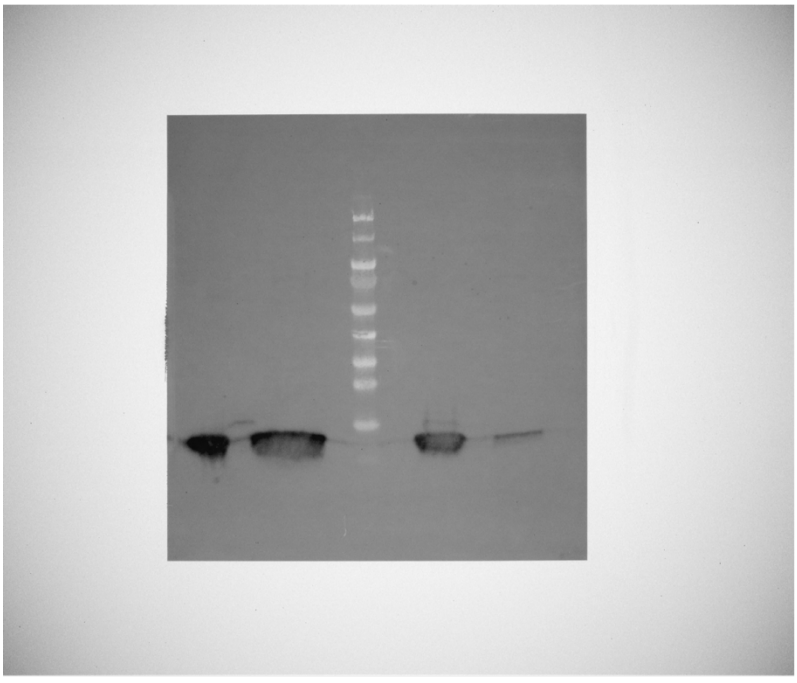

Supplementary Figure 3.22. Unmodified immunoblot image used to prepare characterization of samples heated prior to loading in Figure 3.4D.

Molecular weight standard utilized includes markers at 180, 130, 100, 70, 55, 40, 35, 25, 15, and 10 kDa.

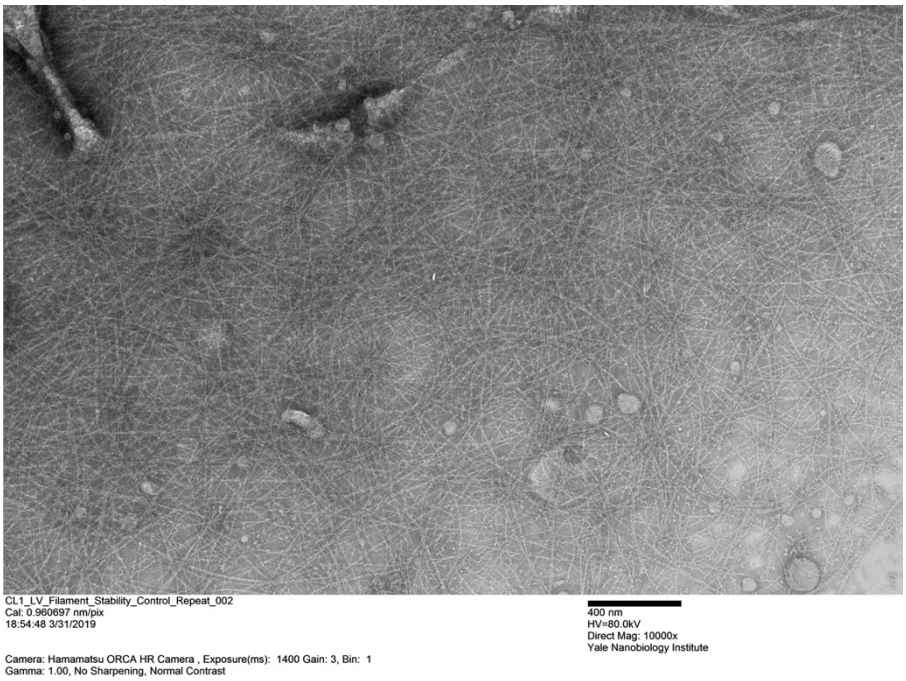

Supplementary Figure 3.23. Unmodified TEM image used to prepare Figure 3.7A.

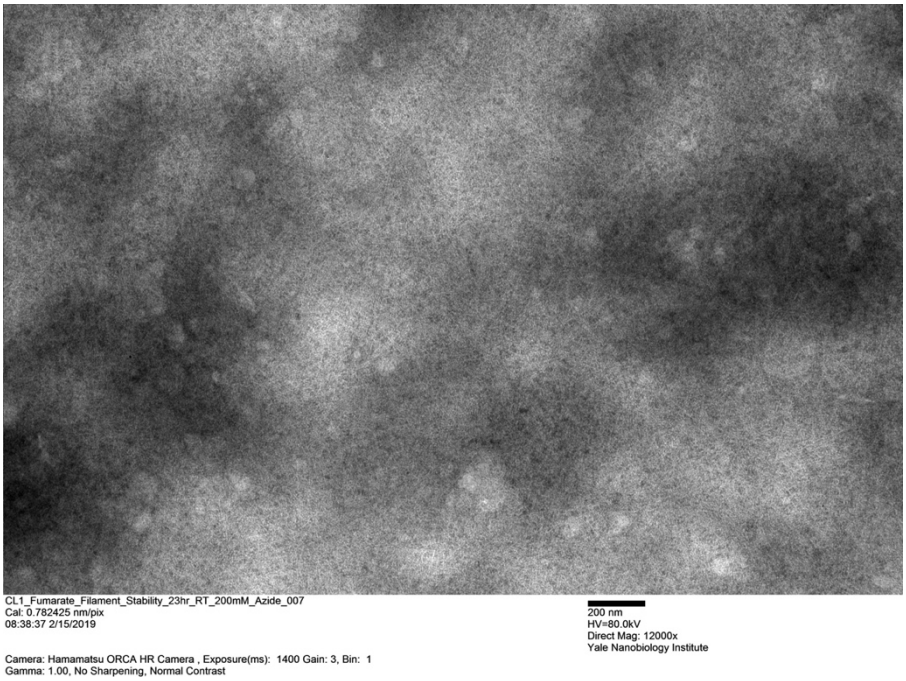

Supplementary Figure 3.24. Unmodified TEM image used to prepare Figure 3.7B.

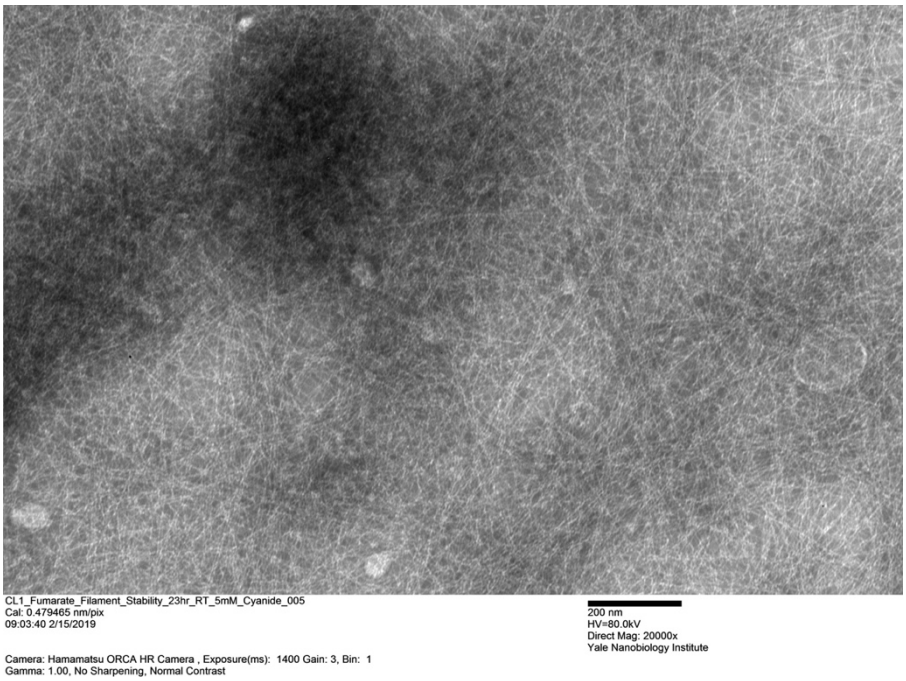

Supplementary Figure 3.25. Unmodified TEM image used to prepare Figure 3.7C.

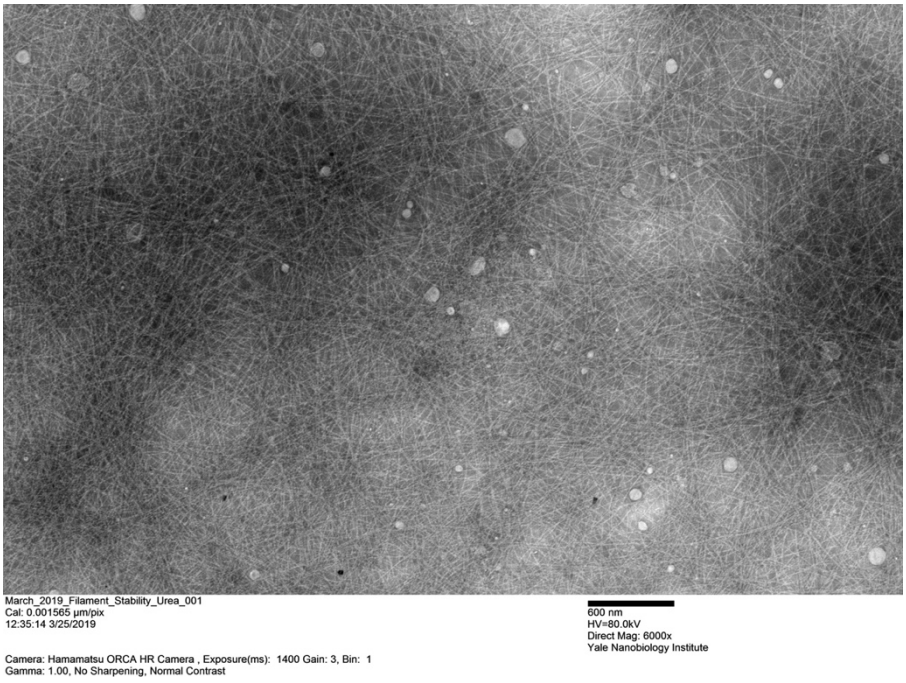

Supplementary Figure 3.26. Unmodified TEM image used to prepare Figure 3.7D.

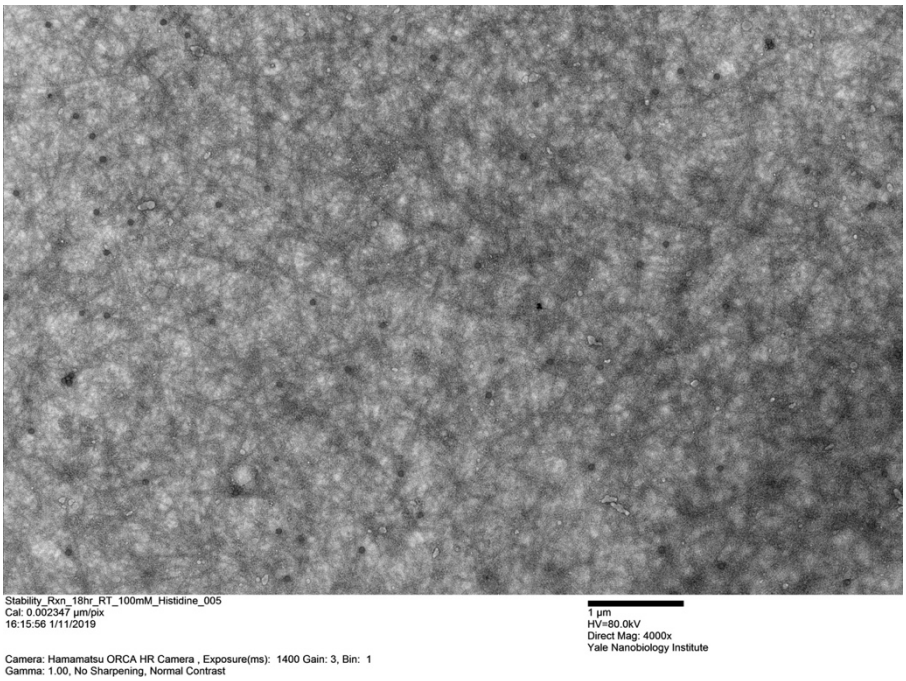

Supplementary Figure 3.27. Unmodified TEM image used to prepare Figure 3.7E.

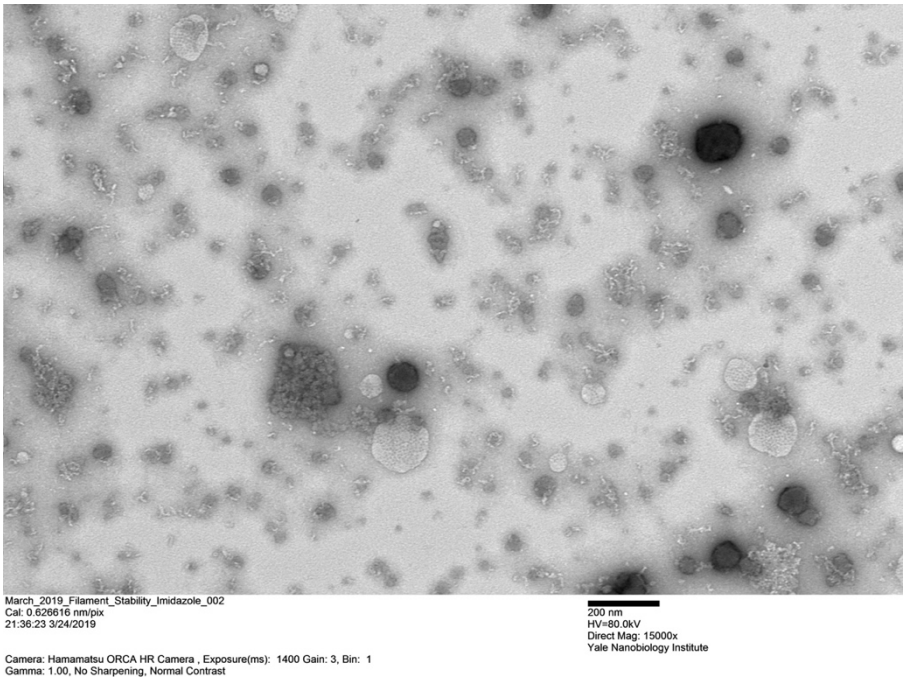

Supplementary Figure 3.28. Unmodified TEM image used to prepare Figure 3.7F.

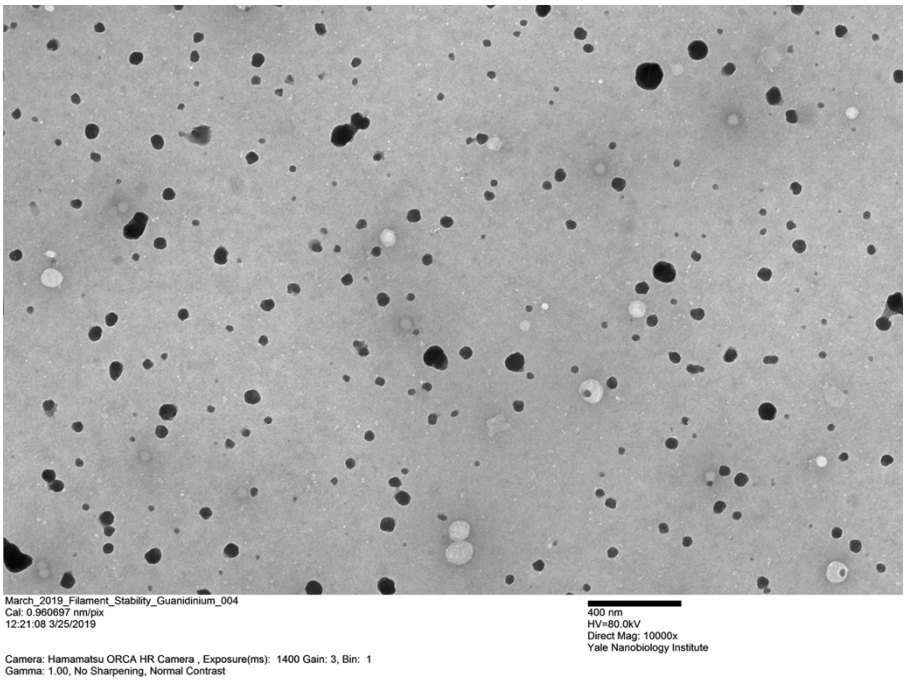

Supplementary Figure 3.29. Unmodified TEM image used to prepare Figure 3.7G.

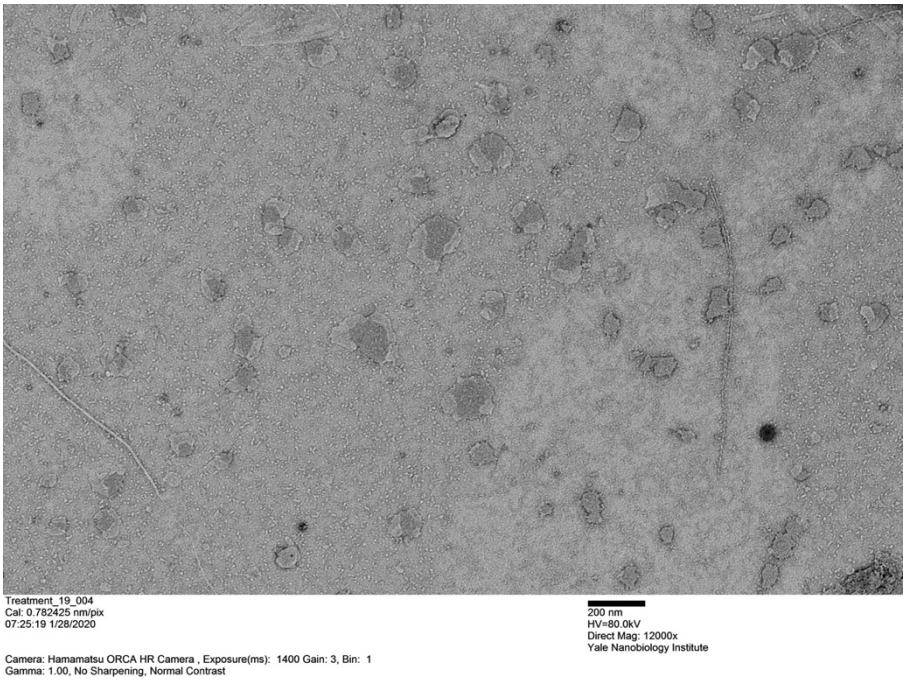

Supplementary Figure 3.30. Unmodified TEM image used to prepare Figure 3.7H.

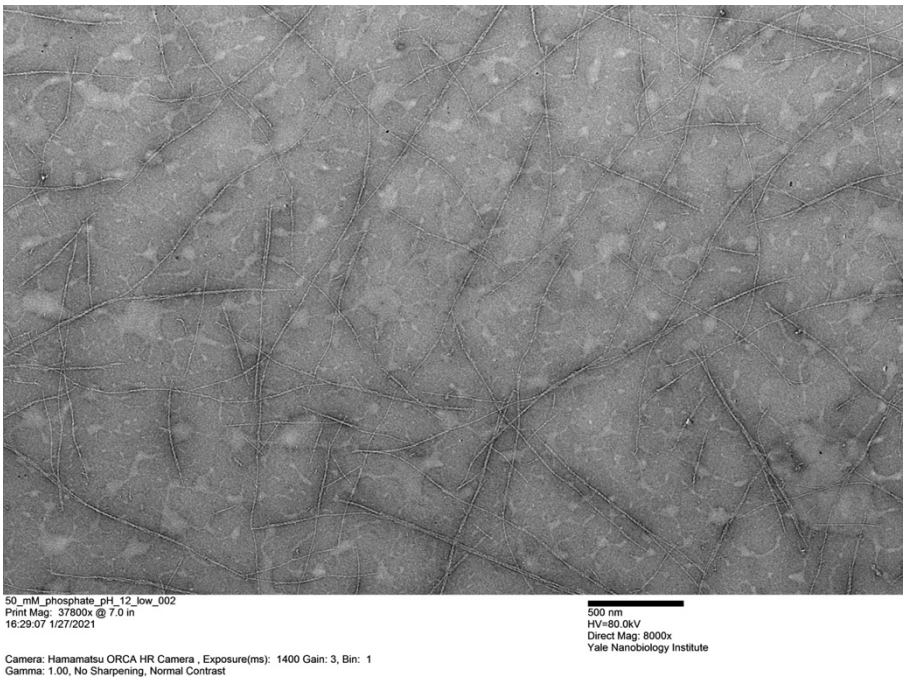

Supplementary Figure 3.31. Unmodified TEM image used to prepare Figure 3.16A.

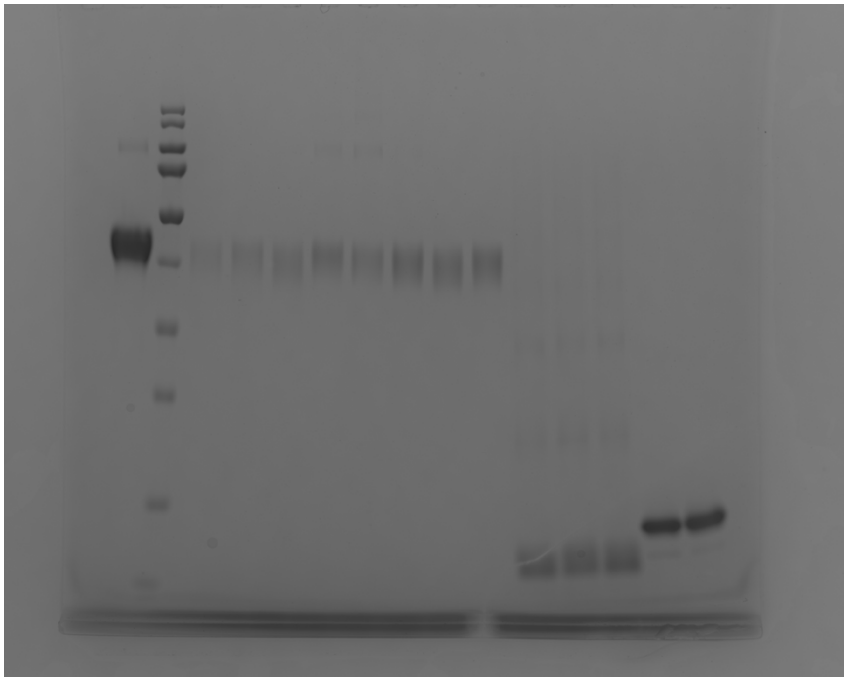

Supplementary Figure 3.32. Unmodified gel image used to prepare Figure 3.5A and Figure 3.19D. Molecular weight standard utilized includes markers at 180, 130, 100, 70, 55, 40, 35, 25, 15, and 10 kDa.

Structural evidence suggests diverse microbial species have the potential to utilize OmcS-like nanowires for EET

This chapter is based on a submitted manuscript:

Shen, C., Srikanth, V., Gu, Y., Salazar-Morales, A.I., Shipps, C.C., Yalcin, S.E., Samatey, F.A., and Malvankar, N.S. "A conserved gene cluster drives formation of cytochrome OmcS nanowires in diverse bacteria."

The source material has been abridged to highlight discussion of the structure and function of OmcS-like cytochromes and their potential to form nanowires utilized for EET.

The complete author contribution description accompanying this manuscript is reproduced below (emphasis added):

N.S.M. and C.S. designed the project. C.S. performed bioinformatic analyses, bacterial growth, RT-PCR, negative-stain TEM, AFM imaging, device fabrication, purification of *G. subterraneus* filaments, conductivity measurements, genetic constructions, biochemical analyses, iron oxide reduction assay, manganese oxide reduction, subcellular fractionation, purification of recombinant proteins from *E. coli*, and DLS. **V.S. conducted negative-staining TEM, collected cryo-EM data, solved the structure [of the *G. subterraneus* filament], and built the atomic and AlphaFold models [of OmcS-like protomers].** Y.G. conducted negative-staining TEM, power spectra analyses of filaments from *A. dehalogenans* and 2D classification of negative-staining TEM images of recombinant OscG. A.I.S.-M. carried out iron oxide reduction assays. C.C.S. performed measurements of midpoint redox potential. S.E.Y. performed AFM imaging of recombinant OscG. F.A.S. conducted purification of recombinant proteins from *E. coli* and built AlphaFold models. N.S.M. supervised the work. **C.S., V.S., and N.S.M. wrote the manuscript with input from all the authors.**

4.1 Summary

Microbial extracellular electron transfer drives various globally-important environmental processes and biotechnological applications[130]. Well-known modes of short-range (< 1 μm) EET use soluble molecules and membrane-bound monomeric cytochromes[130]. Although "nanowires" of polymerized cytochrome OmcS have also been described for long-range (> 10 μm) EET[53, 54], the basis for their formation and existence beyond *Geobacter sulfurreducens* remains unknown. By analyzing *omcS* genetic patterns, here we identify a previously-unknown ~10-gene cluster, herein named *osc*, in diverse environmentally-important bacteria. We find that *Geoalkalibacter subterraneus* and *Anaeromyxobacter dehalogenans* also use OmcS-like nanowires for EET through the action of their *osc* clusters. Combining cryo-electron microscopy and structural modeling with functional studies, we show that these bacteria produce distinct nanowires structures with varied conductivity and redox properties. As OmcS-like structures and related gene clusters are widespread, our studies establish a prevalence of specialized biogenesis systems for cytochrome nanowires across diverse species and environments.

4.2 Introduction

Geobacter species serve as a model for EET due to their importance in diverse natural environments[56, 63]. *Geobacter* are often abundant species in soils and sediments in which EET significantly impacts the biogeochemical cycling of carbon, nutrients, and metals, as well as in bioremediation of toxic organic and metal contaminants in groundwater[5]. *Geobacter* species are also frequently syntrophic partners of methanogens relying on direct interspecies electron transfer (DIET)[5]. *Geobacter* species are often enriched in bioelectrochemical systems generating electricity from waste, and *G. sulfurreducens* generates the highest current densities of all known isolates by forming a nanowire network in biofilms that can transport electrons over 100 cell lengths[5]. Thus, *Geobacter* are among the most efficient species for EET and DIET, serving as an ideal model system for various biotechnological applications such as electrocatalysis, metal corrosion and production of fuels[17, 63].

It has been hypothesized that the key to high performance of *Geobacter* species is their ability to directly contact electron acceptors via conductive surface appendages called "nanowires," thus

eliminating the need for diffusive redox mediators[56, 63]. These nanowires were thought to be pili[56]. However, recent structural, functional, and localization studies[63, 217] have found that filaments on the bacterial surface during EET are made up of polymerized cytochromes OmcS[53, 54] and OmcZ[62], whereas pili are required for the secretion of cytochrome nanowires[166].

Cryogenic electron microscopy of OmcS nanowires shows a seamless heme stacking[53, 54] that enables highly-efficient electron transfer over micrometer distances[218, 219]. Out of 111 putative cytochrome genes, *omcS* is the only nanowire-forming cytochrome known to be essential for DIET[19] and EET to Fe(III) oxides abundant in natural environments[40]. OmcS is also important for EET to electrodes during early stages of biofilm growth[20]. In addition to playing a role in whole-cell catalysis by *G. sulfurreducens*[220, 221], OmcS was found to increase the performance of cyanobacteria in diverse catalytic processes when it was heterologously expressed in those microbes[222-224]. These studies highlight the important role of OmcS in biocatalysis. While these studies suggest that OmcS nanowires are involved in EET, the molecular basis for nanowire formation and function, and the existence of nanowires beyond *G. sulfurreducens* is unknown.

4.3 Results

4.3.1 *omcS* is co-localized with a gene cluster

OmcS homologs were thought to be rare in the microbial world[57]. However, our bioinformatic analysis revealed that diverse environmentally-important bacteria show high evolutionary conservation of OmcS homologs which are encoded in a shared ~10 gene cluster (Figure 4.1A, Figure 4.2A). In *G. sulfurreducens*, these genes (*oscB-K*) reside within a single operon (Supplementary Figure 4.1) and are overexpressed under three conditions[225-227] previously known to induce *OmcS* expression (Figure 4.1B). These results suggest that the expression of all genes in the cluster are collectively regulated and this *omcS*-related gene cluster, herein named '*osc*,' may be important in the formation of OmcS nanowires.

We found that OmcS homologs and the related *osc* gene cluster are present in multiple phyla including *Deltaproteobacteria, Thermodesulfobacteria,* and *Aquificae* (Figure 4.2). Most of the species

showing OmcS homologs are anaerobic and metabolize sulfur or sulfate. Many of these species are unculturable. Our phylogenetic analysis classified them into four main clades (Figure 4.1C):

Clade I: primarily mesophilic bacteria, such as *Geobacter*, inhabiting soils, and aquatic sediments

Clade II: primarily thermophilic bacteria, including DIET-performing syntrophic partners of methane oxidizing archaea in marine sediments, especially near hydrothermal vents[228]

Clades III and IV: detected only by metagenomics[229, 230]

Analysis of evolutionary conservation of OmcS revealed highly conserved heme binding motifs and key residues (Figure 4.3A-B). Notably, among the highly-conserved residues was His16, which is required for OmcS polymerization by coordinating the iron atom from the fifth heme of the adjacent monomer[53] (Figure 4.3C). Furthermore, the residues near the central electron transport chain of hemes were highly conserved (Figure 4.3B). The evolutionary conservation of these key residues and motifs suggest that diverse bacteria could polymerize OmcS homologs into nanowires to perform EET.

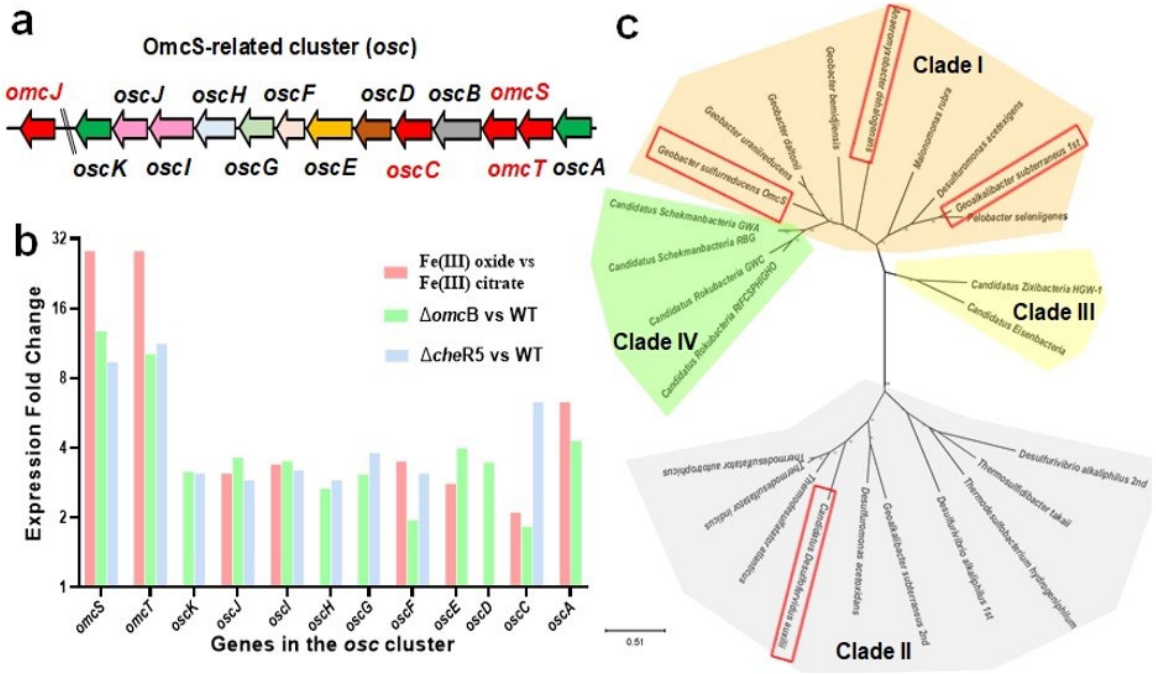

Figure 4.1. OmcS homologs and the related *osc* gene cluster are widespread in environmentally important bacteria.

a, Genomic organization of the *osc* genes surrounding *omcS* in *G. sulfurreducens* showing *omcS* homolog genes (red) and non-conserved genes (grey). Each gene homolog is shown by the same color. Not to scale. For other bacteria, see Figure 4.2. **b**, The *osc* cluster is upregulated under previosly reported conditions where OmcS is upregulated (analysis of data from Leang et al.[225], Tran[226], and Aklujkar et al.[227]). **c**, Phylogenetic distance tree derived from amino acid sequence alignments (Figure 4.3) with key species marked.

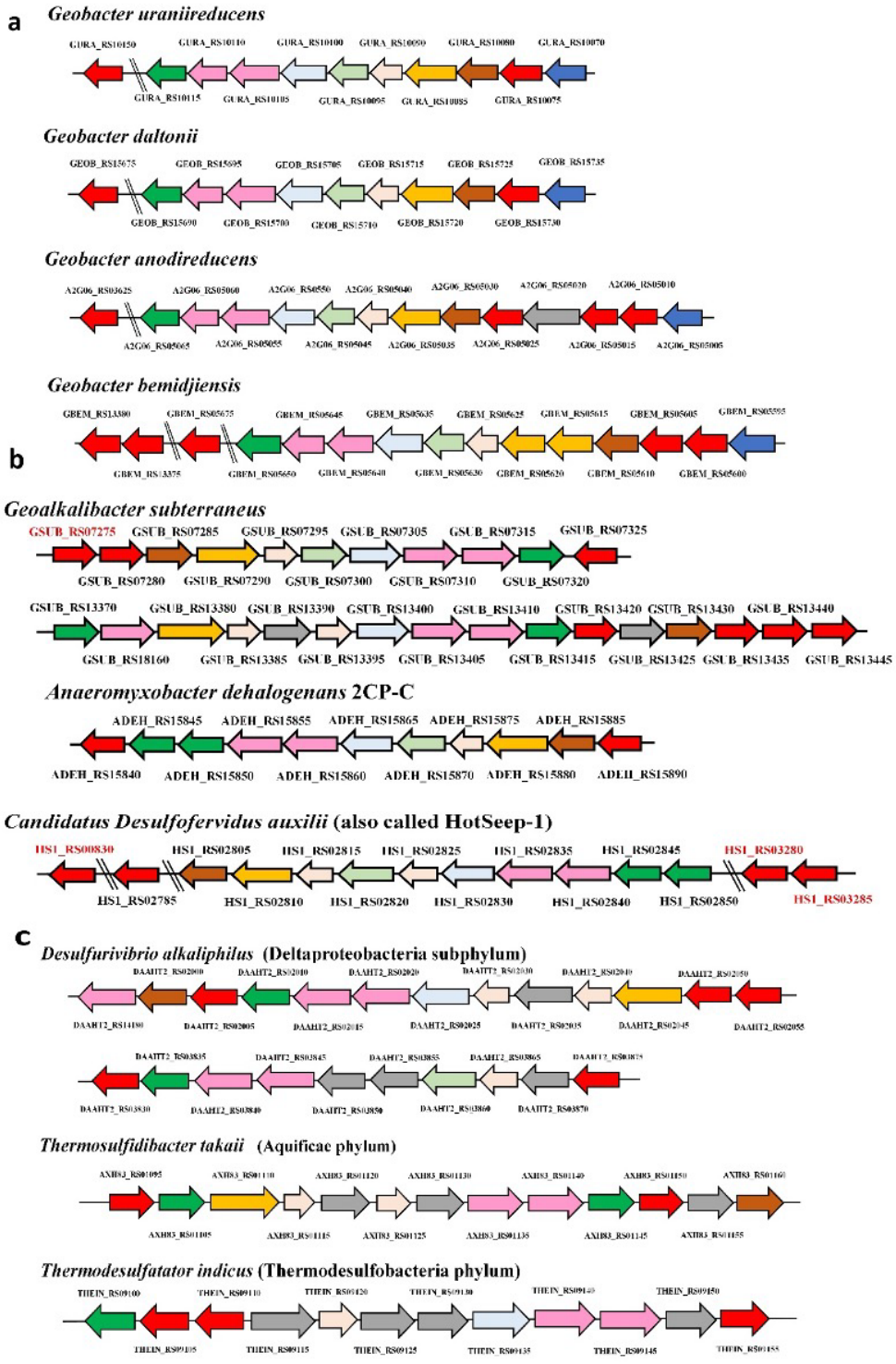

Figure 4.2. OmcS homologs and related gene cluster are widespread.

Genomic organization of the *osc* genes surrounding *omcS* in **a**, *Geobacteraceae* and **b**, three key species discussed in this work. **c**, Other bacteria including other phyla, showing *omcS* homolog genes (red) and non-conserved or remote genes (grey). Each gene homolog is shown by the same color among different species. OmcS homologs named in red either form cytochrome filaments or are significantly upregulated in cocultures.

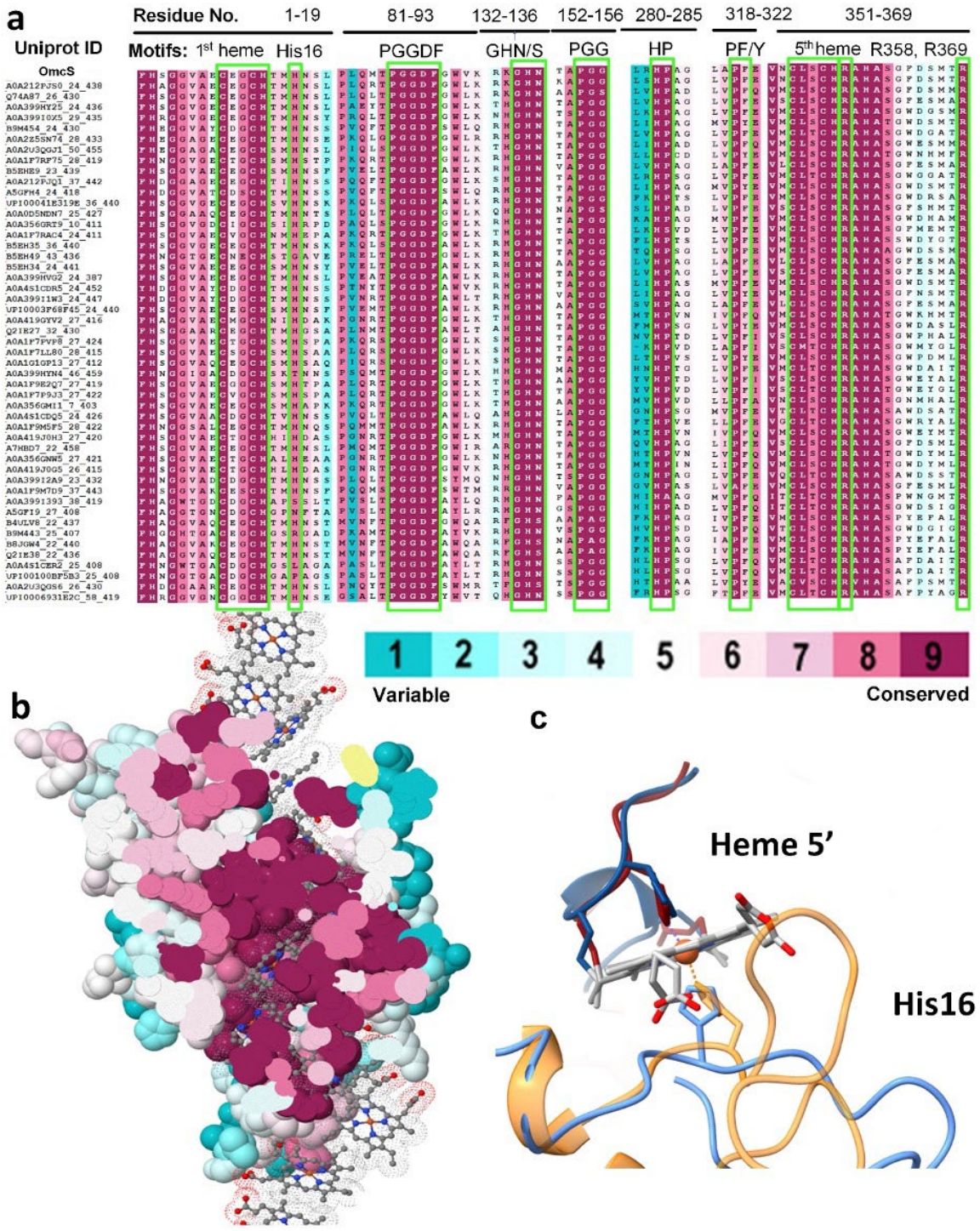

Figure 4.3. Key motifs and residue required for OmcS polymerization are evolutionarily conserved in diverse bacteria.

a, Multiple sequence alignments of OmcS Clade I homologs from UniRef 90 database shows highly-conserved motifs and residues (green boxes). Ten prolines were also highly conserved. **b**, Section view of OmcS protomer structure. **c**, Comparison of the His16 inter-subunit metal interaction between neighbouring subunits of the *G. subterraneus* (blue) and *G. sulfurreducens* OmcS (orange) nanowire structures.

4.3.2 Diverse bacteria use OmcS-like nanowires

To evaluate whether diverse bacteria can assemble OmcS-like nanowires through the action of their *osc* clusters, we focused on two key species: *Geoalkalibacter subterraneus* and *Anaeromyxobacter dehalogenans*. *G. subterraneus* is a thermophile isolated from an oilfield at 1.5 km depth[231] and encodes both Clade I and II *osc* clusters. We found that *G. subterraneus* produces OmcS-like filaments when grown at higher as well as lower temperatures (Figure 4.4A-B). Our mass spectrometry analysis indicated that these filaments are made up of an OmcS homolog protein encoded by gene GSUB_RS07275 (Supplementary Figure 4.2), which is overall ~40% identical in amino acid sequence to *G. sulfurreducens* OmcS.

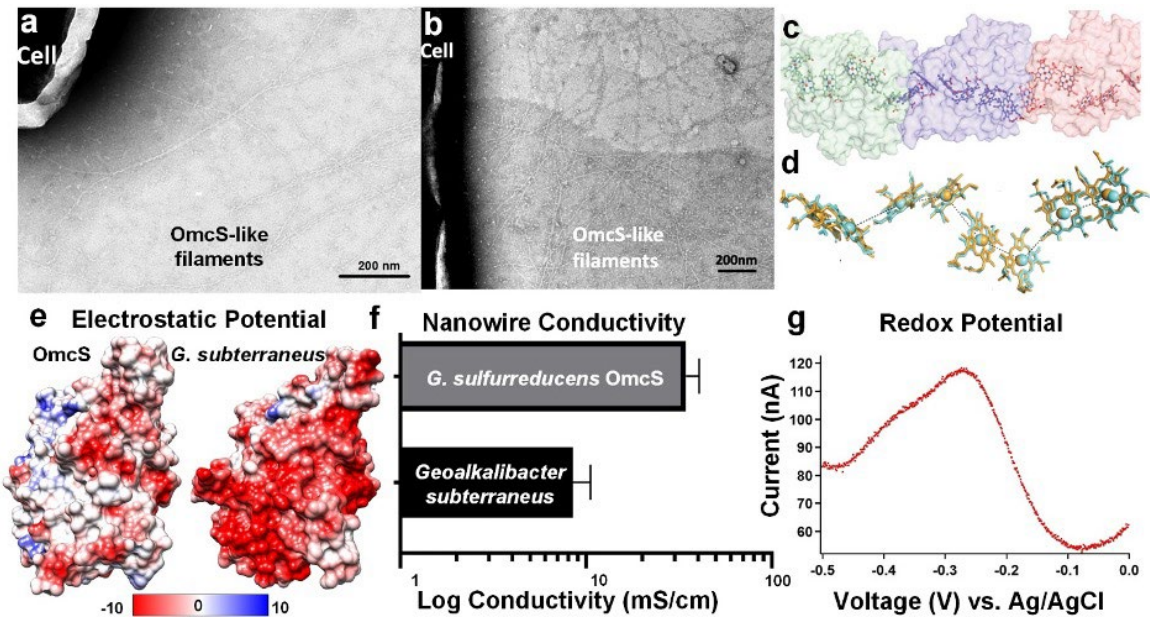

Figure 4.4. Thermophilic *G. subterraneus* shows distinct nanowire structure with different redox properties and electronic conductivity vs. OmcS.

Negatively-stained TEM of *G. subterraneus* cells producing OmcS-like filaments when grown at **a**, 42 °C and **b**, 37 °C. **c**, Cryo-EM structure of *G. subterraneus* nanowires. **d**, Superimposed hemes in cryo-EM structures of *G. subterraneus* (cyan) and OmcS nanowire (orange). **e**, Greater estimated negative surface charge of *G. subterraneus* vs. OmcS at circumneutral pH. **f**, Conductivity of individual nanowires. Error bars, s.d. (n=3). **g**, Differential pulse voltammetry (DPV) characterization of *G. subterraneus* nanowires showing a peak at the midpoint redox potential.

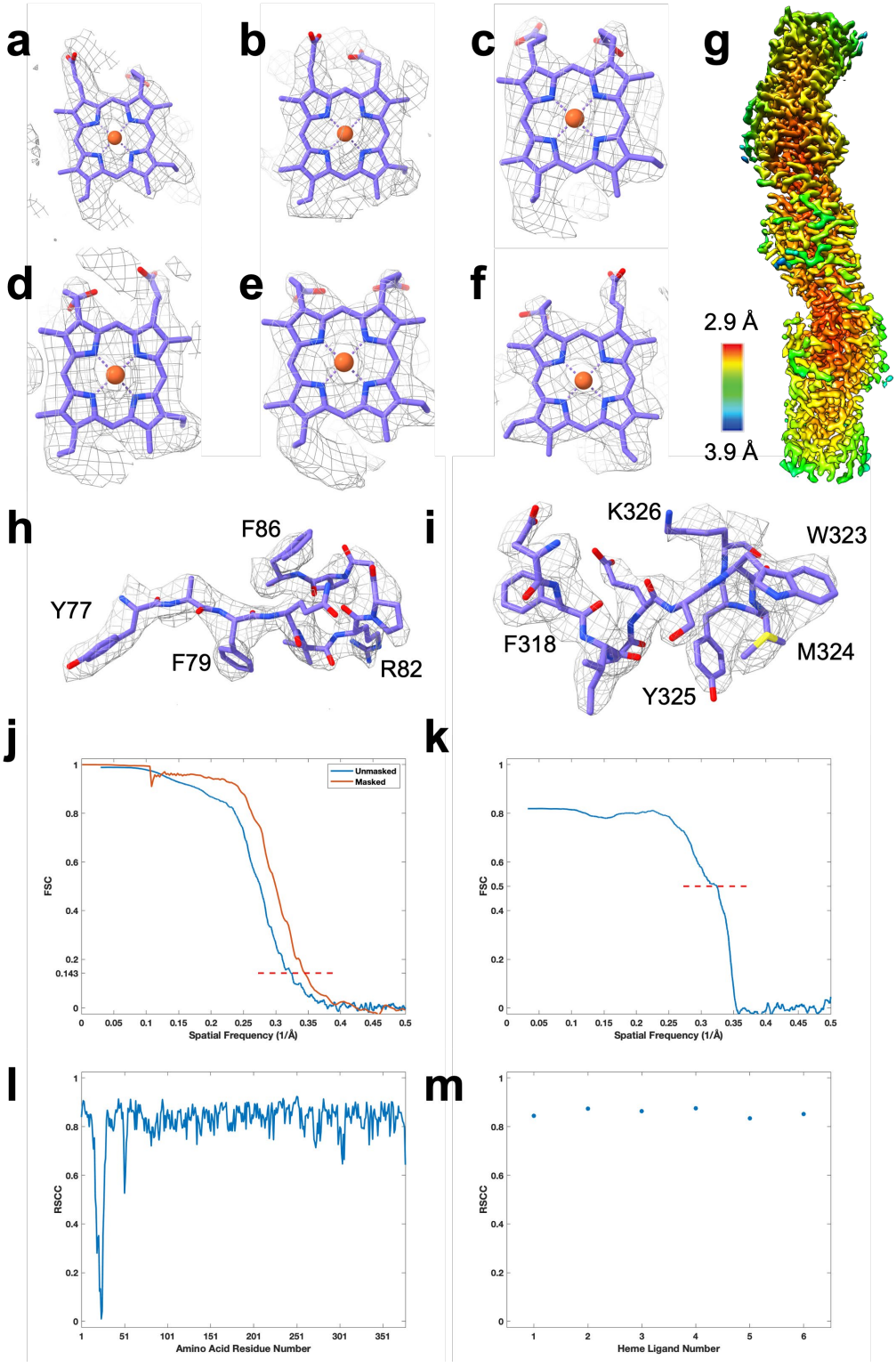

Figure 4.5. Illustration of cryo-EM map quality.

a-**f**, Density fitting of individual heme cofactors. **g**, Resolution distribution of the cryo-EM map. **h**-**i**, Representative density corresponding to sidechains of residues in the model. **j**, Map to map Fourier shell correlation (FSC). **k**, Map to model FSC. **l**, Real space correlation coefficient (RSCC) for amino acid residues in the model. **m**, RSCC for heme ligands in the model.

Table 4.1. Cryo-EM data collection, refinement, and validation statistics for *G. subterraneus* OmcS-like filament.

	OmcS-like Cytochrome Filament from *Geoalkalibacter subterraneus* (EMDB-27398) (PDB 8DET)
Data collection and processing	
Magnification	105,000
Voltage (kV)	300
Electron exposure (e–/Å^2)	49.73
Defocus range (μm)	1.0 – 2.5
Pixel size (Å)	0.828
Symmetry imposed	-79.1°/ 47.4 Å
Initial particle images (no.)	404,877
Final particle images (no.)	84,472
Map resolution (Å)	2.90
FSC threshold	0.143
Map resolution range (Å)	2.9 – 4.4
Refinement	
Initial model used (PDB code)	N/A
Model resolution (Å)	3.10
FSC threshold	0.5
Model resolution range (Å)	N/A
Map sharpening *B* factor (Å^2)	-59.7715
Model composition	
Non-hydrogen atoms	9,060
Protein residues	1,131
Ligands	24
B factors (Å^2)	
Protein	N/A
Ligand	N/A
R.m.s. deviations	
Bond lengths (Å)	0.008
Bond angles (°)	1.004
Validation	
MolProbity score	2.01
Clashscore	14.26
Poor rotamers (%)	0
Ramachandran plot	
Favored (%)	94.93
Allowed (%)	5.07
Disallowed (%)	0

We obtained a 3.1 Å resolution cryo-EM map for purified *G. subterraneus* nanowires using iterative helical real space reconstruction (Figure 4.4C, Figure 4.5, Table 4.1, Figure 4.6E). Although the helical symmetry of these filaments was slightly different than OmcS[53] (helical rise 47.4 Å vs. 46.7 Å for OmcS, helical twist -79.1° vs -83.1° for OmcS), the stacking of hemes was similar to OmcS, forming a continuous

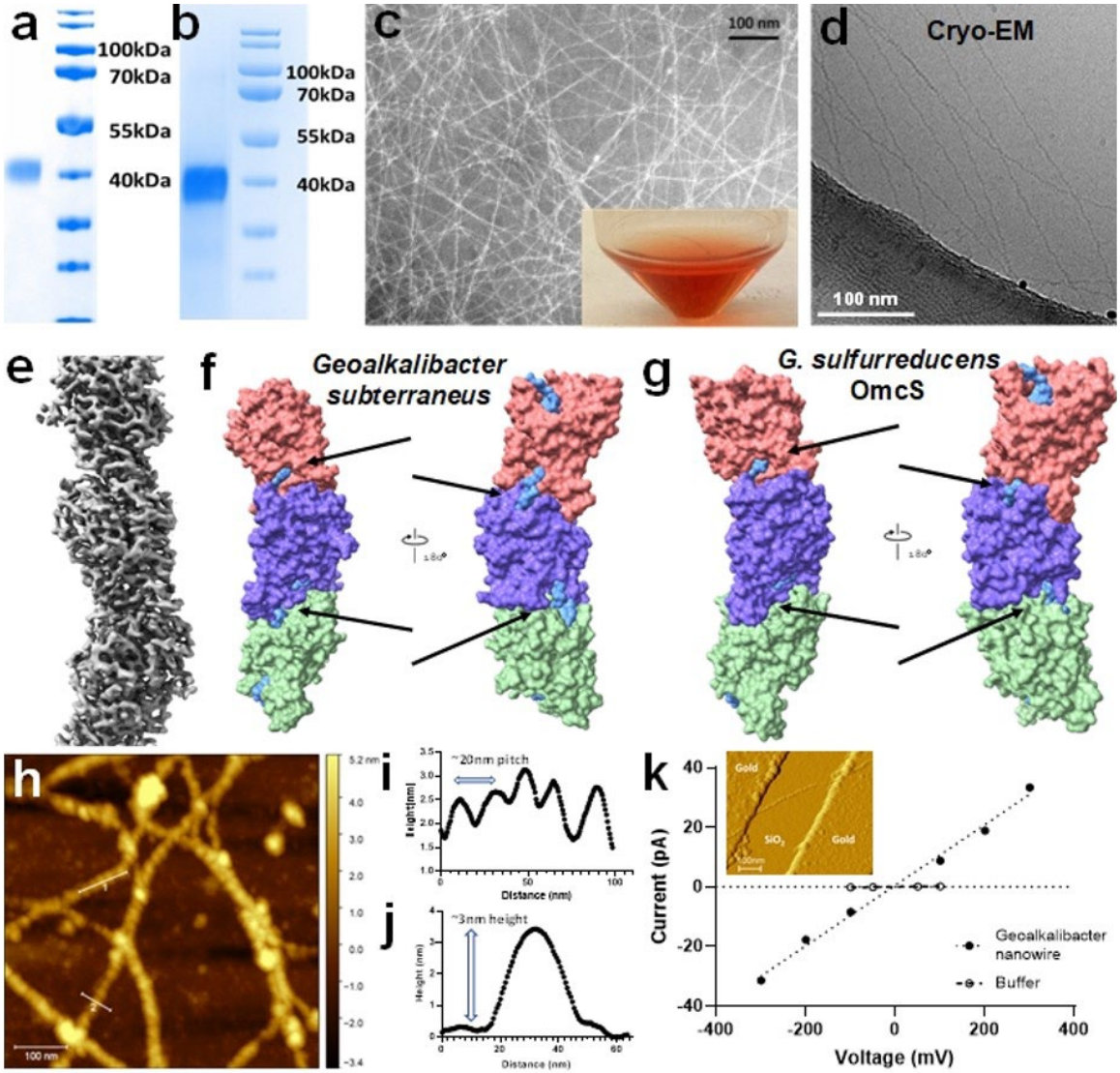

Figure 4.6. Thermophilic *G. subterraneus* shows distinct nanowire structure with varied electronic conductivity.

a, Coomassie-stained gel, **b**, heme-stained gel **c**, Negative-stain TEM **d**, cryo-EM image and **e**, electron density map of purified *G. subterraneus* nanowires. Inset in **c**, nanowire solution. Surface exposure of hemes (blue) in **f**, *G. subterraneus* and **g**, OmcS nanowires. **h**, AFM height images of *G. subterraneus* nanowires with corresponding **i**, axial and **j,** lateral height profiles **k,** Representative current-voltage profile of *G. subterraneus* nanowires. Inset: AFM phase image of a nanowire bridging the non-conductive gap across gold electrodes.

chain (Figure 4.4D). Similar to OmcS, *G. subterraneus* nanowires showed relatively few helices (22%) and beta strands (5%).

Notably, *G. subterraneus* nanowires also showed inter-subunit metal coordination via His16, further highlighting its importance in the polymerization (Figure 4.3C). However, there were important structural differences between OmcS and *G. subterraneus* nanowires. G. *subterraneus* nanowires showed higher surface exposure of hemes (71% vs. 57% for OmcS) (Figure 4.6F-G). *G. subterraneus* nanowires also showed less buried positive charge than OmcS due to the presence of glutamate and tyrosine, near an arginine pair, forming a salt bridge and a cation-pi interaction, respectively. The surface loops also diverged by ~30%. Furthermore, *G. subterraneus* nanowires showed a larger pocket on their surface (5400 $Å^3$ vs. 4800 $Å^3$ for OmcS). The surface charge of the *G. subterraneus* protomer forming the nanowires was substantially different from that of the OmcS protomer (Figure 4.4E, net charge of -25 vs. -3 for OmcS; pI of 4.9 vs. 7.1 for OmcS). This negatively charged patch, larger pockets, and higher heme exposure on the *G. subterraneus* nanowire surface could be physiologically important to bind cationic electron acceptors.

To evaluate the effect of these structural differences on functional properties, we compared the electronic conductivity and redox potential of *G. subterraneus* nanowires to OmcS. We found that individual *G. subterraneus* nanowires show substantially lower conductivity than OmcS (~8.5 mS/cm vs. 35 mS/cm for OmcS) (Figure 4.4F, Figure 4.6K, Supplementary Figure 4.3). The midpoint redox potential of hemes of *G. subterraneus* nanowires was also substantially more positive than that of the OmcS monomer (ca. -73 mV vs. SHE, compared to -212 mV for OmcS[49]). As most periplasmic cytochromes show redox potentials ca. -130 mV vs. SHE[232], our results suggest that *G. subterraneus* nanowires could accept electrons from periplasmic electron carriers. Therefore, our studies could explain *G. subterraneus*' ability for EET to iron oxide and manganese oxide[231], and for EET to electrodes to generate high current densities (4.7 A/m^2)[233], which requires EET over multiple cell lengths by forming thick, conductive biofilms[32, 234]. These differences between biophysical and structural properties of OmcS and *G. subterraneus* nanowires might play important roles in the two bacterial species' growth and adaptation in diverse environments.

Next, we evaluated nanowires formed by *A. dehalogenans*, which is a rod-shaped, spore-forming species capable of EET for use in bioremediation of toxic metals[235, 236] and compounds[237]. We found that *A. dehalogenans* produces OmcS-like filaments on cell surfaces with helical symmetry akin to conductive OmcS nanowires[53] (helical rise 48.1 Å vs. 46.7 Å for OmcS, helical twist -88° vs -83.1° for OmcS) (Figure 4.7A-C). Consistent with this structure, we found that *A. dehalogenans* can generate electricity through EET to electrodes (Figure 4.7D). In contrast, *Desulfovibrio ferrophilus* lacks the *osc* cluster, and produced no OmcS-like nanowires for EET even when its OmcS-homolog was highly expressed[238]. These results suggest that the *osc* cluster is required for the biogenesis and secretion of OmcS-like nanowires by diverse species.

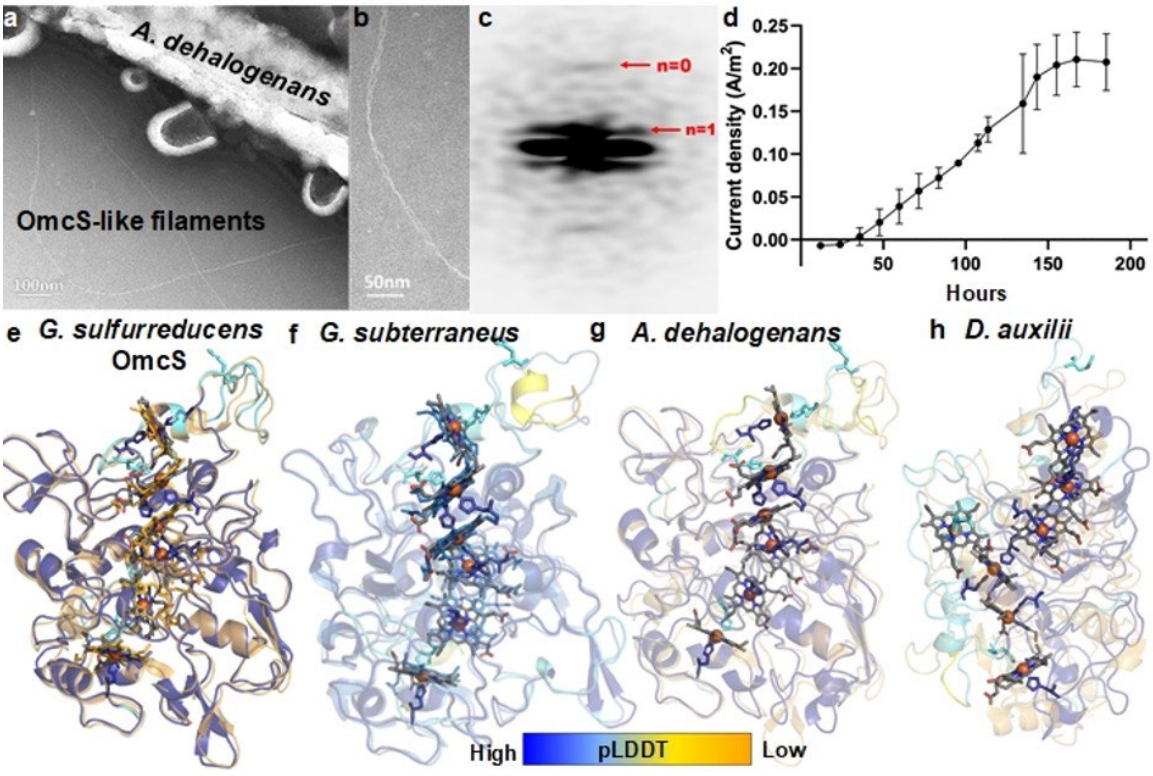

Figure 4.7. *A. dehalogenans* produces electricity and OmcS -like filaments.

a-**b**, Negative-staining TEM images showing *A. dehalogenans* produces OmcS-like filaments. **c**, Power spectra analysis of *A. dehalogenans* OmcS-like filaments suggests filament rise ~48 Å and pitch ~200 Å. **d**, Electricity produced by *A. dehalogenans*. **e**, *G. sulfurreducens* cryo-EM structure (brown) and **f**, *G. subterraneus* cryo-EM structure (cyan) superimposed with AlphaFold predicted models (blue-yellow), showing good agreement. **g**, *A. dehalogenans* and **h**, *Candidatus* D. auxilii, predicted protomers compared with cryo-EM structure of *G. sulfurreducens* OmcS.

4.4 Discussion

In addition to *G. sulfurreducens* and *G. subterraneus*, we found that *Candidatus* Desulfofervidus auxilii (also called HotSeep-1) also shows an *osc* cluster. Notably, HotSeep-1 is a syntrophic DIET-performing partner of methanotrophic archaea; this DIET process protects the Earth from the methane released from ocean sediments[10, 228]. HotSeep-1 contains four copies of OmcS homologs and a complete set of the *osc* cluster (Figure 4.2B). Three homologs were overexpressed up to ~600-fold during DIET with methanotrophic archaea[228, 239].

To evaluate if this protein could form an OmcS-like structure, we first used AlphaFold[240] to compare the accuracy of the predicted models of *G. sulfurreducens* OmcS and *G. subterraneus* nanowires. Remarkably, both models show good agreement with the cryo-EM structures (RMSD 1.13 Å for OmcS, 1.84 Å for *G. subterraneus*), validating our methodology (Figure 4.7E-F). Next, we built models of OmcS homologs in *A. dehalogenans* and HotSeep-1 (gene HS1_RS03280) which showed high structural identity to nanowire-forming OmcS (Figure 4.7G-H). As methane is the most abundant hydrocarbon and highly potent greenhouse gas that affects Earth's atmosphere, our results suggest that diverse microbes could be using OmcS-like nanowires for globally important processes, such as regulating atmospheric methane levels. OmcS nanowires could explain the ability of these microbes to transfer electrons rapidly at rates too fast for molecular diffusion[228, 241] .

Our bioinformatic analyses did not show evidence of any recent horizontal transfers of the *osc* genes, suggesting that nanowire assembly machinery and its persistence could be an ancient and conserved feature (Figure 4.8). The *osc* cluster exhibits sporadic distribution on phylogenetic trees constructed based on comparisons of "housekeeping" proteins. Within the *Geobacter* genus itself, only a fraction of genomes contains OmcS homologs. Although this suggests that OmcS nanowires and the *osc* cluster may have spread to these organisms via horizontal gene transfer, we found that the GC content of *osc* cluster exhibits no difference from the corresponding genome backgrounds, even for species with genomic GC content >70% (*A. dehalogenans*) or < 40% (HotSeep-1). Therefore, our analysis suggests that in contrast to *Geobacter* pili[73], OmcS-like nanowires could be a widespread and ancient adaptation for bacterial survival via EET and DIET in environments that lack oxygen-like soluble electron

acceptors. Our work thus suggests the prevalence of potential nanowire-mediated EET and DIET systems across diverse species and environments.

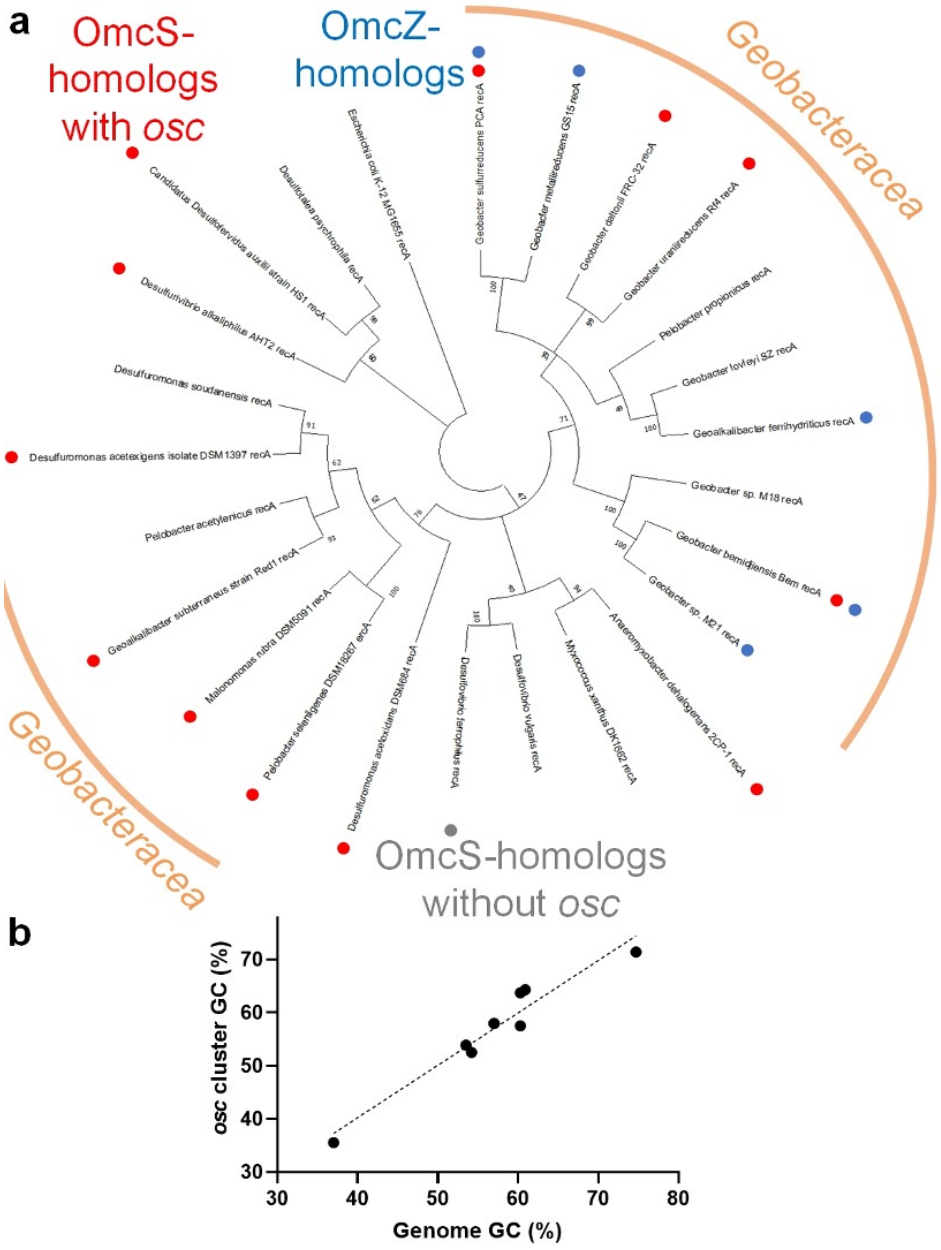

Figure 4.8. *osc* cluster is widespread and ancient.

a, OmcS homologs and the *osc* cluster exhibit sporadic distribution on a phylogenetic tree. Within the *Geobacter* genus, only some published genomes have OmcS homologs. Other species outside the *Geobacter* genus that encode OmcS homologs are phylogenetically distant from each other. **b**, The GC contents of the *osc* cluster exhibits no difference from the genome backgrounds of the species encoding them, even for species with genomic GC content over 70% (*A. dehalogenans*) or below 40% (*Candidatus* D. auxilii).

4.5 Methods

4.5.1 Bacterial strains and culture conditions

Geobacter sulfurreducens strain CL-1[48] (ΔGSU1240 on lab PCA strain background) and strain Δ*pilA-N*[68] (based on PCA strain background) were obtained from our laboratory culture collection. Strain CL-1 constantly expresses OmcS filaments in NBAF liquid culture and is used as a positive control in this study. Other deletion mutants (*oscEFGH* & *omcS* deletions) and their complementations based on the CL-1 strain were constructed in this study. As previously described[53, 166], all *G. sulfurreducens* liquid cultures were kept in sterilized and degassed NBAF medium at 30 °C under strictly anaerobic conditions in the dark. 10 mM acetate was used as an electron donor, 40 mM fumarate was used as an electron acceptor, and 1 mM cysteine was added as an oxygen scavenger. *G. subterraneus* (DSMZ 29995) was purchased from DSMZ and cultured at 37 °C under strictly anaerobic conditions in the dark with DSMZ Medium 1249. *A. dehalogenans* 2CP-C (BAA-259) was purchased from ATCC and cultured at 30 °C under strictly anaerobic conditions in the dark with ATCC Medium 2282.

4.5.2 Bioinformatic analyses

Protein sequences of OmcS homologs were obtained from the NCBI Non-Redundant (NR) database, filtering for sequences with an e-value < 1e-5 and coverage of more than 70%. The ConSurf server and Uniref90 database were used for multiple sequence alignments and conservation mapping to OmcS structure[242]. Phylogeny trees of OmcS homologs and the housekeeping gene *recA* were constructed by maximum likelihood method using Mega-X software[101]. The homologs of the *osc* cluster were revealed by local protein-protein BLAST search[243, 244] against the local protein database from OmcS homolog-containing bacteria, filtering for sequences with e-value < 1e-5. Multi-sequence alignments of OscG homologs were constructed using Mega-X software[101]. Gene expression data for Figure 4.1C and HotSeep-1 coculture under DIET conditions are analyzed and summarized from transcriptome data of previous publications.

4.5.3 Reverse-transcription PCR

20 mL of late-exponential stage cultures of *G. sulfurreducens* cells were harvested and saved in RNAprotect (Qiagen) and frozen at -80 °C. Cells were lysed with 200 µL TE buffer pH 8.0 supplemented

with 320 μg/ml lysozyme and 100 μg/ml proteinase K. RNeasy Mini Kit (Qiagen) was used for RNA extraction. Contaminant DNA was removed using a TURBO DNA-free kit (Invitrogen). cDNA first strands were synthesized using a SuperScript First-Strand Synthesis System for RT-PCR kit (Invitrogen). In order to probe the operon structure of the *osc* cluster, the intergenic regions of the *osc* cluster from genomic DNA, cDNA from extracted RNA, and no-reverse-transcriptase-control were amplified by PCR.

4.5.4 Negative-staining transmission electron microscopy and power spectrum analysis

CF400-CU grids (Electron Microscopy Sciences) were first plasma-cleaned at low power for 40 seconds, then the samples containing filament proteins or bacteria were drop-cast onto the grids and allowed to adsorb to the grid surface for 5 minutes. Excess liquid was removed using filter paper, and then the grids were floated on top of 50 μL droplets of a 1% phosphotungstic acid solution (pH adjusted to 7), with the carbon side facing the liquid, staining for 2 minutes for protein samples or 30 seconds for bacterial samples. Then, the excess staining solution was removed using filter paper and the grids were allowed to air-dry before imaging in TEM. TEM images were taken with a JEM-1400 series (JEOL) microscope located on Yale West Campus operating at 80 kV. Segments from TEM images with the same pixel size were pooled for power spectrum analysis. e2helixboxer.py implemented in EMAN2[245] was used for picking segments along the OmcS-like filaments. The boxed filaments were further segmented into particles with 384-pixel size in SPRING[110]. The averaged power spectrum was generated based on the picked particles by using segmentexam implemented in SPRING.

4.5.5 Atomic force microscopy imaging

Atomic force microscopy experiments were conducted with soft cantilevers (OMCL-AC240TS-R3, OLYMPUS) whose nominal force constant is 2 N/m and resonance frequencies is 70 kHz. Asylum Research software was used for the calibration of the tips' free-air amplitude and the thermal vibration method was used for the capture of spring constant. AC-air topography mode was used to image samples with a Cypher ES scanner. For the imaging of whole cells, 20 μL of diluted cultures were added on a mica surface, washed with DI water, and air-dried overnight. For the imaging of individual filaments, 5 μL of diluted filament preparations were added onto a 300-nm silicon dioxide dielectric layer patterned with gold electrodes by electron beam lithography and air-dried overnight. AFM

imaging proved that individual filaments bridged gold electrodes and preconditioned conductivity measurements. For the visualization of helical features, attractive force imaging mode was used, and height and phase channels were both reported for axial periodicity. Gwyddion[117] software was utilized for height analyses of filaments.

4.5.6 Conductivity measurements

Measurements of direct current were conducted on nanofabricated gold electrodes with a 300 nm gap. AFM was used to inspect individual filaments across the electrodes and to determine the number of filaments contacting the electrodes. Later, a probe station connected to a Keithley 4200A-SCS parameter analyzer was used for I-V measurements of filaments bridging the electrodes. At each fixed voltage, to reduce faradic currents, a stable level of currents was maintained, and the average value was calculated after 1 minute waiting period. To efficiently reduce ionic current from buffer, 20 mM bis-tris buffer was used[166]. The current was measured within a physiologically-related and linear-response voltage range (< 300 mV). By fitting the measured I-V curve with a linear function, the observed conductance (G) was extracted and converted into conductivity (σ) by using the relationship $\sigma = G(L/\pi r^2)$, where r is the radius of the filaments recorded from AFM and L is the gap distance across two gold electrodes[32].

4.5.7 Mass spectrometry

Protein bands on 4-20% gradient SDS-PAGE gel stained with SimplyBlue (Thermo Scientific) were carefully excised and send to the Mass Spectrometry & Proteomics Resource at Yale University. Filament samples were processed through trypsin digestion and liquid chromatography with tandem mass spectrometry. LC-MS/MS analysis was performed on a Thermo Scientific Q Exactive HF-X equipped with a Waters Acquity M-class UPLC system utilizing a binary solvent system (A: 100% water, 0.1% formic acid; B: 100% acetonitrile, 0.1% formic acid). Proteome Discoverer software (version 2.2.0.388, Thermo Scientific) was used to extract tandem mass spectra and the Mascot algorithm (version 2.6.1, Matrix Science) was used to search in-house against a *G. subterraneus* proteome with methionine oxidation and cysteine carbamidomethylation configured as variable modifications. Searches of normal and decoy databases were operated at 95% confidence level ($p < 0.05$). The validation of MS/MS based

peptide and protein identifications were conducted by Scaffold Q+S (version 4.8.9, Proteome Software). The Scaffold Local FDR algorithm accepted peptide identifications which were established at greater than 95% probability and accepted protein identifications which were established more than 99% probability and contained at least 2 identified peptides[106, 107].

4.5.8 Cryogenic electron microscopy

3 µL of sample containing GSUB_RS07275 filaments purified from *G. subterraneus* were applied to 400 mesh holey carbon Quantifoil gold grids (R 2 µm/2 µm) which had been pre-treated via floating on a 0.1% Triton X-100 detergent as previously described[246]. The grids were then transferred to an FEI Vitrobot Mark IV operating at 22 °C with 100% humidity, which was used to blot the grid for 8 seconds with a blot force of -4 and then plunge-freeze the sample in liquid ethane. Frozen grids were imaged on a Titan Krios G3i+ operating at 300 kV equipped with a K3 detector and utilizing a quantum energy filter with a slit width of 20 eV. Micrographs were recorded with super-resolution mode at 0.828 Å/pixel, with a total dose of ~60 $e^-/Å^2$ fractioned into 50 frames. A target defocus range of 1 µm – 2.5 µm was used to collect ~7300 images in total. Movies were motion-corrected utilizing MotionCorr implemented in RELION 3.0.8[108] and the CTF of the motion-corrected images was estimated using GCTF v1.10 [109]. Using a box size of 480 pixels, filament segments were first manually picked to generated a reliable 2D classification, which was then used as a template for RELION auto-picking; after subsequent 2D classification, ~400,000 particles were used for initial 3D helical reconstruction using a starting reference generated from the 2D classes using RELION 3.1[247] and estimates of the helical symmetry (helical rise ~49 Å, helical twist ~78 °). Multiple rounds of 3D refinement of the reconstruction and helical symmetry parameters combined with 3D classification, followed by CTF refinement and Bayesian polishing yielded a map with RELION-reported resolution of 2.9 Å (gold-standard map:map FSC) from a total of ~80,000 filament segment images. The model of the mature GSUB_RS07275 sequence, including six covalently bound heme moieties, was manually built in this map using Coot[248] and refined using Phenix[249] to obtain the final model.

4.5.9 Microbial fuel cells

Microbial fuel cells were operated following methods described previously[23, 77]. A glass fuel cell was constructed with both anode and cathode chambers, separated by a Nafion 117 proton exchange membrane (Electrolytica). Sanded graphite electrodes with dimensions of 1 x 3 x 0.5 inches were used as the anode and cathode. For each chamber, the medium volume was about 150 mL. 20 mM acetate was used as electron donor and 40 mM fumarate was used as electron acceptor in the early stages of fuel cell growth. Bacteria were inoculated into the anode chamber, with potential poised at +300 mV vs AgCl/Ag. The fuel cells were operated in a dark environment at 25 or 32 °C, with constant sparging of 80:20 N_2/CO_2 gas mix in the fuel cell chambers.

4.5.10 Differential pulse voltammetry

Platinum wire with 0.5 mm diameter served as the counter electrode while an Electrolytica C-925 1 mm (Ag/AgCl with 3.4 M KCl) served as the reference electrode. The reference was compared to a standard before each use. DPV scans were performed using a Gamry 1000B potentiostat. All DPV was performed from 0.4 to -0.7 V with a step size of 1 mV, sample period of 0.5 seconds, pulse size of 25 mV and pulse time of 0.1 seconds in an anaerobic glove box. The platinum counter electrode was freshly cut or cleaned in 0.5M H_2SO_4, identically to the gold electrodes before use, by holding 2.04 V for 5 seconds, -0.31 V for 10 seconds, followed by cyclic voltammetry from -0.26 V to 1.6 V at 4000 mV/s for 20 cycles then at 100 mV/s for 4 cycles[250]. Electrodes were washed in ethanol, then water, and dried in stream of N_2. 1.5 µL of filament solution was drop-cast onto the device and air-dried overnight before measurement. The electrolyte in all cases was 50 mM KH_2PO_4,100 mM KCl at pH 7, sparged with N_2 for at least 1 hour and stored in a serum tube to remain anaerobic[251]. Anodic and cathodic scans were analyzed for each sample. Peak fitting and statistical analysis were performed using MATLAB[252] scripts utilizing the EzyFit[253] and peakfit[254] modules for DPV result. Each DPV curve was fit with an unconstrained Gaussian and the peak center was reported as the midpoint. All Ag/AgCl potentials were converted to SHE by adding +200 mV.

4.5.11 Filament preparation

Filament preparations were collected following methods described previously[53], with minor modifications. 300 mL of *G. sulfurreducens* culture were collected in 50 mL Falcon tubes and spun at 2500 x *g* for 15 minutes. The supernatant was decanted, and tubes containing culture were inverted for 15 minutes to remove the remaining liquid. Then, the whole cell wet weights were measured and used to normalize loading volume of samples for subsequent SDS-PAGE analysis. The cell pellets were resuspended in 150 mM ethanolamine pH10.5, and the cell suspension was then blended in a Waring commercial blender at low speed for 2 minutes. A 30 minute-long 13000 x *g* centrifugation was used to remove the bacterial cells debris. Then, a 1 hour-long 23000 x *g* centrifugation was used to remove the remaining impurities. 12.5% v/v of a saturated ammonium sulfate solution was added, the sample was incubated at 4 °C overnight, and then cytochrome filaments were precipitated via another 1 hour-long 13000 x *g* centrifugation. The resulting red pellets were carefully resuspended in 500 µL 150 mM ethanolamine pH 10.5. The same method was applied to produce filament preparations from both *G. subterraneus* and *A. dehalogenans*.

4.5.12 Sodium dodecyl sulfate–polyacrylamide gel electrophoresis and heme staining gels

After boiling in 1x Laemmli Sample buffer (Bio-Rad) with 2.5% β-mercaptoethanol for 12 minutes, the protein samples were run on 4-20% gradient SDS-PAGE gels (Bio-Rad). The electrophoresis was powered by PowerPac Basic (Bio-Rad) at 190 V for 35 minutes. PageRuler Prestained Protein Standard (Thermo Scientific) was used to evaluate molecular weights. Standard SDS-PAGE gels were stained in GelCode Blue Safe Protein Stain (Thermo Scientific) for 1 hour and de-stained in deionized water overnight. For heme staining, under dark conditions, 4-20% gradient SDS-PAGE gels were soaked in a mixture of 35 mL 0.5 M sodium acetate (pH 5.0) and 15 mL methanol with 30 mg TMBZ (3,3,5,5-tetramethylbenzidine) thoroughly dissolved. 300 µL of H_2O_2 was added after 3-5 minutes. Heme containing bands turned blue after another 5 minutes[255, 256].

4.5.13 AlphaFold prediction of OmcS and OmcS-homolog structures

AlphaFold[240] was downloaded and installed from https://github.com/deepmind/alphafold. For the prediction of OmcS homologs, the sequences were downloaded from NCBI. The signaling peptide was

predicted by SignalP 6.0[257] online server and removed from the sequence based on the prediction. Then the sequences were used as input for AlphaFold prediction without use of templates; 5 models were generated for each sequence. The top ranked models, based on the model confidence generated by the program, were used for all the subsequent analysis. Hemes were then manually built inside the model structure based on the predicted heme binding motifs. The heme arrangement in the models was obtained based on the position of cysteines and histidines that form heme binding motif. A PyMOL[258] command "pair_fit" was used to insert hemes in the AlphaFold structure which showed a good agreement with the cryo-EM structure. The backbone RMSD for conserved residues, in comparing AlphaFold models to cryo-EM structures, was computed using the "align" command in PyMOL.

4.6 Acknowledgements

We thank A. Goodman, C. Roy, J. Liu, G. Brudvig and R. Jain for discussions; E. Martz for comparing cryo-EM structures of cytochrome filaments and critical reading of the manuscript; D. Bond for providing the plasmids and genetic protocols; D. Lovley, K. Inoue for providing strains; J. Neu for device fabrication; J. Kanyo for help with mass spectrometry analysis; the Biophysics Resource of Keck Laboratory at Yale School of Medicine for DLS; the W. M. Keck Foundation Biotechnology Resource Laboratory Mass Spectrometry & Proteomics Resource for mass spectrum data collection and analyses; Yale West Campus Imaging Core for AFM and TEM imaging; Yale Center for Genome Analysis for whole genome sequencing and analyses of in-frame deletion mutants. High-resolution cryo-EM data collection was performed at the Case Western Reserve University Cryo-Electron Microscopy Core facility with the assistance of Kunpeng Li and Sudha Chakrapani. This research was supported by NSF CAREER award no. 1749662 (to N.S.M.) and NIH Training Grant T32 GM007223 (supporting V.S.).

4.7 Appendix

The following pages contain the supplementary information accompanying the portions of the manuscript discussed within this chapter.

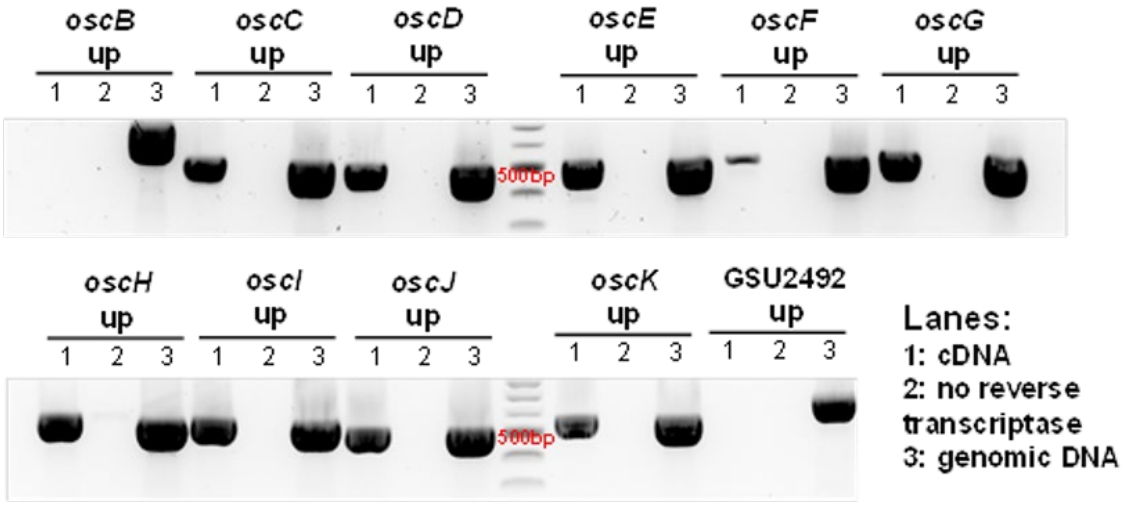

Supplementary Figure 4.1. *oscB* to *oscK* in the *osc* cluster form an intact operon and are upregulated alongside *omcS*.

All tested regions are intergenic regions between two open reading frames; only the name of the gene at the 3′ end of the region is listed, e.g., the intergenic region between *oscB* and *oscC* is denoted as "*oscC* up". Three conditions are shown for each tested region: (1) cDNA, (2) control reaction with no reverse transcriptase, (3) control reaction with genomic DNA. Bands in the included DNA marker are separated by 100 bp. The most intense band within the marker is 500 bp in size.

a

Gene ID	MW(kDa)	Total Spectrum Count		Total Spectrum Coverage	
		Semi Trypsin	Trypsin	Semi Trypsin	Trypsin
GSUB_RS07275	42	352	204	53%	26%
GSUB_RS15870	50	16	21	24%	28%
GSUB_RS14695	29	7	9	41%	48%

b

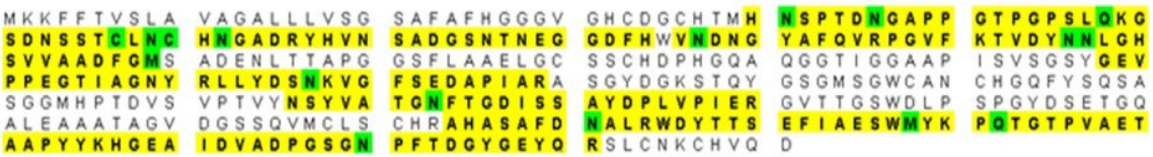

Supplementary Figure 4.2. Mass spectrometry confirms the identity of OmcS-like filaments from *G. subterraneus*.

a, Spectral counts and percent coverage and **b**, sequence coverage mapping from mass spectrometry of purified GSUB_RS07275 filaments.

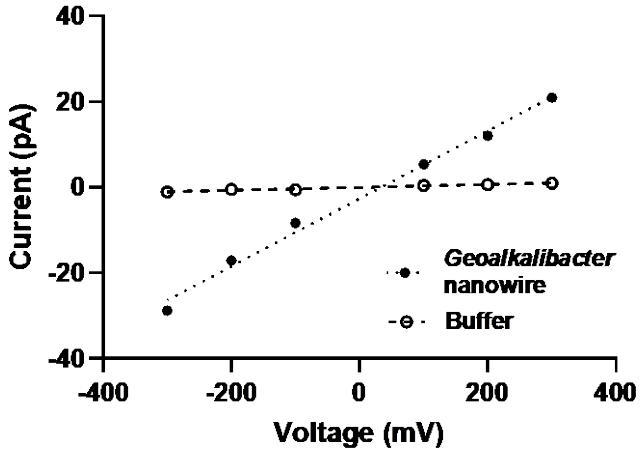

Supplementary Figure 4.3. Representative current-voltage measurements of GSUB_RS07275 filaments from *G. subterraneus*.

I-V curves of GSUB_RS07275 filaments. 4 filaments bridging gold electrodes with 300 nm gap were measured in 20 mM bis-tris buffer.

Supplementary Table 4.1. Summary of gene information in the *osc* cluster.

Summary of *omcS* -related cluster					
Assigned Gene Name	New Gene ID	Old Gene ID	Length (aa)	MW (kDa)*	Annotation
oscA	GS_RS12585	GSU2505	315	33.88	NHL repeat domain-containing protein
		GSUR3014			cyclic dinucleotide responsive riboswitch
omcS	GS_RS12580	GSU2504	432	45.39	6 heme cytochrome
omcT	GS_RS12575	GSU2503	430	45.53	6 heme cytochrome, OmcS homologue
oscB	GS_RS12570	GSU2502	1017	110.54	spermine/spermidine synthase-like protein
oscC	GS_RS12565	GSU2501	437	46.14	6 heme cytochrome, OmcS homologue
oscD	GS_RS12560	GSU3586	482	51.95	YVTN family beta-propeller domain-containing protein
oscE	GS_RS12555	GSU2499	725	80.18	hypothetical protein
oscF	GS_RS12550	GSU2498	199	21.29	lipoprotein
oscG	GS_RS12545	GSU2497	392	43.43	lipoprotein
oscH	GS_RS12540	GSU2496	571	64.64	peptidyl-prolyl cis-trans isomerase
oscI	GS_RS12535	GSU2495	646	69.69	26 heme-binding sites
oscJ	GS_RS12530	GSU2494	426	47.19	16 heme-binding sites **
oscK	GS_RS12525	GSU2493	301	32.37	NHL repeat domain-containing protein
omcJ	GS_RS03500	GSU0701	427	44.36	6 heme cytochrome, OmcS homologue

* These molecular weights are calculated based on the genomic sequence, including any signal peptide, and not including cofactors such as heme *c*.

** A frameshift is found in the updated NCBI gene prediction.

Supplementary Table 4.2. Summary of OmcS homologs in key species.

(a) OmcS homologues of *G. sulfurreducens*								
Locus tag	**Length (aa)**	**MW(kDa)**	**Max Score**	**Query Coverage**	**E value**	**Perc. Ident**	**Protein_ID**	**Note**
omcS	**432**	**45.39**	**857**	**100%**	**0**	**100%**	**WP_010943141.1**	**1)**
omcT	430	45.53	498	94%	4.00E-177	62.98%	WP_010943140.1	
oscC	437	46.13	451	94%	2.00E-158	56.73%	WP_010941362.1	
omcJ	427	44.36	419	93%	1.00E-145	52.66%	WP_010943138.1	

(b) OmcS homologues of *G. subterraneus*								
Locus_tag	**Length (bp)**	**MW (kDa)**	**Max score**	**Query cover**	**E value**	**Perc. ident**	**Protein_ID**	**Note**
GSUB_RS07280	424	44.81	264	95%	3.00E-85	40.48%	WP_052464713.1	
GSUB_RS07275	**401**	**41.68**	**226**	**100%**	**6.00E-71**	**36.72%**	**WP_040199988.1**	**2)**
GSUB_RS07325	341	37.51	170	96%	2.00E-50	32.39%	WP_040199996.1	
GSUB_RS13445	359	37.42	65.9	85%	8.00E-13	24.94%	WP_040201252.1	
GSUB_RS13440	371	39.42	64.7	87%	2.00E-12	22.89%	WP_040201250.1	
GSUB_RS13435	388	40.6	60.8	83%	4.00E-11	24.48%	WP_040201249.1	
GSUB_RS13420	374	39.36	56.2	78%	1.00E-09	24.18%	WP_084212057.1	

(c) OmcS homologues in *A. dehalogenans*								
Locus tag	**Length (aa)**	**MW(kDa)**	**Max Score**	**Query Coverage**	**E value**	**Perc. Ident**	**Protein_ID**	**Note**
A2CP1_RS16400	430	44.16	356	93%	1.00E-120	47.71%	WP_011422115.1	
A2CP1_RS16450	440	45.3	266	99%	1.00E-85	41.32%	WP_015934414.1	

(d) OmcS homologues in *Candidatus D. auxilii* *								
Locus tag	**Length (aa)**	**MW(kDa)**	**Max Score**	**Query Coverage**	**E value**	**Perc. Ident**	**Accession**	**Note**
HS1_RS00830	**348**	**37.6**	**43.1**	**85%**	**1.00E-05**	**23.56%**	**WP_066060288.1**	**3)**
HS1_RS02785	340	37.32	44.3	86%	5.00E-06	23.76%	WP_066060680.1	
HS1_RS03280	**393**	**42.19**	**58.9**	**88%**	**2.00E-10**	**25.69%**	**WP_066060857.1**	**3)**
HS1_RS03285	**380**	**39.81**	**46.2**	**86%**	**2.00E-06**	**23.39%**	**WP_066060859.1**	**3)**

Summary of OmcS homologs in *G. sulfurreducens* (**a**), *G. subterraneus* (**b**), *A. dehalogenans* (**c**) and *Candidatus* D. auxilii (**d**).

Notes:

1) *omcS*-encoded protein forms the known cytochrome nanowire in *G. sulfurreducens*.

2) GSUB_RS07275-encoded protein forms the known cytochrome nanowire in *G. subterraneus*.

3) The genes highlighted in yellow are the significantly upregulated cytochrome genes in *Candidatus* D. auxilii in coculture conditions[10, 228].

* The comparison statistics for *Candidatus* D. auxilii use its homologs in a protein-protein BLAST search against the *G. sulfurreducens* OmcS protein sequence. The statistics used for other species use the *G. sulfurreducens* OmcS protein sequence in a protein-protein BLAST search against the homolog protein sequences from the indicated species.

Conclusions & Future Directions

The order of events in which an OmcS protomer is synthesized, matured, and incorporated into a filament does not depend only on structural factors relating to the OmcS protein itself. Strain Δ*omcS* produces large quantities of PilA-N and PilA-C. Strains such as Δ*omcZ* and Δ*pilA-N:pilA-NC* can display both PilA-N–C filaments and OmcS filaments on the cell surface simultaneously, which could suggest that these two filaments do not directly utilize the same secretion machinery. Other studies have found that amino acid substitutions that affect the formation of OmcS filaments can also result in the display of PilA-N–C filaments on the cell surface[259]. Together, these observations suggest some mechanism by which the protein abundance of PilA proteins and cytochrome filament-forming proteins are co-regulated, a finding further corroborated by other studies[260]. Further understanding could help illuminate the degree to which PilA proteins are indirectly or directly involved in the secretion of cytochrome nanowires.

Disruption of OmcS filaments at a pH sufficiently low to break bis-histidinyl coordination of hemes in OmcS indicates that metal coordination, including inter-subunit metal coordination, is important for the filament structure. The OmcS protomer itself may require metal coordination interactions to maintain its proper structure, especially given that it contains so few defined secondary structure motifs. This low-pH method does not specifically target inter-protomer metal coordination. It might be expected that structural factors such as local electrostatics near the hemes could mean that different hemes in OmcS are more or less susceptible to having their heme metal coordination interactions disrupted at low pH. The depolymerization behavior that we observed appears relatively binary, but it is likely that *in vitro* depolymerization and re-polymerization are dependent on protein concentration and other factors, e.g., ionic strength, that have yet to be fully explored.

In vivo mutations that inhibit OmcS polymerization might also perturb cellular regulation of the maturation and localization of OmcS, which could be intertwined with the cellular processes that control where and how OmcS filaments are assembled. This may be understood as a mechanism of avoiding intracellular polymerization or toxicity due to an excess of free monomers in the periplasm. It is difficult to directly determine whether the mutation destabilizes the OmcS protomer, causing it to be

degraded and thus preventing filament formation, or whether instead the inability of the protomers to polymerize causes them to be targeted for degradation by the cell. This also raises the question of whether *G. sulfurreducens* cells produce any significant amount of 'stable,' mature OmcS monomers, or instead whether OmcS subunits are incorporated into filaments almost immediately following their maturation in the periplasm. Further study will be necessary to address these questions.

Direct observation of OmcS-like filaments in non-*Geobacter* species is an important advance that ties the bioinformatic finding of OmcS homologs in diverse species to observed biological behavior. Similar work of this nature will be needed to understand the function of the OmcS homologs that have not been characterized in such detail. While predicted structures of these OmcS-like proteins suggest they may have features in common with protomers in *G. sulfurreducens* OmcS filaments, it is worth remembering that the three OmcS-like proteins within *G. sulfurreducens* would also be predicted to have such features – yet there is no evidence that those proteins are assembled into extracellular cytochrome filaments. This suggests that not only structural, but also other biological factors – such as specific protein-protein interactions and regulatory mechanisms affecting protein abundance – control the ability of OmcS-like proteins to assemble into filaments.

The discovery of OmcS filaments in *G. sulfurreducens* has been followed by characterization of other cytochrome filaments. However, questions are still being raised about the involvement of OmcS filaments in EET and the relevance of such a mechanism within and beyond *Geobacter* species. Further understanding of how metabolic electrons are transferred to cytochrome filaments involved in EET may bring added clarity. In *G. sulfurreducens*, these pathways could involve both periplasmic cytochromes and membrane-embedded cytochrome complexes; the interactions of these proteins with nanowire-forming cytochromes will need to be investigated further. Such studies would also be capitalizing on *G. sulfurreducens*' utility as a model system. OmcS-like filaments may be found to directly facilitate important EET processes in diverse bacterial species, but characterization of these filaments' function in a biological context will remain critically important to the next generation of studies.

References

1. Gray, H.B. and Winkler, J.R. Electron flow through metalloproteins. *Biochim Biophys Acta* **1797**, 1563-72 (2010).

2. Torres, C.I., Marcus, A.K., Lee, H.S., Parameswaran, P., Krajmalnik-Brown, R. and Rittmann, B.E. A kinetic perspective on extracellular electron transfer by anode-respiring bacteria. *FEMS Microbiol Rev* **34**, 3-17 (2010).

3. Lovley, D.R. Dissimilatory Fe(III) and Mn(IV) reduction. *Microbiol Rev* **55**, 259-87 (1991).

4. Lovley, D.R. Syntrophy Goes Electric: Direct Interspecies Electron Transfer. *Annu Rev Microbiol* **71**, 643-664 (2017).

5. Reguera, G., McCarthy, K.D., Mehta, T., Nicoll, J.S., Tuominen, M.T. and Lovley, D.R. Extracellular electron transfer via microbial nanowires. *Nature* **435**, 1098-101 (2005).

6. Gorby, Y.A., Yanina, S., McLean, J.S., Rosso, K.M., Moyles, D., Dohnalkova, A., Beveridge, T.J., Chang, I.S., Kim, B.H., Kim, K.S., Culley, D.E., Reed, S.B., Romine, M.F., Saffarini, D.A., Hill, E.A., Shi, L., Elias, D.A., Kennedy, D.W., Pinchuk, G., Watanabe, K., Ishii, S., Logan, B., Nealson, K.H. and Fredrickson, J.K. Electrically conductive bacterial nanowires produced by *Shewanella oneidensis* strain MR-1 and other microorganisms. *Proc Natl Acad Sci U S A* **103**, 11358-63 (2006).

7. Meysman, F.J.R. Cable Bacteria Take a New Breath Using Long-Distance Electricity. *Trends in Microbiology* **26**, 411-422 (2018).

8. Nealson, K.H. and Saffarini, D. Iron and manganese in anaerobic respiration: environmental significance, physiology, and regulation. *Annu Rev Microbiol* **48**, 311-43 (1994).

9. Vargas, M., Kashefi, K., Blunt-Harris, E.L. and Lovley, D.R. Microbiological evidence for Fe(III) reduction on early Earth. *Nature* **395**, 65-7 (1998).

10. Chadwick, G.L., Skennerton, C.T., Laso-Perez, R., Leu, A.O., Speth, D.R., Yu, H., Morgan-Lang, C., Hatzenpichler, R., Goudeau, D., Malmstrom, R., Brazelton, W.J., Woyke, T., Hallam, S.J., Tyson, G.W., Wegener, G., Boetius, A. and Orphan, V.J. Comparative genomics reveals electron transfer and syntrophic mechanisms differentiating methanotrophic and methanogenic archaea. *PLoS Biol* **20**, e3001508 (2022).

11. Logan, B.E., Rossi, R., Ragab, A. and Saikaly, P.E. Electroactive microorganisms in bioelectrochemical systems. *Nat Rev Microbiol* **17**, 307-319 (2019).

12. Wang, X., Aulenta, F., Puig, S., Esteve-Núñez, A., He, Y., Mu, Y. and Rabaey, K. Microbial electrochemistry for bioremediation. *Environmental Science and Ecotechnology* **1**, 100013 (2020).

13. Cai, T., Meng, L., Chen, G., Xi, Y., Jiang, N., Song, J., Zheng, S., Liu, Y., Zhen, G. and Huang, M. Application of advanced anodes in microbial fuel cells for power generation: A review. *Chemosphere* **248**, 125985 (2020).

14. Tian, B. and Lieber, C.M. Nanowired Bioelectric Interfaces. *Chem Rev* **119**, 9136-9152 (2019).

15. Su, L., Fukushima, T., Prior, A., Baruch, M., Zajdel, T.J. and Ajo-Franklin, C.M. Modifying Cytochrome *c* Maturation Can Increase the Bioelectronic Performance of Engineered *Escherichia coli*. *ACS Synth Biol* **9**, 115-124 (2020).

16. Tseng, C.P., Silberg, J.J., Bennett, G.N. and Verduzco, R. 100th Anniversary of Macromolecular Science Viewpoint: Soft Materials for Microbial Bioelectronics. *ACS Macro Lett* **9**, 1590-1603 (2020).

17. Lovley, D.R., Ueki, T., Zhang, T., Malvankar, N.S., Shrestha, P.M., Flanagan, K.A., Aklujkar, M., Butler, J.E., Giloteaux, L., Rotaru, A.E., Holmes, D.E., Franks, A.E., Orellana, R., Risso, C. and Nevin, K.P. *Geobacter*: the microbe electric's physiology, ecology, and practical applications. *Adv Microb Physiol* **59**, 1-100 (2011).

18. Childers, S.E., Ciufo, S. and Lovley, D.R. *Geobacter metallireducens* accesses insoluble Fe(III) oxide by chemotaxis. *Nature* **416**, 767-9 (2002).

19. Summers, Z.M., Fogarty, H.E., Leang, C., Franks, A.E., Malvankar, N.S. and Lovley, D.R. Direct exchange of electrons within aggregates of an evolved syntrophic coculture of anaerobic bacteria. *Science* **330**, 1413-5 (2010).

20. Holmes, D.E., Chaudhuri, S.K., Nevin, K.P., Mehta, T., Methe, B.A., Liu, A., Ward, J.E., Woodard, T.L., Webster, J. and Lovley, D.R. Microarray and genetic analysis of electron transfer to electrodes in *Geobacter sulfurreducens*. *Environ Microbiol* **8**, 1805-15 (2006).

21. Dumas, C., Basseguy, R. and Bergel, A. Microbial electrocatalysis with *Geobacter sulfurreducens* biofilm on stainless steel cathodes. *Electrochimica Acta* **53**, 2494-2500 (2008).

22. Caccavo, F., Jr., Lonergan, D.J., Lovley, D.R., Davis, M., Stolz, J.F. and McInerney, M.J. *Geobacter sulfurreducens* sp. nov., a hydrogen- and acetate-oxidizing dissimilatory metal-reducing microorganism. *Appl Environ Microbiol* **60**, 3752-9 (1994).

23. Bond, D.R. and Lovley, D.R. Electricity production by *Geobacter sulfurreducens* attached to electrodes. *Appl Environ Microbiol* **69**, 1548-55 (2003).

24. Coppi, M.V., Leang, C., Sandler, S.J. and Lovley, D.R. Development of a genetic system for *Geobacter sulfurreducens*. *Appl Environ Microbiol* **67**, 3180-7 (2001).

25. Chan, C.H., Levar, C.E., Zacharoff, L., Badalamenti, J.P. and Bond, D.R. Scarless Genome Editing and Stable Inducible Expression Vectors for *Geobacter sulfurreducens*. *Appl Environ Microbiol* **81**, 7178-86 (2015).

26. Nevin, K.P., Richter, H., Covalla, S.F., Johnson, J.P., Woodard, T.L., Orloff, A.L., Jia, H., Zhang, M. and Lovley, D.R. Power output and columbic efficiencies from biofilms of *Geobacter sulfurreducens* comparable to mixed community microbial fuel cells. *Environ Microbiol* **10**, 2505-14 (2008).

27. Ayers, M., Howell, P.L. and Burrows, L.L. Architecture of the type II secretion and type IV pilus machineries. *Future Microbiol* **5**, 1203-18 (2010).

28. Craig, L., Forest, K.T. and Maier, B. Type IV pili: dynamics, biophysics and functional consequences. *Nat Rev Microbiol* **17**, 429-440 (2019).

29. Vargas, M., Malvankar, N.S., Tremblay, P.L., Leang, C., Smith, J.A., Patel, P., Snoeyenbos-West, O., Nevin, K.P. and Lovley, D.R. Aromatic amino acids required for pili conductivity and long-range extracellular electron transport in *Geobacter sulfurreducens*. *mBio* **4**, e00105-13 (2013).

30. Liu, X., Tremblay, P.L., Malvankar, N.S., Nevin, K.P., Lovley, D.R. and Vargas, M. A *Geobacter sulfurreducens* Strain Expressing *Pseudomonas aeruginosa* Type IV Pili Localizes OmcS on Pili but

Is Deficient in Fe(III) Oxide Reduction and Current Production. *Applied and Environmental Microbiology* **80**, 1219-1224 (2014).

31. Tan, Y., Adhikari, R.Y., Malvankar, N.S., Ward, J.E., Woodard, T.L., Nevin, K.P. and Lovley, D.R. Expressing the *Geobacter metallireducens* PilA in *Geobacter sulfurreducens* Yields Pili with Exceptional Conductivity. *mBio* **8**, e02203-16 (2017).

32. Malvankar, N.S., Vargas, M., Nevin, K.P., Franks, A.E., Leang, C., Kim, B.C., Inoue, K., Mester, T., Covalla, S.F., Johnson, J.P., Rotello, V.M., Tuominen, M.T. and Lovley, D.R. Tunable metallic-like conductivity in microbial nanowire networks. *Nat Nanotechnol* **6**, 573-9 (2011).

33. Adhikari, R.Y., Malvankar, N.S., Tuominen, M.T. and Lovley, D.R. Conductivity of individual *Geobacter* pili. *Rsc Advances* **6**, 8363-8366 (2016).

34. Tan, Y., Adhikari, R.Y., Malvankar, N.S., Pi, S., Ward, J.E., Woodard, T.L., Nevin, K.P., Xia, Q., Tuominen, M.T. and Lovley, D.R. Synthetic Biological Protein Nanowires with High Conductivity. *Small* **12**, 4481-5 (2016).

35. Steidl, R.J., Lampa-Pastirk, S. and Reguera, G. Mechanistic stratification in electroactive biofilms of *Geobacter sulfurreducens* mediated by pilus nanowires. *Nat Commun* **7**, 12217 (2016).

36. Liu, X., Zhan, J., Jing, X., Zhou, S. and Lovley, D.R. A pilin chaperone required for the expression of electrically conductive *Geobacter sulfurreducens* pili. *Environ Microbiol* **21**, 2511-2522 (2019).

37. Malvankar, N.S., Vargas, M., Nevin, K., Tremblay, P.L., Evans-Lutterodt, K., Nykypanchuk, D., Martz, E., Tuominen, M.T. and Lovley, D.R. Structural basis for metallic-like conductivity in microbial nanowires. *mBio* **6**, e00084 (2015).

38. Xiao, K., Malvankar, N.S., Shu, C.J., Martz, E., Lovley, D.R. and Sun, X. Low Energy Atomic Models Suggesting a Pilus Structure that could Account for Electrical Conductivity of *Geobacter sulfurreducens* Pili. *Scientific Reports* **6**, 23385 (2016).

39. Ueki, T. Cytochromes in Extracellular Electron Transfer in *Geobacter*. *Appl Environ Microbiol* **87**, e03109-20 (2021).

40. Mehta, T., Coppi, M.V., Childers, S.E. and Lovley, D.R. Outer membrane *c*-type cytochromes required for Fe(III) and Mn(IV) oxide reduction in *Geobacter sulfurreducens*. *Appl Environ Microbiol* **71**, 8634-41 (2005).

41. Nevin, K.P., Kim, B.C., Glaven, R.H., Johnson, J.P., Woodard, T.L., Methe, B.A., Didonato, R.J., Covalla, S.F., Franks, A.E., Liu, A. and Lovley, D.R. Anode biofilm transcriptomics reveals outer surface components essential for high density current production in *Geobacter sulfurreducens* fuel cells. *PLoS One* **4**, e5628 (2009).

42. Malvankar, N.S., Tuominen, M.T. and Lovley, D.R. Lack of cytochrome involvement in long-range electron transport through conductive biofilms and nanowires of *Geobacter sulfurreducens*. *Energy & Environmental Science* **5**, 8651-8659 (2012).

43. Malvankar, N.S., Tuominen, M.T. and Lovley, D.R. Comment on "On electrical conductivity of microbial nanowires and biofilms" by S. M. Strycharz-Glaven, R. M. Snider, A. Guiseppi-Elie and L. M. Tender, Energy Environ. Sci., 2011, 4, 4366. *Energy & Environmental Science* **5**, 6247-6249 (2012).

44. Strycharz-Glaven, S.M., Snider, R.M., Guiseppi-Elie, A. and Tender, L.M. On the electrical conductivity of microbial nanowires and biofilms. *Energy & Environmental Science* **4**, 4366-4379 (2011).

45. Yates, M.D., Strycharz-Glaven, S.M., Golden, J.P., Roy, J., Tsoi, S., Erickson, J.S., El-Naggar, M.Y., Barton, S.C. and Tender, L.M. Measuring conductivity of living *Geobacter sulfurreducens* biofilms. *Nat Nanotechnol* **11**, 910-913 (2016).

46. Voordeckers, J.W., Kim, B.C., Izallalen, M. and Lovley, D.R. Role of *Geobacter sulfurreducens* outer surface *c*-type cytochromes in reduction of soil humic acid and anthraquinone-2,6-disulfonate. *Appl Environ Microbiol* **76**, 2371-5 (2010).

47. Leang, C., Qian, X., Mester, T. and Lovley, D.R. Alignment of the *c*-type cytochrome OmcS along pili of *Geobacter sulfurreducens*. *Appl Environ Microbiol* **76**, 4080-4 (2010).

48. Leang, C., Malvankar, N.S., Franks, A.E., Nevin, K.P. and Lovley, D.R. Engineering *Geobacter sulfurreducens* to produce a highly cohesive conductive matrix with enhanced capacity for current production. *Energy & Environmental Science* **6**, 1901-1908 (2013).

49. Qian, X., Mester, T., Morgado, L., Arakawa, T., Sharma, M.L., Inoue, K., Joseph, C., Salgueiro, C.A., Maroney, M.J. and Lovley, D.R. Biochemical characterization of purified OmcS, a *c*-type cytochrome required for insoluble Fe(III) reduction in *Geobacter sulfurreducens*. *Biochim Biophys Acta* **1807**, 404-12 (2011).

50. Wilson, G.S. Electrochemical studies of porphyrin redox reactions as cytochrome models. *Bioelectrochemistry and Bioenergetics* **1**, 172-179 (1974).

51. Marques, H.M., Cukrowski, I. and Vashi, P.R. Co-ordination of weak field ligands by N-acetylmicroperoxidase-8 (NAcMP8), a ferric haempeptide from cytochrome *c*, and the influence of the axial ligand on the reduction potential of complexes of NAcMP8†. *Journal of the Chemical Society, Dalton Transactions* 1335-1342 (2000).

52. Battistuzzi, G., Borsari, M., Cowan, J.A., Ranieri, A. and Sola, M. Control of cytochrome *c* redox potential: axial ligation and protein environment effects. *J Am Chem Soc* **124**, 5315-24 (2002).

53. Wang, F., Gu, Y., O'Brien, J.P., Yi, S.M., Yalcin, S.E., Srikanth, V., Shen, C., Vu, D., Ing, N.L., Hochbaum, A.I., Egelman, E.H. and Malvankar, N.S. Structure of Microbial Nanowires Reveals Stacked Hemes that Transport Electrons over Micrometers. *Cell* **177**, 361-369 e10 (2019).

54. Filman, D.J., Marino, S.F., Ward, J.E., Yang, L., Mester, Z., Bullitt, E., Lovley, D.R. and Strauss, M. Cryo-EM reveals the structural basis of long-range electron transport in a cytochrome-based bacterial nanowire. *Commun Biol* **2**, 219 (2019).

55. Lovley, D.R. and Walker, D.J.F. *Geobacter* Protein Nanowires. *Front Microbiol* **10**, 2078 (2019).

56. Lovley, D.R. On the Existence of Pilin-Based Microbial Nanowires. *Front Microbiol* **13**, 872610 (2022).

57. Lovley, D.R. Microbial nanowires. *Current Biology* **32**, R110-R112 (2022).

58. Margoliash, E. and Lustgarten, J. Interconversion of horse heart cytochrome *c* monomer and polymers. *J Biol Chem* **237**, 3397-405 (1962).

59. Hirota, S., Hattori, Y., Nagao, S., Taketa, M., Komori, H., Kamikubo, H., Wang, Z.H., Takahashi, I., Negi, S., Sugiura, Y., Kataoka, M. and Higuchi, Y. Cytochrome *c* polymerization by successive

domain swapping at the C-terminal helix. *Proceedings of the National Academy of Sciences of the United States of America* **107**, 12854-12859 (2010).

60. Hayashi, Y., Yamanaka, M., Nagao, S., Komori, H., Higuchi, Y. and Hirota, S. Domain swapping oligomerization of thermostable *c*-type cytochrome in *E. coli* cells. *Sci Rep* **6**, 19334 (2016).

61. Hirota, S. Oligomerization of cytochrome *c*, myoglobin, and related heme proteins by 3D domain swapping. *J Inorg Biochem* **194**, 170-179 (2019).

62. Yalcin, S.E., O'Brien, J.P., Gu, Y., Reiss, K., Yi, S.M., Jain, R., Srikanth, V., Dahl, P.J., Huynh, W., Vu, D., Acharya, A., Chaudhuri, S., Varga, T., Batista, V.S. and Malvankar, N.S. Electric field stimulates production of highly conductive microbial OmcZ nanowires. *Nat Chem Biol* **16**, 1136-1142 (2020).

63. Yalcin, S.E. and Malvankar, N.S. The blind men and the filament: Understanding structures and functions of microbial nanowires. *Curr Opin Chem Biol* **59**, 193-201 (2020).

64. Michel, G.P. and Voulhoux, R. The type II secretory system (T2SS) in Gram-negative bacteria: a molecular nanomachine for secretion of Sec and Tat-dependent extracellular proteins. *Bacterial secreted proteins: secretory mechanisms and role in pathogenesis* 67-92 (2009).

65. Nivaskumar, M. and Francetic, O. Type II secretion system: a magic beanstalk or a protein escalator. *Biochim Biophys Acta* **1843**, 1568-77 (2014).

66. McCallum, M., Burrows, L.L. and Howell, P.L. The Dynamic Structures of the Type IV Pilus. *Microbiol Spectr* **7**, 7.2. 02 (2019).

67. Reguera, G., Nevin, K.P., Nicoll, J.S., Covalla, S.F., Woodard, T.L. and Lovley, D.R. Biofilm and nanowire production leads to increased current in *Geobacter sulfurreducens* fuel cells. *Appl Environ Microbiol* **72**, 7345-8 (2006).

68. Richter, L.V., Sandler, S.J. and Weis, R.M. Two Isoforms of *Geobacter sulfurreducens* PilA Have Distinct Roles in Pilus Biogenesis, Cytochrome Localization, Extracellular Electron Transfer, and Biofilm Formation. *Journal of Bacteriology* **194**, 2551-2563 (2012).

69. Liu, X., Zhuo, S., Rensing, C. and Zhou, S. Syntrophic growth with direct interspecies electron transfer between pili-free *Geobacter* species. *ISME J* **12**, 2142-2151 (2018).

70. Lebedev, N., Mahmud, S., Griva, I., Blom, A. and Tender, L.M. On the electron transfer through *Geobacter sulfurreducens* PilA protein. *Journal of Polymer Science Part B: Polymer Physics* **53**, 1706-1717 (2015).

71. Yan, H., Chuang, C., Zhugayevych, A., Tretiak, S., Dahlquist, F.W. and Bazan, G.C. Inter-aromatic distances in *Geobacter sulfurreducens* pili relevant to biofilm charge transport. *Adv Mater* **27**, 1908-11 (2015).

72. Ru, X., Zhang, P. and Beratan, D.N. Assessing Possible Mechanisms of Micrometer-Scale Electron Transfer in Heme-Free *Geobacter sulfurreducens* Pili. *J Phys Chem B* **123**, 5035-5047 (2019).

73. Holmes, D.E., Dang, Y., Walker, D.J.F. and Lovley, D.R. The electrically conductive pili of *Geobacter* species are a recently evolved feature for extracellular electron transfer. *Microb Genom* **2**, e000072 (2016).

74. Richter, L.V. Mutational analysis of geopilin function in *Geobacter sulfurreducens*. *University of Massachusetts Amherst* (2011).

75. Shu, C., Xiao, K., Yan, Q. and Sun, X. Comparative Analysis of Type IV Pilin in *Desulfuromonadales*. *Front Microbiol* **7**, 2080 (2016).

76. Pasek, S., Risler, J.L. and Brezellec, P. Gene fusion/fission is a major contributor to evolution of multi-domain bacterial proteins. *Bioinformatics* **22**, 1418-1423 (2006).

77. O'Brien, J.P. and Malvankar, N.S. A Simple and Low-Cost Procedure for Growing *Geobacter sulfurreducens* Cell Cultures and Biofilms in Bioelectrochemical Systems. *Curr Protoc Microbiol* **43**, A 4K 1-A 4K 27 (2016).

78. Wang, E., Sun, H., Wang, J., Wang, Z., Liu, H., Zhang, J.Z.H. and Hou, T. End-Point Binding Free Energy Calculation with MM/PBSA and MM/GBSA: Strategies and Applications in Drug Design. *Chem Rev* **119**, 9478-9508 (2019).

79. Vignon, G., Kohler, R., Larquet, E., Giroux, S., Prevost, M.C., Roux, P. and Pugsley, A.P. Type IV-like pili formed by the type II secreton: specificity, composition, bundling, polar localization, and surface presentation of peptides. *J Bacteriol* **185**, 3416-28 (2003).

80. Durand, E., Michel, G., Voulhoux, R., Kurner, J., Bernadac, A. and Filloux, A. XcpX controls biogenesis of the *Pseudomonas aeruginosa* XcpT-containing pseudopilus. *J Biol Chem* **280**, 31378-89 (2005).

81. Wang, F., Coureuil, M., Osinski, T., Orlova, A., Altindal, T., Gesbert, G., Nassif, X., Egelman, E.H. and Craig, L. Cryoelectron Microscopy Reconstructions of the *Pseudomonas aeruginosa* and *Neisseria gonorrhoeae* Type IV Pili at Sub-nanometer Resolution. *Structure* **25**, 1423-1435 e4 (2017).

82. Richter, L.V., Franks, A.E., Weis, R.M. and Sandler, S.J. Significance of a Posttranslational Modification of the PilA Protein of *Geobacter sulfurreducens* for Surface Attachment, Biofilm Formation, and Growth on Insoluble Extracellular Electron Acceptors. *J Bacteriol* **199**, e00716-16 (2017).

83. Parge, H.E., Forest, K.T., Hickey, M.J., Christensen, D.A., Getzoff, E.D. and Tainer, J.A. Structure of the fibre-forming protein pilin at 2.6 Å resolution. *Nature* **378**, 32-38 (1995).

84. Harvey, H., Bondy-Denomy, J., Marquis, H., Sztanko, K.M., Davidson, A.R. and Burrows, L.L. *Pseudomonas aeruginosa* defends against phages through type IV pilus glycosylation. *Nature Microbiology* **3**, 47-52 (2018).

85. Vik, Å., Aspholm, M., Anonsen, J.H., Børud, B., Roos, N. and Koomey, M. Insights into type IV pilus biogenesis and dynamics from genetic analysis of a C-terminally tagged pilin: a role for O-linked glycosylation. *Molecular microbiology* **85**, 1166-1178 (2012).

86. Craig, L., Pique, M.E. and Tainer, J.A. Type IV pilus structure and bacterial pathogenicity. *Nat Rev Microbiol* **2**, 363-78 (2004).

87. Lopez-Castilla, A., Thomassin, J.L., Bardiaux, B., Zheng, W., Nivaskumar, M., Yu, X., Nilges, M., Egelman, E.H., Izadi-Pruneyre, N. and Francetic, O. Structure of the calcium-dependent type 2 secretion pseudopilus. *Nat Microbiol* **2**, 1686-1695 (2017).

88. Li, J., Egelman, E.H. and Craig, L. Structure of the *Vibrio cholerae* Type IVb Pilus and stability comparison with the *Neisseria gonorrhoeae* type IVa pilus. *J Mol Biol* **418**, 47-64 (2012).

89. Shipps, C., Kelly, H.R., Dahl, P.J., Yi, S.M., Vu, D., Boyer, D., Glynn, C., Sawaya, M.R., Eisenberg, D., Batista, V.S. and Malvankar, N.S. Intrinsic electronic conductivity of individual atomically

resolved amyloid crystals reveals micrometer-long hole hopping via tyrosines. *Proc Natl Acad Sci U S A* **118**, e2014139118 (2021).

90. Inoue, K., Qian, X., Morgado, L., Kim, B.C., Mester, T., Izallalen, M., Salgueiro, C.A. and Lovley, D.R. Purification and characterization of OmcZ, an outer-surface, octaheme *c*-type cytochrome essential for optimal current production by *Geobacter sulfurreducens*. *Appl Environ Microbiol* **76**, 3999-4007 (2010).

91. Cosert, K.M., Castro-Forero, A., Steidl, R.J., Worden, R.M. and Reguera, G. Bottom-Up Fabrication of Protein Nanowires via Controlled Self-Assembly of Recombinant *Geobacter* Pilins. *mBio* **10**, e02721-19 (2019).

92. Ueki, T., Walker, D.J.F., Tremblay, P.L., Nevin, K.P., Ward, J.E., Woodard, T.L., Nonnenmann, S.S. and Lovley, D.R. Decorating the Outer Surface of Microbially Produced Protein Nanowires with Peptides. *ACS Synth Biol* **8**, 1809-1817 (2019).

93. Ueki, T., Walker, D.J.F., Woodard, T.L., Nevin, K.P., Nonnenmann, S.S. and Lovley, D.R. An *Escherichia coli* Chassis for Production of Electrically Conductive Protein Nanowires. *ACS Synth Biol* **9**, 647-654 (2020).

94. Mehta, T., Childers, S.E., Glaven, R., Lovley, D.R. and Mester, T. A putative multicopper protein secreted by an atypical type II secretion system involved in the reduction of insoluble electron acceptors in *Geobacter sulfurreducens*. *Microbiology (Reading)* **152**, 2257-2264 (2006).

95. Shi, L., Deng, S., Marshall, M.J., Wang, Z., Kennedy, D.W., Dohnalkova, A.C., Mottaz, H.M., Hill, E.A., Gorby, Y.A., Beliaev, A.S., Richardson, D.J., Zachara, J.M. and Fredrickson, J.K. Direct involvement of type II secretion system in extracellular translocation of *Shewanella oneidensis* outer membrane cytochromes MtrC and OmcA. *J Bacteriol* **190**, 5512-6 (2008).

96. Bouhenni, R.A., Vora, G.J., Biffinger, J.C., Shirodkar, S., Brockman, K., Ray, R., Wu, P., Johnson, B.J., Biddle, E.M. and Marshall, M.J. The role of *Shewanella oneidensis* MR-1 outer surface structures in extracellular electron transfer. *Electroanalysis: An International Journal Devoted to Fundamental and Practical Aspects of Electroanalysis* **22**, 856-864 (2010).

97. Liu, X., Ye, Y., Xiao, K., Rensing, C. and Zhou, S. Molecular evidence for the adaptive evolution of *Geobacter sulfurreducens* to perform dissimilatory iron reduction in natural environments. *Mol Microbiol* **113**, 783-793 (2020).

98. Hager, A.J., Bolton, D.L., Pelletier, M.R., Brittnacher, M.J., Gallagher, L.A., Kaul, R., Skerrett, S.J., Miller, S.I. and Guina, T. Type IV pili-mediated secretion modulates *Francisella* virulence. *Mol Microbiol* **62**, 227-37 (2006).

99. Koebnik, R. The role of bacterial pili in protein and DNA translocation. *Trends Microbiol* **9**, 586-90 (2001).

100. Tan, Y., Adhikari, R.Y., Malvankar, N.S., Ward, J.E., Nevin, K.P., Woodard, T.L., Smith, J.A., Snoeyenbos-West, O.L., Franks, A.E., Tuominen, M.T. and Lovley, D.R. The Low Conductivity of *Geobacter uraniireducens* Pili Suggests a Diversity of Extracellular Electron Transfer Mechanisms in the Genus *Geobacter*. *Front Microbiol* **7**, 980 (2016).

101. Kumar, S., Stecher, G., Li, M., Knyaz, C. and Tamura, K. MEGA X: Molecular Evolutionary Genetics Analysis across Computing Platforms. *Mol Biol Evol* **35**, 1547-1549 (2018).

102. Guindon, S., Dufayard, J.F., Lefort, V., Anisimova, M., Hordijk, W. and Gascuel, O. New algorithms and methods to estimate maximum-likelihood phylogenies: assessing the performance of PhyML 3.0. *Syst Biol* **59**, 307-21 (2010).

103. Lefort, V., Longueville, J.E. and Gascuel, O. SMS: Smart Model Selection in PhyML. *Mol Biol Evol* **34**, 2422-2424 (2017).

104. Yu, G.C., Smith, D.K., Zhu, H.C., Guan, Y. and Lam, T.T.Y. GGTREE: an R package for visualization and annotation of phylogenetic trees with their covariates and other associated data. *Methods in Ecology and Evolution* **8**, 28-36 (2017).

105. Team, R.C. R: A language and environment for statistical computing. (2013).

106. Shevchenko, A., Tomas, H., Havlis, J., Olsen, J.V. and Mann, M. In-gel digestion for mass spectrometric characterization of proteins and proteomes. *Nat Protoc* **1**, 2856-60 (2006).

107. Cox, J. and Mann, M. MaxQuant enables high peptide identification rates, individualized ppb-range mass accuracies and proteome-wide protein quantification. *Nature Biotechnology* **26**, 1367-1372 (2008).

108. Zivanov, J., Nakane, T., Forsberg, B.O., Kimanius, D., Hagen, W.J., Lindahl, E. and Scheres, S.H. New tools for automated high-resolution cryo-EM structure determination in RELION-3. *Elife* **7**, e42166 (2018).

109. Zhang, K. Gctf: Real-time CTF determination and correction. *J Struct Biol* **193**, 1-12 (2016).

110. Desfosses, A., Ciuffa, R., Gutsche, I. and Sachse, C. SPRING - an image processing package for single-particle based helical reconstruction from electron cryomicrographs. *J Struct Biol* **185**, 15-26 (2014).

111. He, S. and Scheres, S.H.W. Helical reconstruction in RELION. *J Struct Biol* **198**, 163-176 (2017).

112. Egelman, E.H. The iterative helical real space reconstruction method: surmounting the problems posed by real polymers. *J Struct Biol* **157**, 83-94 (2007).

113. Zivanov, J., Nakane, T. and Scheres, S.H.W. A Bayesian approach to beam-induced motion correction in cryo-EM single-particle analysis. *IUCrJ* **6**, 5-17 (2019).

114. Pettersen, E.F., Goddard, T.D., Huang, C.C., Couch, G.S., Greenblatt, D.M., Meng, E.C. and Ferrin, T.E. UCSF Chimera--a visualization system for exploratory research and analysis. *J Comput Chem* **25**, 1605-12 (2004).

115. Emsley, P. and Cowtan, K. Coot: model-building tools for molecular graphics. *Acta Crystallogr D Biol Crystallogr* **60**, 2126-32 (2004).

116. Afonine, P.V., Poon, B.K., Read, R.J., Sobolev, O.V., Terwilliger, T.C., Urzhumtsev, A. and Adams, P.D. Real-space refinement in *PHENIX* for cryo-EM and crystallography. *Acta Crystallogr D Struct Biol* **74**, 531-544 (2018).

117. Nečas, D. and Klapetek, P. Gwyddion: an open-source software for SPM data analysis. *Open Phys* **10**, 181-188 (2012).

118. Gray, H.B. and Winkler, J.R. Electron tunneling through proteins. *Q Rev Biophys* **36**, 341-72 (2003).

119. Dempsey, J.L. and Hartings, M.R. Hop to It. *Biochemistry* **56**, 5623-5624 (2017).

120. Reguera, G. Biological electron transport goes the extra mile. *Proc Natl Acad Sci U S A* **115**, 5632-5634 (2018).

121. El-Naggar, M.Y., Wanger, G., Leung, K.M., Yuzvinsky, T.D., Southam, G., Yang, J., Lau, W.M., Nealson, K.H. and Gorby, Y.A. Electrical transport along bacterial nanowires from *Shewanella oneidensis* MR-1. *Proc Natl Acad Sci U S A* **107**, 18127-31 (2010).

122. Pfeffer, C., Larsen, S., Song, J., Dong, M., Besenbacher, F., Meyer, R.L., Kjeldsen, K.U., Schreiber, L., Gorby, Y.A., El-Naggar, M.Y., Leung, K.M., Schramm, A., Risgaard-Petersen, N. and Nielsen, L.P. Filamentous bacteria transport electrons over centimetre distances. *Nature* **491**, 218-21 (2012).

123. Bjerg, J.T., Boschker, H.T.S., Larsen, S., Berry, D., Schmid, M., Millo, D., Tataru, P., Meysman, F.J.R., Wagner, M., Nielsen, L.P. and Schramm, A. Long-distance electron transport in individual, living cable bacteria. *Proc Natl Acad Sci U S A* **115**, 5786-5791 (2018).

124. Meysman, F.J.R., Cornelissen, R., Trashin, S., Bonne, R., Martinez, S.H., van der Veen, J., Blom, C.J., Karman, C., Hou, J.L., Eachambadi, R.T., Geelhoed, J.S., Wael, K., Beaumont, H.J.E., Cleuren, B., Valcke, R., van der Zant, H.S.J., Boschker, H.T.S. and Manca, J.V. A highly conductive fibre network enables centimetre-scale electron transport in multicellular cable bacteria. *Nat Commun* **10**, 4120 (2019).

125. Kjeldsen, K.U., Schreiber, L., Thorup, C.A., Boesen, T., Bjerg, J.T., Yang, T., Dueholm, M.S., Larsen, S., Risgaard-Petersen, N., Nierychlo, M., Schmid, M., Boggild, A., van de Vossenberg, J., Geelhoed, J.S., Meysman, F.J.R., Wagner, M., Nielsen, P.H., Nielsen, L.P. and Schramm, A. On the evolution and physiology of cable bacteria. *Proc Natl Acad Sci U S A* **116**, 19116-19125 (2019).

126. Myers, C.R. and Nealson, K.H. Bacterial manganese reduction and growth with manganese oxide as the sole electron acceptor. *Science* **240**, 1319-21 (1988).

127. Nealson, K.H., Belz, A. and McKee, B. Breathing metals as a way of life: geobiology in action. *Antonie Van Leeuwenhoek* **81**, 215-22 (2002).

128. Gralnick, J.A. and Newman, D.K. Extracellular respiration. *Mol Microbiol* **65**, 1-11 (2007).

129. Kowalchuk, G.A., Jones, S.E. and Blackall, L.L. Microbes orchestrate life on Earth. *ISME J* **2**, 795-6 (2008).

130. Shi, L., Dong, H.L., Reguera, G., Beyenal, H., Lu, A.H., Liu, J., Yu, H.Q. and Fredrickson, J.K. Extracellular electron transfer mechanisms between microorganisms and minerals. *Nature Reviews Microbiology* **14**, 651-662 (2016).

131. Snider, R.M., Strycharz-Glaven, S.M., Tsoi, S.D., Erickson, J.S. and Tender, L.M. Long-range electron transport in *Geobacter sulfurreducens* biofilms is redox gradient-driven. *Proc Natl Acad Sci U S A* **109**, 15467-72 (2012).

132. Clarke, T.A. and Edwards, M.J. Uncovering nature's electronics. *Nat Chem Biol* **16**, 1041-1042 (2020).

133. Jiang, X., van Wonderen, J.H., Butt, J.N., Edwards, M.J., Clarke, T.A. and Blumberger, J. Which Multi-Heme Protein Complex Transfers Electrons More Efficiently? Comparing MtrCAB from *Shewanella* with OmcS from *Geobacter*. *J Phys Chem Lett* **11**, 9421-9425 (2020).

134. Someya, T., Bao, Z. and Malliaras, G.G. The rise of plastic bioelectronics. *Nature* **540**, 379-385 (2016).

135. Wallace, C.J. and Clark-Lewis, I. Functional role of heme ligation in cytochrome *c*. Effects of replacement of methionine 80 with natural and non-natural residues by semisynthesis. *J Biol Chem* **267**, 3852-61 (1992).

136. Waleed Shinwari, M., Jamal Deen, M., Starikov, E.B. and Cuniberti, G. Electrical Conductance in Biological Molecules. *Advanced Functional Materials* **20**, 1865-1883 (2010).

137. Balakrishnan, G., Hu, Y. and Spiro, T.G. His26 protonation in cytochrome *c* triggers microsecond beta-sheet formation and heme exposure: implications for apoptosis. *J Am Chem Soc* **134**, 19061-9 (2012).

138. Coelho, A.V., Matias, P., Fülöp, V., Thompson, A., Gonzalez, A. and Carrondo, M.A. Desulfoferrodoxin structure determined by MAD phasing and refinement to 1.9-Å resolution reveals a unique combination of a tetrahedral FeS_4 centre with a square pyramidal $FeSN_4$ centre. *JBIC Journal of Biological Inorganic Chemistry* **2**, 680-689 (1997).

139. Abreu, I.A., Lourenco, A.I., Xavier, A.V., LeGall, J., Coelho, A.V., Matias, P.M., Pinto, D.M., Armenia Carrondo, M., Teixeira, M. and Saraiva, L.M. A novel iron centre in the split-Soret cytochrome *c* from *Desulfovibrio desulfuricans* ATCC 27774. *J Biol Inorg Chem* **8**, 360-70 (2003).

140. Kolks, G., Frihart, C.R., Coughlin, P.K. and Lippard, S.J. Synthetic, Spectroscopic, and Solution Studies of Imidazolate-Bridged Dicopper(II) Complexes. *Inorganic Chemistry* **20**, 2933-2940 (1981).

141. Strothkamp, K.G. and Lippard, S.J. Chemistry of the imidazolate-bridged bimetallic center in the copper-zinc superoxide dismutase and its model compounds. *Accounts of Chemical Research* **15**, 318-326 (1982).

142. Ikezaki, A. and Nakamura, M. Models for cytochromes *c*': spin states of mono(imidazole)-ligated (meso-tetramesitylporphyrinato)iron(III) complexes as studied by UV-Vis, ^{13}C NMR, ^{1}H NMR, and EPR spectroscopy. *Inorg Chem* **41**, 6225-36 (2002).

143. Blumenthal, D.C. and Kassner, R.J. Azide binding to the cytochrome *c* ferric heme octapeptide. A model for anion binding to the active site of high spin ferric heme proteins. *J Biol Chem* **254**, 9617-20 (1979).

144. Winkler, W.C., Gonzalez, G., Wittenberg, J.B., Hille, R., Dakappagari, N., Jacob, A., Gonzalez, L.A. and Gilles-Gonzalez, M.A. Nonsteric factors dominate binding of nitric oxide, azide, imidazole, cyanide, and fluoride to the rhizobial heme-based oxygen sensor FixL. *Chem Biol* **3**, 841-50 (1996).

145. Erman, J.E., Chinchilla, D., Studer, J. and Vitello, L.B. Binding of imidazole, 1-methylimidazole and 4-nitroimidazole to yeast cytochrome *c* peroxidase (CcP) and the distal histidine mutant, CcP(H52L). *Biochim Biophys Acta* **1854**, 869-81 (2015).

146. Miyashita, Y., Wazawa, T., Mogami, G., Takahashi, S., Sambongi, Y. and Suzuki, M. Hydration-state change of horse heart cytochrome *c* corresponding to trifluoroacetic-acid-induced unfolding. *Biophys J* **104**, 163-72 (2013).

147. Greenfield, N.J. Using circular dichroism spectra to estimate protein secondary structure. *Nat Protoc* **1**, 2876-90 (2006).

148. Santucci, R. and Ascoli, F. The Soret circular dichroism spectrum as a probe for the heme Fe(III)-Met(80) axial bond in horse cytochrome *c*. *Journal of Inorganic Biochemistry* **68**, 211-214 (1997).

149. Pielak, G.J., Oikawa, K., Mauk, A.G., Smith, M. and Kay, C.M. Elimination of the negative soret Cotton effect of cytochrome *c* by replacement of the invariant phenylalanine using site-directed mutagenesis. *Journal of the American Chemical Society* **108**, 2724-2727 (2002).

150. Degli Esposti, M., Palmer, G. and Lenaz, G. Circular dichroic spectroscopy of membrane haemoproteins. The molecular determinants of the dichroic properties of the *b* cytochromes in various ubiquinol:cytochrome *c* reductases. *Eur J Biochem* **182**, 27-36 (1989).

151. Blauer, G., Sreerama, N. and Woody, R.W. Optical activity of hemoproteins in the Soret region. Circular dichroism of the heme undecapeptide of cytochrome *c* in aqueous solution. *Biochemistry* **32**, 6674-9 (1993).

152. Palmer, G. and Degli Esposti, M. Application of exciton coupling theory to the structure of mitochondrial cytochrome *b*. *Biochemistry* **33**, 176-85 (1994).

153. Andersson, K.K., Lipscomb, J.D., Valentine, M., Munck, E. and Hooper, A.B. Tetraheme cytochrome *c*-554 from Nitrosomonas europaea. Heme-heme interactions and ligand binding. *J Biol Chem* **261**, 1126-38 (1986).

154. Vickery, L., Nozawa, T. and Sauer, K. Magnetic circular dichroism studies of myoglobin complexes. Correlations with heme spin state and axial ligation. *J Am Chem Soc* **98**, 343-50 (1976).

155. Peisach, J., Blumberg, W., Ogawa, S., Rachmilewitz, E. and Oltzik, R. The effects of protein conformation on the heme symmetry in high spin ferric heme proteins as studied by electron paramagnetic resonance. *Journal of Biological Chemistry* **246**, 3342-3355 (1971).

156. Brautigan, D.L., Feinberg, B.A., Hoffman, B.M., Margoliash, E., Preisach, J. and Blumberg, W. Multiple low spin forms of the cytochrome *c* ferrihemochrome. EPR spectra of various eukaryotic and prokaryotic cytochromes *c*. *Journal of Biological Chemistry* **252**, 574-582 (1977).

157. Ponomarenko, N., Niklas, J., Pokkuluri, P.R., Poluektov, O. and Tiede, D.M. Electron Paramagnetic Resonance Characterization of the Triheme Cytochrome from Geobacter sulfurreducens. *Biochemistry* **57**, 1722-1732 (2018).

158. da Silva, G.F., Shinkarev, V.P., Kamensky, Y.A. and Palmer, G. Spectroscopic Evidence of the Role of an Axial Ligand Histidinate in the Mechanism of Adrenal Cytochrome b_{561}. *Biochemistry* **51**, 8730-8742 (2012).

159. Blumberg, W.E. and Peisach, J. Low—Spin Compounds of Heme Proteins in *Bioinorganic Chemistry*, 271-291. AMERICAN CHEMICAL SOCIETY (1971).

160. Kleifeld, O., Frenkel, A., Martin, J.M. and Sagi, I. Active site electronic structure and dynamics during metalloenzyme catalysis. *Nat Struct Biol* **10**, 98-103 (2003).

161. Dai, Z. and Boon, E.M. Probing the local electronic and geometric properties of the heme iron center in a H-NOX domain. *J Inorg Biochem* **105**, 784-92 (2011).

162. Della Longa, S., Pin, S., Cortes, R., Soldatov, A.V. and Alpert, B. Fe-heme conformations in ferric myoglobin. *Biophys J* **75**, 3154-62 (1998).

163. Korshin, G.V., Frenkel, A.I. and Stern, E.A. EXAFS study of the inner shell structure in copper(II) complexes with humic substances. *Environmental Science & Technology* **32**, 2699-2705 (1998).

164. D'Angelo, P., Lapi, A., Migliorati, V., Arcovito, A., Benfatto, M., Roscioni, O.M., Meyer-Klaucke, W. and Della-Longa, S. X-ray absorption spectroscopy of hemes and hemeproteins in solution: multiple scattering analysis. *Inorg Chem* **47**, 9905-18 (2008).

165. Smith, D.M., Dupuis, M., Vorpagel, E.R. and Straatsma, T.P. Characterization of electronic structure and properties of a Bis(histidine) heme model complex. *J Am Chem Soc* **125**, 2711-7 (2003).

166. Gu, Y., Srikanth, V., Salazar-Morales, A.I., Jain, R., O'Brien, J.P., Yi, S.M., Soni, R.K., Samatey, F.A., Yalcin, S.E. and Malvankar, N.S. Structure of *Geobacter* pili reveals secretory rather than nanowire behaviour. *Nature* **597**, 430-434 (2021).

167. Liu, X., Gao, H., Ward, J.E., Liu, X., Yin, B., Fu, T., Chen, J., Lovley, D.R. and Yao, J. Power generation from ambient humidity using protein nanowires. *Nature* **578**, 550-554 (2020).

168. Lovley, D.R. and Holmes, D.E. Protein Nanowires: the Electrification of the Microbial World and Maybe Our Own. *J Bacteriol* **202**, e00331-20 (2020).

169. Liu, X., Walker, D.J.F., Nonnenmann, S.S., Sun, D. and Lovley, D.R. Direct Observation of Electrically Conductive Pili Emanating from *Geobacter sulfurreducens*. *mBio* **12**, e0220921 (2021).

170. Sun, Y.L., Montz, B.J., Selhorst, R., Tang, H.Y., Zhu, J., Nevin, K.P., Woodard, T.L., Ribbe, A.E., Russell, T.P., Nonnenmann, S.S., Lovley, D.R. and Emrick, T. Solvent-Induced Assembly of Microbial Protein Nanowires into Superstructured Bundles. *Biomacromolecules* **22**, 1305-1311 (2021).

171. Akiyama, K., Fukuda, M., Kobayashi, N., Matsuoka, A. and Shikama, K. The pH-dependent swinging-out of the distal histidine residue in ferric hemoglobin of a midge larva (*Tokunagayusurika akamusi*). *Biochim Biophys Acta* **1208**, 306-9 (1994).

172. Mara, M.W., Hadt, R.G., Reinhard, M.E., Kroll, T., Lim, H., Hartsock, R.W., Alonso-Mori, R., Chollet, M., Glownia, J.M., Nelson, S., Sokaras, D., Kunnus, K., Hodgson, K.O., Hedman, B., Bergmann, U., Gaffney, K.J. and Solomon, E.I. Metalloprotein entatic control of ligand-metal bonds quantified by ultrafast X-ray spectroscopy. *Science* **356**, 1276-1280 (2017).

173. Xiao, H., Peters, F.B., Yang, P.Y., Reed, S., Chittuluru, J.R. and Schultz, P.G. Genetic incorporation of histidine derivatives using an engineered pyrrolysyl-tRNA synthetase. *ACS Chem Biol* **9**, 1092-6 (2014).

174. Hayashi, T., Tinzl, M., Mori, T., Krengel, U., Proppe, J., Soetbeer, J., Klose, D., Jeschke, G., Reiher, M. and Hilvert, D. Capture and characterization of a reactive haem-carbenoid complex in an artificial metalloenzyme. *Nature Catalysis* **1**, 578-584 (2018).

175. Moore, E.J. and Fasan, R. Effect of proximal ligand substitutions on the carbene and nitrene transferase activity of myoglobin. *Tetrahedron* **75**, 2357-2363 (2019).

176. Eaton, W.A. and Hofrichter, J. Sickle Cell Hemoglobin Polymerization in *Advances in Protein Chemistry*, 63-279. Academic Press (1990).

177. Gorla, M. and Sepuri, N.B. Perturbation of apoptosis upon binding of tRNA to the heme domain of cytochrome *c*. *Apoptosis* **19**, 259-68 (2014).

178. Kuleta, P., Lasham, J., Sarewicz, M., Ekiert, I., Sharma, V., Ekiert, R. and Osyczka, A. Hydrogen bonding rearrangement by a mitochondrial disease mutation in cytochrome bc_1 perturbs heme b_H redox potential and spin state. *Proc Natl Acad Sci U S A* **118**, e2026169118 (2021).

179. Cao, B., Xu, H. and Mao, C. Controlled self-assembly of rodlike bacterial pili particles into ordered lattices. *Angew Chem Int Ed Engl* **50**, 6264-8 (2011).

180. Arslan, E., Schulz, H., Zufferey, R., Kunzler, P. and Thony-Meyer, L. Overproduction of the *Bradyrhizobium japonicum c*-type cytochrome subunits of the cbb_3 oxidase in *Escherichia coli*. *Biochem Biophys Res Commun* **251**, 744-7 (1998).

181. Londer, Y.Y., Pokkuluri, P.R., Tiede, D.M. and Schiffer, M. Production and preliminary characterization of a recombinant triheme cytochrome c_7 from *Geobacter sulfurreducens* in *Escherichia coli*. *Biochimica et Biophysica Acta (BBA) - Bioenergetics* **1554**, 202-211 (2002).

182. Shrestha, P.M., Rotaru, A.E., Summers, Z.M., Shrestha, M., Liu, F. and Lovley, D.R. Transcriptomic and genetic analysis of direct interspecies electron transfer. *Appl Environ Microbiol* **79**, 2397-404 (2013).

183. Savitzky, A. and Golay, M.J.E. Smoothing and Differentiation of Data by Simplified Least Squares Procedures. *Analytical Chemistry* **36**, 1627-1639 (2002).

184. Virtanen, P., Gommers, R., Oliphant, T.E., Haberland, M., Reddy, T., Cournapeau, D., Burovski, E., Peterson, P., Weckesser, W., Bright, J., van der Walt, S.J., Brett, M., Wilson, J., Millman, K.J., Mayorov, N., Nelson, A.R.J., Jones, E., Kern, R., Larson, E., Carey, C.J., Polat, I., Feng, Y., Moore, E.W., VanderPlas, J., Laxalde, D., Perktold, J., Cimrman, R., Henriksen, I., Quintero, E.A., Harris, C.R., Archibald, A.M., Ribeiro, A.H., Pedregosa, F., van Mulbregt, P. and SciPy, C. SciPy 1.0: fundamental algorithms for scientific computing in Python. *Nat Methods* **17**, 261-272 (2020).

185. Griffith, J.S. Theory of EPR in Low-Spin Ferric Haemoproteins. *Molecular Physics* **21**, 135-& (1971).

186. Taylor, C. The EPR of low spin heme complexes Relation of the τ_{2g} hole model to the directional properties of the *g* tensor, and a new method for calculating the ligand field parameters. *Biochimica et Biophysica Acta (BBA)-Protein Structure* **491**, 137-148 (1977).

187. Hendrich, M.P., Petasis, D., Arciero, D.M. and Hooper, A.B. Correlations of structure and electronic properties from EPR spectroscopy of hydroxylamine oxidoreductase. *J Am Chem Soc* **123**, 2997-3005 (2001).

188. Yatsunyk, L.A., Dawson, A., Carducci, M.D., Nichol, G.S. and Walker, F.A. Models of the cytochromes: Crystal structures and EPR spectral characterization of low-spin bis-imidazole complexes of (OETPP)Fe^{III} having intermediate ligand plane dihedral angles. *Inorganic chemistry* **45**, 5417-5428 (2006).

189. Clarke, T.A., Edwards, M.J., Gates, A.J., Hall, A., White, G.F., Bradley, J., Reardon, C.L., Shi, L., Beliaev, A.S., Marshall, M.J., Wang, Z., Watmough, N.J., Fredrickson, J.K., Zachara, J.M., Butt, J.N. and Richardson, D.J. Structure of a bacterial cell surface decaheme electron conduit. *Proc Natl Acad Sci U S A* **108**, 9384-9 (2011).

190. Salmeen, I. and Palmer, G. Electron paramagnetic resonance of beef-heart ferricytochrome *c*. *J Chem Phys* **48**, 2049-52 (1968).

191. Upadhyay, A.K., Petasis, D.T., Arciero, D.M., Hooper, A.B. and Hendrich, M.P. Spectroscopic characterization and assignment of reduction potentials in the tetraheme cytochrome *c*554 from *Nitrosomonas europaea*. *Journal of the American Chemical Society* **125**, 1738-1747 (2003).

192. Barrozo, A., El-Naggar, M.Y. and Krylov, A.I. Distinct Electron Conductance Regimes in Bacterial Decaheme Cytochromes. *Angew Chem Int Ed Engl* **57**, 6805-6809 (2018).

193. Phillips, J.C., Braun, R., Wang, W., Gumbart, J., Tajkhorshid, E., Villa, E., Chipot, C., Skeel, R.D., Kale, L. and Schulten, K. Scalable molecular dynamics with NAMD. *J Comput Chem* **26**, 1781-802 (2005).

194. Best, R.B., Zhu, X., Shim, J., Lopes, P.E., Mittal, J., Feig, M. and MacKerell Jr, A.D. Optimization of the additive CHARMM all-atom protein force field targeting improved sampling of the backbone φ, ψ and side-chain χ1 and χ2 dihedral angles. *Journal of chemical theory and computation* **8**, 3257-3273 (2012).

195. Autenrieth, F., Tajkhorshid, E., Baudry, J. and Luthey-Schulten, Z. Classical force field parameters for the heme prosthetic group of cytochrome *c*. *J Comput Chem* **25**, 1613-22 (2004).

196. Lovley, D.R. and Phillips, E.J. Organic matter mineralization with reduction of ferric iron in anaerobic sediments. *Appl Environ Microbiol* **51**, 683-9 (1986).

197. Case, D.A., Cheatham, T.E., 3rd, Darden, T., Gohlke, H., Luo, R., Merz, K.M., Jr., Onufriev, A., Simmerling, C., Wang, B. and Woods, R.J. The Amber biomolecular simulation programs. *J Comput Chem* **26**, 1668-88 (2005).

198. Case, D.A., Belfon, K., Ben-Shalom, I.Y., Brozell, S.R., Cerutti, D.S., Cheatham III, T.E., Cruzeiro, V.W.D., Darden, T.A., Duke, R.E., Giambasu, G., Gilson, M.K., Gohlke, H., Goetz, A.W., Harris, R., Izadi, S., Izmailov, S.A., Kasavajhala, K., Kovalenko, A., Krasny, R., Kurtzman, T., Lee, T.S., LeGrand, S., Li, P., Lin, C., Liu, J., Luchko, T., Luo, R., Man, V., Merz, K.M., Miao, Y., Mikhailovskii, O., Monard, G., Nguyen, H., Onufriev, A., Pan, F., Pantano, S., Qi, R., Roe, D.R., Roitberg, A., Sagui, C., Schott-Verdugo, S., Shen, J., Simmerling, C.L., Skrynnikov, N.R., Smith, J., Swails, J., Walker, R.C., Wang, J., Wilson, L., Wolf, R.M., Wu, X., Xiong, Y., Xue, Y., York, D.M. and Kollman, P.A. AMBER 2020. *University of California, San Francisco* (2020).

199. Hornak, V., Abel, R., Okur, A., Strockbine, B., Roitberg, A. and Simmerling, C. Comparison of multiple Amber force fields and development of improved protein backbone parameters. *Proteins* **65**, 712-25 (2006).

200. Crespo, A., Marti, M.A., Kalko, S.G., Morreale, A., Orozco, M., Gelpi, J.L., Luque, F.J. and Estrin, D.A. Theoretical study of the truncated hemoglobin HbN: exploring the molecular basis of the NO detoxification mechanism. *J Am Chem Soc* **127**, 4433-44 (2005).

201. Henriques, J.o., Costa, P.J., Calhorda, M.J. and Machuqueiro, M. Charge Parametrization of the D*v*H-c_3 Heme Group: Validation Using Constant-(pH,*E*) Molecular Dynamics Simulations. *The Journal of Physical Chemistry B* **117**, 70-82 (2013).

202. Cruzeiro, V.W.D., Amaral, M.S. and Roitberg, A.E. Redox potential replica exchange molecular dynamics at constant pH in AMBER: Implementation and validation. *J Chem Phys* **149**, 072338 (2018).

203. Cruzeiro, V.W.D., Feliciano, G.T. and Roitberg, A.E. Exploring Coupled Redox and pH Processes with a Force-Field-Based Approach: Applications to Five Different Systems. *J Am Chem Soc* **142**, 3823-3835 (2020).

204. Jorgensen, W.L., Chandrasekhar, J., Madura, J.D., Impey, R.W. and Klein, M.L. Comparison of Simple Potential Functions for Simulating Liquid Water. *Journal of Chemical Physics* **79**, 926-935 (1983).

205. Joung, I.S. and Cheatham III, T.E. Determination of alkali and halide monovalent ion parameters for use in explicitly solvated biomolecular simulations. *The journal of physical chemistry B* **112**, 9020-9041 (2008).

206. Darden, T., York, D. and Pedersen, L. Particle Mesh Ewald - an N•Log(*N*) Method for Ewald Sums in Large Systems. *Journal of Chemical Physics* **98**, 10089-10092 (1993).

207. Ryckaert, J.-P., Ciccotti, G. and Berendsen, H.J. Numerical integration of the Cartesian equations of motion of a system with constraints: molecular dynamics of *n*-alkanes. *Journal of computational physics* **23**, 327-341 (1977).

208. Miyamoto, S. and Kollman, P.A. Settle - an Analytical Version of the SHAKE and RATTLE Algorithm for Rigid Water Models. *Journal of Computational Chemistry* **13**, 952-962 (1992).

209. Gotz, A.W., Williamson, M.J., Xu, D., Poole, D., Le Grand, S. and Walker, R.C. Routine Microsecond Molecular Dynamics Simulations with AMBER on GPUs. 1. Generalized Born. *J Chem Theory Comput* **8**, 1542-1555 (2012).

210. Hamelberg, D., Mongan, J. and McCammon, J.A. Accelerated molecular dynamics: a promising and efficient simulation method for biomolecules. *J Chem Phys* **120**, 11919-29 (2004).

211. Hamelberg, D., de Oliveira, C.A. and McCammon, J.A. Sampling of slow diffusive conformational transitions with accelerated molecular dynamics. *J Chem Phys* **127**, 155102 (2007).

212. Miao, Y., Sinko, W., Pierce, L., Bucher, D., Walker, R.C. and McCammon, J.A. Improved Reweighting of Accelerated Molecular Dynamics Simulations for Free Energy Calculation. *J Chem Theory Comput* **10**, 2677-2689 (2014).

213. Jing, Z. and Sun, H. A comment on the reweighting method for accelerated molecular dynamics simulations. *J Chem Theory Comput* **11**, 2395-7 (2015).

214. Xin, Y., Doshi, U. and Hamelberg, D. Examining the limits of time reweighting and Kramers' rate theory to obtain correct kinetics from accelerated molecular dynamics. *J Chem Phys* **132**, 224101 (2010).

215. Doshi, U. and Hamelberg, D. Extracting Realistic Kinetics of Rare Activated Processes from Accelerated Molecular Dynamics Using Kramers' Theory. *J Chem Theory Comput* **7**, 575-81 (2011).

216. Miller III, B.R., McGee Jr, T.D., Swails, J.M., Homeyer, N., Gohlke, H. and Roitberg, A.E. MMPBSA. py: an efficient program for end-state free energy calculations. *Journal of chemical theory and computation* **8**, 3314-3321 (2012).

217. Yalcin, S. and Malvankar, N. Seeing is believing: Novel imaging methods help identify structure and function of *Geobacter* nanowires in electricity-producing biofilms in Roadmap on emerging concepts in the physical biology of bacterial biofilms: from surface sensing to community formation. *Phys Biol* **18**, 051501 (2021).

218. Dahl, P.J., Yi, S.M., Gu, Y.Q., Acharya, A., Shipps, C., Neu, J., O'Brien, J.P., Morzan, U.N., Chaudhuri, S., Guberman-Pfeffer, M.J., Vu, D., Yalcin, S.E., Batista, V.S. and Malvankar, N.S. A 300-fold conductivity increase in microbial cytochrome nanowires due to temperature-induced restructuring of hydrogen bonding networks. *Science Advances* **8**, eabm7193 (2022).

219. Neu, J., Shipps, C.C., Guberman-Pfeffer, M.J., Shen, C., Srikanth, V., Spies, J.A., Kirchhofer, N.D., Yalcin, S.E., Brudvig, G.W., Batista, V.S. and Malvankar, N.S. Microbial biofilms as living photoconductors due to ultrafast electron transfer in cytochrome OmcS nanowires. *Nature Communications* **13**, 5150 (2022).

220. Zhang, B., Cheng, H.Y. and Wang, A.J. Extracellular electron transfer through visible light induced excited-state outer membrane *c*-type cytochromes of *Geobacter sulfurreducens*. *Bioelectrochemistry* **138**, 107683 (2021).

221. Li, D.B., Cheng, Y.Y., Li, L.L., Li, W.W., Huang, Y.X., Pei, D.N., Tong, Z.H., Mu, Y. and Yu, H.Q. Light-driven microbial dissimilatory electron transfer to hematite. *Phys Chem Chem Phys* **16**, 23003-11 (2014).

222. Sekar, N., Jain, R., Yan, Y. and Ramasamy, R.P. Enhanced photo-bioelectrochemical energy conversion by genetically engineered cyanobacteria. *Biotechnol Bioeng* **113**, 675-9 (2016).

223. Dong, F.Y., Lee, Y.S., Gaffney, E.M., Liou, W. and Minteer, S.D. Engineering Cyanobacterium with Transmembrane Electron Transfer Ability for Bioelectrochemical Nitrogen Fixation. *Acs Catalysis* **11**, 13169-13179 (2021).

224. Meng, H., Zhang, W., Zhu, H., Yang, F., Zhang, Y., Zhou, J. and Li, Y. Over-expression of an electron transport protein OmcS provides sufficient NADH for D-lactate production in cyanobacterium. *Biotechnol Biofuels* **14**, 109 (2021).

225. Leang, C., Adams, L.A., Chin, K.J., Nevin, K.P., Methe, B.A., Webster, J., Sharma, M.L. and Lovley, D.R. Adaptation to disruption of the electron transfer pathway for Fe(III) reduction in *Geobacter sulfurreducens*. *J Bacteriol* **187**, 5918-26 (2005).

226. Tran, H.T. Investigation of chemotaxis genes and their functions in *Geobacter* species. *University of Massachusetts Amherst* (2009).

227. Aklujkar, M., Coppi, M.V., Leang, C., Kim, B.C., Chavan, M.A., Perpetua, L.A., Giloteaux, L., Liu, A. and Holmes, D.E. Proteins involved in electron transfer to Fe(III) and Mn(IV) oxides by *Geobacter sulfurreducens* and *Geobacter uraniireducens*. *Microbiology (Reading)* **159**, 515-535 (2013).

228. Wegener, G., Krukenberg, V., Riedel, D., Tegetmeyer, H.E. and Boetius, A. Intercellular wiring enables electron transfer between methanotrophic archaea and bacteria. *Nature* **526**, 587-U315 (2015).

229. Anantharaman, K., Brown, C.T., Hug, L.A., Sharon, I., Castelle, C.J., Probst, A.J., Thomas, B.C., Singh, A., Wilkins, M.J., Karaoz, U., Brodie, E.L., Williams, K.H., Hubbard, S.S. and Banfield, J.F. Thousands of microbial genomes shed light on interconnected biogeochemical processes in an aquifer system. *Nat Commun* **7**, 13219 (2016).

230. Anantharaman, K., Hausmann, B., Jungbluth, S.P., Kantor, R.S., Lavy, A., Warren, L.A., Rappe, M.S., Pester, M., Loy, A., Thomas, B.C. and Banfield, J.F. Expanded diversity of microbial groups that shape the dissimilatory sulfur cycle. *Isme Journal* **12**, 1715-1728 (2018).

231. Greene, A.C., Patel, B.K.C. and Yacob, S. *Geoalkalibacter subterraneus* sp nov., an anaerobic Fe(III)- and Mn(IV)-reducing bacterium from a petroleum reservoir, and emended descriptions of the family *Desulfuromonadaceae* and the genus *Geoalkalibacter*. *International Journal of Systematic and Evolutionary Microbiology* **59**, 781-785 (2009).

232. Santos, T.C., Silva, M.A., Morgado, L., Dantas, J.M. and Salgueiro, C.A. Diving into the redox properties of *Geobacter sulfurreducens* cytochromes: a model for extracellular electron transfer. *Dalton Transactions* **44**, 9335-9344 (2015).

233. Badalamenti, J.P., Krajmalnik-Brown, R. and Torres, C.I. Generation of high current densities by pure cultures of anode-respiring *Geoalkalibacter* spp. under alkaline and saline conditions in microbial electrochemical cells. *mBio* **4**, e00144-13 (2013).

234. Malvankar, N.S., Tuominen, M.T. and Lovley, D.R. Biofilm conductivity is a decisive variable for high-current-density *Geobacter sulfurreducens* microbial fuel cells. *Energy & Environmental Science* **5**, 5790-5797 (2012).

235. Sanford, R.A., Cole, J.R. and Tiedje, J.M. Characterization and description of *Anaeromyxobacter dehalogenans* gen. nov., sp. nov., an aryl-halorespiring facultative anaerobic myxobacterium. *Appl Environ Microbiol* **68**, 893-900 (2002).

236. Thomas, S.H., Wagner, R.D., Arakaki, A.K., Skolnick, J., Kirby, J.R., Shimkets, L.J., Sanford, R.A. and Loffler, F.E. The mosaic genome of *Anaeromyxobacter dehalogenans* strain 2CP-C suggests an aerobic common ancestor to the delta-proteobacteria. *PLoS One* **3**, e2103 (2008).

237. Strycharz, S.M., Gannon, S.M., Boles, A.R., Franks, A.E., Nevin, K.P. and Lovley, D.R. Reductive dechlorination of 2-chlorophenol by *Anaeromyxobacter dehalogenans* with an electrode serving as the electron donor. *Environmental microbiology reports* **2**, 289-294 (2010).

238. Deng, X., Dohmae, N., Nealson, K.H., Hashimoto, K. and Okamoto, A. Multi-heme cytochromes provide a pathway for survival in energy-limited environments. *Sci Adv* **4**, eaao5682 (2018).

239. Krukenberg, V., Riedel, D., Gruber-Vodicka, H.R., Buttigieg, P.L., Tegetmeyer, H.E., Boetius, A. and Wegener, G. Gene expression and ultrastructure of meso- and thermophilic methanotrophic consortia. *Environ Microbiol* **20**, 1651-1666 (2018).

240. Jumper, J., Evans, R., Pritzel, A., Green, T., Figurnov, M., Ronneberger, O., Tunyasuvunakool, K., Bates, R., Zidek, A., Potapenko, A., Bridgland, A., Meyer, C., Kohl, S.A.A., Ballard, A.J., Cowie, A., Romera-Paredes, B., Nikolov, S., Jain, R., Adler, J., Back, T., Petersen, S., Reiman, D., Clancy, E., Zielinski, M., Steinegger, M., Pacholska, M., Berghammer, T., Bodenstein, S., Silver, D., Vinyals, O., Senior, A.W., Kavukcuoglu, K., Kohli, P. and Hassabis, D. Highly accurate protein structure prediction with AlphaFold. *Nature* **596**, 583-589 (2021).

241. Scheller, S., Yu, H., Chadwick, G.L., McGlynn, S.E. and Orphan, V.J. Artificial electron acceptors decouple archaeal methane oxidation from sulfate reduction. *Science* **351**, 703-7 (2016).

242. Ashkenazy, H., Abadi, S., Martz, E., Chay, O., Mayrose, I., Pupko, T. and Ben-Tal, N. ConSurf 2016: an improved methodology to estimate and visualize evolutionary conservation in macromolecules. *Nucleic Acids Res* **44**, W344-50 (2016).

243. Altschul, S.F., Gish, W., Miller, W., Myers, E.W. and Lipman, D.J. Basic local alignment search tool. *J Mol Biol* **215**, 403-10 (1990).

244. Altschul, S.F., Madden, T.L., Schaffer, A.A., Zhang, J., Zhang, Z., Miller, W. and Lipman, D.J. Gapped BLAST and PSI-BLAST: a new generation of protein database search programs. *Nucleic Acids Res* **25**, 3389-402 (1997).

245. Tang, G., Peng, L., Baldwin, P.R., Mann, D.S., Jiang, W., Rees, I. and Ludtke, S.J. EMAN2: an extensible image processing suite for electron microscopy. *J Struct Biol* **157**, 38-46 (2007).

246. Cheung, M., Kajimura, N., Makino, F., Ashihara, M., Miyata, T., Kato, T., Namba, K. and Blocker, A.J. A method to achieve homogeneous dispersion of large transmembrane complexes within the holes of carbon films for electron cryomicroscopy. *J Struct Biol* **182**, 51-6 (2013).

247. Scheres, S.H.W. Amyloid structure determination in RELION-3.1. *Acta Crystallogr D Struct Biol* **76**, 94-101 (2020).

248. Emsley, P., Lohkamp, B., Scott, W.G. and Cowtan, K. Features and development of Coot. *Acta Crystallogr D Biol Crystallogr* **66**, 486-501 (2010).

249. Liebschner, D., Afonine, P.V., Baker, M.L., Bunkoczi, G., Chen, V.B., Croll, T.I., Hintze, B., Hung, L.W., Jain, S., McCoy, A.J., Moriarty, N.W., Oeffner, R.D., Poon, B.K., Prisant, M.G., Read, R.J., Richardson, J.S., Richardson, D.C., Sammito, M.D., Sobolev, O.V., Stockwell, D.H., Terwilliger, T.C., Urzhumtsev, A.G., Videau, L.L., Williams, C.J. and Adams, P.D. Macromolecular structure determination using X-rays, neutrons and electrons: recent developments in *Phenix*. *Acta Crystallogr D Struct Biol* **75**, 861-877 (2019).

250. Ma, W., Ying, Y.L., Qin, L.X., Gu, Z., Zhou, H., Li, D.W., Sutherland, T.C., Chen, H.Y. and Long, Y.T. Investigating electron-transfer processes using a biomimetic hybrid bilayer membrane system. *Nat Protoc* **8**, 439-50 (2013).

251. Yates, M.D., Golden, J.P., Roy, J., Strycharz-Glaven, S.M., Tsoi, S., Erickson, J.S., El-Naggar, M.Y., Calabrese Barton, S. and Tender, L.M. Thermally activated long range electron transport in living biofilms. *Phys Chem Chem Phys* **17**, 32564-70 (2015).

252. MATLAB. Version 9.12.0 (R2022a), The Mathworks, Inc. (2022).

253. Moisy, F. EzyFit. 2.44, MATLAB Central File Exchange (2016).

254. O'Haver, T. peakfit.m. 9.0.0.0, MATLAB Central File Exchange (2018).

255. Thomas, P.E., Ryan, D. and Levin, W. An improved staining procedure for the detection of the peroxidase activity of cytochrome *P*-450 on sodium dodecyl sulfate polyacrylamide gels. *Anal Biochem* **75**, 168-76 (1976).

256. Francis Jr, R.T. and Becker, R.R. Specific indication of hemoproteins in polyacrylamide gels using a double-staining process. *Analytical biochemistry* **136**, 509-514 (1984).

257. Teufel, F., Almagro Armenteros, J.J., Johansen, A.R., Gislason, M.H., Pihl, S.I., Tsirigos, K.D., Winther, O., Brunak, S., von Heijne, G. and Nielsen, H. SignalP 6.0 predicts all five types of signal peptides using protein language models. *Nat Biotechnol* **40**, 1023-1025 (2022).

258. The PyMOL Molecular Graphics System. Version 2.4.0, Schrödinger, LLC (2020).

259. Wang, F., Mustafa, K., Suciu, V., Joshi, K., Chan, C.H., Choi, S., Su, Z., Si, D., Hochbaum, A.I., Egelman, E.H. and Bond, D.R. Cryo-EM structure of an extracellular Geobacter OmcE cytochrome filament reveals tetrahaem packing. *Nat Microbiol* **7**, 1291-1300 (2022).

260. Hernandez-Eligio, A., Huerta-Miranda, G.A., Martinez-Bahena, S., Castrejon-Lopez, D., Miranda-Hernandez, M. and Juarez, K. GSU1771 regulates extracellular electron transfer and electroactive biofilm formation in *Geobacter sulfurreducens*: Genetic and electrochemical characterization. *Bioelectrochemistry* **145**, 108101 (2022).